UNIVERSITY OF CALIFORNIA SAN DIEGO

A Micro-Mechanical CFD-DEM Investigation of Proppant Flow and Transport with Field Analogue Injection and Rough Fractures

A dissertation submitted in partial satisfaction of the
requirements for the degree Doctor of Philosophy

in

Structural Engineering

by

Brian Yamashiro

Committee in charge:

Professor Ingrid Tomac, Chair
Professor Veronica Eliasson
Professor John Scott McCartney
Professor David Saintillan
Professor Qiang Zhu

2021

The Dissertation of Brian Yamashiro is approved, and it is acceptable in quality and form for publication on microfilm and electronically.

University of California San Diego

2021

DEDICATION

To my wife Connie, for her love and support.

TABLE OF CONTENTS

LIST OF FIGURES

LIST OF TABLES

LIST OF SYMBOLS

a	Fracture mechanical aperture
$\mathrm{A}, \mathrm{B}, \mathrm{C}$	Polynomial coefficients
A	Amplification parameter
B	Proportionality Constant
C	Particle volumetric concentration
C_D	Coefficient of drag
d	Particle diameter
D	Euclidian spatial dimension / fractal dimension
D_r	Durand-Froude number
E	Young's Modulus
$\boldsymbol{f}$	Force on particle in DEM simulations
f_c	Modification factor for attenuated particle settling rate due to concentration effects
f_r	Modification factor for attenuated particle settling rate due to fracture wall roughness
f_w	Modification factor for attenuated particle settling rate due to wall effects
F_r	Froude number
$\boldsymbol{F}$	Force
$\boldsymbol{g}$	Gravity
$g()$	Probability density function
$G()$	Spectral density function
G_s	Ratio of particle to fluid densities
h	Height
H	Fracture height
$\boldsymbol{I}$	Identity tensor
I	Moment of inertia
k	Wavenumber
L_h	Maximum distance traveled by upper injected particle
L_{Neigh}	Distance to particle's nearest neighboring particle
m	Body's mass
M	Shape measure
$\hat{\boldsymbol{n}}$	Surface normal vector
n	Exponent value for attenuated particle settling rate due to concentration
n_w	Number of windows evaluated
N_p	Number of evaluated particles
p	Fluid pressure
P	Number of points within a considered window
Q	Volumetric flow rate
r	Particle radius
R	Ruler length
$Re_{\|\|}$	Flow Reynolds number
Re_p	Particle Reynolds number
RMS, s	Root-mean-square (standard deviation)
S	Shear modulus
S_t	Stokes number
$\boldsymbol{t}$	Traction
t	Time
t_{relax}	Relaxation time
$\boldsymbol{T}$	Torque
T_{Hertz}	Hertz contact time scale
$T_{Rayleigh}$	Rayleigh wave propagation time scale
$\boldsymbol{u}$	Fluid velocity
$\boldsymbol{v}$	Particle velocity
$\boldsymbol{v}_t$	Single particle unrestricted terminal settling rate

v_c	Attenuated mean particle settling rate due to concentration effects
v_w	Attenuated mean particle settling rate due to wall effects
V	Volume
$\boldsymbol{V}_h$	Horizontal mean flow velocity for simplified proppant transport evaluation
$\boldsymbol{V}_v$	Considered particle settling velocity for simplified proppant transport evaluation
w	Window size length
x	Distance along fracture length
x_{cfd}	CFD cell size
y	Distance from centerline of flow profile
z	Residual value
$\propto$	Power spectral density function slope in log-log scale
α_f	Void fraction
γ	Viscoelastic damping coefficient
Γ_s	Fluid-solid interface
δ	Degree of body overlap
η	Coulomb friction coefficient
Θ, Ψ	Parameters for attenuation due to rough surfaces formulation
κ	Spring coefficient
λ	Surface asperity feature height
μ	Fluid dynamic viscosity
ν	Poisson's ratio
ρ	Density
$\boldsymbol{\sigma}$	Fluid stress tensor
$\boldsymbol{\tau}$	Shear stress tensor
$\boldsymbol{\Omega}$	Rotational velocity
Ω	Material phase domain

Miscellaneous
Subscripts

A, B	Relating to unresolved CFD-DEM "Model A" or "Model B" formulation
$buoy$	Buoyancy
$drag$	Drag
c	Relating to CFD cell
f	Relating to fluid phase
$hyd.$	Hydraulic
i, j	Designation between objects or iteration value
n, t	Normal and tangential, respectively
p	Relating to particle
s	Relating to solids phase
V	Volume
$*$	Reduced or effective

ACKNOWLEDGEMENTS

First, I would like to thank my advisor, Dr. Ingrid Tomac, for her support during this process. I came into this program with little numerical experience, and I greatly appreciate Dr. Tomac taking me on as a student and entrusting me with this work.

To my dissertation's committee members, Drs. John McCartney, Veronica Eliasson, Qiang Zhu, and David Saintillan, I am greatly appreciative of their review, feedback, and support during this research and my various interactions with them during my time at UC San Diego. I wish to also thank Dr. Daniel Tartakovsky for our conversations and his commentary during the later portions of this project.

Thank you to the other faculty, staff, and fellow students for their support during my time in this program. Especially thank you to Dr. Lelli Van Den Einde and Yvonne Wollmann for the encouraging conversations and support. Thank you to Julie Storing, Joana Halnez, Sandra de Sousa, and Kyung Brown for their help. Fatemah Behbehani, Mahta Movasat, Javier Buenrostro, and Wenpei Ma, I have greatly appreciated your friendship throughout these past years. I wish to say thank you as well for the continued support from my past advisors, Drs. Binod Tiwari and Beena Ajmera. Their encouragement and motivation have been greatly appreciated as I progressed through this work. Thank you as well to Dr. Mark Vondracek, for believing in me long ago, even when I didn't yet believe in myself. Thank you as well to the many others not mentioned here that helped me progress through this process.

Thank you most of all to my spouse, Dr. Connie Yamashiro. Your care, love, and encouragement during this time has meant the world to me. I do not know how I would have completed this without you. Thank you to my brother and sister in law for their support. Thank you to Penny and Buddy for bringing much needed levity during the stressful times.

Financial support for this research was provided by the U.S. National Science Foundation, Division of Civil, Mechanical and Manufacturing Innovation under grant NSF CMMI 1563614 and the Regents of the University of California, San Diego and is gratefully acknowledged. The opinions expressed in this dissertation are those of the author and not the NSF nor Regents of the University of California, San Diego.

This dissertation contains a combination of published and unpublished material, as described below.

Chapter 4 of this dissertation contains materials from a published manuscript with the journal, Computers and Geotechnics, titled "Particle clustering dynamics in dense-phase particle-fluid slurries"; a published manuscript with the journal, Geomechanics for Energy and the Environment, titled, "A Numerical Study of Neutrally Buoyant

Slickwater Proppant Flow and Transport in Rough Fractures"; and a manuscript submitted for publication (in review) with the journal, Powder Technology, tentatively titled, "Fracture Roughness Effects on Slickwater Proppant Slurry Settling Attenuation". Authors for all three of these works are Brian D. Yamashiro and Ingrid Tomac (2021). This dissertation's author is the first author of these papers.

Chapter 5 of this dissertation contains materials from a published manuscript with the journal, Computers and Geotechnics, titled "Particle clustering dynamics in dense-phase particle-fluid slurries". Authors are Brian D. Yamashiro and Ingrid Tomac (2021). This dissertation's author is the first author of this paper.

Chapter 6 of this dissertation contains materials from a published manuscript with the journal, Geomechanics for Energy and the Environment, titled, "A Numerical Study of Neutrally Buoyant Slickwater Proppant Flow and Transport in Rough Fractures". Authors are Brian D. Yamashiro and Ingrid Tomac. This dissertation's author is the first author of this paper.

Chapter 7 of this dissertation contains materials from a manuscript submitted for publication (in review) with the journal, Powder Technology, tentatively titled, "Fracture Roughness Effects on Slickwater Proppant Slurry Settling Attenuation". Authors are Brian D. Yamashiro and Ingrid Tomac. This dissertation's author is the first author of this paper.

Chapter 8 of this dissertation contains materials from a published manuscript with the journal, Computers and Geotechnics, titled "Particle clustering dynamics in dense-phase particle-fluid slurries"; a published manuscript with the journal, Geomechanics for Energy and the Environment, titled, "A Numerical Study of Neutrally Buoyant Slickwater Proppant Flow and Transport in Rough Fractures"; and a manuscript submitted for publication (in review) with the journal, Powder Technology, tentatively titled, "Fracture Roughness Effects on Slickwater Proppant Slurry Settling Attenuation". Authors for all three of these works are Brian D. Yamashiro and Ingrid Tomac (2021). This dissertation's author is the first author on these papers.

VITA

2007	Bachelor of Science in Civil Engineering, Iowa State University
2017	Master of Science in Civil Engineering, California State University, Fullerton
2021	Doctor of Philosophy in Structural Engineering, University of California San Diego

PUBLICATIONS

Peer-reviewed Journals and Special Publications

B.D. Yamashiro, I. Tomac, Resolved CFD-DEM Evaluation of Slickwater Proppant Slurry Settling Behavior in Rough Fractures, In review with Powder Technology.

B.D. Yamashiro, I. Tomac, A Numerical Study of Neutrally Buoyant Slickwater Proppant Flow and Transport in Rough Fractures, Geomech. Energy Environ. (2021) 100266. https://doi.org/10.1016/j.gete.2021.100266.

B.D. Yamashiro, I. Tomac, Particle clustering dynamics in dense-phase particle-fluid slurries, Comput. Geotech. 132 (2021) 104038. https://doi.org/10.1016/j.compgeo.2021.104038.

B. Tiwari, D. Pradel, B. Ajmera, B. Yamashiro, D. Khadka, Landslide Movement at Lokanthali during the 2015 Earthquake in Gorkha, Nepal, J. Geotech. Geoenvironmental Eng. 144 (2018) 05018001. https://doi.org/10.1061/(asce)gt.1943-5606.0001842.

B. Tiwari, B. Ajmera, B. Yamashiro, Q.-H. Phan, Effect of Overburden Pressure, Mineralogical Composition, and Plasticity on the Cyclic Behavior of Fine-Grained Soils, IFCEE Geotechnical Special Publication, American Society of Civil Engineers, (2018): pp. 266–275. https://doi.org/10.1061/9780784481585.027.

Conference Proceedings

B. Yamashiro, I. Tomac, Particle-fluid flow and transport within rough fractures, in: E3S Web Conf. 205, 2020. https://doi.org/10.1051/e3sconf/202020508010.

B.D. Yamashiro, I. Tomac, Particle clustering mechanisms and influence on proppant flow and transport, in: 54th U.S. Rock Mech. Symp., 2020.

B.D. Yamashiro, I. Tomac, Proppant slurry flow and transport within fractures with rough surfaces, in: 54th U.S. Rock Mech. Symp., 2020.

I, Tomac, B. Yamashiro, Particle-Fluid Flow and Transport Between Rough Surface Boundaries, in: 8th Int. Conf. on Discrete Elem. Meth., 2019.

I. Tomac, B. Yamashiro, Micromechanics of Dense-Phase Sand-Fluid Flow and Transport in Fractures, in: XVI PanAmerican Conference on Soil Mechanics and Geotechnical Engineering, 2019.

B.D. Yamashiro, I. Tomac, Proppant Behavior in Varying Fracture Alignments and Concentration Distributions, in: 53rd U.S. Rock Mech. Symp., 2019.

B. Ajmera, B. Tiwari, B. Yamashiro, Q.-H. Phan, Influence of Consolidation Pressure on Cyclic and Post-cyclic Response of Fine-Grained Soils with Varying Mineralogical Compositions and Plasticity Characteristics, in: Proc. GeoShanghai 2018 Int. Conf. Adv. Soil Dyn. Found. Eng., 2018: pp. 158–167. https://doi.org/10.1007/978-981-13-0131-5_18.

B. Tiwari, B. Ajmera, B. Yamashiro, N. Sitoula, Post-cyclic Strength Degradation of Black Cotton Soil in Kathmandu and its Effect on Landslide at Lokanthali of Araniko Highway During Mw 7.8 2015 Gorkha Earthquake, in: Proc. IPL Symp., UNESCO 2016: pp. 52-57.

B. Tiwari, B. Ajmera, B. Yamashiro, Causes of Cyclic Shear Failure at Lokanthali of Araniko Highway after Mw7.8 2015 Gorkha Earthquake, in: Proc. Fifth Int. Conf. Forensic Geotech. Eng., ISSMGE 2016: pp. 78-91.

Thesis

B. Yamashiro, Evaluation of Cyclic Mobility on Fine Grained Soil Due to Earthquake Induced Ground Motion, California State University, Fullerton, 2017.

ABSTRACT OF THE DISSERTATION

A Micro-Mechanical CFD-DEM Investigation of Proppant Flow and Transport with Field Analogue Injection and Rough Fractures

by

Brian Yamashiro

Doctor of Philosophy in Structural Engineering

University of California San Diego, 2021

Professor Ingrid Tomac, Chair

This work focuses on providing a better understanding of the proppant enhancement process utilized in hydraulic fracturing of rock networks. During rock fracture enhancement, proppants (i.e., rigid particles), are typically mixed with a carrier fluid and injected into a fracture network that has been initiated/propagated by a 'clean' particle-free fluid under pressure. Once introduced into an opened fracture, these proppant particles become confined between fracture faces once pressure is released and dissipates. This 'propped' material in turn provides a porous pathway for production fluid (e.g., hydrocarbons, cycled geothermal fluid) through the fracture network, improving productivity and/or yield.

The design of proppant applications is commonly reliant on simplified particle-fluid behavior. Several of these simplifications and assumptions include taking proppant horizontal transport rate as equal to averaged Poiseuille flow velocity, basing settling behavior of particles on Stokes law, and considering slurry settling behavior to be analogous to that between smooth parallel plates. It has been observed however, that the variance between in-lab

versus field achieved performance can vary by upwards of 90 %. To evaluate potential causes for this discrepancy, this work focuses on modeling of field-realistic conditions with high accuracy, including in-flow behavior of concentrated proppant slurries and proppant behavior within realistically rough fracture openings. The investigation is performed using combined computational fluid dynamics with the discrete element method (CFD-DEM). This method provides a detailed micro-scale representation of the complex interactions exhibited by this two-phase system, allowing for extraction and measure of difficult-to-capture fluid-solid interactions. Both the unresolved and resolved implementations of this modeling method are used to explore the meso and micro-scale behaviors of proppant slurries.

Findings reveal that complex particle clustering structures in flowing slurries can affect particle travel capacity and lead to variance from simplified slurry flow models. Proppant settling, flow, and transport within realistic rough fracture environments are also shown to exhibit notable fluid-particle-fracture surface interactions leading to significant variance from simplified modeling formulations that are based on smooth-walled domain behavioral simplifications. Overall, this work provides a greater understanding of proppant behavior in more field accurate conditions and contributes to better design considerations for future proppant treatments.

1 INTRODUCTION

1.1 Research Motivation

Two-phase, particle-fluid flow and transport is a subject of great interest to environmental and industrial practitioners. Hydraulic fracturing of rock reservoirs is one such sector, utilizing proppant particle-fluid injections for fracture enhancement projects.

The hydraulic fracturing process has been utilized for over half a century after first being introduced in 1949 [1]. Hydraulic fracturing aims to enhance a rock fracture system for more productive hydrocarbons recovery or improved fluid circulation and heat collection in geothermal energy systems. The general steps/stages of hydraulic fracturing with proppant enhancement are illustrated in Figure 1.1 and consists of [2,3]:

1) A particle-free fluid is first pumped into a wellbore that has been drilled into a rock formation. This fluid is pumped with increasing pressure that eventually initiates and propagates fracture(s) within the formation.
2) As fractures propagate, new rock formation areas become available, and the network of fractures expands. Continued and increased pumping maintains propagation and growth as some fluids are 'leaked-off' to the formation.
3) A particle-laden fluid (proppant slurry) is then pumped into the fracture system.
4) Once pumping is complete, the well is 'shut-in'. Fluid continues to leak off and pressure reduces, leading to closure of the networks' fractures. However, the fractures do not entirely close as the pumped in proppant particles become lodged between the faces and hold them open.

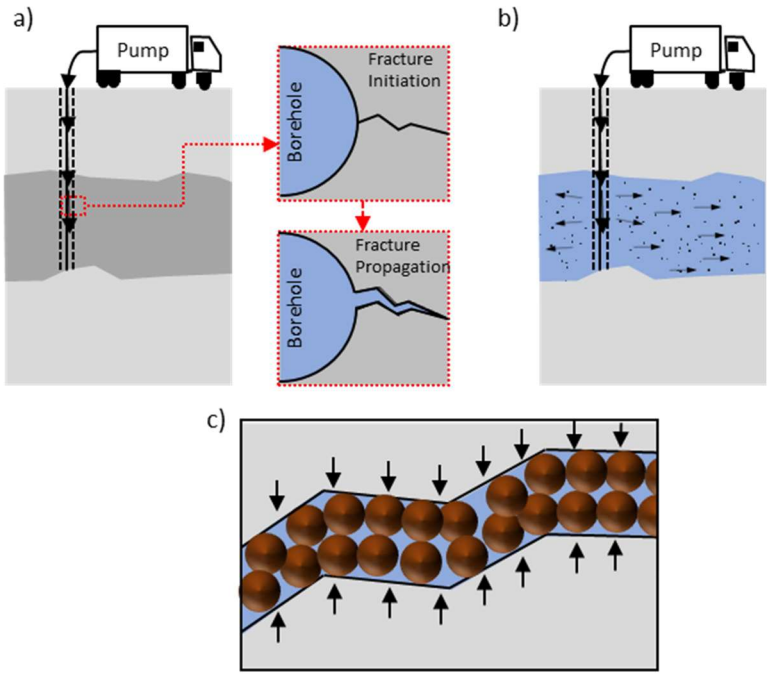

Figure 1.1: Diagram of hydraulic fracturing with proppant enhancement steps (images not to scale). a) Clean fluid injection to initiate and propagate fractures. b) Injection of proppant slurry into opened fractures. c) Closure of fracture about injected proppant particles.

Proppant itself is typically natural sand or manufactured ceramic granules, though other manufactured proppant shapes and unconventional materials have also been utilized [4]. Examples of typical proppant particles used in industry are shown in Figure 1.2.

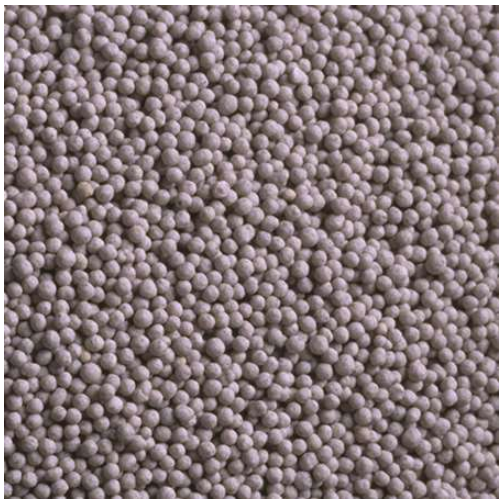

Figure 1.2: CARBOLITE ceramic proppant. CARBO Ceramics Inc., n.d. *CARBOLITE-450x450.png*, image, viewed 18 August 2021, Reprinted with permission from CARBO Ceramics Inc., <https://carboceramics.com/products/ceramic-proppant/carbolite-product-detail>.

A predominant carrier fluid used with proppant slurry enhancement is “slickwater”. Slickwater is a low viscosity fluid primarily consisting of water with a friction reducer or linear gel [5]. Slickwater treatments were noted to be the most utilized carrier fluid in fracture stimulation projects in the U.S. in 2004, accounting for approximately 31.1 % of all treatments [5,6]. Despite slickwater’s poorer proppant carrying capacity due to its lower viscosity, it has the added advantages of causing lower formation damage, being more easily recyclable, and having potential greater cost savings than crosslinked gel carrier fluids [5].

The successful design of proppant enhancement projects requires a clear understanding of the slurry’s dynamics and interactions as it flows and settles within a rock fracture system. Past studies and in use practices have derived and utilized behavioral formulations for proppant flow and transport based on simplified assumptions and conditions, including:

1) Evaluation of settling behavior based on Stokes law and/or derived from conditions that do not fully reflect an in-fracture geometry and flow state [7].
2) Horizontal transport of proppants is based on the mean flow velocity of the fluid [2,8].
3) Fracture wall effects are treated the same as though walls were smooth parallel plates [7,9–12].

These assumptions however may be too much of an oversimplification and cause inaccurate modeling of true in-field slurry behavior. Specific areas of concern that may lead to deviation from these simplified evaluations include:

1) Laboratory evaluation of slurry settling is typically performed in a quiescent or ‘creeping flow’ state [7]. Proppant injection however is a dynamic process and equivalence to quiescent settling behavior may be inaccurate in these flowing conditions. Further complex behaviors such as particle agglomeration are observed in slurry experiments which can cause further deviation from Stokes law-based settling behavior.
2) Horizontal flow behavior of even fluid-only flow in rough fractures is complex and can lead to the generation of eddies at rough surface features [13–15]. The influence of this complex flow on particles is unclear and adherence to simplified horizontal transport behavior is equally uncertain.
3) As mentioned above, fracture walls are not smooth and settling behavior between these rough boundaries is unlikely to be accurately modeled by the assumption of settling like that between smooth, parallel plates.

The concerns of inaccurate representation of proppant behavior are realized in the real world, as the variance between laboratory and field observed conductivity can be 90 % or greater [4]. Resolving such significant discrepancies in performance requires an understanding of proppant behavior on a more realistic context.

1.2 Research Objectives

The specific objectives of this study are to:

1) Evaluate the occurrence of particle agglomerations (i.e., clusters) in flowing proppant slurries and the conditions that result in variances to agglomeration characteristics.
2) Evaluate qualitative and quantitative clustering in flowing proppant slurries as well as their influences on slurry flow and transport.
3) Evaluate the extents of influence that rough fracture features have on proppant conveyance and settling behavior as well as sensitivity to behavioral variance due to differing slurry and fracture characteristics (e.g., concentration, flowrate, aperture, degree of roughness).
4) To evaluate adherence or deviation from simplified evaluations for above studied slurry evaluations.
5) Evaluate the micro-mechanical causes of behavior variances.

1.3 Research Approach

In order to gain insight into flow and transport behaviors, as well as evaluate micro-scale interactions within proppant slurries, this two-phase system is modeled with computational methods in this work. Computational evaluations are noted to provide accurate, detailed representation of physical systems while allowing for broader problem considerations than possible with analytical approaches [16]. In addition, computational approaches have greater cost efficiency (both fiscally and timewise) compared to experimental approaches. Two of the more prominent approaches to evaluate two-phase, solids-fluid systems are two -fluid models (TFM) and coupled computational fluid dynamics with the discrete element method (CFD-DEM) [17]. In a TFM, the solids are represented as a second interpenetrating continuum phase with the surrounding immersive fluid [17,18]. The flow domain is discretized with cell size larger than the particle size, modeling the two continuum phases' behavior using the averaged Navier-Stokes and continuity equations. While computationally less expensive than CFD-DEM, a TFM approach does present limitations. In a TFM approach, individual particles cannot be observed, only the characteristics of clusters [17]. Further, to represent maximum packing fraction conditions in the solids phase, an additional granular pressure term or ad-hoc method is needed [19]. By contrast, the CFD-DEM method tracks each particle individually and allows for detailed particle-scale information, including trajectories and forces acting on individual particles [18]. When particle interactions are described with soft (deformable) collisions that occur over a period of time, more than one particle

can be in contact at a time [17]. The CFD-DEM formulation approach is found to be appropriate for both dilute and dense phases in dynamic and quasi-static conditions. This detailed information and greater capability to represent the complex interactions between the fluid and each particle are important in evaluating the mechanisms occurring in these complex two-phase systems [18]. In practical application, Golshan et al. [20] found that CFD-DEM simulations were found to provide more accurate voidage and velocity distribution representation than TFM when compared against experimental results from the literature. Therefore, CFD-DEM is used in this work.

Both the unresolved and resolved CFD-DEM methods (see Figure 1.3) are used in this work to evaluate the behaviors of proppant-fluid slurries. The unresolved method is selected to evaluate particle agglomeration capacity and behavior of flowing slurries. In this method, CFD cells are of larger size than the particles. The coupling between particles and fluid cells is evaluated with theoretical or empirically developed correlations [17]. The less refined CFD mesh makes the computation less expensive and more capable for evaluations containing large quantities of particles in larger-sized domains. Since clustering occurs when there is concentrated, numerous particles present and also since flowing, settling slurries can travel over long lengths (i.e., large domains), the unresolved CFD-DEM is considered the more appropriate option to study flowing slurry agglomeration behavior.

The resolved CFD-DEM method is implemented for the study of particle slurry behavior in rough fractures. While the unresolved CFD-DEM approach can provide a geometric representation of large-scale roughness features relative to particle size, small-scale roughness and surface unevenness characteristics are not well captured. As discretized fluid mesh cell sizes are larger than individual particles for the unresolved CFD-DEM approach, typically by a factor greater than 1.5 [21], generating a CFD mesh that adheres to these fine roughness features is not realistic. The possible narrowness of an aperture while maintaining an adequately resolved mesh across the opening is also greatly limited due to the largeness of the CFD cells. Small scale roughness features however may play an important role in proppant behavior within rough fractures, especially for flowing proppant slurries and at a narrow aperture. Various works [13–15] have demonstrated the development of eddies at rough surface features that affect fluid-only flow behavior within fractures. Works that specifically examine these small-scale roughness impacts on proppant flows are not present in the current literature to the author's knowledge.

As CFD cells are of size smaller than the particle in the resolved method, fluid mesh adherence to surface features smaller than particle size is possible, thus providing capability to study the influence from these features. Fluid interaction with particles is also better represented in the resolved method compared to the unresolved method

[17]. Whereas unresolved CFD-DEM utilizes correlative empirical and theoretical relationships to model fluid-particle interactions, resolved CFD-DEM evaluates fluid interaction about the individual particles' surfaces [17,22]. Unfortunately, the higher mesh resolution utilized with the resolved method makes it only practical for simulations containing at most a few hundred particles [17].

To generate rough fracture surfaces to use with the resolved CFD-DEM simulations, a spectral method is employed that uses quantitative roughness parameters that describe both the textural and asperity feature height roughness characteristics. A more in-depth explanation of both the resolved and unresolved CFD-DEM methods, as well as generation of synthetic fracture surfaces, is presented in Chapter 3.

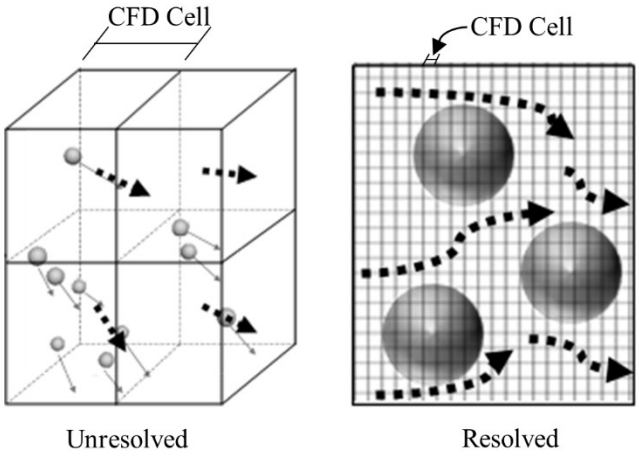

Figure 1.3: Diagrams of unresolved and resolved CFD-DEM implementations.

1.4 Dissertation Organization

This dissertation is prepared as a paper-based dissertation. The different chapters are comprised of excerpts of submitted or published works in peer-reviewed journals. The organization of the subsequent chapters for this dissertation are as follows:

Chapter 2 presents background and literature review relating to proppant enhancement, particle fluid behaviors, and rock surface roughness description.

Chapter 3 presents details regarding the CFD-DEM methodologies and properties employed in this study. Processes utilized in the generation of synthetic fracture surfaces are also presented.

Chapter 4 provides information regarding model verification and validation steps taken to evaluate the fitness of proposed methods for use in the study.

Chapter 5 presents an evaluation of flowing proppant slurry behavior focusing on agglomeration capacity and influences on proppant flow and transport.

Chapter 6 presents an evaluation of proppant flow and transport within rough fractures, focusing on rough fracture influence on neutrally buoyant particle slurry flows. This evaluation includes studying the impact of complex flow behavior induced by rough fracture surfaces and particle-fracture interaction influence on injected slurry behavior compared to smooth wall fracture behavior.

Chapter 7 presents an evaluation of settling slurry behavior in quiescent and flowing states in both smooth and rough fracture settlings. Proposed quiescent settling behavior formulation to incorporate additional attenuation from rough fracture surfaces is also presented.

Chapter 8 summarizes conclusions and future directions for this research.

2 BACKGROUND AND LITERATURE REVIEW

2.1 Background

This section provides a background of particle-fluid behavioral understanding relevant proppant flow and transport considerations. Background information of rock surface roughness measurement is also presented.

2.1.1 Single Particle Settling Behavior

As initially demonstrated by Stokes, a single particle moving in a viscous fluid will experience a drag force proportional to the particle's size, speed, and viscosity of the surrounding fluid [23]. In the case of a particle settling in an infinite fluid, the force of gravity and buoyancy balances with this drag force and results in the particle achieving a terminal settling velocity ($\boldsymbol{v}_t$) [24]:

$$\boldsymbol{v}_t = \sqrt{\frac{4}{3}\frac{\boldsymbol{g}d}{C_D}\left(\frac{\rho_s - \rho_f}{\rho_f}\right)} \tag{1.1}$$

with ρ_s equaling the particle's density, ρ_f equaling the fluid's density, d is the particle's diameter, $\boldsymbol{g}$ equaling gravity, and C_D equaling the coefficient of drag. Within the Stokes regime (i.e., Re_p<<1) C_D can be evaluated as $C_D = 24/Re_p$, where Re_p is the particle Reynolds number, expressed as:

$$Re_p = \frac{\rho_f d|\boldsymbol{u} - \boldsymbol{v}|}{\mu} \tag{1.2}$$

here, $\boldsymbol{u}$ is the fluid's velocity, $\boldsymbol{v}$ the particle's velocity, and μ is the fluid's dynamic viscosity. The Reynolds number itself is a dimensionless value that represents the ratio of inertial forces, in this case from the relative particle motion, to viscous forces from the fluid [17]. Outside of the Stokes regime, as inertial effects become more influential, C_D is empirically determined. An approximation of C_D presented by Dalla Valle [25] is expressed as:

$$C_D = \left(0.63 + \frac{4.8}{\sqrt{Re_p}}\right)^2 \tag{1.3}$$

Further, the force of drag on the particle ($\boldsymbol{F}_{drag}$) can be found by:

$$\boldsymbol{F}_{drag} = C_D \frac{\pi}{8}\frac{\mu^2}{\rho_f} {Re_p}^2 \tag{1.4}$$

As indicated by Barbati et al. [3], maximum values for Re_p in proppant slurries are approximately 100 or less. This range, along with the empirically determined values of C_D and the approximation by Dalla Valle [25] for spherical particles is shown in Figure 2.1.

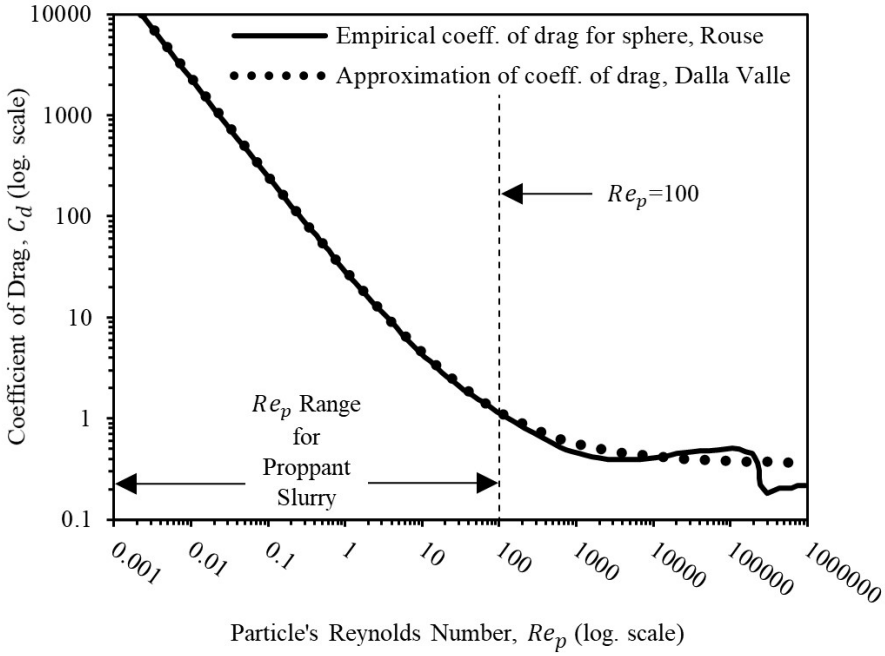

Figure 2.1: Empirical evaluation of coefficient of drag from Rouse [26] and approximation of coefficient of drag per Dalla Valle [25] for spherical particles. Range of Re_p values for proppant slurries per Barbati et al. [3] also indicated.

2.1.2 Hindered Settling Rates Due to Particle Volumetric Concentration Effects

Particle settling behavior is complicated when present in dense particle concentrations due to the enhanced particle-particle and particle-fluid interactions [27]. These complex interactions can lead to hindered settling behavior in some suspensions. Various researchers have determined formulations to describe the average reduction in particle settling rate due to this attenuation. Several of these formulations are expressed in Table 2.1. Here the ratio for average terminal settling velocity of particles in a concentrated slurry ($\boldsymbol{v}_c$) to terminal settling velocity of a single, unrestricted particle ($\boldsymbol{v}_t$) is expressed as f_c. C is the particle volumetric concentration in the slurry.

Table 2.1:Attenuated settling rate from concentration effects formulations

Formulation*	Author(s)	Exponent Values
$f_c = \frac{v_c}{v_t} = (1-C)^n$ (2.1)	Richardson and Zaki [28]	$n = 4.35Re_p^{-0.03}$ for $0.2 < Re_p < 1$ $n = 4.45Re_p^{-0.1}$ for $1 < Re_p < 200$
$f_c = \frac{v_c}{v_t} = 2.37C^2 - 3.08C + 1$ (2.2)	Gadde et al. [29]	n/a
$f_c = \frac{v_c}{v_t} = (1-C)^n$ (2.3)	Garside and Al-Dibouni [30]	$n = \frac{5.09 + 0.2839Re_p^{0.877}}{1 + 0.104Re_p^{0.87}}$
$f_c = \frac{v_c}{v_t} = (1-C)^n$ (2.4)	Novotny [31]	$n = 5.5$ for $Re_p \leq 2$ $n = 3.5$ for $2 < Re_p < 500$

*Ignoring boundary influences.

2.1.3 Wall Effects

Proximity to boundaries also causes additional attenuation in particle settling rate. Most past studies and in use proppant modeling approaches assume slurry settling can be adequately modeled by assuming smooth-surfaced fracture walls and their associated influences [7,32]. Many researchers have evaluated wall attenuation effects on particle settling [33,34], including specific focus on proppant settling attenuation due to wall effects [29,31,35,36]. Liu and Sharma [35] in their experiments of particle settling rates between smooth walls in water concluded that wall effects are mostly unimportant until fracture opening width was 10 % to 20 % larger than the particle diameter. It is noted that Liu and Sharma's attenuation results in low viscosity fluids are more subdued than other researchers' reported experimental findings for settling particles between smooth walls (e.g., Tachibana and Kitasho [37]; Miyamura et al. [38]). In a study by Novotny [31] on proppant particle settling in fractures, they presented a wall effect reduction factor (f_w), that describes the attenuated settling rate of a particle due to wall effects (v_w) relative to that of an unbounded particle (i.e. v_w/v_t), as:

$$f_w = \frac{v_w}{v_t} = 1 - 0.6526\left(\frac{d}{a}\right) + 0.147\left(\frac{d}{a}\right)^3 - 0.131\left(\frac{d}{a}\right)^4 - 0.0644\left(\frac{d}{a}\right)^5 \quad for\ (Re_p < 1) \tag{2.5}$$

$$f_w = \frac{v_w}{v_t} = 1 - \left(\frac{d}{2a}\right)^{\frac{3}{2}}, \qquad for\ (Re_p \geq 100) \tag{2.6}$$

Novotny noted good agreement between their attenuation approximation and laboratory measured settling results.

In addition to attenuated settling effects, confinement between two parallel walls can cause variance in horizontal particle velocity depending on aperture (i.e., mechanical aperture, a) to particle size (i.e., ratio of d/a). Staben et al. [39] performed numerical simulations of particle transport within a smooth-walled domain with varying

d/a ratios. Their results were later experimentally validated by Staben and Davis [40]. The work of Staben et al. and Staben and Davis were performed at small Reynolds number flows where the Reynolds number for flow between parallel plates ($Re_{||}$) is defined as:

$$Re_{||} = \frac{2\rho_f \bar{\boldsymbol{u}} a}{\mu} \tag{2.7}$$

As slickwater proppant flows are at typically higher rates, Blyton [41], presented particle transport behavior for $Re_{||}$ = 1000 and 2000 in their work. Deviation in behavior for these higher flow rates as aperture narrowed was reported by Blyton and attributed to reduced wall retardation with increased inertial effects with these higher flow rates. Figure 2.2 shows combination of the results reported by Staben et al. [39], Staben and Davis [40], and Blyton [41]. Curves for Staben et al. [39] and Blyton [41] are from linear extrapolation between result values presented in those works. Extracted values from Staben and Davis [40] are for an averaging of data points from particles located from a normalized position (i.e., particle centroid position divided by mechanical aperture) of 0.45 to 0.55 within their smooth wall tests for both the blunted and angled channel entrance results presented in that work.

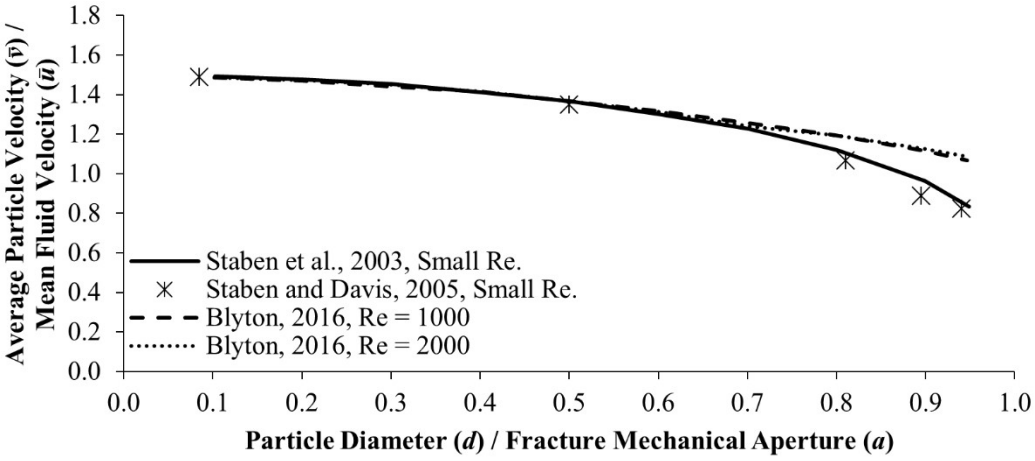

Figure 2.2: Particle diameter to fracture mechanical aperture ratio (i.e., d/a ratio) versus average particle velocity to mean fluid velocity ratio (i.e. $\bar{\boldsymbol{v}}/\bar{\boldsymbol{u}}$) results from Staben et al.[39], Staben and Davis [40], and Blyton [41].

Liu [42] and Liu and Sharma [35], in their experimental work of particles flowing between parallel walled slots found similar results to those reported by Staben et al. [39].

Staben et al. [39] and Staben and Davis [40] also evaluated average multiparticle conveyance behavior for particles between varying apertures. Numerical evaluation from Staben et al. [39] were based on a uniform

concentration of particles within a channel's aperture and empirical values from Staben and Davis [40] were taken from the averaged measured particle velocities of particle solutions injected into their experimental channel. Figure 2.3 shows the simulated and experimentally validated findings from these works. As can be seen in Figure 2.3, good agreement was found between the simulated and experimental results.

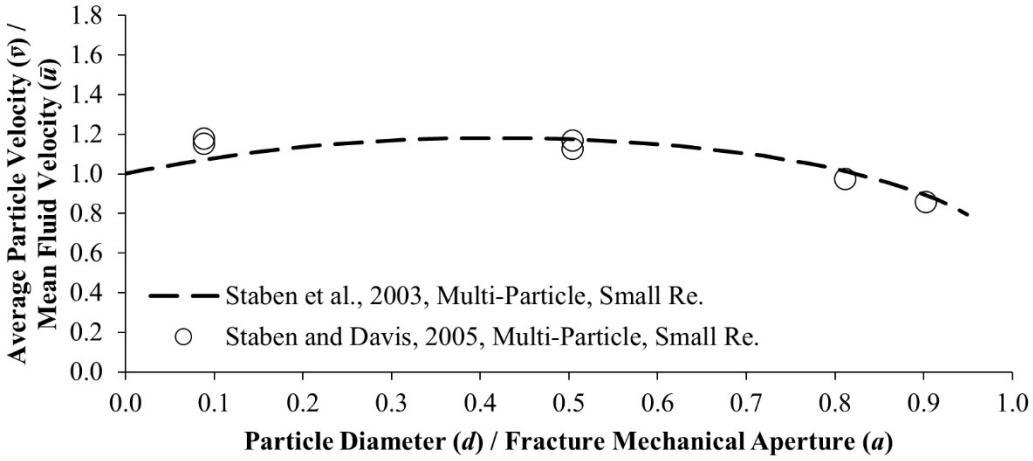

Figure 2.3: d/a ratio versus multiparticle $\bar{v}/\bar{u}$ findings from Staben et al. [39] and Staben and Davis [40].

There exists very limited literature on the effects of fluid flow itself on particle settling when confined within narrow slots with flow rates beyond the Stokes regime. Liu and Sharma [35] presented the results of three tests for a particle settling in flow within a slot and indicated that particle settling velocity was not affected by the flow condition within the confined slot. Others however have noted variance in particle behavior in flowing conditions and within close proximity of a boundary. Wham et al. [43] numerically evaluated the drag on a fluidized particle centered within cylinders at varying Reynolds number values (up to 100) and various particle diameter to cylinder diameter ratios. They found that in cylinders with larger relative diameters to particle size, increases in Reynolds number corresponded with a rapid increase in the drag. Additionally, at like Reynolds numbers, a decrease in the cylinder diameter relative to particle diameter caused the fluid wake trailing the particle to shrink (suppressing the wake formation size). In a study of wall effects on spheroid particles within cylinders, Kishore and Gu [44] likewise found that increased confinement, while maintaining the same Reynolds number flow, suppressed the trailing wake size. Additionally, they noted that with this increased confinement and like Reynolds number flow conditions, an increase in the pressure coefficient was observed about the spheroids' bodies. Thus, the studies by Wham et al. [43] and Kishore and Gu [44] do imply that the influence of flow on a confined body can be significant. Still, as these investigations focused on

evaluating stationary bodies, a detailed understanding of the influence of these effects on bodies sedimenting while confined is unclear.

2.1.4 Rough Rock Surface Description as Fractals

Fractals have been shown to provide a topographical description of fractured rock surfaces [45,46]. A fractal can be described as a shape that topologically exists between Euclidian spatial shapes such as lines, surfaces, and cubes, i.e. between 1-D, 2-D, and 3-D [47,48]. Majumdar and Bhushan [48] elaborate that measurement of objects defined at Euclidian spatial designations, i.e., integer values, does not vary based on the unit of measure. In general terms, the measure of a shape, M, of Euclidian space, D, is expressed as:

$$M = \sum R^D \tag{2.8}$$

where R is the linear ruler's length. In this case, the size of R is irrelevant, as it will always sum to the total shape dimension. Fractals, such as rock surface topology, are expressed with spatial dimensions, D, that lies between these Euclidian space integer values, i.e., are represented by fractional or fractal dimensions. Typical rock surfaces have fractal dimensions ranging from 2.0 to 2.5 [49–51]. Smaller fractal dimensions correspond to smoother surfaces and increasing fractal dimensions indicate increasing textural roughness. Respective profile fractal dimension, $D_{profile}$, relating to a surface fractal dimension, $D_{surface}$, can be expressed as [49]:

$$D_{profile} = D_{surface} - 1 \tag{2.9}$$

Fractal dimension provides spatial correlation of the surface roughness features, however standard deviation, i.e., root-mean-square (*RMS*), of surface asperity heights is also needed to describe local height distribution about a mean value [49,50]. It is additionally noted that measured values of fractal dimension have been shown to be insensitive to *RMS* for certain fractal dimension measurement methods [52].

Classic examples of fractals, such as the Koch curve, have 'self-similar' characteristics. Self-similarity means that when a subsection of the shape is magnified isotopically in all directions, the subsection is statistically identical to the shape as a whole [53]. Rock fracture surfaces, particularly at the scales of interest for this study, have been noted to have 'self-affine' characteristics [46,47,52]. Self-affine fractal sets differ from self-similar sets in that a magnified subsection will only appear statistically identical if magnified at differing scales for the dimensions parallel and perpendicular to a surface [53].

Various methods for synthetically generating fractal surfaces exist including, but not limited to, displacement, Weierstrass-Mandelbrot equation-based, and spectral synthesis (also called Fourier filtering) methods [54,55]. Brown [50] proposed a spectral synthesis-based method for the generation of realistic rock surfaces. For Brown's method, surface asperity height features, λ, are described based on a probability density function, $g(\lambda)$, such as Gaussian distribution:

$$g(\lambda) = \frac{1}{s\sqrt{2\pi}} e^{-\frac{\lambda-\lambda_{mean}}{2s^2}} \tag{2.10}$$

where s is the standard deviation, i.e. *RMS*, of the asperity height features and λ_{mean} is the mean surface height value.

The spatial correlation of roughness features, i.e., its textural description, is expressed by an autocorrelation function or the equivalent Fourier transform of that function, the power spectrum [50]. Power spectrum is constructed by decomposing the spatial series into sinusoidal parts, including each component's phase, wavelength, and amplitude. Plotting of the components' inverse wavelength, i.e., wavenumber, versus the squared amplitude (i.e., power) results in the power spectrum. Specific normalization of the power spectrum results in the power spectral density (PSD). Power spectral density function, $G(k)$, for rock fractures have been shown to exhibit decreasing power law behavior expressed by [50]:

$$G(k) = Bk^{-\propto} \tag{2.11}$$

with B equaling the proportionality constant, k equaling the wavenumber, and $\propto$ equaling the power-law exponent. When plotted in log-log scale, the function is linear in appearance where, B, is the intercept of the power spectrum line and $-\propto$ is the slope. The relationship between fractal dimension and the slope, $\propto$, is found to be $D_{surface} = (7-\propto)/2$ for rock fracture surfaces and $D_{prof} = (5-\propto)/2$ for profiles [50].

Asperity height *RMS* values are noted to relate to considered rock length or window size and fractal dimension by [49,53,56,57]:

$$RMS(w) = Aw^{2-D} \tag{2.12}$$

where w is the considered window size length and A is an amplitude parameter. Further discussion of determining *RMS* heights for rock surfaces as utilized in this work are presented in Chapter 6 (section 6.2.1).

2.2 Literature Review

This section focuses on current understanding and in use practice of evaluating proppant behavior within fractures. Specific discussion of proppant transport mechanisms, clustering of particles within proppant slurries, and fracture wall influences are included.

2.2.1 Proppant Transport Mechanisms

Early study into the mechanisms that lead to proppant transport within a fracture mostly point to the concept of critical equilibrium bed height [9,10,58,59]. In this mechanism, particles gradually settle within the fracture domain until a point is reached where the reduced flow cross-sectional area above the bed leads to a critically high fluid velocity, causing re-fluidization of upper mound particles and progressing particle travel down fracture. This has also been described as 'bed-load' transport [8,11,60]. One of the earliest studies of this mechanism is from Kern et al. [9]. For their study, sand slurries were injected into a 0.56 m x 0.19 m x 0.00635 m experimental slot fracture. As described above, mounding of sand particles was observed within the slot till a critical mound height was achieved, at which point, down fracture sand transport re-initiated. Many others have built upon the study of 'bed-load' transport in this context, most notably including Babcock et al. [10], Patankar et al. [58], and Wang et al. [59].

The importance of bed-load contribution to proppant particle transport at field scale though has been questioned by other researchers based on empirical and analytical evaluations. In evaluating contributing mechanisms of proppant particle transport in low viscosity fluid slurries (e.g., bed load, viscous drag of suspended load, and turbulent load transport) Biot and Medlin [60] and Medlin et al. [11] concluded that viscous drag of suspended particles was the only significant transport mechanism in field scale proppant transport. The significance of viscous drag load was also emphasized by McClure [8], who evaluated laboratory transport behavior and provided comparisons to sediment and pipeline slurry transport relationships. McClure [8] noted that in the great majority of field proppant treatments, required conditions for dominant contribution of bed-load transport are not met. Further, it was emphasized that experimental correlations of bed load transport capacity do not appear to scale with in field fracture heights. Biot and Medlin [60] additionally commented on 'stimulated' turbulence's influence at injection perforation points, noting that it "dies out very rapidly away from the entrance", and "is not an important factor in fractures of much length" so therefore "…natural and stimulated turbulence can be ignored as a transport mechanisms".

Assessment of suspended particle conveyance in flow is simplified in some evaluations, modeling transport based on the quiescent settling behavior with the horizontal flow based on the fluid's mean velocity [2,8,29]. Figure 2.4 shows a diagram of simple travel and settling behavior following these assumptions [2,8].

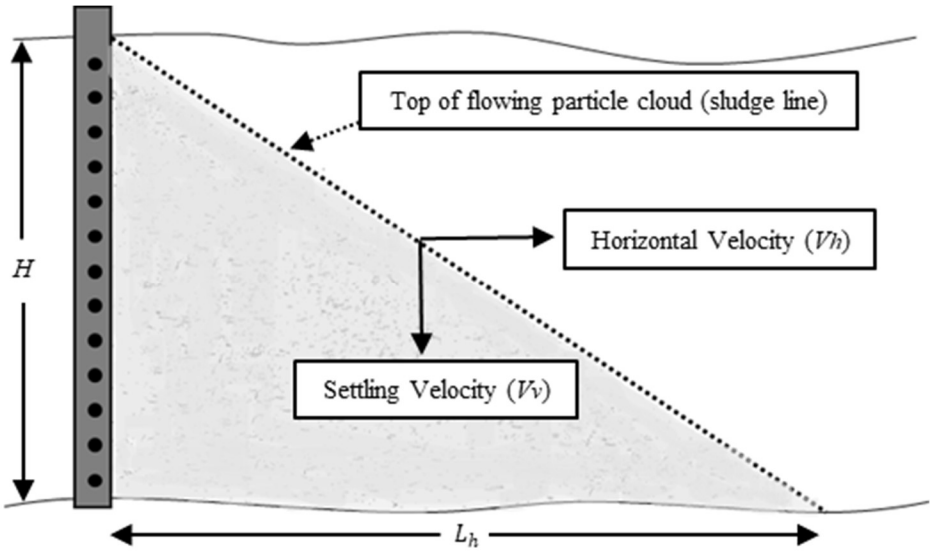

Figure 2.4: Simplified particle transport evaluation and travel distance for proppant injection.

The distance that a proppant particle travels before deposition due to gravity can be estimated as [2,8]:

$$L_h = \frac{\boldsymbol{V}_h H}{\boldsymbol{V}_v} \tag{2.13}$$

where L_h is the maximum distance traveled by the upper injected particle, $\boldsymbol{V}_h$ is the horizontal mean flow velocity, H is the height of the fracture, and $\boldsymbol{V}_v$ is the particle settling velocity, which can be taken as the hindered settling rate.

2.2.2 Clustering in Concentrated Slurries

Influences from complex particle-fluid interactions within suspended, concentrated slurry loads and their impacts on transport is further of concern. Some studies have noted that particle agglomeration (i.e., clustering) can cause variance from the attenuated settling behavior discussed in subsection 2.1.2 [2,8].

Kirkby and Rockefeller [61] performed evaluations of sedimenting proppant slurries in an annular slot apparatus (constructed from two plastic cylinders of different diameter) under non-flowing conditions. They noted that particle clustering with enhanced sedimentation rates was observed for typical proppant slurry particle volumetric

concentrations. McMechan and Shah likewise noted for several of their large slot experiments with quiescently settling proppant slurries that formation of clustered sand particle groups were observed with higher settling rates than non-clustered particles. Luo and Tomac [62], from their quiescent settling slot experiments, found that agglomerations were more prevalent in narrower wall aperture slots with higher particle volumetric concentration slurries in quiescently settling slurry slot experiments. Further, agglomerations lead to higher overall settling rates in both smooth and rough wall slot experiments.

Though the above illustrates the clustering capability and influence of concentrated particle slurries in static states, the prevalence and influence in flowing states is less agreed upon. Liu and Sharma [35] observed proppant particle clustering in concentrated, quiescently settling slurries for their vertical slot fracture experiments, but noted that particle clustering was insignificant for flowing slurries. It is noted that Liu and Sharma do not specify what flowing slurry concentrations were evaluated for clustering occurrence. Additionally, only visual video image analysis appears to have been used in determining the occurrence or absence of clustering. This method can become unreliable as particle concentrations increase and lead to visual obscuration [63]. Other vertical fracture slot experiments do note clustering in flowing slurries. In work looking at proppant injection in a vertical slot model, Kadhim et al. [64] noted proppant clustering occurring in early sections of the slot during the initial stage of the injection process. Additionally, Clark et al. [65] performed experiments with flowing slurries in a 4-ft × 12-ft vertical fracture slot model and noted that particles tended to travel as clusters. Clusters were observed for particle concentrations above 0.5 lb/gal in both Newtonian and Non-Newtonian fluids. In a follow-up study by Sievert et al. [66], it was again noted that in proppant slurries with non-Newtonian fluids, particles tended to flow more as clusters than as individual particles. Recent flowing slurry slot experiments by Ma and Tomac [67] also found that agglomeration formation was promoted with increasing slurry proppant volumetric concentration.

Numerical simulation work by Tomac and Gutierrez [68] further comment on the importance of lubrication effect in the formation of clustering bodies for proppant slurries. As rebound is dampened due to the lubrication effect between submerged colliding bodies, particles were noted to be more prone to remain adjacent to each other and form clustering groups. Zhang et al. [69] performed a numerical simulation study of particles settling in quiescent conditions as well as horizontal flow behavior between rough and smooth walls at low concentration. This work also pointed to instances of clustering between particles due to particle-particle and particle-wall interactions.

Outside of the commentary on clustering in proppant transport studies, observation of particle clustering phenomena has been noted in other non-quiescent fluid-particle systems. In simulations of flowing particles, Farhan et al. [70] found that clustering shape was found to be influenced by the Froude number (ratio of inertial to gravitational forces) and Stokes number (ratio of particle's momentum response time to the flow-field time scale) [24,70]. Variance in these values led to different particle 'chain-like' and 'curtain-like' shaped clustering. Graham and Steele [63] and Graham and Bird [71] performed experimentation in a homogeneous shear flow apparatus to study motion and interaction of spherical, nearly neutrally buoyant, concentrations of particles due to hydrodynamic forces. Continuous cluster formation and destruction was observed in both dilute and concentrated suspensions, with increasing particle concentration leading to larger cluster formation. Additionally, increases in Reynolds number, via increased shear rate, led to slightly decreased cluster size. As touched upon earlier, Graham and Steele [63] additionally point out that direct observation of clusters in concentrated suspensions was infeasible in their work. Again, this is due to concentrations above approximately 5 % causing visual obscuration. To overcome this visual obstruction, observations for Graham and Steele's [63] work were done by utilizing transparent particles with a smaller fraction of opaque particles intermixed. Cluster sizes were then able to be determined based on the experimental data combined with information theory and the Maximum Entropy Principle.

Clustering has also been observed in hydraulic fluidization experiments. An example is observed in 2-D, liquid-solid fluidized bed experiments performed by An et al. [72]. The study utilized poly-formaldehyde and ceramic particles with densities of 1420 kg/m^3 and 2670 kg/m^3, respectively, using water as the carrier fluid. It was noted that many of the particles were observed to move upward in clustered groupings, mostly forming horizontal strands of particles oriented perpendicular to the flow.

The question remains though, how can clustering particles affect flowing slurry behavior? Investigation of horizontal slurry flows by Campbell et al. [73] noted unexpected observation of downward acting force in their experiments. For that study, 0.5 and 1 mm glass bead and water slurries with mean concentrations between 17 to 40 % were circulated through a slurry pipe loop. Pressure probes included at the top, bottom, and an intermediate moveable probe within the pipe were used to measure pressure differentials. The experiments found a positive pressure gradient, leading to downward forces at intermediate regions of the particle slurry flow. Downward forces due to the developed pressure gradient were hypothesized to be due to a Bernoulli effect. The Bernoulli effect was caused by a negative concentration gradient, i.e., higher concentration transitioning to lower in the positive vertical direction, leading to

correspondingly higher fluid velocities overlain by lower velocities through the varying particle porosities. From the Bernoulli principle, this results in higher pressures in the slower moving fluid, over lower pressures in the faster moving fluid below. This is believed to be the cause of the generated downward acting force. Based on this, since non-homogeneous concentration distributions are seen to occur in dense, clustering slurries, it may be possible for upward or downward acting pressure gradients to occur for these cases as well.

2.2.3 Fracture Wall Influences on Slurry Flow and Transport

Influences on quiescently settling proppant slurries within rough fracture domains have been commented on in the past by various researchers. Experimental results from Novotny's [31] work also included observation of particle settling behavior between both a smooth Lucite walled slot and a rough walled slot made from fractured calcium-carbonite. They indicated that their proposed wall attenuation factor (see subsection 2.1.3) adequately described attenuation effects for both the smooth and rough walled slot experiments

Others have noted contrary observations. Liu and Sharma [35] and Liu [42] in their evaluation of particle settling through rough slots concluded that settling was substantially hindered by rough walls. In experiments within a slot with one side consisting of a 3D printed rough surface, Luo and Tomac [62] found that particles became trapped in narrow, rough fracture slots. Investigations from Alotaibi and Miskimins [74] looked at effects from roughness by using a computerized drill bit to form rough surfaces on Plexiglas. Friction from the slot walls was believed to slow particle settling velocity.

Effects on settling and conveyance of proppant particles flowing within rough fractures have also been commented on in past studies. Liu and Sharma [35] and Liu [42] in evaluating proppant flow through their rough slots commented that roughness severely retarded the proppant's velocity. Injected fluid fingering, i.e., diverged channeling, was also noted to develop in highly rough fractures. On experiments specifically evaluating the behavior of a single particle through a rough fracture, Liu and Sharma [35] and Liu [42] concluded that horizontal particle velocity was hindered within the rough wall fractures with velocities much lower than those between smooth-walled fracture configurations. While lower velocities were presented for all tested mechanical apertures in the 'large roughness' surface configuration in Liu and Sharma's [35] and Liu's [42] work, it is noted here that the 'small roughness' configuration shows an increased velocity compared to the smooth walled fracture at the largest comparative mechanical aperture in that work. The increased relative velocity for the 'small roughness' data point was not commented on in either works by Liu and Sharma [35] or Liu [42]. A set of experimental investigations by Huang,

Babadagli, and Li [75]; Huang, Babadagli, Li, and Develi [76]; and Huang, Babadagli, Li, Develi, and Zhou [77], using rough vertical fractures constructed from transparent castings of fractured rock samples noted highly uncertain proppant transport occurs in rough fractures with distorted flow fields through rough fractures. Proppant behavior was noted to be 'totally different' than that within a smooth walled fracture. It was further noted that roughness can cause a reduction in both horizontal and vertical velocity of proppant particles and that the rough nature of a fracture could cause enhanced proppant deposition. Roughness features were noted to lead to particle-wall contacting which caused interruptions in particle conveyance behavior. Further, proppant bridging, i.e., jamming, was noted to occur within rough fractures leading to significant disturbance in the flow of proppant past these clusters of jammed particles. Raimbay et al. [78] performed experimentation on proppant transport through horizontal fractures with transparent castings of several fractured rock samples. Their findings concluded that proppant transport varied based on the surface characteristics of the rock, controlling both flow path of fluid as well as stability of proppant placement. Fracture slot experiments by Kadhim et al. [64] also found that roughness more greatly impacted settling velocity than horizontal velocity, pointing to proppant mounding heights within their fracture experiments.

Numerical evaluations have been performed to determine proppant behaviors between rough walls. Huang et al. [79] performed simulation of slurry flow and transport in rough fractures using a multiphase computational fluid dynamics (CFD) approach. Roughness, in this case, was modeled as an applied drag force at near-wall flow and found that horizontal, parallel to flow, transport, and vertical settling rates were attenuated. With this approach, however actual geometric roughness features' impact on granular, flowing material does not appear to be well represented. In 2-D simulations of particles within rough fractures using unresolved coupled computational fluid dynamics with the discrete element method (CFD-DEM), Zhang et al. [69] concluded that increased wall-particle and particle-particle contacting led to more greatly hindered transport. In 3-D unresolved CFD-DEM simulations of particle flows in rough fractures, Wang et al. (2020) found that flow vortices generated between rough surfaces (with rotational axis normal to the surface walls) caused entrapment of particles leading to higher particle-wall and inter-particle interactions. This higher interaction was observed to lead to loss of kinetic energy and greater particle deposition. Suri et al. (2020) found in their unresolved 3-D CFD-DEM simulation of proppant slurry in rough fractures that vorticity between fracture walls led to greater particle suspension with greater horizontal transport.

Others have provided insights into fluid-only flow behavior between rough rock surfaces. Early investigations into flow effects due to rough surfaces in fractures were provided by Tsang [82] and Brown [49]. Both

works pointed to deviations from smooth-walled flow behavior that was attributed to the tortuosity of flow paths within the fracture. Briggs et al. [15] synthetically generated 2-D rough fracture openings to evaluate fluid flow through rough fractures. Root-mean-square (*RMS*) asperity height of 1 mm was applied for all rough surfaces. Eddies developed within the rough features at rock surfaces boundaries, with higher eddy volumes in fractures with higher fractal dimension (i.e. higher textural roughness). Eddy size was found to increase rapidly while progressively increasing Reynolds number value at smaller magnitudes, i.e. $Re_{||} \sim O(1)$. Less rapid growth of eddies at higher magnitude Reynolds number values was also noted. The reduced growth rate was attributed to increasing flow through the fracture constraining greater development. Briggs et al. [15] further noted that eddy formation resulted in reduced 'hydraulic aperture' within fractures, with rougher fractures having lower hydraulic aperture values overall. Hydraulic aperture (a_{hyd}) is expressed as a varied form of cubic law by [15,49,83]:

$$a_{hyd} = \left(-\frac{Q_x 12\mu}{H} \frac{1}{\left(\frac{dp}{dx}\right)} \right)^{1/3} \tag{2.14}$$

where Q_x is the volumetric flow rate and $\frac{dp}{dx}$ is the pressure gradient along the length of the fracture, i.e. parallel to flow direction. As pressure gradient increases due to the influence of rough fracture surface effects, mechanical aperture (a), the physical mean distance between fracture faces, no longer satisfactory describes through fracture flow with cubic law and utilization of a_{hyd} is needed.

Apart from textural complexity, which is described by fractal dimension, heights of asperity features are also of concern for fluid flow behavior. Zhang et al. [84] investigated the effects of varying asperity heights on flow within 2-D synthetic rough fractures by varying *RMS* asperity height values. It was found that this varying degree of asperity height contributed to largely altering the velocity and pressure behavior in rough fractures compared to smooth-walled fractures. Fluid flow became more torturous with increasingly asymmetric with increased asperity heights and narrowing fracture aperture. Zhang et al. [84] also found that the ratio of the hydraulic aperture to the mechanical aperture increased for rough fractures as mechanical aperture increased, however the ratio decreased for relatively smooth fractures when mechanical aperture increased.

2.3 Concluding Remarks

It is clear from the above literature review that areas of proppant slurry behavior in field realistic conditions have contradictory findings and/or are lacking in the literature. The influence of clustering on proppant slurries in flow, roughness influences on proppant flow, and roughness effects on proppant settling behavior all warrant more comprehensive consideration. As discussed in the Introduction, both unresolved and resolved CFD-DEM approaches are considered in this work to provide greater insight into these topics. The following chapter discusses these methods in more detail.

3 METHODOLOGY

3.1 Fluid-Particle Computational Modeling with CFD-DEM

The below sections detail the computational approach of DEM, CFD and their coupling for both unresolved and resolved implementations.

3.1.1 Discrete Element Method (DEM)

To provide spatial and temporal resolution of individual particles' motion within the slurry, LIGGGHTS DEM modeling software package [85] is used. Equations of motion considered in the DEM model are:

$$m_i \frac{d\mathbf{v_i}}{dt} = \sum \boldsymbol{F}_i \tag{3.1}$$

$$I_i \frac{d\boldsymbol{\Omega_i}}{dt} = \sum \boldsymbol{T_i} \tag{3.2}$$

here m_i is a particle i's mass, $\mathbf{v_i}$ is the particle's velocity, $\boldsymbol{F_i}$ are forces acting on the particle (e.g., gravity, contact forces, etc.), I_i is the moment of inertia of the particle, $\boldsymbol{\Omega_i}$ is the rotational velocity, $\boldsymbol{T}_i$ are torques acting on the particle, and t is time. Contact and deformation behavior for the particles is modeled as an overlapping of particle radii rather than actual physical deformation. Force-displacement law modeled via a spring and dashpot during contact provides behavioral collision energy transfer and loss. A nonlinear Hertz-Mindlin contact model is implemented during particle contacting [85–87] for all models in this work. Sliding is also accounted for when tangential forces exceed Coulomb friction force during contact. Equations of normal and tangential contact forces are [85]:

$$\boldsymbol{F}_n = -\boldsymbol{\kappa}_n \delta_n + \gamma_n \Delta \boldsymbol{v}_n \tag{3.3}$$

$$\boldsymbol{F}_t = min\left\{\left|\boldsymbol{\kappa}_t \int_{t_0}^{t} \Delta \boldsymbol{v}_t \, dt + \gamma_t \Delta \boldsymbol{v}_t\right|, \eta \boldsymbol{F}_n\right\} \tag{3.4}$$

here, $\boldsymbol{F}$ is the force for the normal (n) or tangential (t) components, κ is the spring coefficient, δ represents the degree of overlap, γ describes the viscoelastic damping coefficient, $\Delta \boldsymbol{v}$ is the relative velocity between the bodies, and η represents Coulomb friction coefficient.

Choosing the appropriate timestep for DEM simulation is an important consideration as to large a timestep can result in instability whereas too small a timestep resulting in unnecessarily long computation time. There is no definite established criteria for determining appropriate DEM timestep size (Δt_{DEM}), though general guidelines

suggest adoption of a limiting fraction of the Hertz contact time scale (T_{Hertz}) or Rayleigh ($T_{Rayleigh}$) wave propagation time scale, which are defined as [88,89]:

$$T_{Hertz} = 2.8683\left(\frac{{m_*}^2}{r_* u_{i,j} {E_*}^2}\right)^{1/5} \tag{3.5}$$

$$T_{Rayleigh} = \frac{\pi r_{min}\sqrt{\frac{\rho_s}{S}}}{0.1631\upsilon + 0.8766} \tag{3.6}$$

where m_* is the reduced mass of the two particles ($1/m_* = 1/m_i + 1/m_j$), u_{ij} is the relative velocity between the two bodies, r_* is the reduced radius of the two particles ($1/r_* = 1/r_i + 1/r_j$), E_* is the effective young's modulus ($E_* = 1/\{(1-\nu_i)/E_i + (1-\nu_j)/E_j)\}$), r_{min} is the minimum particle radius of two contacting bodies, S is the materials shear modulus, and υ is the particle Poisson's ratio. For instances of a particle-plane collision, m_* and r_* reduce to the mass and radius of the colliding particle, respectively.

3.1.2 Computational Fluid Dynamics (CFD)

CFD provides solution for the Navier-Stokes equations of fluid behavior in a discretized flow domain by finite approximation methods. To model the fluid phase of the slurry, OpenFOAM [90], a finite volume CFD software, is used. The form of the Navier Stokes equations for an incompressible, Newtonian fluid utilized in OpenFOAM are:

$$\nabla \cdot \mathbf{u} = 0 \tag{3.7}$$

$$\rho_f \frac{\partial \mathbf{u}}{\partial t} + \rho_f(\mathbf{u}\cdot\nabla)\mathbf{u} = -\nabla p + \mu\nabla^2\mathbf{u} \tag{3.8}$$

in which, p is the fluid pressure. To assure stability and accuracy of simulations, CFD timestep (Δt_{CFD}) is implemented as where the Courant-Friedrichs-Lewy (CFL) number is of value below one. CFL number relationship is defined as [16]:

$$1 \geq \frac{\mathbf{u}\Delta t_{CFD}}{x_{cfd}} \tag{3.9}$$

where x_{cfd} is the CFD mesh cell size.

3.1.3 Unresolved CFD-DEM Coupling

Unresolved CFD-DEM particle and fluid coupling is implemented using CFDEM®coupling toolkit as developed by Goniva et al. [91]. Exchange of interactive forces is further discussed herein. Di Felice [92] proposed a

semi-empirically based modified drag force to represent the variance in drag that occurs for a particle that is within a concentration of suspended particles. This is expressed as:

$$\boldsymbol{f}_{drag,DiFelice} = \boldsymbol{f}_0(1-C)^{-\chi} \tag{3.10}$$

with,

$$\chi = 3.7 - 0.65\exp\left(-\frac{\left(1.5 - log_{10}Re_p\right)^2}{2}\right) \tag{3.11}$$

where $\boldsymbol{f}_{drag}$ is the modified drag force for an individual particle in a particle concentration C. Coefficient of drag in this evaluation is evaluated per Eq 1.3. The indicated relationship has been shown to be usable for a wide range of particle Reynold's number values and particle concentration conditions [92,93].

Another possible resolution for the drag force of concentrated particles in suspension is that developed by Koch and Hill [94] and Koch and Sangani [95]. Expression of this as implemented by van Buijtenen et al. [96] to evaluate drag force in concentration is as shown in the below equations:

$$\boldsymbol{f}_{drag,Koch\ and\ Hill} = \frac{\left(\frac{4}{3}\pi r^3\right)\beta}{C}\ (\boldsymbol{u}-\boldsymbol{v}) \tag{3.12}$$

with,

$$\beta = \frac{18\mu C(1-C)^2}{d^2}\left(F_o(C) + \frac{1}{2}F_3(C)\ Re_p\right) \tag{3.13}$$

and where $F_o(C)$ and $F_3(C)$ are defined as,

$$F_o(C)\begin{cases} \dfrac{1+3\left(\frac{C}{2}\right)^{1/2} + \left(\frac{135}{64}\right)C\ln(C) + 16.14C}{1+0.681C - 8.48C^2 + 8.16C^3} & for\ C < 40\ \% \quad (3.14) \\ \dfrac{10C}{(1-C)^3} & for\ C \geq 40\ \% \quad (3.15) \end{cases}$$

$$F_3(C) = 0.0673 + 0.212C + \frac{0.0232}{(1-C)^5} \tag{3.16}$$

With one of the drag force resolutions, the evaluation of fluid interaction contributions on solid particles within a fluid CFD cell can be evaluated.

Zhou et al., [18] specifies three coupling formulations utilized in past CFD-DEM studies, Set I, Set II, and Set III. Set I and Set II are shown to be mathematically the same in that work. Set III is shown to be a simplification of Set I, assuming steady and uniform flow through the particle phase. Set II and Set III are designated as "Model A" and "Model B", respectively, in the CFDEM®coupling toolkit. These two coupling approaches are considered in this

work and will be referred to as "Model A" and "Model B" throughout the remainder of this dissertation. Their respective modified fluid equations of continuity and momentum are [17,18]:

$$\frac{\partial(\rho_f \alpha_f)}{\partial t} + \nabla \cdot \left(\alpha_f \vec{u}\right) = 0\,, \quad for\ Model\ A\ and\ Model\ B \tag{3.17}$$

$$\frac{\partial(\rho_f \alpha_f \boldsymbol{u})}{\partial t} + \nabla \cdot \left(\rho_f \alpha_f \boldsymbol{u}\boldsymbol{u}\right) = -\alpha_f \nabla p + \alpha_f \nabla \cdot \boldsymbol{\tau} - \boldsymbol{F}_{p,A} + \rho_f \alpha_f \boldsymbol{g}\,, \quad for\ Model\ A \tag{3.18}$$

$$\frac{\partial(\rho_f \alpha_f \boldsymbol{u})}{\partial t} + \nabla \cdot \left(\rho_f \alpha_f \boldsymbol{u}\boldsymbol{u}\right) = -\nabla p + \nabla \cdot \boldsymbol{\tau} - \boldsymbol{F}_{p,B} + \rho_f \alpha_f \boldsymbol{g}\,, \quad for\ Model\ B \tag{3.19}$$

where α_f is the void fraction (i.e., 1- C), $\boldsymbol{\tau}$ is the shear stress, and $\boldsymbol{F}_p$ is the volumetric interaction force from the particles on the fluid in the cell.

Fluid interaction forces on particles ($\boldsymbol{f}_{p-f}$), and particle interaction forces on the fluid ($\boldsymbol{F}_p$) for "Model A" and "Model B" can be expressed as [17,18]:

$$\boldsymbol{f}_{p-f\ A,i} = \boldsymbol{f}_{drag,i} + \boldsymbol{f}_{\nabla\cdot\boldsymbol{\tau},i} + \boldsymbol{f}_{\nabla p,i}\,,\ with\ \boldsymbol{f}_{\nabla\cdot\boldsymbol{\tau},i} = -V_i(\nabla\cdot\boldsymbol{\tau})\ \ and\ \ \boldsymbol{f}_{\nabla p,i} = -V_i(\nabla p)\,, for\ Model\ A \tag{3.20}$$

$$\boldsymbol{f}_{p-f\ B,i} = \frac{1}{\alpha_f}\boldsymbol{f}_{drag,i} - \rho_f V_i \boldsymbol{g}\,, \quad for\ Model\ B \tag{3.21}$$

$$\boldsymbol{F}_{p,A} = \frac{1}{V_c}\sum_{i=1}^{n} \boldsymbol{f}_{drag,i}\,,\ \ for\ Model\ A \tag{3.22}$$

$$\boldsymbol{F}_{p,B} = \frac{1}{\alpha_f V_c}\sum_{i=1}^{n} \boldsymbol{f}_{drag,i} - \frac{1}{V_c}\sum_{i=1}^{n} \rho_f V_i \boldsymbol{g}\,, \quad for\ Model\ B \tag{3.23}$$

with V_i equaling the particle's volume and V_c equaling the cell volume. Formulation shown in Eq. 3.20 for "Model A" includes fluid to particle interaction forces from drag ($\boldsymbol{f}_{drag,i}$), pressure gradient ($\boldsymbol{f}_{\nabla p,i}$), and viscous forces from fluid shear stress or deviatoric stress tensor ($\boldsymbol{f}_{\nabla\cdot\boldsymbol{\tau},i}$). It is noted that buoyancy force is considered as included in the pressure gradient force of "Model A" as described by Zhou et al. [18]. "Model B" includes drag and buoyant force in fluid to particle interaction as shown in Eq. 3.21. It is noted that in these simplified equations for "Model B", pressure gradient and viscous forces are not distributed to the particle phase, as seen in Eqns. 3.19 and 3.21.

Each portion of the coupled simulation (CFD, DEM) are run individually and exchange phase information at a shared, coupled timestep. A diagram of the unresolved CFD-DEM algorithm steps is shown in Figure 3.1 [17,22].

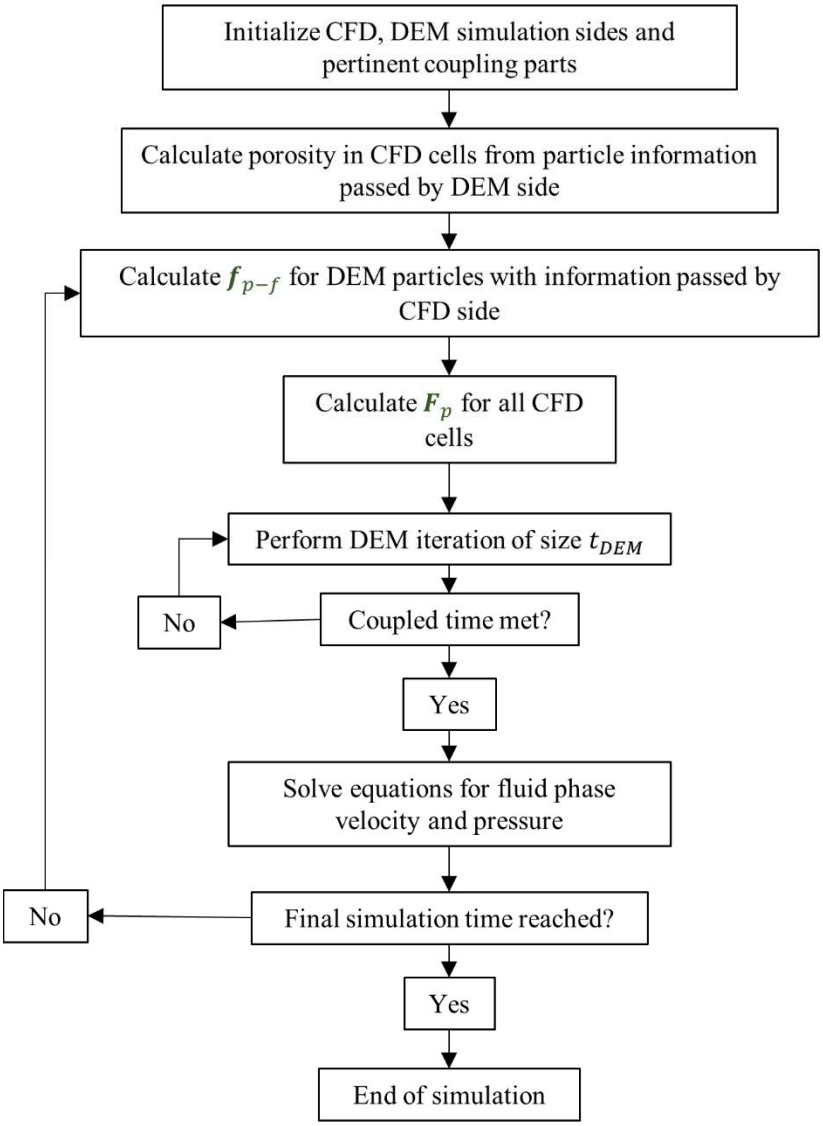

Figure 3.1: Unresolved CFD-DEM coupled simulation steps diagram

3.1.4 Resolved CFD-DEM

While these unresolved CFD-DEM approaches can provide a geometric representation of large-scale roughness features relative to particle size, as discussed in Chapter 1, small-scale roughness and surface unevenness characteristics are not well captured. As discretized fluid mesh cell sizes are larger than individual particles for the unresolved CFD-DEM approach, typically by a factor greater than 1.5 [21], generating a CFD mesh that adheres to these fine roughness features is not realistic. The possible narrowness of an aperture while maintaining an adequately resolved mesh across the opening is also greatly limited due to the largeness of the cells' size. Small scale roughness

features however may play an important role in proppant behavior within rough fractures, especially for flowing proppant slurries and at a narrow aperture. As noted in Chapter 2's literature review, various works [13–15] have demonstrated the development of eddies at rough surface features that affect fluid-only flow behavior within fractures.

To provide a greater understanding of the micromechanical influences and effects to proppant behavior within rough fractures, resolved CFD-DEM is opted for. As mentioned in Chapter 1, the resolved CFD-DEM method utilizes CFD cells of size smaller than the immersed solids particles. Because of this smaller size, the resolved method allows the CFD mesh to better conform to fracture wall features smaller than a typical proppant particle size. Additionally, this smaller size allows for a more highly resolved CFD mesh across narrow apertures relative to particle size. Fluid and particle interactions are also more accurately modeled in the resolved method, in that fluid interaction is resolved about each particles' surface [17,22].

Coupled interaction of the solids particle phase and the fluid phase of the slurry is completed using the CFDEM®coupling toolkit developed by Goniva et al. [91]. Specifically, this toolkit's immersed boundary solver [22,97] is implemented.

The methodology is based on the works of Patankar [98] and Shirgaonkar et al. [99]. The coupling as implemented by Hager [22] and Hager et al. [97] is detailed below.

Figure 3.2 shows an example particle immersed within a fluid domain. Here, the traction about a point on the surface of the immersed particle ($\boldsymbol{t}_{\Gamma_s}$) is described by:

$$\boldsymbol{\sigma} \cdot \hat{\boldsymbol{n}} = \boldsymbol{t}_{\Gamma_s} \tag{3.24}$$

with $\boldsymbol{\sigma}$ equaling the fluid stress tensor and $\hat{\boldsymbol{n}}$ being the surface normal vector.

Integrating about the whole particle body's surface gives:

$$\int_{\Gamma_s} \boldsymbol{\sigma} \cdot \hat{\boldsymbol{n}}\, d\Gamma_s = \int_{\Gamma_s} \boldsymbol{t}_{\Gamma_s}\, d\Gamma_s \tag{3.25}$$

Gauss's divergence theorem can then be applied to express the left side of the equation as a volume integral:

$$\int_{\Omega_s} \nabla \cdot \sigma d\Omega_s = \int_{\Gamma_s} \boldsymbol{t}_{\Gamma_s}\, d\Gamma_s \tag{3.26}$$

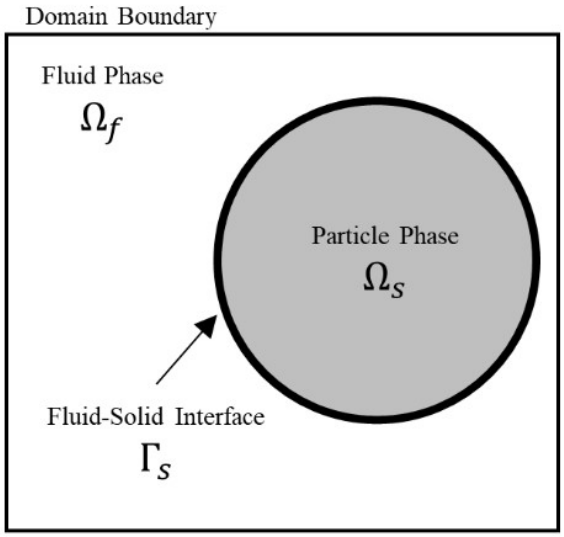

Figure 3.2: Particle immersed within fluid domain.

An incompressible fluid's stress is expressed as:

$$\boldsymbol{\sigma} = -p\boldsymbol{I} + \boldsymbol{\tau} \tag{3.27}$$

where $\boldsymbol{I}$ is the identity tensor. For a Newtonian fluid, the deviatoric stress tensor can further be decomposed as:

$$\boldsymbol{\tau} = \mu(\nabla \boldsymbol{u} + (\nabla \boldsymbol{u})^T) \tag{3.28}$$

Eqns. 3.27 and 3.28 can then be substituted into the left side of Eq. 3.26, giving:

$$\int_{\Omega_s} -\nabla p + \nabla \cdot \mu(\nabla \boldsymbol{u} + (\nabla \boldsymbol{u})^T)\, d\Omega_s = \int_{\Gamma_s} \boldsymbol{t}_{\Gamma_s}\, d\Gamma_s \tag{3.29}$$

the second term on the left-hand side can further be expressed as:

$$\nabla \cdot (\nabla \boldsymbol{u} + (\nabla \boldsymbol{u})^T) = \nabla^2 \boldsymbol{u} + \nabla(\nabla \cdot \boldsymbol{u}) = \nabla^2 \boldsymbol{u} \tag{3.30}$$

where the dropping of the second term is per continuity. This results in Eq. 3.29 simplifying to:

$$\int_{\Omega_s} -\nabla p + \mu \nabla^2 \vec{u}\ d\Omega_s = \int_{\Gamma_s} \boldsymbol{t}_{\Gamma_s}\, d\Gamma_s \tag{3.31}$$

From the left-hand side, force acting on the particle is comprised of the pressure and viscous contributions from the fluid phase. The right-hand side integration of traction about the particle is then just the fluid drag ($\boldsymbol{F}_{drag}$) from these contributions. Expanding the integral over entire system domain (Ω) and considering that pressure and viscous stresses on the body act at points occupied by the body, the expression becomes:

$$\boldsymbol{F}_{drag} = \int_{\Omega} (-\nabla p + \mu \nabla^2 \vec{u})\, \xi_\Omega d\Omega\,, where\ \xi_\Omega \begin{cases} = 1\ if\ element\ of\ \Omega \in \Omega_s \\ = 0\ if\ not \end{cases} \tag{3.32}$$

Considering the domain, Ω, discretized into fluid cell elements and designated as T_h, the evaluation becomes:

$$\boldsymbol{F}_{drag} = \sum_{c \in T_h} \int_{V(c)} (-\nabla p + \mu \nabla^2 \vec{u})\, \xi_\Omega \; dV(c) \;\; = \sum_{c \in \overline{T_h}} (-\nabla p_c + \mu \nabla^2 \vec{u}_c) V_c \tag{3.33}$$

with fluid pressure and velocity at each cell represented by p_c and $\boldsymbol{u}_c$ and $\overline{T_h}$ representing the set of cells encompassed by the particle. CFD cells only partially occupied by the particle, are evaluated as 1/8 × the cell volume for each cell vertex encompassed by the particle. Figure 3.3 shows a sketch of a particle within a CFD mesh with cells sized smaller than the particle for the resolved CFD-DEM method.

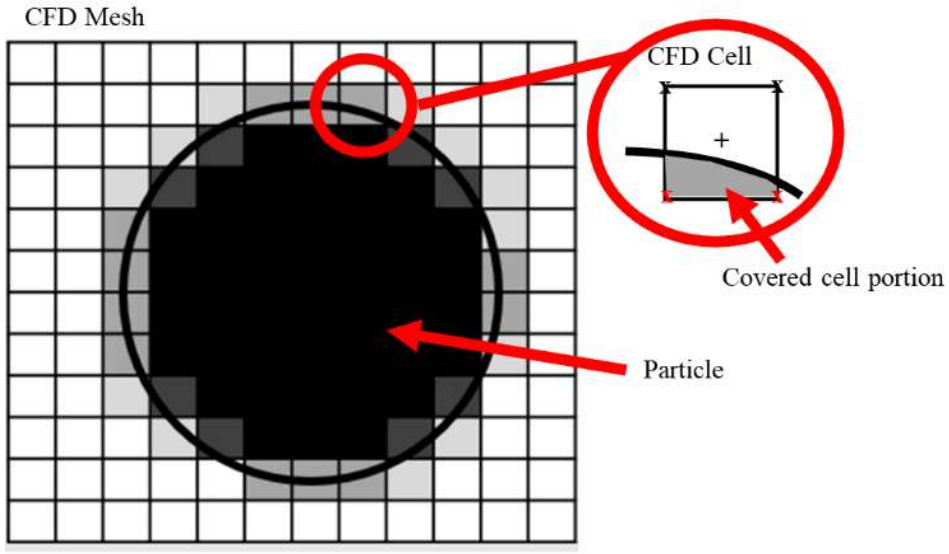

Figure 3.3: Diagram of particle within CFD mesh for resolved CFD-DEM method. The volumetric proportion of particle overlapping CFD cells is indicated as the degree of shading within the cell.

Particle motion influence on the fluid field is provided in a three-step process. Briefly, this is accomplished by [22,97]:

1. Fluid behavior in the domain is solved while neglecting the particles.
2. Particle velocity is implemented at respective cells encompassed by a particle from information provided by the DEM side of the simulation.
3. A velocity correction operation is applied to ensure continuity.

In-depth derivation and explanation of the particle-fluid interaction process can be found in Hager [22] and Hager et al. [97]. Buoyancy effects from the difference between the solids and fluid phase density differences ($\boldsymbol{F}_{buoy}$) is also evaluated by:

$$\boldsymbol{F}_{buoy} = -\frac{1}{6}\pi d^3 \rho_f \boldsymbol{g} \tag{3.34}$$

Like with the unresolved method, both CFD and DEM sides are run individually with a coupled timestep and pertinent information exchanged between simulation sides to provide momentum coupling.

3.2 Synthetic Rock Surface Generation

Figure 3.4 shows the general steps utilized in this work for generating synthetic rough fracture domains used in the resolved CFD-DEM simulations. This process is further detailed below.

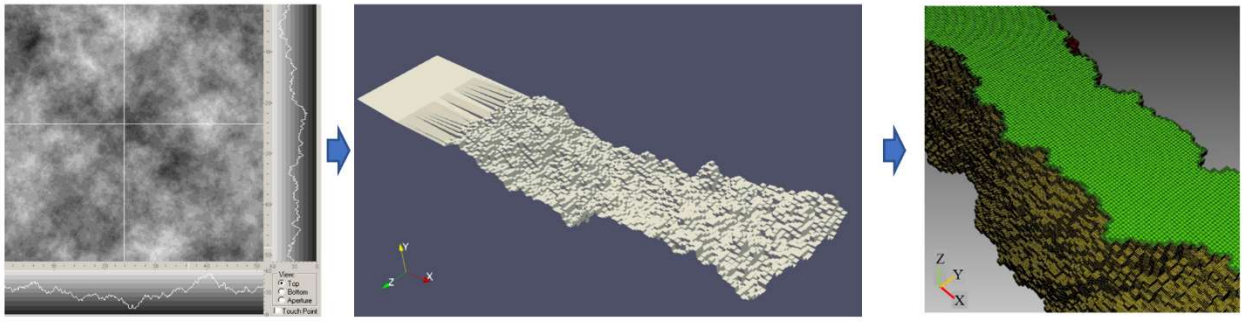

- Generation of fracture surface data in SynFrac
- Subsegment of data from SynFrac extracted (adjusted if need be)
- Generate STL file using Python script (example pictured above)
- STL files used for DEM side for fracture walls
- STL files further used to create CFD mesh (example pictured above)

Figure 3.4: Diagram of particle within CFD mesh for resolved CFD-DEM method. The volumetric proportion of particle overlapping CFD cells is indicated as the degree of shading within the cell.

Using a spectrally based method proposed by Brown [50] (as described in section 2.1.4), fractal dimension and *RMS* asperity height values are used to generate a synthetic rock surface. SynFrac software [100], a GUI implementation of Brown's method, is used to produce rough fracture surfaces in this study. SynFrac software was obtained from Paul Glover of Université Laval, Canada. Rock fracture surfaces are created with isotropic roughness and assumed to be matched in this study.

Laboratory fractured shale samples by Hyman et al. [101] indicated that surfaces were well-matched. Additionally, evaluation of fracture characteristics in carbonate reservoir rock by Al-Fahmi et al. [102] indicated that most observed fractures indicated matching walls. Therefore, fracture walls are assumed to be matched for this work.

To create the fracture geometry, first, a square matrix of asperity data values is generated in SynFrac. Once the data is generated, the target *RMS* asperity height value of the surface is then confirmed or adjusted with a uniform factor to meet the desired value. Following this correction, a subsection of data is taken at the desired simulation surface dimensions. As surfaces are generated to be isotopically rough, this subsegment is assumed to accurately

reflect roughness characteristics identical to those of the surface as a whole. Using an in-house developed Python script, STL files of the surfaces at desired aperture are created using the data points. Fracture walls for the DEM side of the simulation are directly generatable with these STL files. OpenFOAM's SnappyHexMesh meshing application (or its GUI implementation, Helyx-OS) is then utilized to generate the conforming cell meshes using the STL files. Study specific surface generation roughness criteria, specific implementation, and exemplar surfaces are presented in Chapters 6 and 7.

4 MODEL VERIFICATION AND VALIDATION

4.1 Introduction

To evaluate fitness of the proposed computational methods, several verifications and validations of both the unresolved and resolved methods are performed. These evaluations are discussed within this chapter.

4.2 Unresolved CFD-DEM Verifications and Validations

4.2.1 Particle Elasto-Hydrodynamic Rebound

As elastic bodies collide, loss of energy from the collision results in reduced rebound velocity. This can be characterized by the coefficient of restitution (e), defined as:

$$e = \frac{\boldsymbol{v}_{after}}{\boldsymbol{v}_{before}} = \sqrt{\frac{h_{after}}{h_{starting}}} \tag{4.1}$$

where v_{after} is the rebound velocity of a body after contact and v_{before} is the body's velocity prior to contact and in the case of a particle contacting a surface, $h_{starting}$ represents the starting height of an initially immobile body and h_{after} equals the maximum height reached post-impact. An early theory of elasto-hydrodynamic collision between two elastic bodies submerged in a viscous fluid was proposed by Davis et al. [103]. Through evaluation of colliding particle-to-wall behavior and elastic deformation coupled with the lubrication force derived from the lubrication approximation of the Navier-Stokes equation, an evaluation of nonlinear coefficient of restitution of a submerged particle was developed. Davis et al.'s work provided an evaluation into whether the submerged colliding particles would inelastically rebound or stick.

Collision between two particles, i and j, in a viscous fluid can be characterize by the non-dimensional Stokes particle number, defined as [103–106]:

$$S_{t,p} = \frac{m_* u_{i,j}}{6\pi\mu r_*^2} \tag{4.2}$$

Coefficient of restitution for submerged bodies is further found to be related to the Stokes particle number. Kidanemariam and Uhlmann [107] indicated that for cases where the Stokes particle number is of value 10 or below, rebound is not expected to occur due to viscously damped collision. Non-rebounding behavior is further supported by the empirical work performed by Schmeeckle et al. [106]. Experimenting on particle collisions in water, it was found that natural particles with Stokes particle numbers less than 39 had no rebound following collision. Tested glass

particles also had no rebound for Stokes particle numbers less than 38. Unresolved CFD-DEM simulations conducted in this work (see Chapter 5) were a posteriorly evaluated and found a maximum Stoke particle number for colliding bodies is ~15.2.

To ensure captured rebound behavior is representative of that expected with the above maximum Stoke particle number, e within the unresolved CFD-DEM models competed in this work are set to 0.051. The lowest default limit for e in LIGGGHTS DEM software package is > 0.05.

To confirm representative behavior, several simulations of different density particles is conducted. Particle properties for this evaluation are summarized in Table 4.1. To reduce computational cost, a reduced Young's modulus value compared to actual granular particles is implemented. As indicated by Tsuji et al. [108], calculation of particle motion in flow with a reduced modulus is not greatly affected by this adjustment.

Table 4.1: Material properties for elasto-hydrodynamic rebound verification

Proppant Parameters:		Units	Fluid Parameters:		Units
Particle Diameter	500	μm	Dynamic Viscosity	0.003	Pa·s
Particle Density	2600, 5200, 7600	kg/m^3	Density	1000	kg/m^3
Contact friction value	0.6	-			
Young's Modulus	5x10^6	N/m^2			
Poisson Ratio	0.3	-			

The verification simulation domain is generated as an eight mm cube. Gravity is active in the -Z direction. A planar wall is assigned at the -Z boundary for particles to collide with. For the CFD portion of the simulation, an identical sized domain was generated. No-slip condition is assigned at the -Z wall boundary. Other boundaries are assigned a zero-gradient condition for their parameters. CFD mesh resolution (x_{cfd}) for this evaluation is set to 3.33d. A single particle is generated for each tested particle density at a 4.5 mm height and allowed to fall till it contacts the -Z boundary. A DEM timestep of 2 x 10^{-7} and CFD-DEM coupling interval of 100 is utilized. Simulation data is recorded at each DEM timestep. Di Felice drag model [92] and the more comprehensive "Model A" coupling (see Chapter 3) is used.

The resulting coefficient of restitution behavior for the verification tests is summarized in Table 4.2. Results show negligible rebound and appear to be adequate for representing appropriate elasto-hydrodynamic rebound behavior based on the Stoke particle numbers experienced in the unresolved CFD-DEM simulations.

Table 4.2: Elasto-hydrodynamic rebound verification results

Particle Assigned Density (kg/m^3)	Pre- Impact Stoke Particle Number (-)	Coefficient of Restitution (-)
2600	2.2	0.60%
5200	8.7	1.20%
7600	17.2	1.80%

4.2.2 Mesh Sensitivity and Refinement, Drag Formulation Evaluation

As discussed in Chapter 3, CFD numerical evaluation involves the discretization of the Navier-Stokes equations over a computational mesh. Since the evaluation of fluid behavior is dependent on this discretization, the coarseness of the computational mesh can have significant impact on accuracy. Additionally, overly refined mesh leads to a higher computational expense and can severely impact solution time. For unresolved CFD-DEM, there does not exist a definite, agreed upon sizing ratio in the literature for mesh cell size relative to particle diameter.

Radl and Sundaresan [21] performed simulation of gas-solid fluidization with mesh cell to particle size ratios varying from 1.67 to 26.67. They noted that as mesh size is increased, particle structures such as clusters were not resolved and their effects on system behavior were lost. They found that ratios of 1.67 and 3.33 produced nearly identical representation of domain averaged slip velocity, where larger ratios led to deviations. They concluded that cell size ratio values of 1.67 to 3.33 were required to obtain grid-independent behavior. Li et al., 2017 also found that a ratio of 1.67 or greater is needed, with ratios of 1.67 to 3.33 providing the best representation of expected behavior.

Two relationships for resolving drag behavior in the unresolved CFD-DEM method by Di Felice [92] and Koch and Hill [94]; Koch and Sangani [95] were also presented in section 3.1.3. The suitability of these formulations also requires consideration.

To evaluate an appropriate mesh resolution and drag formulation for this work, several evaluations are performed:

1) Single particle settling behavior verification
2) Validation against empirical fluidization experiments
3) Validation against concentrated slurry sludge-line settling empirical predictions

4.2.2.1 Single particle terminal settling velocity

Settling behavior in CFD meshes of different levels of refinement is first checked. A single particle is simulated settling through a domain like that utilized in the coefficient of restitution evaluations (section 4.2.1). Particle and fluid properties are identical to those listed in Table 4.1, with the exception that only a particle density of 2,400 kg/m^3 is considered. Mesh is refined from a cell size to particle diameter ratio (i.e., x_{cfd}/d) of 1.0 to 6.66. Resulting settling behavior is shown in Figure 4.1 with the expected terminal settling velocity from Eqns. 1.1 to 1.3.

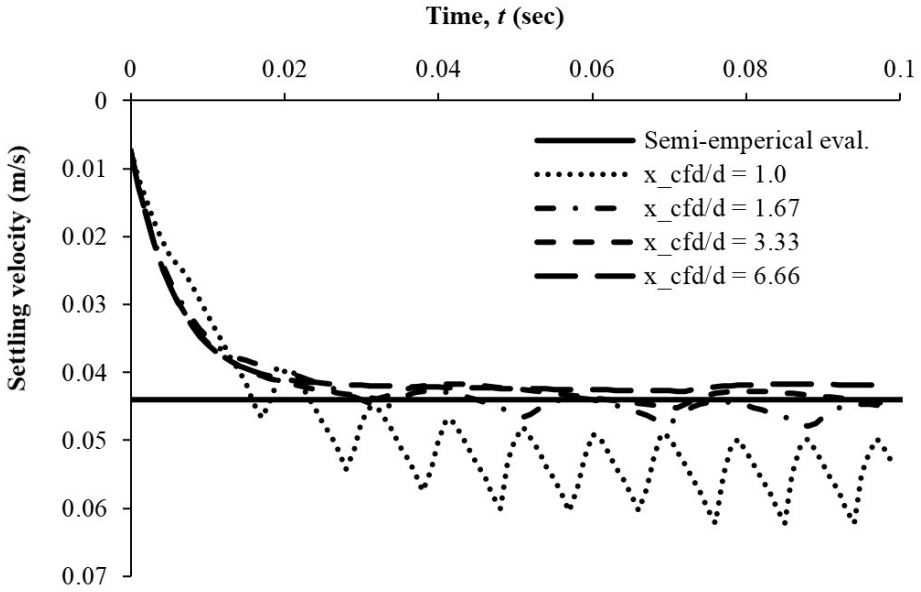

Figure 4.1: Terminal settling velocity for single particle with varying CFD mesh refinement. Expected terminal settling velocity also shown for comparison.

Result for x_{cfd}/d mesh refinement from 1.67 to 6.66 provides a relatively accurate representation of the expected terminal settling velocity. The most refined mesh however at x_{cfd}/d = 1.0 results in an overestimation as well as highly oscillatory behavior. As a x_{cfd}/d ratio above 3.33 is not recommended based on the cited literature, remaining mesh refinement evaluations focus on x_{cfd}/d = 1.67 or 3.33.

In addition to evaluation of mesh refinement, comparison between the two drag formulations from Di Felice [92] and Koch and Hill; Koch and Sangani [94,95] are compared. Figure 4.2 indicates the results of single-particle settling velocity behavior for both “Model A” and “Model B” coupling with both drag formulations. A CFD mesh with x_{cfd}/d = 3.2 is utilized.

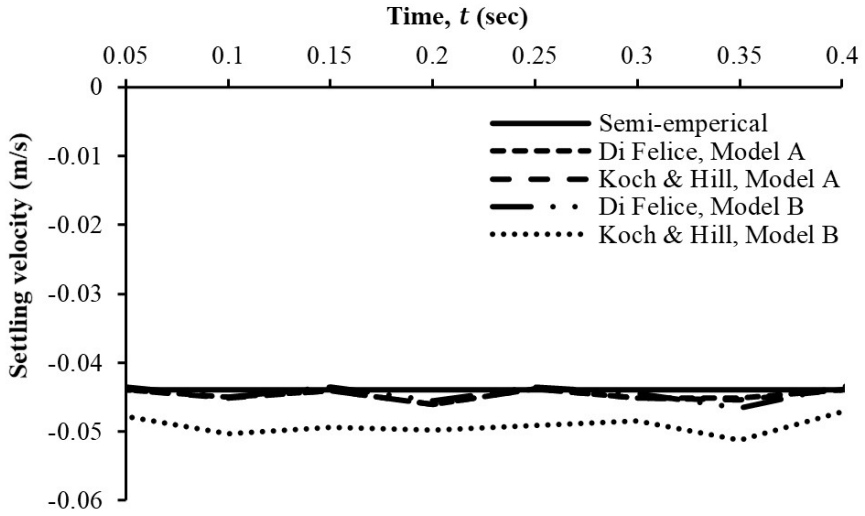

Figure 4.2: Single particle terminal settling velocity evaluation for DiFelice [92] vs. Koch and Hill; Koch and Sangani [94,95] drag force resolution.

Results indicate closer representation of the expected single particle settling behavior from the Di Felice drag force representation for both "Model A" and "Model B" coupling. Di Felice drag model was found to have a mean error of 1.7 and 1.3 % from the semi-empirical evaluation for "Model A" and "Model B", respectively. The Koch and Hill drag model had a 1.8 and 12.3 % mean error for "Model A" and "Model B", respectively. Both models perform well, but given the lower error for both "Model A" and "Model B" implementations, the Di Felice drag model is utilized for further evaluations in this work.

4.2.2.2 Validation Against Fluidization Experiments

Dynamic multi-particle validation is also performed based on pseudo-2D single spout fluidization experiments and simulations performed by van Buijtenen et al. [96]. As part of van Buijtenen et al.'s [96] work, measurement of time-averaged vertical particle velocity of fluidized glass beads within a 145 mm x 20 mm x 2.5 m Lexan and aluminum fluidization cell with a 5 mm x 20 mm centered spout was performed using particle image velocimetry (PIV) and positron emission particle tracking (PEPT) methods. Specifically, 2-D measurement of vertical velocities across horizontal heights of 0.05 and 0.1 m within the cell were taken. Identical geometry, except with only a 1 m domain height, is utilized for simulation in this study. Material properties for the air fluid and 3 mm diameter glass particles provided in van Buijtenen et al [96] are also applied. Lower boundary spout and background flow rates conditions (43.5 & 2.4 m/s, respectively) are also assigned. No-slip CFD conditions and DEM walls at the four sides of the domain are imposed. Open conditions, i.e., zero-gradient velocity, is assigned to the top of the CFD domain.

Gravity is active in the -*Z* direction. Previous validation of CFDEM®coupling with van Buijtenen et al. [96] has been performed by Goniva et al. [91] using the Koch and Hill drag evaluation. In this present work, Di Felice drag force resolution for both "Model A" and "Model B" coupling methods is implemented instead. Figure 4.3 shows simulation results of the time-averaged vertical particle velocities using both "Model A" and "Model B" with x_{cfd}/d = 1.67 and 3.33. Results from the experimental and simulation results of van Buijtenen et al. [96] at the previous mentioned discrete heights are included for comparison.

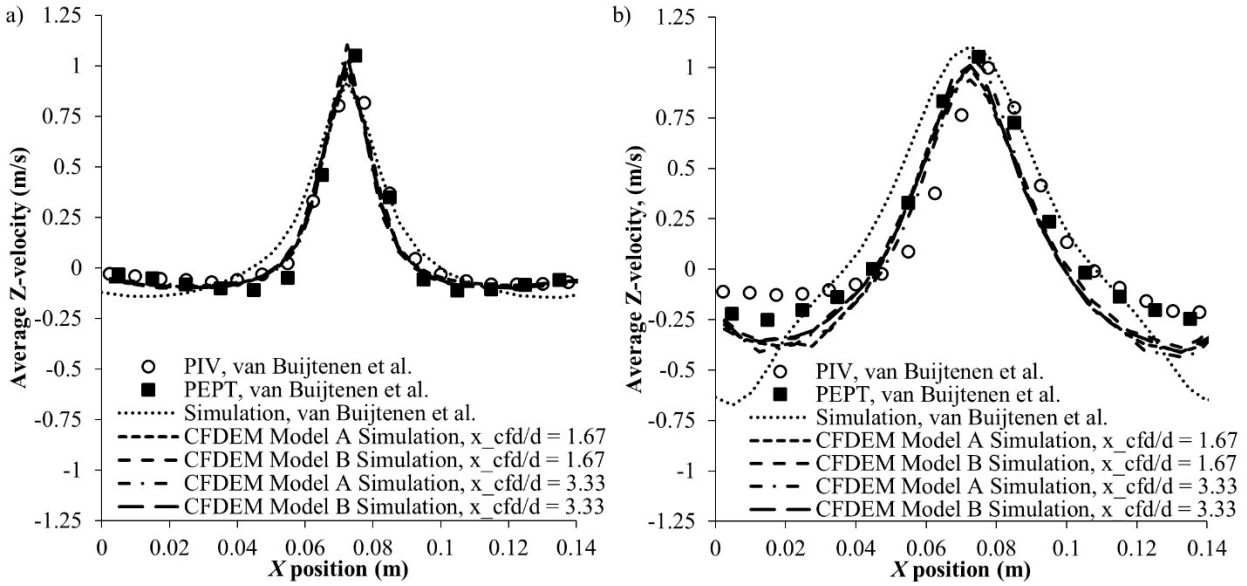

Figure 4.3: Time averaged particle flux in single spout fluidization model at a) 0.05 m and b) 0.1 m heights for unresolved CFD-DEM "Model A" and "Model B" coupling with x_{cfd}/d = 1.67 and 3.33. Empirical and simulation results from van Buijtenen et al. [96] included for comparison.

Good agreement between the empirical results from van Buijtenen et al. [96] and modeled results performed in this work can be seen. Behavior with mesh resolution of x_{cfd}/d = 1.67 and 3.33 are seen to be virtually identical as well. Therefore, use of mesh resolution with x_{cfd}/d = 3.33 is considered suitable for the remaining unresolved CFD-DEM evaluations as this provides a less computationally demanding CFD mesh.

4.2.2.3 Validation Against Slurry Settling Behavior

Comparison to hindered settling behavior as described by Richardson and Zaki [28] (see Eq. 2.1) is next performed. In Richardson and Zaki's [28] work, gentle agitation of particles and fluid within Pyrex tubes was performed to 'homogeneously' suspend a concentration of particles in fluid. Upon stopping agitation, the settling of

the upper, 'sludge-line' particles were measure against time to record the attenuated settling rate due to particle-fluid interaction effects. Proportion of particles was varied within the fluid filled tubes to study the effects of varying particle concentration. Likewise, for this work's comparison, particles are initially randomly placed within an 8 mm x 8 mm x 24 mm rectangular DEM-CFD domain at a set domain-wide concentration. Cyclic conditions in the CFD and DEM sides of the simulation is assigned to *X* and *Y* faces to avoid wall effects. CFD no-slip conditions are applied at the top (+*Z*) and bottom (-*Z*) of the simulation domain, DEM walls are not included, and particles are allowed to 'fall out' of the domain upon reaching the bottom limit. Particle and fluid properties are set to those summarized in Table 4.1 (again only 2,600 kg/m^3 density is considered). Gravity is active in the -*Z* direction. After initial placement of particles within the domain, they are allowed to settle while the upper approximate 0.5 % of particle settling rates are evaluated. Figure 4.4 indicates the results of mean attenuated sludge line settling velocity for particle volumetric concentrations ranging from 10 % to 50 %.

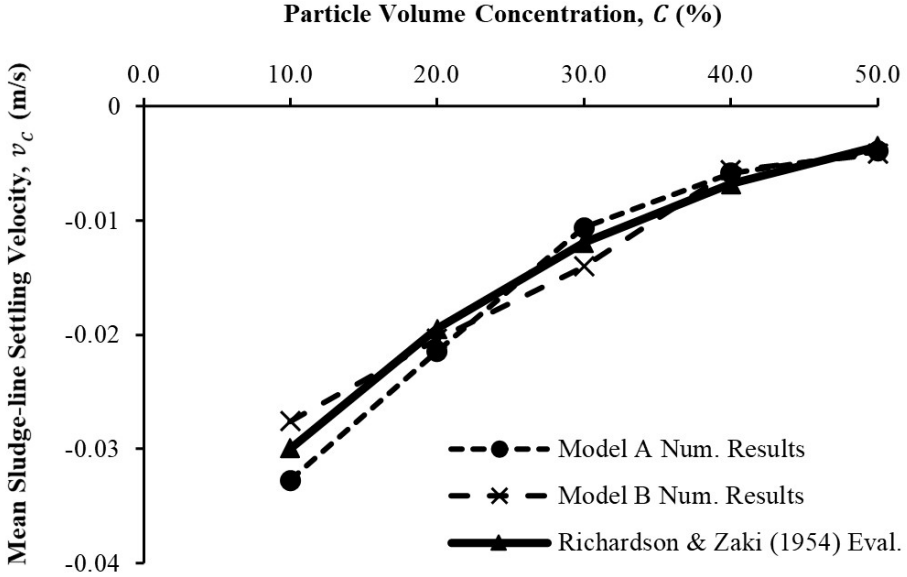

Figure 4.4: Comparison of sludge line hindered settling velocity compared to empirically developed relationship by Richardson and Zaki [28].

Errors between modeled and empirical relationship determined hindered sludge line velocities were found to range from between 9.4 to 13.7 % with mean value of 11.4 % for "Model A" coupling. Error between 4.5 % to 19.6 % with a mean value of 13.4 % was observed with "Model B". With typical errors in empirical results reaching values of 20 % variance or greater, these results were found to be satisfactory for verification of hindered sludge line settling behavior.

Given the outcomes from this and the other unresolved CFD-DEM evaluations, use of the model with the Di Felice drag resolution, x_{cfd}/d = 3.33, and both model coupling methods are further utilized in this study's evaluation. Further comparison of suitability of "Model A" versus "Model B" is conducted as part of Chapter 5 in the study of behaviors of high concentration injections of particle in flowing conditions.

4.3 Resolved CFD-DEM Verifications and Validations

4.3.1 Particle Elasto-Hydrodynamic Rebound

Evaluation of appropriate coefficient of restitution value setting is also evaluated for the resolved CFD-DEM implementation. As flowing particles are likely to contact rough fracture surfaces in these simulations, evaluation of rebound behavior up to a Stoke particle number of ~1000 is conducted by utilizing particle densities equaling 2600 to 200000 kg/m^3. CFD mesh is resolved with x_{cfd}/d = 0.1. Configuration of the simulation domain boundaries and material properties is like that for the unresolved simulations conducted in section 4.2.1. The coefficient of restitution setting is also varied for this set of evaluations from 0.75 to 0.95. Evaluation of values is similar to that performed in the unresolved verification except pre-impact velocity to calculate Stokes particle number is taken from a height of $3d$ above the -Z boundary. This is done to avoid under estimation of pre-impact velocity due to the onset of hydrodynamic effects between the approaching particle and wall. Results from these simulations are presented in Figure 4.5 and are compared to empirical results for e depending on $S_{t,p}$ from the literature [106,109,110]. Based on these results, a value of 0.95 provides the best approximation expected behavior compared to the empirical data and is therefore utilized in further resolved CFD-DEM simulations.

4.3.2 Single and Multiparticle Flow and Transport Verification/Validation

To verify and validate particle flow and transport behavior, resulting average particle velocity of flowing, simulated proppant between smooth walls with varying mechanical aperture is compared to the works of Staben et al. [39], Staben and Davis [40], and Blyton [41] (discussed earlier in section 2.1.3).

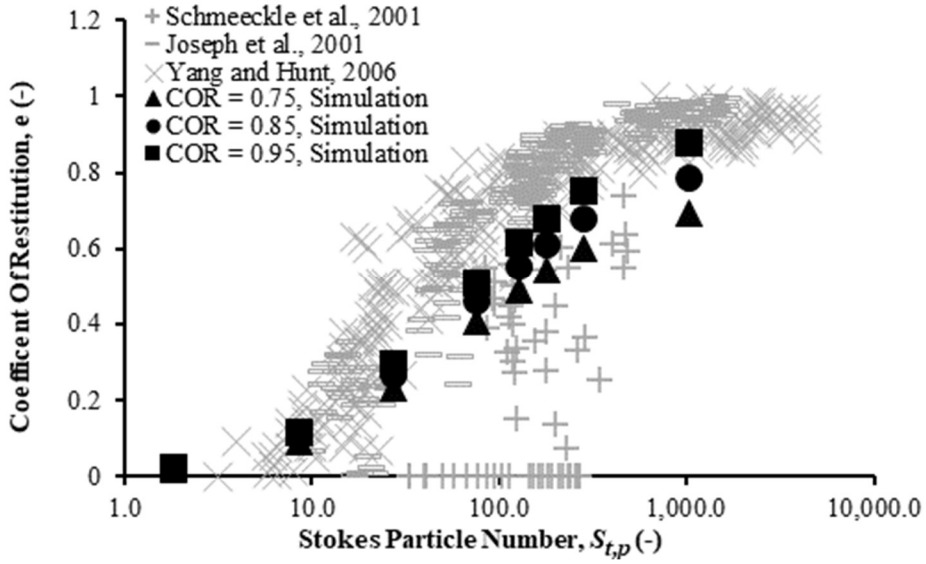

Figure 4.5: Coefficient of restitution value comparison to empirical values from the literature [106,109,110].

As solely conveyance behavior is to be considered in this portion, particle density is set to that of the fluid making the particles neutrally buoyant. Full material properties for this set of simulations are summarized in Table 4.3. A rectangular simulation domain (15 mm in *X*-direction × 3 mm in *Z*-direction) with varying aperture (*Y*-direction) is utilized. A prescribed fixed velocity is assigned at the inlet (-*X* boundary) to convey the proppant. Simulation domain boundary conditions are summarized in Table 4.4. CFD mesh is again resolved with x_{cfd}/d = 0.1

Table 4.3: Model material properties for single and multiparticle flow and transport verification/validation.

Proppant/Wall Parameters:		Units	Fluid Parameters:		Units
Particle Diameter	500	μm	Dynamic Viscosity	0.003	Pa.s
Particle Density	1000	kg/m^3	Density	1000	kg/m^3
Particle/Wall Contact Friction Value	0.6	-			
Particle/Wall Young's Modulus	5x10^6	N/m^2			
Particle/Wall Poisson Ratio	0.3	-			
Particle/Wall Coefficient of Restitution	0.95	-			

Table 4.4: Model boundary conditions for single and multiparticle flow and transport verification/validation.

CFD Boundary Conditions:		DEM Boundary Conditions:	
+/- *Y* faces	No-Slip velocity + zero-gradient pressure	+/- *Y* faces	Wall contact
+/- *Z* faces	Slip velocity + zero-gradient pressure, or Symmetric*	+/- Z face, - *X* face	Reflect
+ *X* faces	Prescribed non-uniform velocity + zero-gradient pressure	+ *X* face	Destroy
- X faces	Zero-gradient velocity, prescribed uniform pressure		

* Slip velocity setting for single particle cases, symmetric for multiparticle cases

For the simulation domains, gravity is active in the -*Z* direction, though this provides no real impact as the particles are neutrally buoyant. To prescribe a developed inlet velocity conditions at the -*X* face, a fluid only simulation is initially completed with a small and uniform velocity prescribed at the +*X* face, flowing in the -*X* direction. These simulations are run till *X*-directional velocity residual is of *O* (10^{-4}) or lower. Values are then extracted from the -*X* face, redirected to the +*X* direction, and rescaled based on the desired mean velocity value.

For single particle cases, fluid only simulation is first run till residual values stabilized before generating the particle within the domain. This initial fluid only simulation allows for particles to generate and travel in a fully developed flow environment. The single particle is then generated one particle diameter from the -*X* domain face and centered about the *Z/Y* plane.

For multiparticle simulations, to evaluate fully developed flow conditions, slurry injection was simulated for twice the duration of a single particle's travel time within the same fracture. The last 25% of the multiparticle simulation data is then used for evaluating averaged slurry transport behavior. Multiparticle bodies are continuously and randomly generated at a fixed volumetric concentration within a section positioned from the -*X* domain face to 2.5 mm in the *X*-direction. Particles are only evaluated from the last 10 mm of the flow domain to capture developed slurry flow behavior.

Figure 4.6 shows simulation results for a single particle conveyance with fluid flow $Re_{||}$ = 100, 1000, and 2000 compared to findings by Staben et al. [39], Staben and Davis [40], and Blyton [41].

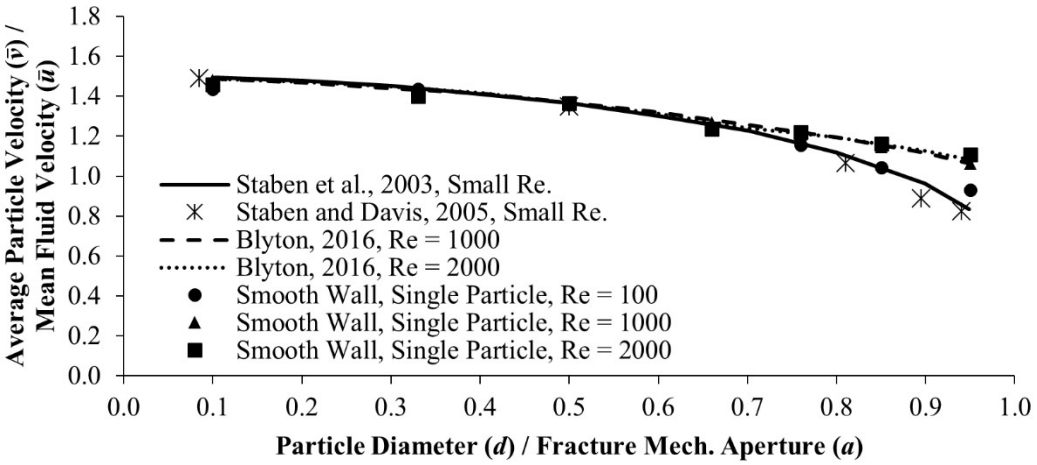

Figure 4.6: Particle diameter to fracture mechanical aperture ratio (i.e. d/a ratio) versus average particle velocity to mean fluid velocity ratio (i.e. $\bar{v}/\bar{u}$) results for a single particle simulation between smooth walls, compared to Staben et al. [39], Staben and Davis [40], and Blyton [41].

Good agreement of values to those of Staben et al. [39] and Staben and Davis [40] are seen for the simulations with lowest considered Reynolds number value of 100. Some variance from Staben et al. [39] and Staben and Davis [40] findings are observed for large particle diameter to fracture mechanical aperture ratio values at Reynolds number values of 1000 and 2000. This was also observed in the results from Blyton [41] and attributed to reduced wall retardation effects with increased inertial influence at higher Reynolds number values. Higher inertia influence effects can be seen by comparing the particle adjacent velocity streamlines within narrow mechanical apertures at different Reynolds number value conditions, as illustrated in Figure 5.

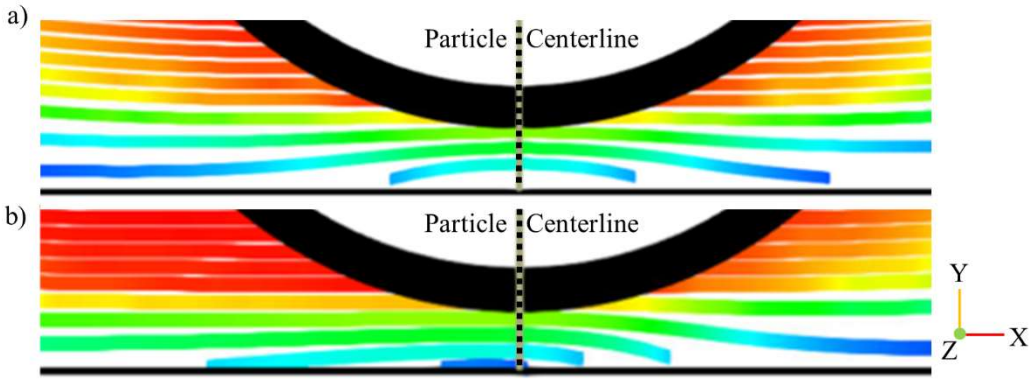

Figure 4.7: d/a ratio of ~0.95 for simulation with $Re_{||}$ of a) 100 and b) 2000. Colored lines are streamlines between wall and particle interfaces.

Higher particle inertia in the $Re_{||}$ = 2000 case coupled with the no-slip conditions at the fracture wall and translating particle interfaces lead to variance in the flow field about the particle. An asymmetry in the streamline shape relative to the particle centerline is clear in Figure 4.7. Figure 4.8a shows the normalized fluid velocity profiles at the tail end of the translating particle for $Re_{||}$= 100 and $Re_{||}$ = 2000 cases. Clear wall adjacent higher fluid velocity occurs in the $Re_{||}$ = 2000 case, with a resultant overall higher relative $\bar{v}/\bar{u}$ ratio value. Figure 4.8b further shows velocity variance due to this inertia effect in the surrounding fluid field around the particles in both the $Re_{||}$ = 100 and $Re_{||}$ = 2000 cases.

Overall, in comparison to prior works findings, a single particle's transport behavior exhibited appears satisfactory.

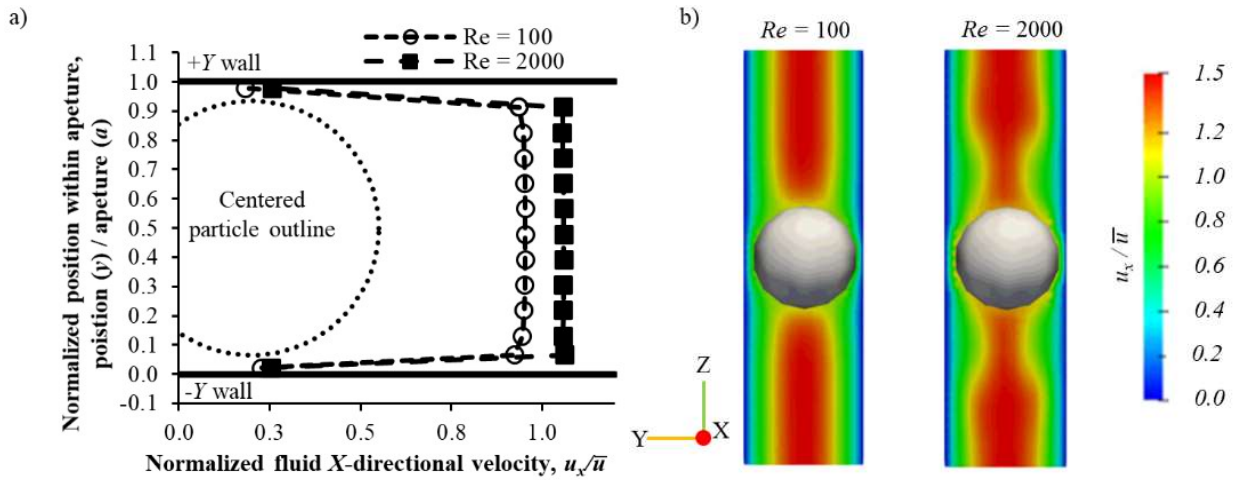

Figure 4.8: a) Normalized fluid *X*-directional velocity profiles for smooth walled $Re_{||}$ = 100 and $Re_{||}$ = 2000 cases. Particle outline shown for clarity of distribution about the particle shape in flow. b) Fluid velocity in the *X*-direction normalized by the mean fluid velocity about particle locations. Values and images are from mechanical aperture a = 0.575 mm simulations.

Multiparticle conveyance simulations are next performed. Figure 4.9 shows results for average particle velocity normalized by mean fluid velocity at varying mechanical apertures, concentration, and flow rate cases compared to the numerical evaluations from Staben et al. [39] and experimental measurements from Staben and Davis [40]. Actual post-simulation measured slurry concentrations are as indicated in Figure 4.9.

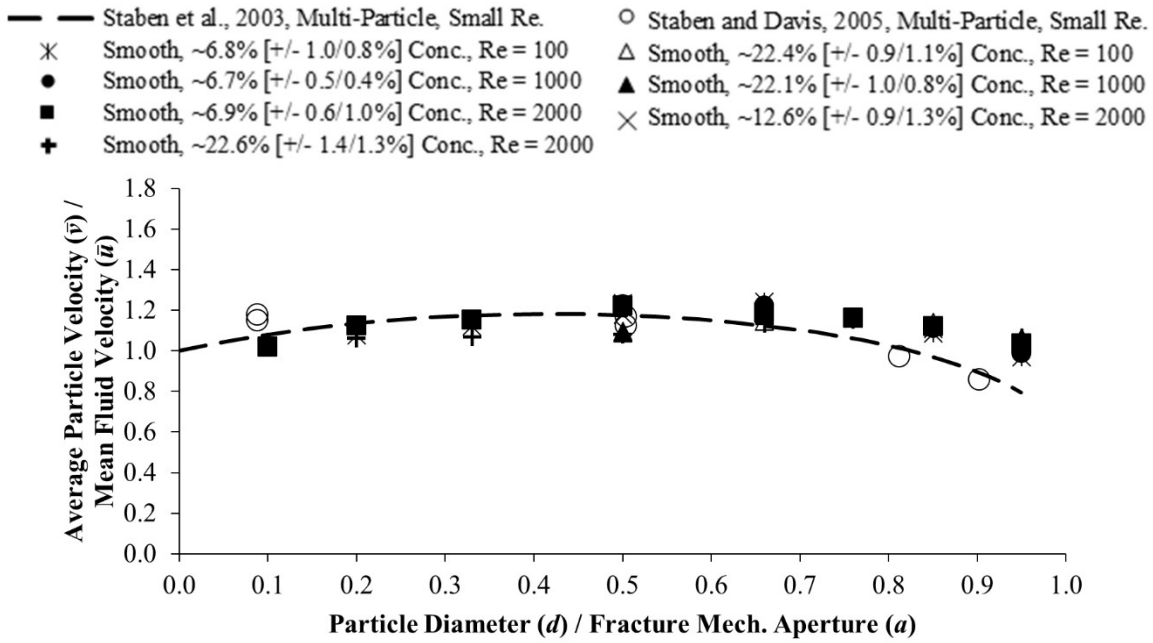

Figure 4.9: d/a ratio versus multiparticle $\bar{v}/\bar{u}$ for simulations compared to findings from Staben et al. [39] and Staben and Davis. [40]

Like the single particle cases, points at large particle diameter to mechanical aperture values are seen to slightly deviate from Staben et al. and Staben and Davis's [40] results due to the increased inertia effects. Other than this expected deviation, good agreement with these past works is seen for simulation results.

4.3.3 Wall Effect Attenuated Settling Validation

Validation of wall influence on quiescently settling particles in the domain is next conducted. Simulation results are compared to the experimental results of Tachibana and Kitasho [37] from their work measuring the settling rate of centrally positioned particles between parallel walls. Material properties for these simulations are summarized in Table 4.5. A rectangular domain (5 mm in *X*-direction × 6 mm in *Z*-direction) with varying aperture (*Y*-direction) is utilized. Gravity in this set of simulations is directed in the +*Z* direction. Simulation boundary conditions are summarized in Table 4.6.

Table 4.5: Model material properties for wall effect attenuated settling validation

Proppant/Wall Parameters:		Units	Fluid Parameters:		Units
Particle Diameter	500	μm	Dynamic Viscosity	0.003	Pa·s
Particle Density	2600	kg/m^3	Density	1000	kg/m^3
Particle/Wall Contact Friction Value	0.6	-			
Particle/Wall Young's Modulus	$5x10^6$	N/m^2			
Particle/Wall Poisson Ratio	0.3	-			
Particle/Wall Coefficient of Restitution	0.95	-			

Table 4.6: Model boundary conditions for wall effect attenuated settling validation

CFD Boundary Conditions:		DEM Boundary Conditions:	
+/- *X* faces	Slip velocity; Uniform, fixed pressure (= 0)	+/- *X* face	Reflect
+/- *Y* faces	No-Slip velocity; Zero-gradient pressure	+/- *Y* faces	DEM wall contact
+/- *Z* faces	Slip velocity; Zero-gradient pressure	+/- Z face	Destroy

The particle is initially generated centrally in the *X/Y* plane and one particle diameter from the -*Z* boundary. Figure 4.10 shows the results of simulated particle settling rate normalized by settling rate in an infinite fluid (i.e., v_w/v_t) for various particle diameter to wall opening aperture ratios (d/a). Averaged values from Tachibana and Kitasho for Re_p from 1 to 20 are considered as $Re_p \approx 7.3$ for a quiescently settling particle based on the material properties summarized in Table 4.5. Simulations are also conducted with a 0.025 mm cell sized mesh (i.e., x_{cfd}/d = 0.05) to evaluate mesh independence for the selected 0.05 mm cell resolution (i.e., x_{cfd}/d = 0.1).

Comparison of results in Figure 4.10 show clear similarity in trend for increasing wall influence on settling particles. Values are also within a reasonable range of experimentally measured results. The minimal variance between the results from the 0.05 mm and 0.025 mm resolved meshes also indicates the adequacy of the utilized mesh size.

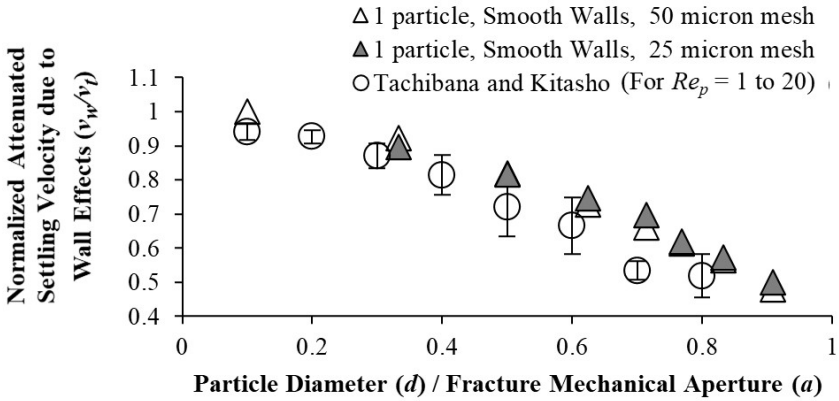

Figure 4.10: Simulated quiescent settling of particles centered between two parallel walls compared to experimental values from Tachibana and Kitasho [37]. Error bars for Tachibana and Kitasho indicate standard deviation from the data values extracted for Re_p = 1 to 20.

4.3.4 Particle-Fluid Interaction Validation

Validation of particle-fluid interaction behavior is also conducted by constructing and comparing simulations against the experimental work of Zhu et al. (1994). Zhu et al.'s study evaluated particle wake effects on the experienced drag of a fixed trailing particle located behind an identically sized fixed leading particle within a uniform flow. Various inter-particle distances were used to measure the varying effect of the wake on experienced drag (see Figure 4.11). A rectangular domain like that described in section 4.3.2 is utilized, with the exception that all walls parallel to the direction of flow have a 'slip' condition and height is 5 mm (*Z*-direction). Additionally, the fluid velocity profile at the -*X* face is uniform. The two particles are centered about the *Z*/*Y* plane (5 mm x 5 mm dimension). The lead particle is placed five particle diameters from the -*X* face. The trailing particle's position is then adjusted to various distances from the leading particle. A x_{cfd}/d ratio of 0.125 is utilized in these validations, i.e. the limit of allowable particle diameter to cell size to provide eight cells across each particle as indicated by Hager [22] and Hager et al. [97]. Particles are generated with infinite mass and gravity is not applied in these simulations to ensure immobility. Full material properties are summarized in Table 4.7.

The resulting reduced drag force for the trailing particles, normalized by the drag force for a single particle (evaluated with Eqns. 1.2 to 1.4), is compared to the findings of Zhu et al. [111] in Figure 4.12. Results in Figure 4.12 show good agreement with the experimental values, with average and maximum variance from experimental results of only 6.3 % and 9.4 %, respectively. With the good agreement observed from the above validations, the resolved CFD-DEM model is considered adequate for representing wall and particle-fluid interaction effects.

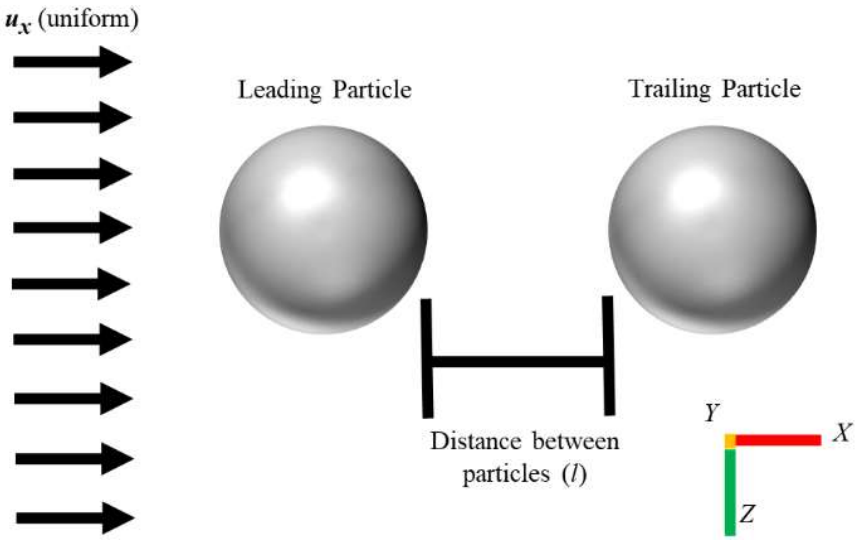

Figure 4.11: Diagram of in series particles for the measure of wake effects on experienced drag of the trailing particle.

Table 4.7: Materials properties for resolved particle-fluid interaction validation

Particle Parameters:		Units	Fluid Parameters:		Units
Particle Diameter	400	μm	Dynamic Viscosity	0.003	Pa·s
Particle Density	∞	kg/m^3	Density	1000	kg/m^3
Particle Contact Friction Value	0.6	-			
Particle Young's Modulus	$5x10^6$	N/m^2			
Particle Poisson Ratio	0.3	-			
Particle Coefficient of Restitution	0.95	-			

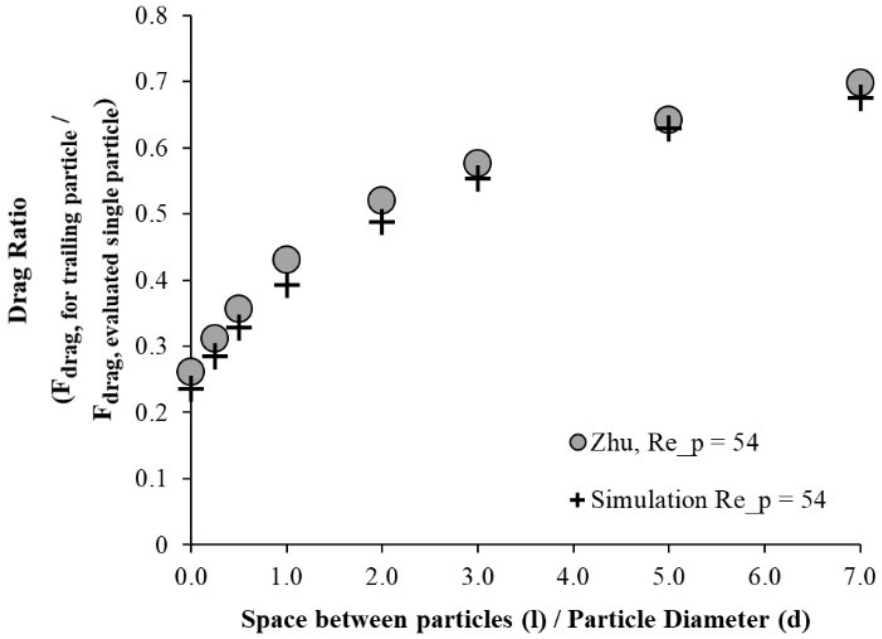

Figure 4.12: Results of reduced drag for trailing particles at varying interparticle distances compared to Zhu et al. [111], for Re_p = 54.

4.4 Synthetic Rock Surface Fractal Dimension Verification

It is important to confirm that prescribed fractal dimension is achieved in the synthetically generated surfaces. Therefore, post evaluation of the full surface data generated with SynFrac is performed. Several methods were utilized to evaluate post generated surface fractal dimension. Evaluation with 1-D PSD analysis [54,112] in this present work is accomplished using the PSD estimation method presented by Welch [113] and available within the SciPy library for Python. Slope of the PSD curve generated from the surface data in log-log is measured using a linear least-squares fit and converted to the respective fractal dimension value using the relationship presented in Chapter 2, section 2.1.4.

For evaluation of actual physical surfaces, PSD analysis proves to be difficult as the method requires non-trivial filtering of data and determination of the appropriate best fit for the PSD function's slope [112,114]. Further, it has been implied that evaluation for fractal dimension using PSD analysis is only an approximation for values of D_{prof} not equal to 1.5 [56]. Therefore, evaluation utilizing 1-*D* Roughness-Length method [56] is also performed. Roughness-Length method has been shown to provide reasonable measure of fractal dimension for both synthetically generated and natural fracture surfaces over a wide range of D values [52,114,115]. In the Roughness-Length method, a profile is evaluated using varying window sampling lengths, w_i, along the profile as shown in Figure 4.13.

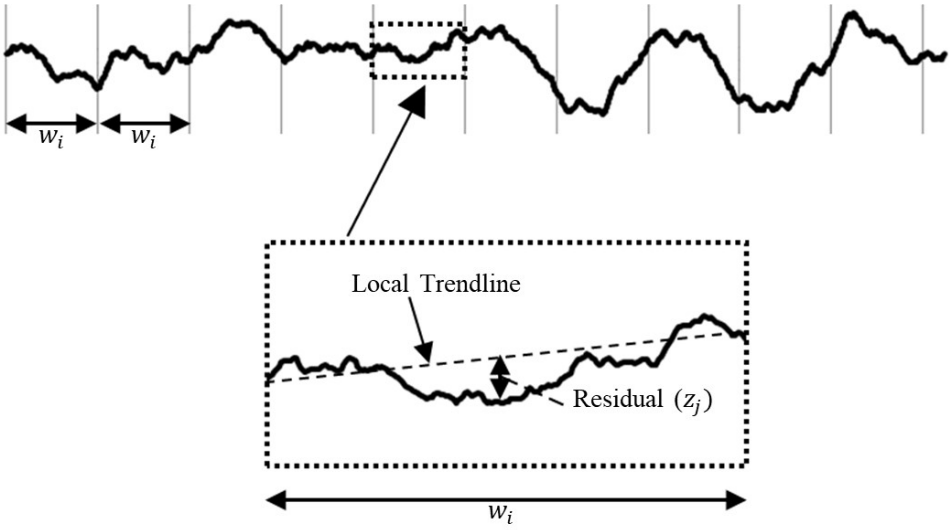

Figure 4.13: Evaluation via Roughness-Length method.

A least-squares, best-fit line is generated for each set of points within the sample window. *RMS* value for the whole profile is calculated as [56]:

$$RMS(w) = \frac{1}{n_w}\sum_{i=1}^{n_w}\sqrt{\frac{1}{P_i - 2}\sum_{j \in w_i}(z_j - \bar{z})^2} \tag{4.3}$$

where n_w equals the number of windows with length w_i along the profile, P_i is the number of points within window w_i, z_j is the residual values between the profile asperity points and the local best-fit trend line, and $\bar{z}$ is the mean residual within window w_i. It is noted that $\bar{z}$ is zero for a least-squares fit line [56]. Calculation of $RMS(w)$ for differing window lengths, w_i, is performed and resultant *RMS* versus w_i is plotted in log-log scale. The resulting slope minus two gives the profile's fractal dimension. More specific details of this method are provided in referenced works by Malinverno [56], Develi and Babadagli [114], Kulatilake and Um [52], and Fardin et al. [53].

Verification of 1-D fractal dimension measurement methods is completed by generating test 1-D fractional Brownian motion profiles with a Fourier transform method described by Saupe [54]. Profiles are generated with D_{prof} values from 1.1 to 1.9. 512 data points are used in the test profiles. Summary of verification for various prescribed fractal dimension profiles is presented in Figure 4.14.

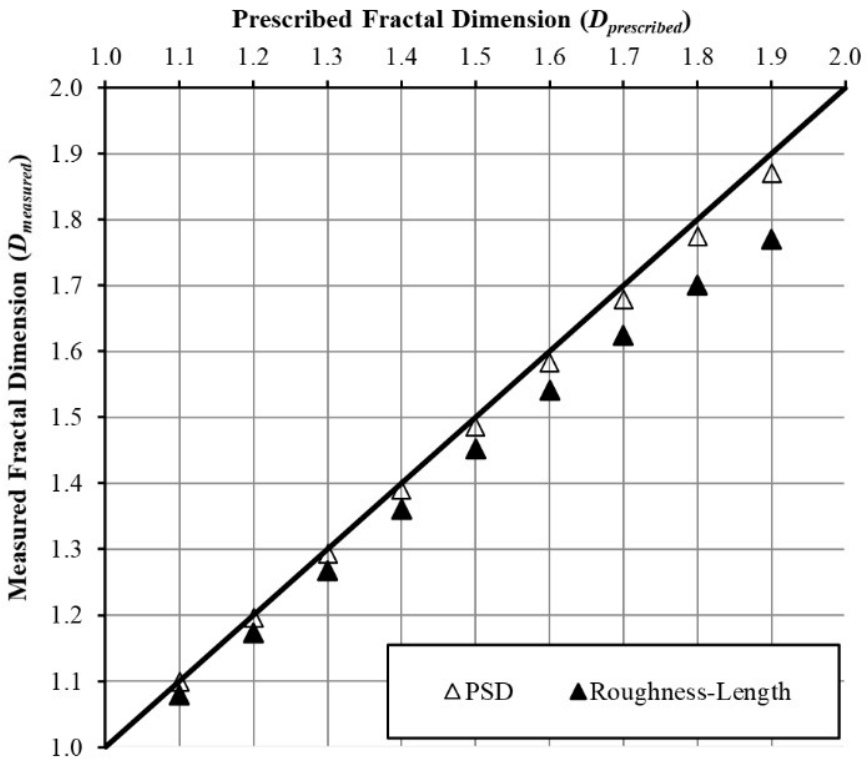

Figure 4.14: Verification of 1-D fractal dimension measurement methods; PSD and Roughness-Length. Diagonal line indicates perfect agreement between prescribed and measured fractal dimension values.

PSD analysis shows the most well matching values, which is expected as the generation and evaluation methods are both spectral based. Average and peak variance from prescribed fractal dimension for PSD analysis is 0.87 % and 1.53 %, respectively. Roughness-Length method also provides very accurate measurement of values, with average and peak variance from prescribed fractal dimension values equal to 3.71 % and 6.88 %, respectively. Better match was observed with the Roughness-Length method for values between 1.1 and approximately 1.6. This is beneficial as rock fracture fractal dimensions are between those ranges as mentioned in Chapter 2 (1.0 to 1.5 for rock profiles).

As Roughness-Length and PSD analysis methods provide sufficiently accurate measure of synthetically generated surface fractal dimensions they will be used to evaluate the data produced by SynFrac.

Three surfaces are generated within SynFrac with fractal dimension values of 2.1, 2.25, and 2.5. Each surface profile in the vertical and horizontal direction is then measured using the 1-D PSD and roughness-length methods and averaged. The results for the synthetic surface measurements are summarized in Table 4.8.

Table 4.8: Summary of SynFrac generated surface fractal dimension verification results

Prescribed Surface Fractal Dimension, (*D*)	1-D PSD	1-D Roughness-Length
2.1 (1.1 Profile)	1.08 average (+0.12 / -0.01)	1.13 average (+0.31/ -0.17)
2.25 (1.25 Profile)	1.22 average (+0.13/ -0.10)	1.26 average (+0.28 / -0.18)
2.5 (1.5 Profile)	1.46 average (+0.13/ -0.11)	1.49 average (+0.21 / -0.17)

With confirmed fractal dimensions in the surfaces data generated with SynFrac, use within CFD-DEM simulation domains is considered acceptable.

ACKNOWLEDGEMENTS

Chapter 4 of this dissertation contains materials from a published manuscript with the journal, Computers and Geotechnics, titled “Particle clustering dynamics in dense-phase particle-fluid slurries”; a manuscript in review for publication (accepted with minor revisions) with the journal, Geomechanics for Energy and the Environment, titled, “A Numerical Study of Neutrally Buoyant Slickwater Proppant Flow and Transport in Rough Fractures”; and a manuscript submitted for publication (in review) with the journal, Powder Technology, tentatively titled, “Fracture Roughness Effects on Slickwater Proppant Slurry Settling Attenuation”. Authors for all three of these works are Brian D. Yamashiro and Ingrid Tomac (2021). This dissertation’s author is the first author of these papers.

5 CLUSTERING IN FLOWING PROPPANT SLURRIES

5.1 Introduction

Given the previous conflicting research results regarding proppant particle clustering occurrence and gap in the knowledge on impact of clusters in flowing, dense proppant slurries discussed in Chapter 2, this chapter investigates behavior of dense-phase fluid-particle slurry micromechanics and particle clustering impact. Unresolved CFD-DEM is implemented to provide insights into general and local dynamics of fluid and particle motion during injection.

Previous researches have utilized the unresolved CFD-DEM method to investigate slickwater proppant transport within hydraulic fractures, however most focus on the bed-load transport mechanism that proceeds proppant mounding [116–118]. However as discussed in Chapter 2, the bed-load transport mechanism is a laboratory-scale phenomena and does not scale with field fracture size [8,11,60]. As such, this chapter's consideration and evaluation are focused on suspended viscous transport of proppants, the slurries' clustering capacity, and clustering influence on proppant flow and transport behavior.

Both "Model A" and "Model B" coupling (as detailed in Chapter 3) are further considered here to evaluate the appropriateness of the more simplistic "Model B" method for use in the evaluation of slurry flows.

This chapter aims to evaluate if and to what extent clustering occurs in flowing proppant slurries. Further, evaluation of the clustering bodies characteristics as well as impacts on flow and transport is considered. Lastly, it is desired to see if proppant conveyance and settling behavior is accurately described by simplified evaluation methods (see Chapter 2, Eq.2.13) or if and at what conditions behavior deviates from this evaluation.

5.1.1 Particle Clustering and Transport Characterization

Variance in several non-dimensional numbers have been previously cited as contributory to a two-phase particle-fluid's flow, transport, and clustering behavior. Of these, those not relating to the flow domain geometry and thereby concerned with the two-phase fluid's composition and flow conditions are the Stokes and Froude numbers, as mentioned in section 2.1.2, as well as the Reynolds particle number, and volumetric particle concentration [3,33,70,107,119,120]. Stokes and Froude numbers can be defined as [70,119,120]:

$$S_t = \left(\frac{\rho_s}{\rho_f}\right)\frac{Re_p}{9} \tag{5.1}$$

$$F_r = \frac{\boldsymbol{u}_{inlet}}{\sqrt{|\vec{g}|d}} \tag{5.2}$$

where S_t is the Stokes number, F_r is the Froude number, and $\boldsymbol{u}_{inlet}$ is the superficial fluid velocity taken at the inlet. The Froude number can further be modified to incorporate difference between the carrier fluid and particle densities as the Durand-Froude number (D_r) [24,121]. Expression with particle size as the characteristic length is [121]:

$$D_r = \frac{\boldsymbol{u}_{inlet}}{\sqrt{[\boldsymbol{g}d(G_s - 1)^{0.8}]}} \tag{5.3}$$

with G_s equal to the ratio of particle to fluid densities.

A review of qualitative definitions of particle clustering structure used by Farhan et al. [70] is provided here with brief description of shape, as similar definitions are utilized in this chapter. Clustering definitions include designation between:

- '1-D Lagrangian attractor', also identified as particle chaining [3].
- '2-D vertical curtain-like layer', structures in which particle group in a 2-D sheet like configuration.
- '3-D structure without any particular structure in the cloud', in which particles group into a non-easily discernable 3-D clustered form.

To evaluate the formation of clusters quantitatively, the mean nearest neighbor distance for particles as described in the work by Park and Lee [122] is determined. In this computation, each particle is evaluated to determine center-to-center distance to its nearest neighboring particle, as shown in Figure 5.1. The mean value of nearest neighbor value is then evaluated as:

$$\overline{L_{Neigh.}} = \frac{1}{N_p}\sum_{i=1}^{N_p} L_{Neigh.,i} \tag{5.4}$$

where $\overline{L_{Neigh.}}$ is the mean nearest neighbor value, N_p is the number of particles evaluated, n is the index of each particle in the evaluation up to N_p, and $L_{Neigh.,i}$ is each individual particle's nearest neighbor distance.

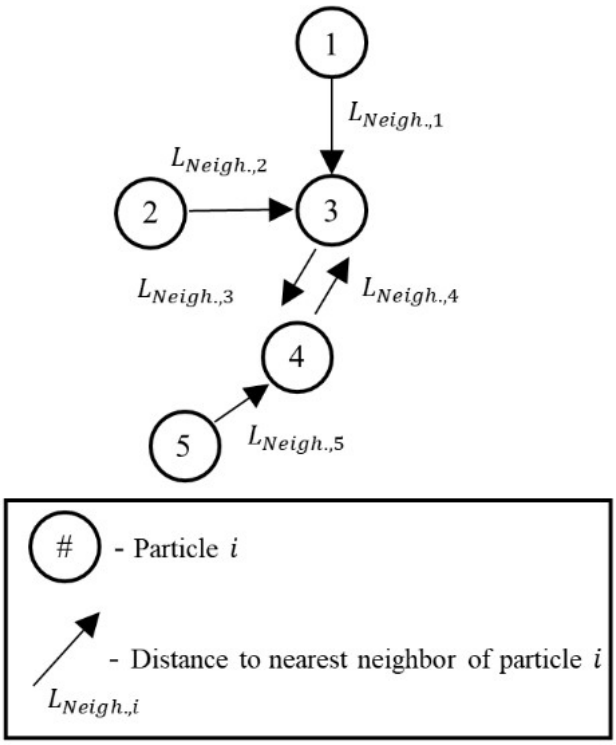

Figure 5.1: Diagram of nearest neighbor evaluation.

5.2 Methods

5.2.1 Material Properties and Domain Settings

Typical in use proppant particle size falls into the range of approximately 100 to 850 μm [3], with sizing in the range of 20/40 mesh for approximately 85 % of proppant applications [1]. Gradation of the Jordan formation, a widely utilized source of natural proppant material, is reported with most particles around 500 μm in diameter [123]. As such, 500 μm sized proppant particles are used in this work. Typical slickwater dynamic viscosity values reported in the literature are around 0.001 to 0.005 Pa·s with specific gravity of approximately 1.0 [3,124–127].A dynamic viscosity value of 0.003 Pa·s and density of 1000 kg/m^3 is implemented in the simulations.

Both neutrally buoyant and non-neutrally buoyant particles are explored in this work. Particle density is varied to match the density of the carrier fluid for the neutral buoyancy cases. Gravity is active in all simulation cases. Further details of material properties are summarized in Table 5.1.

Table 5.1: Model Material Properties for flowing slurry simulations

Proppant Parameters:		Units	Fluid Parameters:		Units
Particle Diameter	500	μm	Dynamic Viscosity	0.003	Pa.s
Particle Density *	2600, 1000	kg/m^3	Density	1000	kg/m^3
Contact friction value	0.6	-			
Young's Modulus	$5x10^6$	N/m^2			
Poisson Ratio	0.3	-			
Coefficient of Restitution	0.051	-			

* - For non-neutrally buoyant and neutrally buoyant simulations, respectively

A CFD timestep of 2.5×10^{-4} seconds is implemented for most cases and reduced to 1×10^{-4} s for several higher flow rate conditions resulting in stable calculations of the cases. A ratio of CFD to DEM timestep size equal to 100 is utilized (i.e., DEM time step = CFD time step / 100).

To implement developed flow condition at the inlet for the CFD portion of the model, first a periodic model of the desired target concentration is run without gravity (see Figure 5.2). *X* and *Y* faces of the domain are set to a periodic condition and the *Z* faces are set to a no-slip condition. Size of the domain is 8 mm (*X*) x 8 mm (*Y*) x 24 mm (*Z*) and CFD cells are made to have length, width, and height of 1.6 mm, each. Consistent flow rate at the desired injection rate is initiated and sustained in the +*X* - direction with use of the 'meanVelocityForce' option available in OpenFOAM, which adds a supplemental force term in the flow solution to maintain a user defined volume averaged mean velocity. Simulations are run till converged flow occurred, in which variance of mean flow velocity was confirmed less than *O* (10^{-7}). In all cases, the convergence occurred within less than two seconds of simulated time. Average values for *X* - directional velocity and void fraction are extracted from the Y/*Z* plane of cells located at the +*X* end of the domain. Average values are then slightly adjusted, if needed, to match target inlet flow rate and void fraction and then mapped to the inlet boundary condition of the injection simulation domain. Mapping of face and cell values in OpenFOAM files is accomplished by ordering and listing values based on their spatial coordinates in initiation files. This ordering structure is easiest viewed as a representation of values in a 3-dimensional matrix. Row values correspond to *X* coordinates, columns to *Y* coordinates, and slices to *Z* coordinates. An ordered list of values is formed by listing all row values for the first column and slice before progressing to the next column value. Likewise, all column values are exhausted before progressing the next slice value in the matrix.

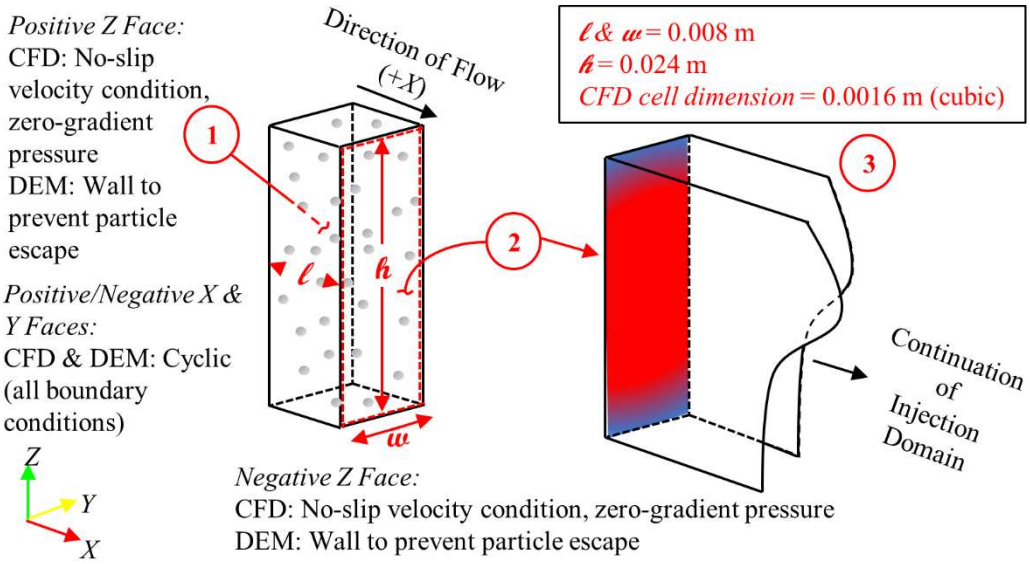

Figure 5.2: Establishment domain conditions and procedure for generating developed inlet condition: 1) run cyclic model to establish converged injection condition, 2) average velocity and void fraction values from cyclic model, 3) map averaged values to inlet boundary condition of injection model. Diagram not to scale.

Configuration of the injection simulation domain for both the CFD and DEM components is indicated in Figure 5.3. As noted in Chapter 2, side wall effects can have an additional influence on particle flow and settling behavior, particularly as ratio of particle diameter to wall opening width decreases [35]. For this work, it was desired to evaluate conditions for clustering and the clustering's effects on slurry transport behavior independent of these possible influences. As such, *Y* faces for the injection simulation domains are kept as cyclic to remove any wall effect influence.

Injected particle slurry is initiated near the -*X* face of the domain with flow directed in the +*X* - direction. Particles themselves are continuously generated at a target volumetric concentration value in a 0.008 m region at the injection end of the domain in what is identified as the 'factory' in Figure 5.3. To allow generated particle to achieve an initial momentum from the inlet flow, the particle factory is sub-divided into 25 layers, each separated by a horizontally oriented wall, where particles can gain momentum in the flow prior to experiencing free fall. Depositing particles in the non-neutrally buoyant condition simulations are destroyed when reaching the bottom of the flow domain to allow for study of suspended behavior uninfluenced by particle mounding +*X* face boundary, for non-neutrally buoyant cases, is generated at a distance of at least 50 % greater than the anticipated maximum particle travel distance evaluated per Eq. 2.13. This is implemented to reduce any possible outlet boundary effects on these simulations.

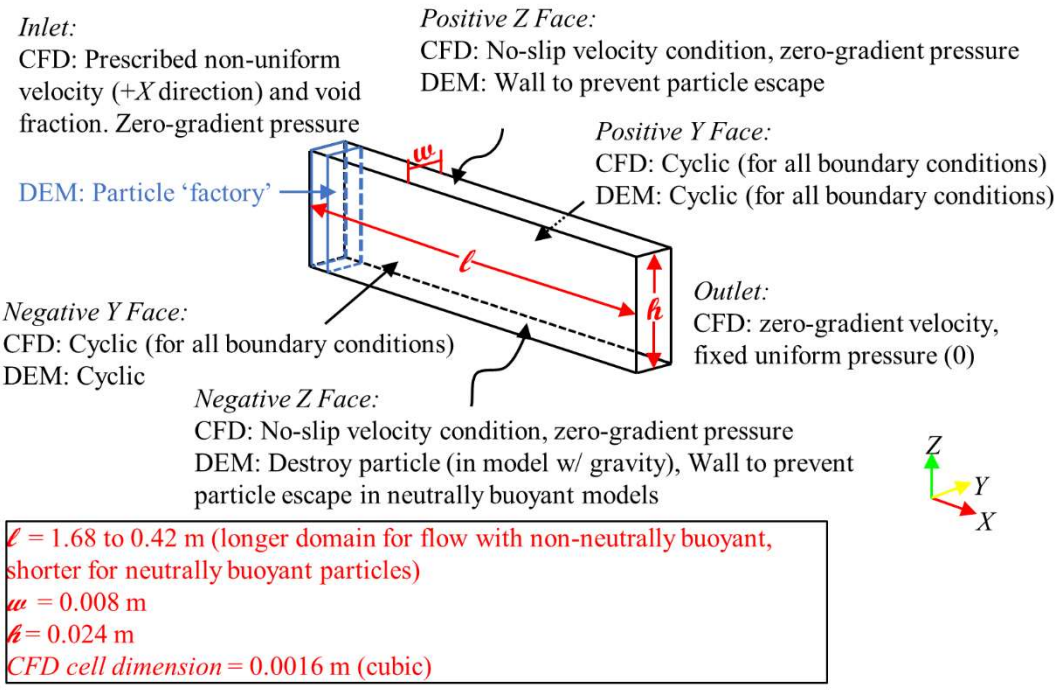

Figure 5.3: Injection simulation domain. Diagram not to scale.

5.2.2 Injection Conditions for Model

Typical proppant injection concentrations for all treatment types are cited as within the range of 0.25 to 10 PPA [3,128,129], where PPA is pounds of proppant added to 1 gallon of proppant free fluid. There is no SI equivalent for PPA. This equates to approximate particle volumetric concentrations of 1.1 % to 31.5 % assuming particle properties as specified earlier for this work. Though the proppant concentrations are typically lower for slickwater type slurries (~0.25 to 3 PPA) [5], these larger concentration levels are still considered to explore their effects on proppant behavior in flow.

Typical injection rates of proppant slurry range from approximately 0.05 to 0.27 m^3/s, with slickwater treatments injected the higher range of these rates [3]. Assuming a typical, bi-wing fracture 70 m in height with 6 mm opening width, this would provide an approximate mean inlet velocity of 0.33 m/s. In this work, this estimated injection velocity is utilized, varying to approximately 50 % greater and 50 % lower magnitudes to evaluate injection rate variance on slurry flow behavior. Summary of injection schedules evaluated are as shown in Table 5.2.

$Re_{||}$ based on Eq. 2.7 for the above conditions and flow rates considered in this work ranges from approximately 2080 to 720. $Re_{||}$ values meeting a critical value of 2100-2800 and greater [2,8] are turbulent. As flow

conditions for this work are below this critical range, flow is modeled as laminar. Further, the fluid is modeled as incompressible and Newtonian in behavior.

Table 5.2: Model run configuration summary for flowing slurry simulations

Model A Coupling				Model B Coupling			
Neutrally Buoyant Particles Simulations		Non-neutrally Buoyant Simulations		Neutrally Buoyant Particles Simulations		Non-neutrally Buoyant Simulations	
Injected Particle Vol. Conc. (%)	Inlet Injection Rate (m/s)	Injected Particle Vol. Conc. (%)	Inlet Injection Rate (m/s)	Injected Particle Vol. Conc. (%)	Inlet Injection Rate (m/s)	Injected Particle Vol. Conc. (%)	Inlet Injection Rate (m/s)
8.0	0.18	7.3	0.17	7.9	0.18	7.2	0.17
14.5	0.18	13.3	0.18	14.6	0.18	13.3	0.18
20.3	0.18	18.6	0.18	20.1	0.18	18.6	0.18
24.9	0.18	23.6	0.18	24.9	0.18	23.5	0.18
29.3	0.18	27.9	0.18	29.3	0.18	27.9	0.18
33.1	0.18	31.9	0.17	33.1	0.18	32.1	0.18
8.0	0.34	7.0	0.34	7.8	0.34	7.0	0.34
14.3	0.35	13.0	0.34	14.2	0.35	13.0	0.34
19.9	0.35	18.5	0.34	19.6	0.35	18.4	0.34
24.8	0.35	23.3	0.34	24.6	0.35	23.2	0.34
29.4	0.35	27.5	0.34	29.0	0.35	27.5	0.34
33.4	0.35	31.1	0.34	33.0	0.34	31.4	0.34
7.7	0.51	6.9	0.51	7.7	0.51	6.9	0.51
19.7	0.53	12.9	0.52	19.6	0.53	12.9	0.52
33.2	0.52	18.1	0.52	33.1	0.52	18.3	0.52
		23.0	0.52			23.1	0.52
		27.0	0.51			27.1	0.51
		30.9	0.51			31.2	0.51

5.3 Findings and Results

5.3.1 Clustering Behavior of Particles in Flow

Qualitative evaluation of injected particles in both the non-neutrally buoyant and neutrally buoyant conditions are first considered. For clarity of identifying clustering formations within the flow, particle to particle contact locations (i.e., regions of dense grouped particle clustered formations) can be seen in Figs. 5.4 through 5.9 for

volumetric particle concentration injections ranging from ~7 % to ~33 % at an injection rates of ~0.18, ~0.34, and ~0.51 m/s, respectively.

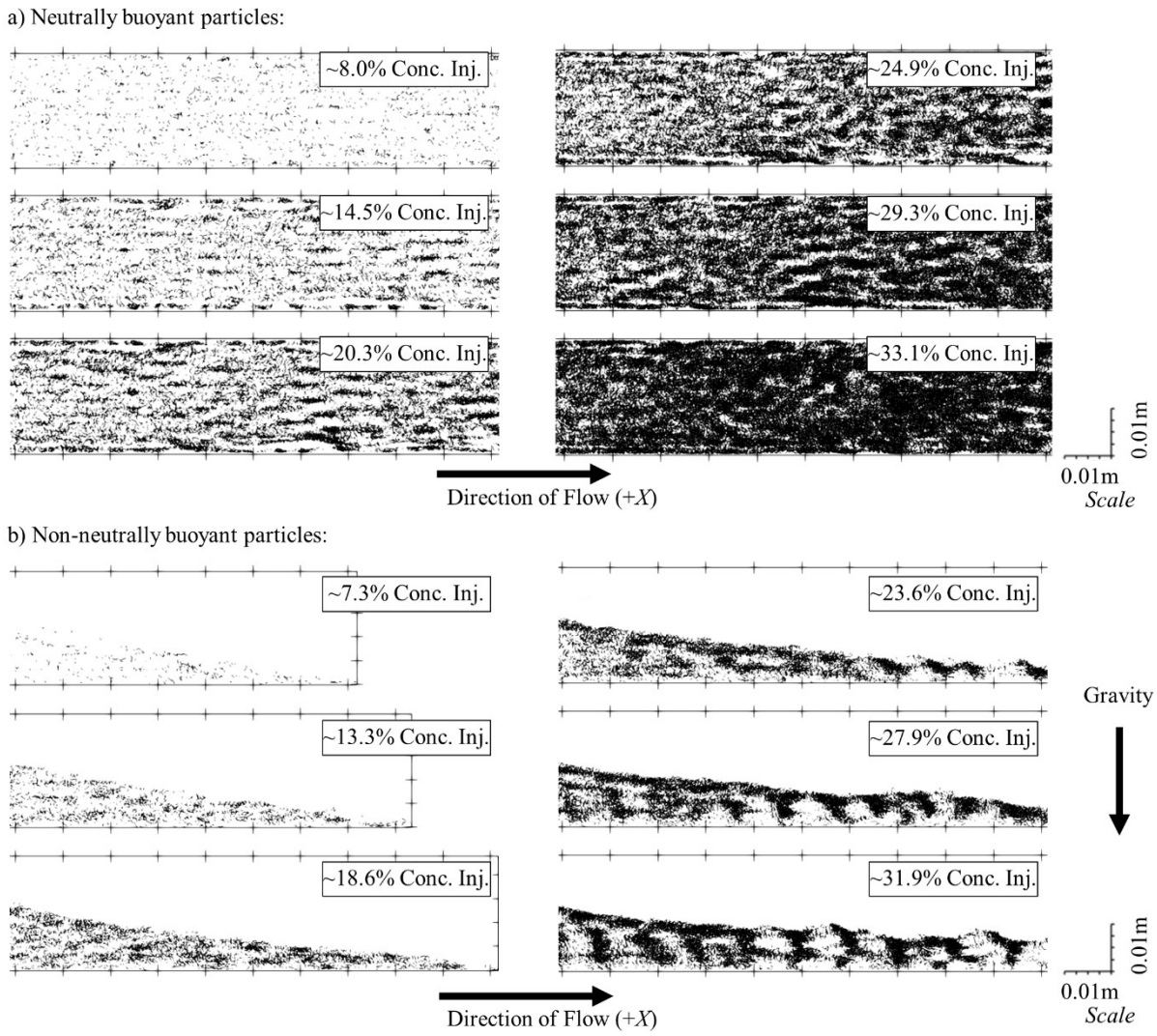

Figure 5.4: Particle to particle contacts, indicating clustering formations, for simulation time t = 3 s, from domain position of X = 0.05 to 0.15 m and injection rate of ~0.18 m/s for a) neutrally buoyant particle injection and b) injection of non-neutrally buoyant particles, "Model A" coupling.

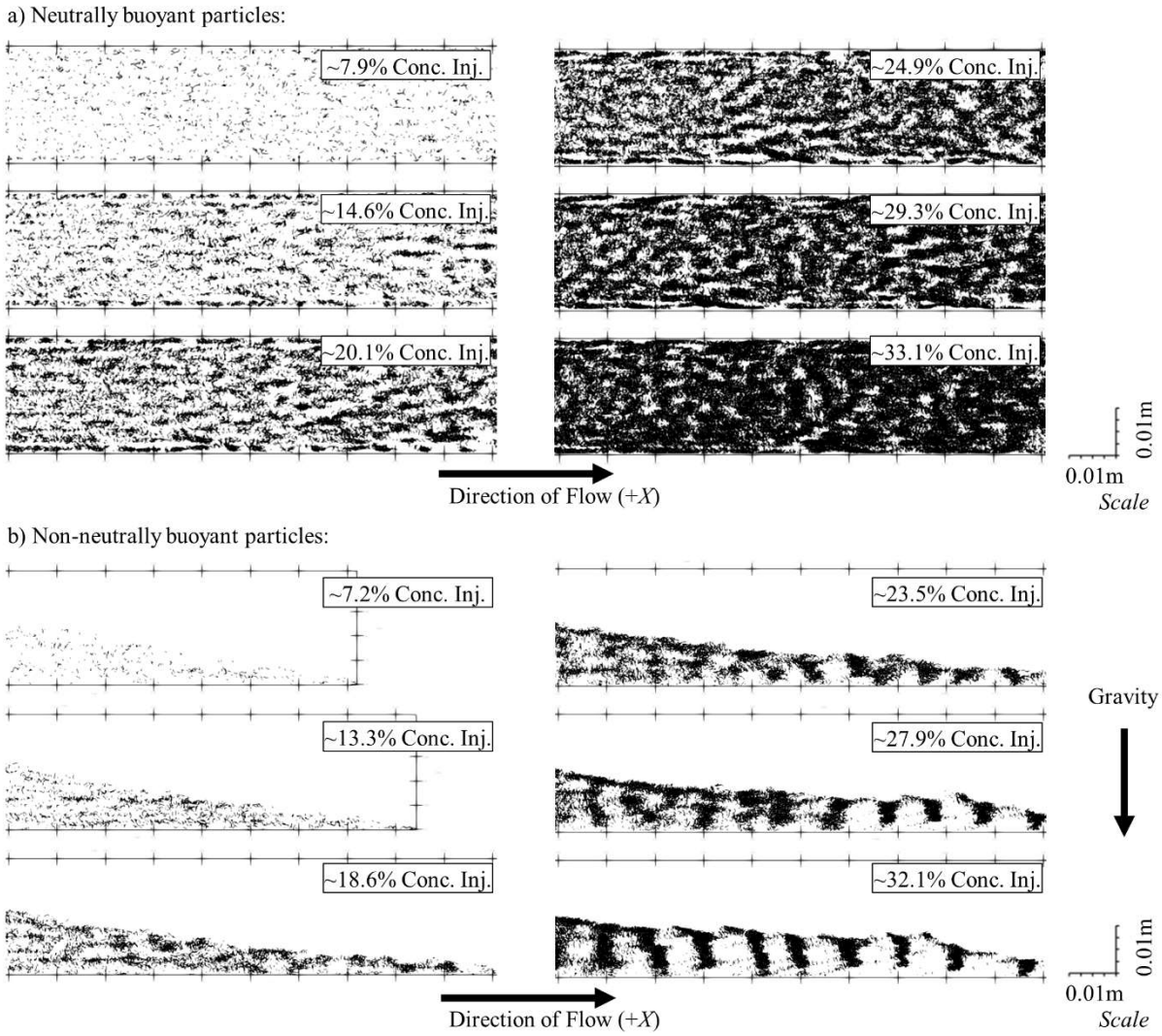

Figure 5.5: Particle to particle contacts, indicating clustering formations, for simulation time t = 3 s, from domain position of X = 0.05 to 0.15 m and injection rate of ~0.18 m/s for a) neutrally buoyant particle injection and b) injection of non-neutrally buoyant particles, "Model B" coupling.

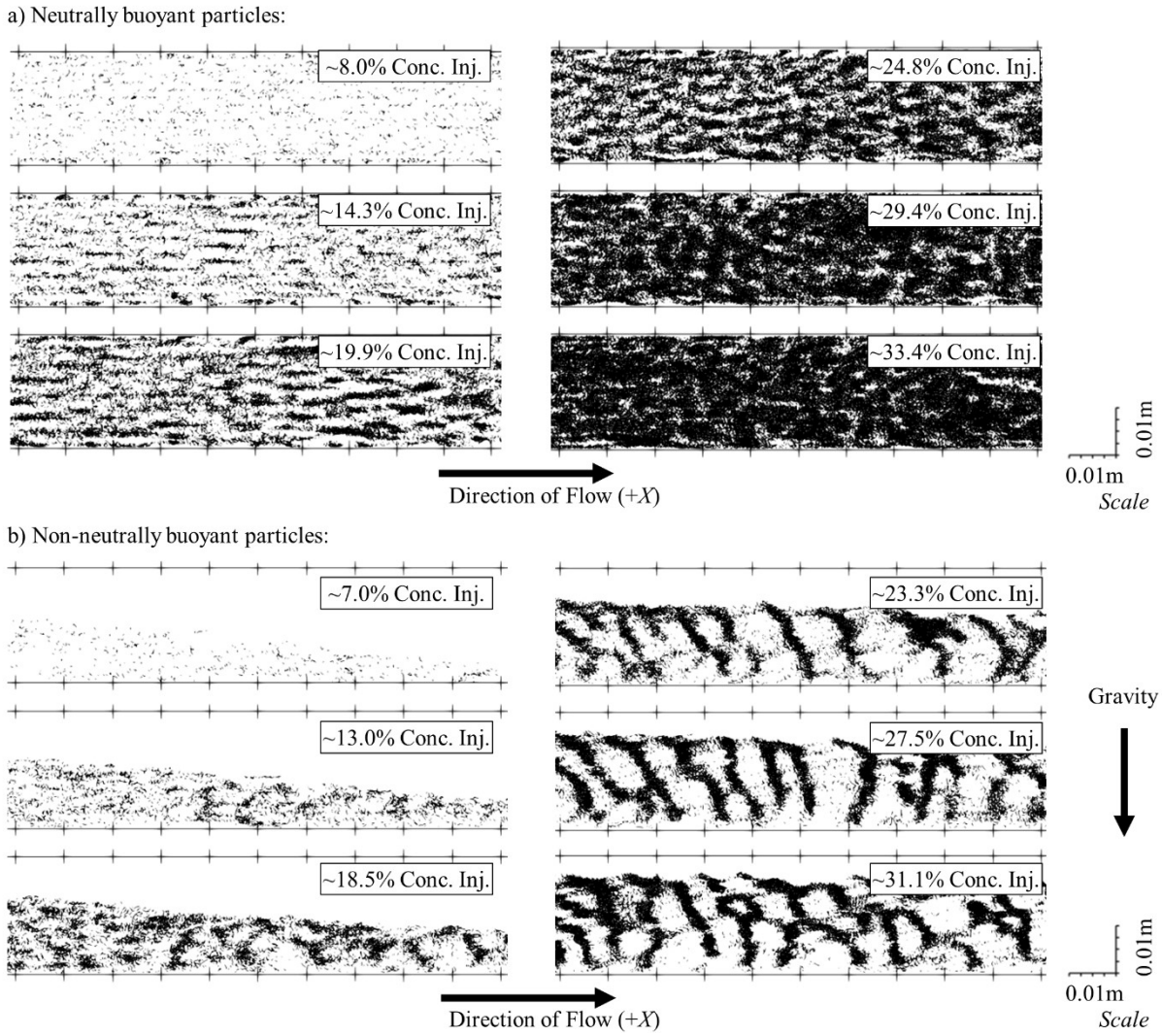

Figure 5.6:Particle to particle contacts, indicating clustering formations, for simulation time t = 3 s, from domain position of X = 0.1 to 0.2 m and injection rate of ~0.34 m/s for a) neutrally buoyant particle injection and b) injection of non-neutrally buoyant particles, “Model A” coupling.

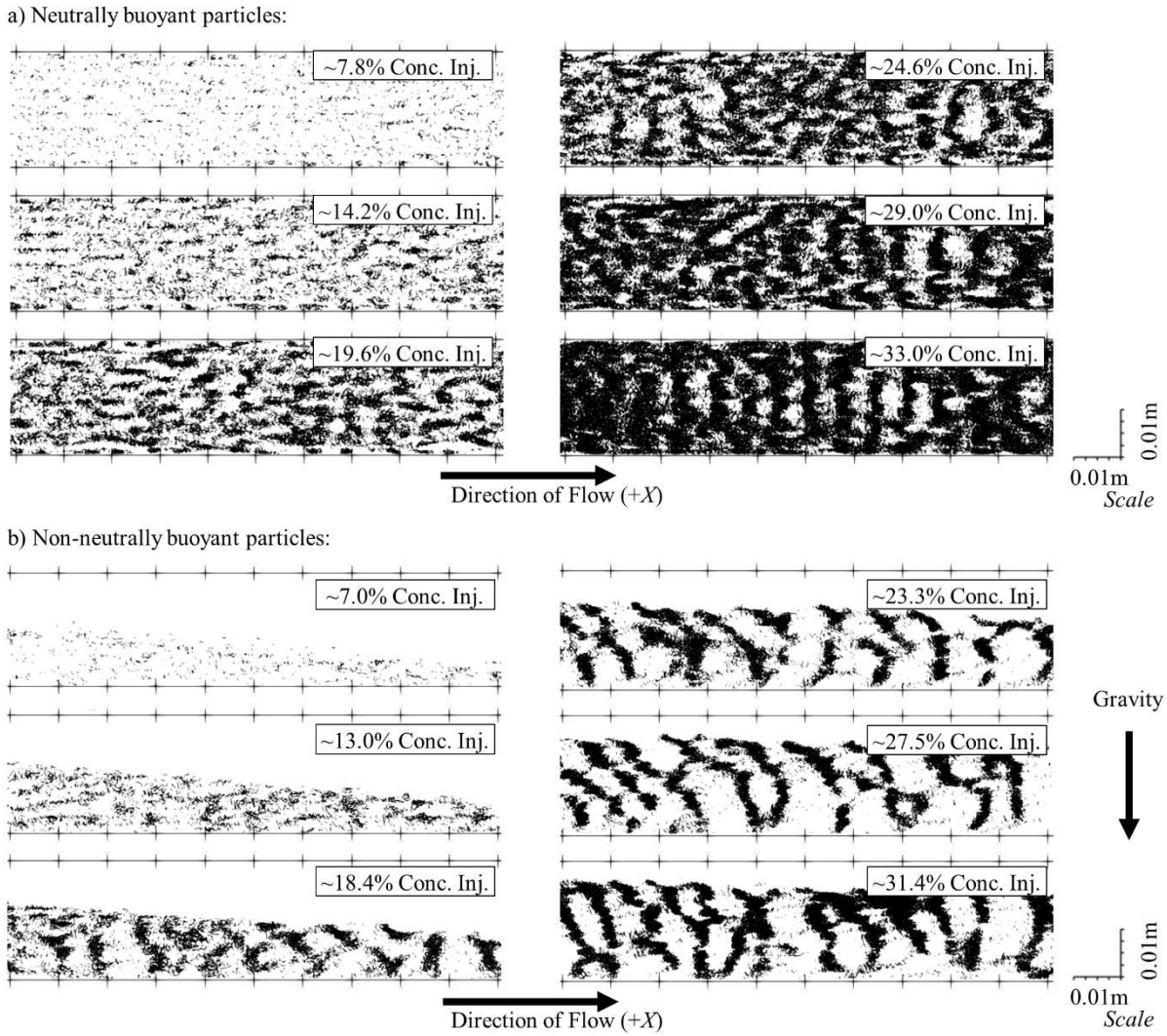

Figure 5.7: Particle to particle contacts, indicating clustering formations, for simulation time t = 3 s, from domain position of X = 0.1 to 0.2 m and injection rate of ~0.34 m/s for a) neutrally buoyant particle injection and b) injection of non-neutrally buoyant particles, "Model B" coupling.

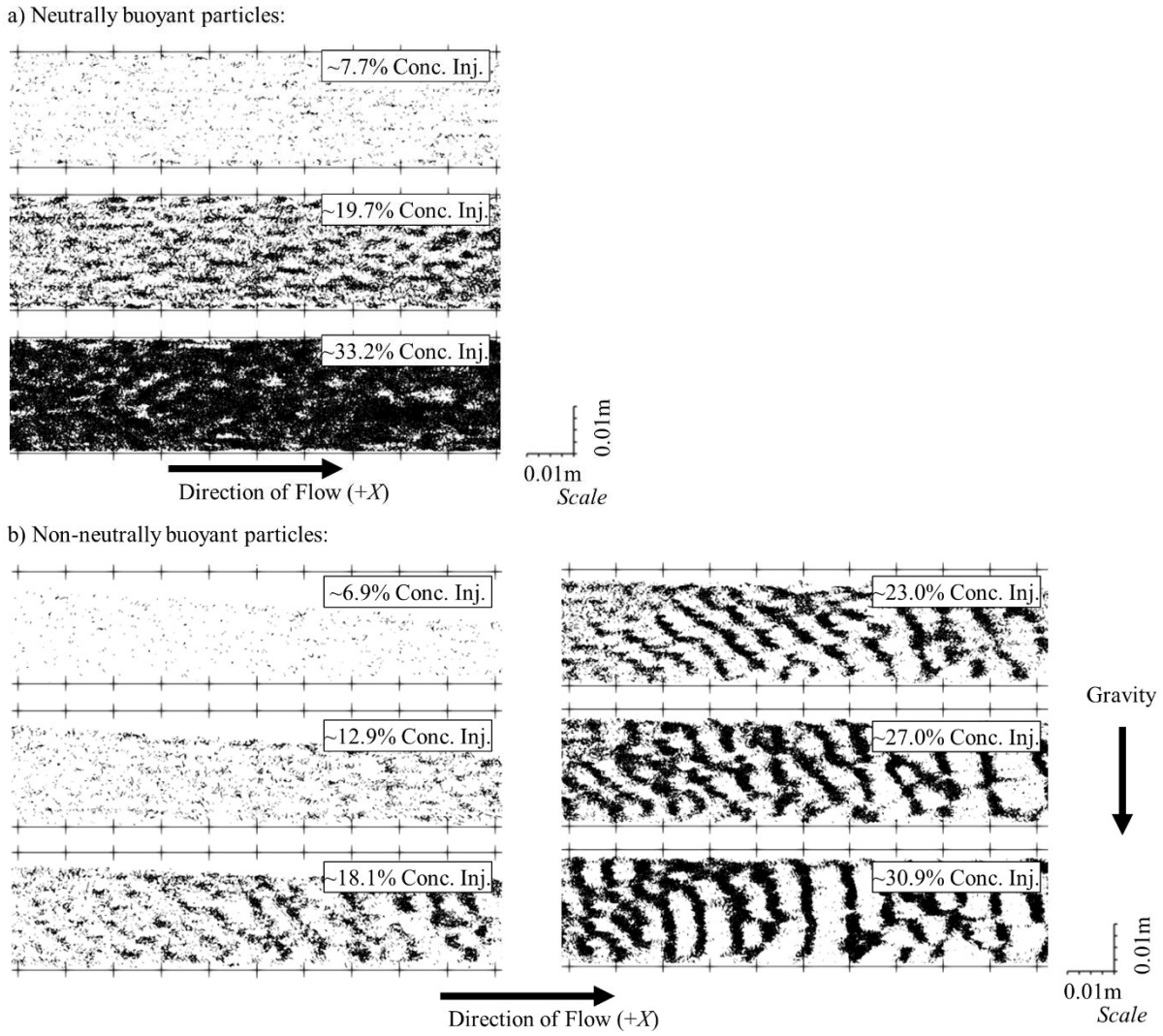

Figure 5.8: Particle to particle contacts, indicating clustering formations, for simulation time $t = 3$ s, from domain position of $X = 0.1$ to 0.2 m for particles with injection rate of ~0.51 m/s for a) neutrally buoyant particle injection and b) injection of non-neutrally buoyant particles, "Model A" coupling.

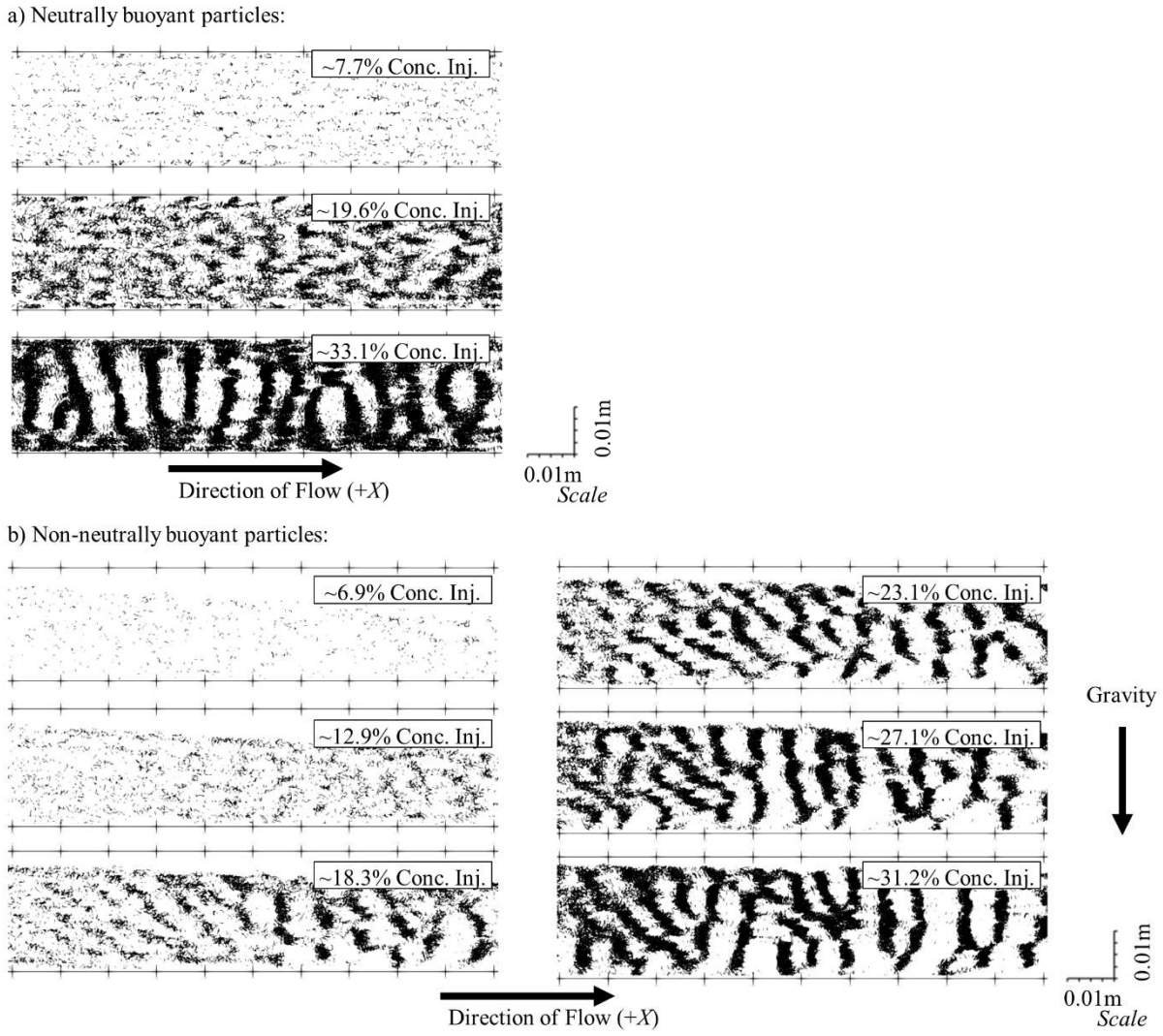

Figure 5.9: Particle to particle contacts, indicating clustering formations, for simulation time $t = 3$ s, from domain position of $X = 0.1$ to 0.2 m for particles with injection rate of ~0.51 m/s for a) neutrally buoyant particle injection and b) injection of non-neutrally buoyant particles, "Model B" coupling.

For the lowest concentration volumetric injection values of approximately 7 %, relatively small, scattered groupings of clustering particles occur. This scattering of small particle groupings can be contrasted with the initiation of distinctly structured particle clusters in a horizontal, chain-like orientation (1-D) in approximate 13 % to 14 % concentration cases in most cases. Figure 5.10a shows a perspective view of particles from the ~13.0 % concentration, ~0.34 m/s injection simulation with "Model B" coupling. Transition in clustering shape to a vertical 'curtain-like' configuration (2-D) occurs for the majority of remaining simulations above ~ 13.0 to 14.0 % concentrations, except several neutrally buoyant high concentration cases, where 3-D clustering is observed. An example of this 2-D curtain

structure is shown in Figure 5.10b, for the ~27.5 % concentration, ~0.34 m/s injection case with non-neutrally buoyant particles, "Model B" coupling. It is also importantly noted that overall it appears that the transition to vertical curtain structures in non-neutrally buoyant conditions emerge at a threshold injection concentration of approximately 20 % in all cases, when comparing Figs. 5.4 through 5.9. The significance of this threshold point will be referred to in subsequent discussions in this and further subsections.

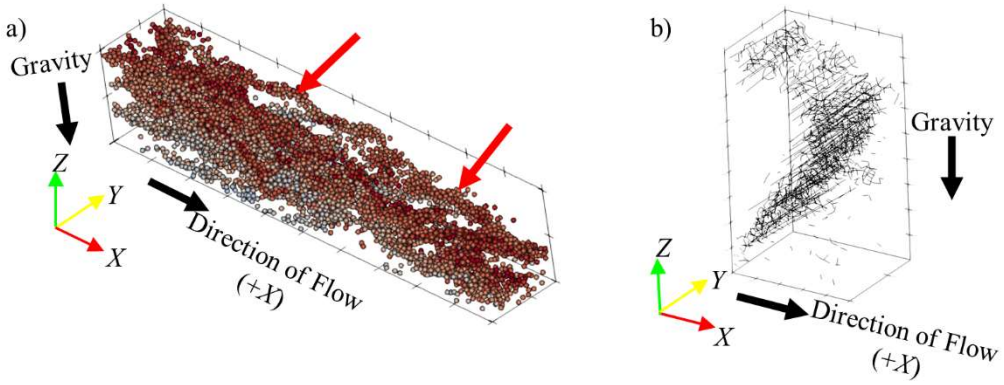

Figure 5.10: a) 1-D horizontal particle clustering ~13 % particle vol. concentration simulation with injection rate of ~0.34 m/s at simulation time t = 3 s, from domain position of X = 0.1 to 0.2 m (particles colored by initial starting elevation in simulation to help visualization of distinct clustering formations) , "Model B" coupling. b) Particle to particle contact image of 2-D 'curtain' clustering formation for 27.8 % vol. concentration simulation with injection rate of ~0.34 m/s at simulation time t = 2.4 s, from domain position X = 0.2 to 0.21 m, "Model B" coupling.

The origination and development of a 2-D clusters is shown in Figure 5.11. Clustering starts in a dense particle slurry due to viscously damped particle collisions, as seen for snapshot of t = 1.19 s in Figure 5.11. Particle drag force is larger at higher particle concentrations (see Eqns. 3.10 and 3.11) and fluid velocity increases locally as the space between particles shrinks. As a result, fluid-particle coupled behavior enhances particle drag forces and leads to higher relative velocities of clustered formations in the direction of flow. Clusters continue to build up as they further collide with additional particles in the flow, as seen for snapshot at t = 1.24 seconds in Figure 5.11. Eventually, particle clusters reach a peak state of loose packing at approximately 50-60 % volumetric particle concentration, where cluster concentration no longer increases. Cluster groups that achieve higher relative velocity than neighbors in the flow separate and create the 2-D curtain clustered assemblages, as seen for snapshot at t = 1.29 seconds in Figure 5.11. It is observed that particle clusters continuously form and dissipate during the flow. Qualitative distinction of clustering shapes for all the simulations performed in this work are summarized in Table 5.3. Slight variances in clustering shape for similar simulations performed with "Model A" and "Model B" coupling can be seen.

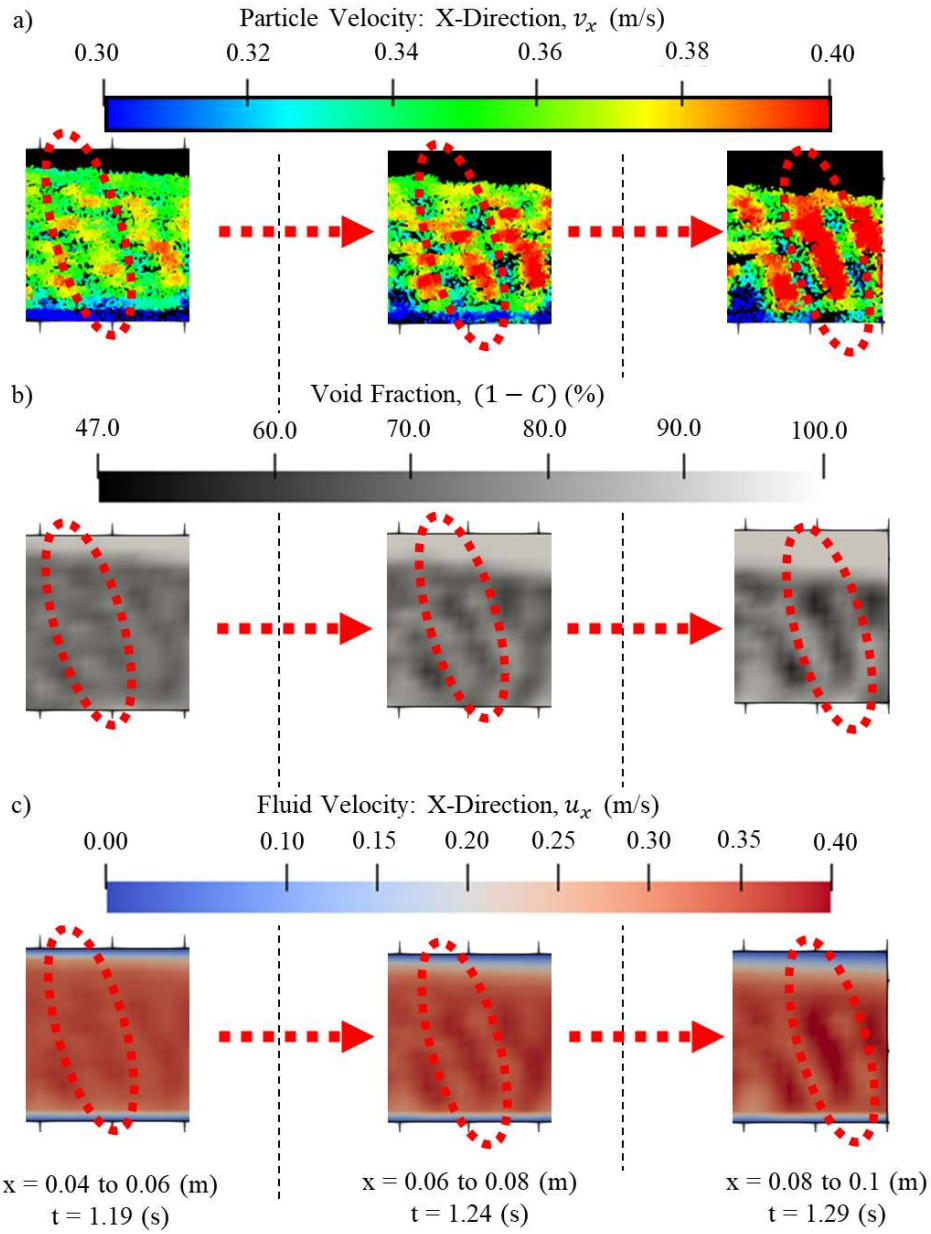

Figure 5.11: Mid *y*-axis slice of 2-D particle cluster, a) particle *x*-direction velocity in flow, b) void fraction in flow, c) corresponding fluid *x*-direction velocity, "Model B" coupling.

Table 5.3: Qualitative clustering shapes for neutrally buoyant and non-neutrally buoyant simulations.

Model A coupling						Model B coupling					
Neutrally Buoyant Particles Simulations			Non-neutrally Buoyant Simulations			Neutrally Buoyant Particles Simulations			Non-neutrally Buoyant Simulations		
Inj. Particle Vol. Conc. (%)	Inlet Inj. Rate (m/s)	Cluster Shape*	Inj. Particle Vol. Conc. (%)	Inlet Inj. Rate (m/s)	Cluster Shape*	Inj. Particle Vol. Conc. (%)	Inlet Inj. Rate (m/s)	Cluster Shape*	Inj. Particle Vol. Conc. (%)	Inlet Inj. Rate (m/s)	Cluster Shape*
8	0.18	None	7.3	0.17	None	7.9	0.18	None	7.2	0.17	None
14.5	0.18	1D	13.3	0.18	1D	14.6	0.18	1D	13.3	0.18	1D
20.3	0.18	1D	18.6	0.18	1D-2D	20.1	0.18	1D-2D	18.6	0.18	1D-2D
24.9	0.18	1D-2D	23.6	0.18	1D-2D	24.9	0.18	1D-2D	23.5	0.18	1D-2D
29.3	0.18	1D-2D	27.9	0.18	2D	29.3	0.18	2D-3D	27.9	0.18	2D
33.1	0.18	3D	31.9	0.17	2D	33.1	0.18	3D	32.1	0.18	2D
8	0.34	None	7	0.34	None	7.8	0.34	None	7	0.34	None
14.3	0.35	1D	13	0.34	1D-2D	14.2	0.35	1D	13	0.34	1D
19.9	0.35	1D-2D	18.5	0.34	1D-2D	19.6	0.35	1D-2D	18.4	0.34	1D-2D
24.8	0.35	1D-2D	23.3	0.34	2D	24.6	0.35	2D	23.3	0.34	2D
29.4	0.35	2D-3D	27.5	0.34	2D	29	0.35	2D	27.5	0.34	2D
33.4	0.35	3D	31.1	0.34	2D	33	0.34	2D	31.4	0.34	2D
7.7	0.51	None	6.9	0.51	None	7.7	0.51	None	6.9	0.51	None
19.7	0.53	1D-2D	12.9	0.52	1D	19.6	0.53	1D-2D	12.9	0.52	1D
33.2	0.52	3D	18.1	0.52	1D-2D	33.1	0.52	2D	18.3	0.52	2D
			23	0.52	2D				23.1	0.52	2D
			27	0.51	2D				27.1	0.51	2D
			30.9	0.51	2D				31.2	0.51	2D

*- The designation 'None' is used to describe the occurrence of little to no distinct clustered structures

Figure 5.12 shows the results of the mean nearest neighbor evaluations for the neutrally buoyant and non-neutrally buoyant simulations. It is noted that results for “Model A” and “Model B” coupling are virtually identical. To illustrate the significant level of clustering that occurs in the simulations beyond what is attributable to increasing concentration effects, mean nearest neighbor values for a homogeneous, body-centered, cubic lattice of distributed particles (see Figure 5.12d for illustration), at varying concentrations are presented in Figure 5.12c. These values are contrasted against the neutrally buoyant simulation results (see Figure 5.12c). As can be seen, concentration effects alone do not account for the significantly reduced mean nearest neighbor values.

For the neutrally buoyant cases, the injection rate of the slurry is seen to have little effect on quantitative clustering, only concentration increase is influential. Additionally, comparison between the macroscopically averaged *X*-directional drag for the ~33 % neutrally buoyant concentrations cases at flow rates of 0.18 and 0.51 m/s reveals a near order of magnitude difference in drag magnitude (~6.5 x 10^{-8} N and ~3.8 x 10^{-7} N), respectively. As both drag and the Stokes number are dependent on the relative differences between the particle and fluid velocities, this would point to contributions of varying Stokes number having less impact on clustering than varying concentration and Durand-Froude number for the conditions considered in this work.

It is further noted in all of the neutrally buoyant cases that particle mean nearest neighbor values approach a limit that is equal to the particle diameter as concentrations increase. This limit is seen to be independent of injection rate. Such limit would be representative of approaching a packed particle state in the clusters where every particle is directly in contact with another particle.

By comparison, the mean nearest neighbor results for injected non-neutrally buoyant particles show a clear deviation in values as injected particle rates increase in like concentration conditions, with greater mean nearest neighbor values than neutrally buoyant cases at similar injection rates. This indicates that combined gravity effects, not balanced by buoyancy, and flow rate influences cluster formation with greater variance occurring in higher concentrations. This therefore points to the importance of the Durand-Froude and Concentration dimensionless values in the clustering behavior of flowing proppant slurries.

The quantitative variance in nearest neighbor values is visually represented in Figure 5.13, which shows a contour plot of nearest neighbor values against concentration and Durand-Froude number for “Model A” coupling values. Low Durand-Froude number values with high injection concentrations yield a clear tendency towards clustering, which is indicated by lower nearest neighbor values. The abundance of clustering is potentially problematic for field operations as particle bridging and clogging in proppant injections would lead to less optimal proppant placement within the fracture.

It is again noted that at all the tested conditions, the mean nearest neighbor values decrease at notably lower rates after approximately ~20 % injection concentration. This ~20 % concentration point is also the approximate threshold for the onset of 2-D curtain clusters in non-neutrally buoyant particle slurries mentioned earlier and appears to be a critical concentration where clustering behavior transitions.

In non-neutrally buoyant conditions, increase in flow rate and therefore Durand-Froude number value, leads to lower occurrence of clustering for like higher concentration injections as seen in the higher mean nearest neighbor values of Figure 5.13. Although the results point to the significance of density difference between the carrier fluid and particle phases, a comprehensive investigation of density effects is outside of the scope of this work. Specifically, this study is focused primarily on neutrally buoyant and dense particle characteristics predominate in proppant injection field operations (i.e., quartz sand proppant).

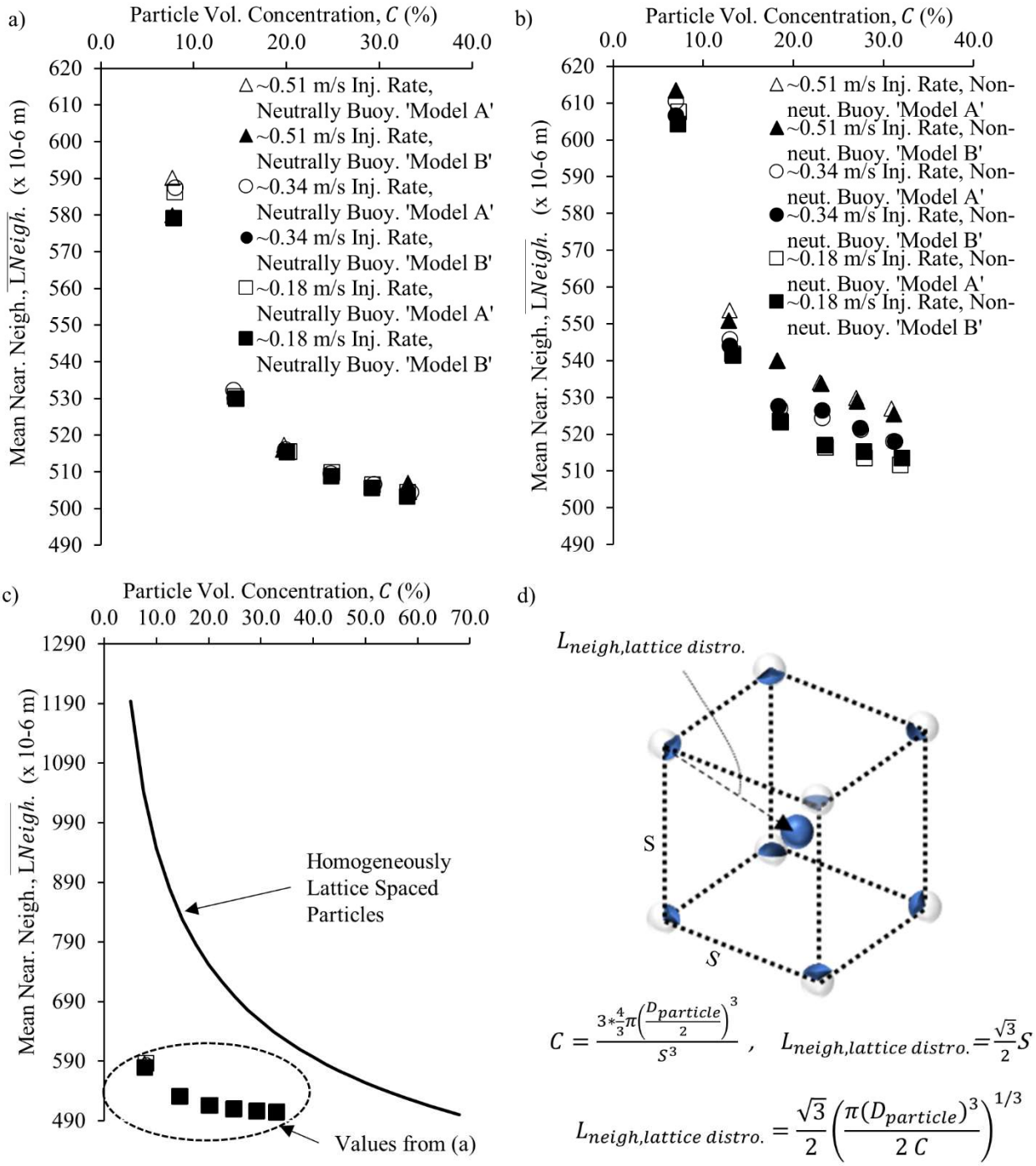

Figure 5.12: a) Neutrally buoyant injected particles mean nearest neighbor results, b) Non-neutrally buoyant injected particles mean nearest neighbor results, c) comparison of homogeneous, lattice distributed particles at varying concentrations compared to neutrally buoyant values, and d) diagram and evaluation for nearest neighbor of a lattice distributed set of particles.

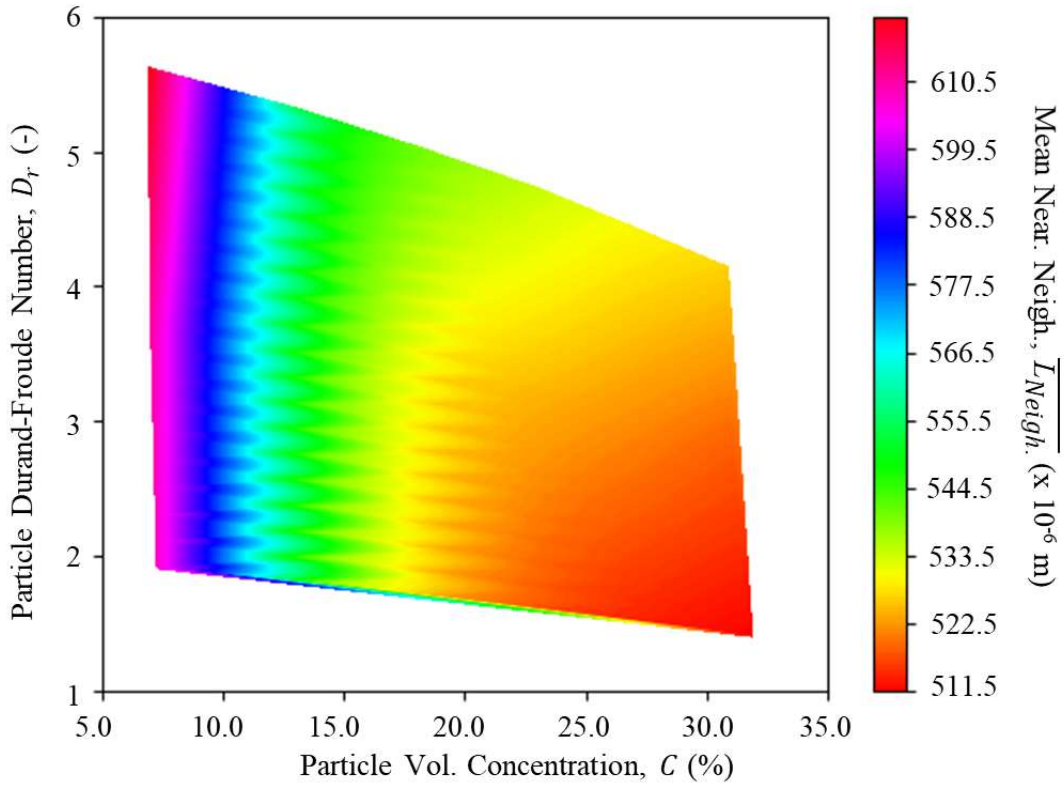

Figure 5.13: Contour plot of nearest neighbor results for injected non-neutrally buoyant particle simulations based on Concentration and Durand-Froude Number, "Model A" coupling.

Clustering shapes become more significant when looking at the meso- and micro-level behavior of individual clusters, specifically in the clusters formed in non-neutrally buoyant cases at mid to high concentrations where 2-D clustering structures occur. Deformation of the curtain clusters into a parabolic shape occurs, as is shown in Figure 5.14. In the deformed parabolic shape, the upper half of the cluster structure can also experience an upward velocity. An example parabolic curtain formation as well as the corresponding fluid void fraction, Z particle velocities, and drag magnitudes experienced is shown in Figure 5.15a-c. The upper cluster half exhibits a greater upward drag force, resembling an effect like a sail with upward facing curvature.

Figure 5.15d further shows the fluid's pressure values at locations along the domain height through the cluster. A distinct negative pressure gradient can be seen occurring through the upper portion of the cluster. This gradient means that fluid is directed from higher pressure below, upwards towards the lower pressure values. The cause of the cluster deformation and resulting pressure variance can be further evaluated by examining the fluid velocity and concentration through the cluster. Figure 5.15e shows the variance in the X - direction fluid velocity through the cluster. Rapid reduction in velocity can be seen in the transition from particle slurry to clear fluid, indicating shear at this

region, causing the upper particle cluster deformation. Concentration distribution through the cluster is shown in Figure 5.15f. Transition from lower concentration to higher concentration through the cluster's upper section occurs. The concentration distribution gradient is accompanied by a slight increase in X - directional fluid velocity in this section in Figure 5.15e, to compensate for the pressure variance through the profile per Bernoulli's principal. This higher X - directional fluid velocity is a consequence of fluid velocity being higher in the more restricted pore space of the higher concentrated cluster section.

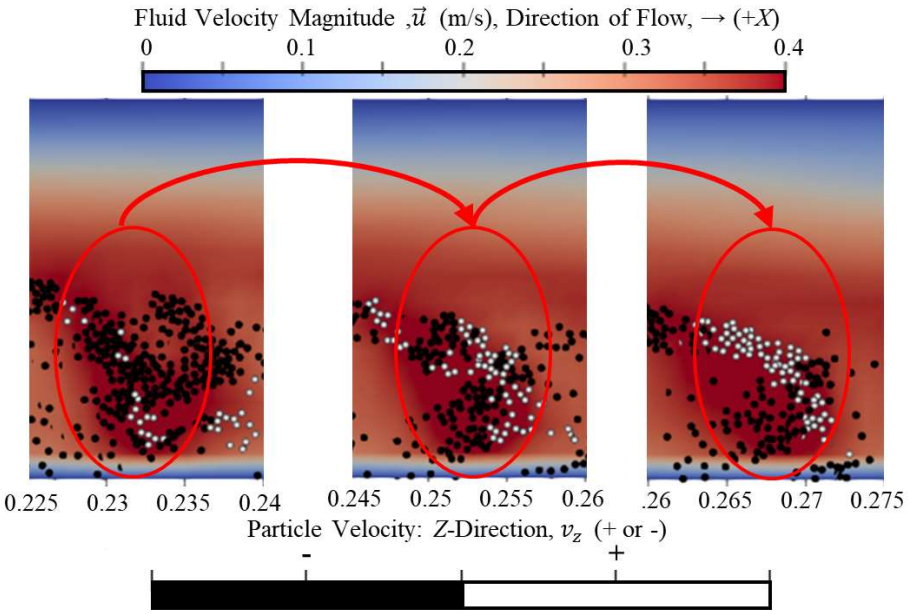

Figure 5.14: Particle curtain cluster deformation in flow in flow in ~23.1 % injection concentration, ~0.34 m/s, tracked from domain position x = ~0.225 to 0.275 from t = 1.23 to 1.3 s in simulation run, "Model A" coupling.

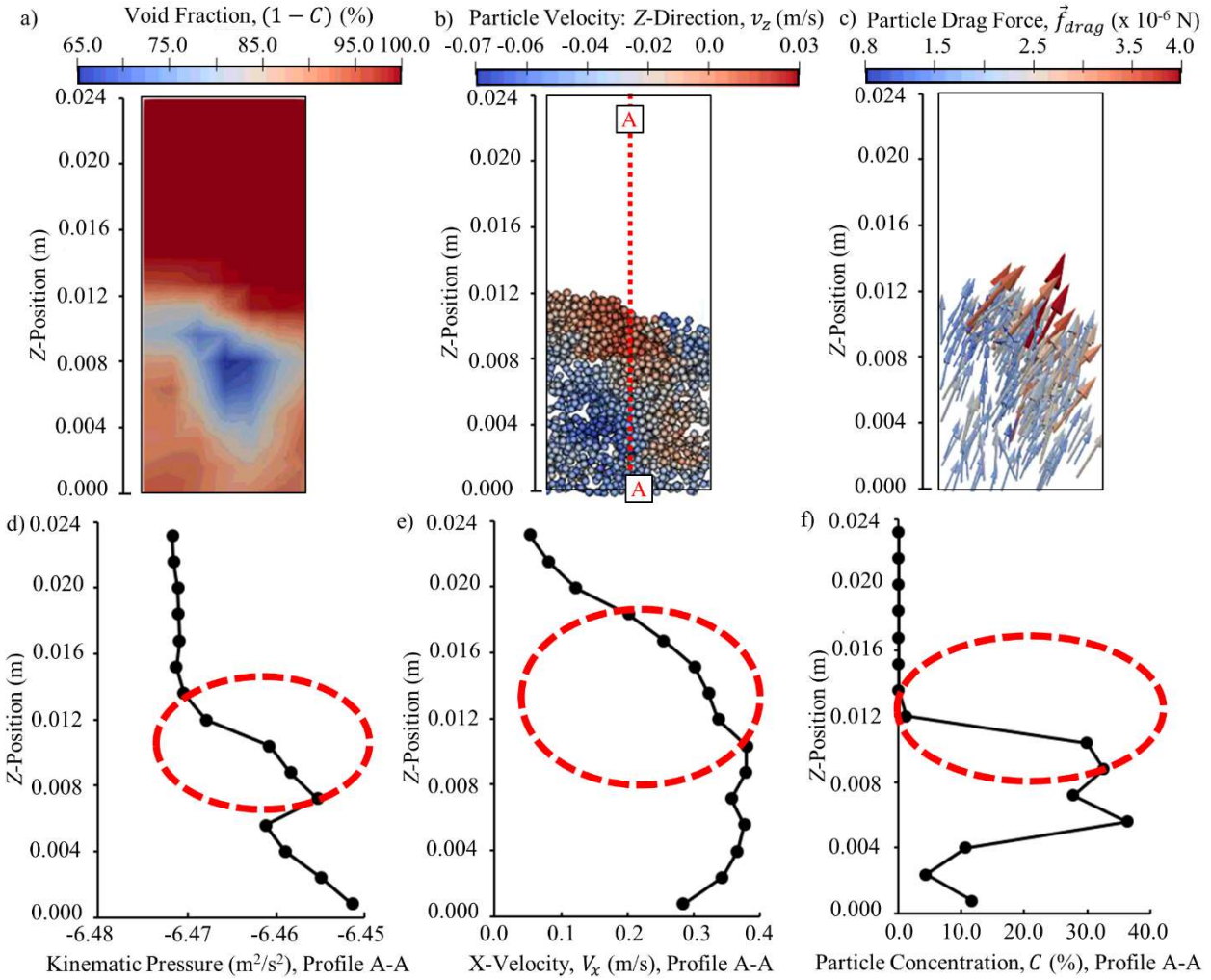

Figure 5.15: 2-D curtain cluster behavior in flow (From ~27.5 % Concentration Injection, ~0.34 m/s injection rate. Time=4 s, From x = 0.315 to 0.325 m). a) Fluid void fraction (i.e., 1-C) b) individual particle drag magnitudes for 2-D curtain cluster and surrounding particles, c) vector representation particle drag magnitude, d) pressure profile values at $x \approx$ 0.32 m, e) velocity profile at x ≈ 0.32 m, and f) particle concentration at $x \approx$ 0.32 m, "Model A" coupling.

Neutrally buoyant simulations with distinct 2-D curtains, by comparison, lack notable cluster deformations with the no-slip CFD conditions at +/- Z faces. The lack in deformation points to the more significant impact on cluster deformation due to the particle slurry, clear fluid interface shearing rather than influence from the boundary conditions. To confirm this, a simulation with slip conditions at the +/- Z boundaries is also considered. A simulation like that discussed in Figure 5.15 is run with slip condition boundaries at the +/- Z faces (see Figure 5.16). Figure 5.16 clearly again indicates a strong velocity gradient at the particle, clear fluid interface coupled with significant deformation of upper portion of the 2-D curtain clusters. Coupled pressure gradient and lift behavior is also again observed. Therefore,

it can be concluded that the +/- Z boundaries have much smaller influence on the strong cluster deformation than that caused by the slurry, clear–fluid interface.

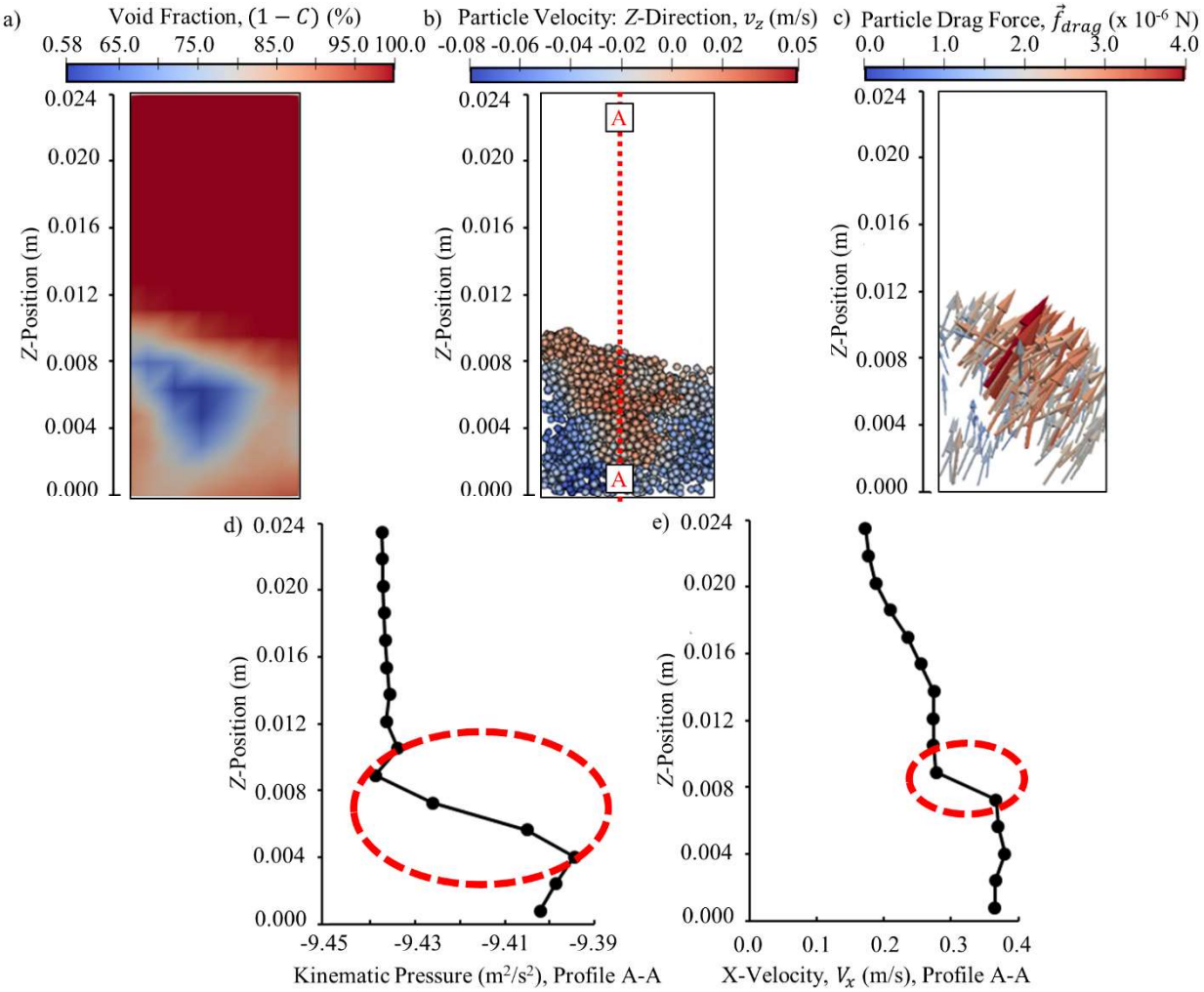

Figure 5.16: Cluster formation with +/- Z slip velocity boundary conditions. (From ~27.3 % Concentration Injection, ~0.34 m/s injection rate. Time=4 s, From x = 0.335 to 0.345 m). a) Fluid void fraction (i.e., 1-C) b) individual particle drag magnitudes for 2-D curtain cluster and surrounding particles, c) vector representation particle drag magnitude, d) pressure profile values at $x \approx 0.34$ m, and e) velocity profile at $x \approx 0.34$ m, "Model A" coupling.

5.3.2 Effects of Clusters on Slurry Settling in Flow

Simplified evaluations of particle settling and conveyance behavior is next compared to the CFD-DEM modeled results. For comparison of particle deposition and maximum travel in the non-neutrally buoyant conditions, particle counts are averaged from between the two to four second marks of each simulation to obtain mean suspended particle counts along the domain's X - direction. Values are evaluated at each Y-Z planar set of CFD cells in the X –

direction. The maximum particle travel distance corresponds to the location of the first set of CFD cells in the X -direction with mean particle count equal to one or less.

Figure 5.17 shows a comparison of the simplified evaluations and modeled mean maximum particle travel results for each injection rate and concentration condition. It can be seen, first, that the modeled injections at particle volumetric concentration of approximately 7 to 23 % show very similar travel distance compared to the simplified evaluation using the hindered settling velocity proposed by Richardson and Zaki [28] and Gadde et al. [29] (see Eqns. 2.1 and 2.2). This shows that to spite the occurrence of clusters, the maximum travel behavior is still well represented by simple hindered settling-based evaluations. This similar maximum travel can be attributed to the lift enhancement experienced in 2-D cluster dominated flows that lead to enhanced travel rather than just accelerated settling in clustered groups. Comparison to Garside and Al-Dibouni [30] (see Eq. 2.3) shows an over estimation of behavior for most cases except at the lowest considered concentration, a couple of intermediate concentration cases at mid to high injection rates for the "Model B" coupling, and the ~ 18.1 % concentration, ~ 0.51 m/s, "Model A" coupled case.

Second, significant variance between "Model A" and "Model B" conveyance results can be seen in many similar cases, especially for intermediate concentration cases at ~0.33 and ~0.51 m/s injection rates. The simplified "Model B" matches behavior with "Model A" for low flow rates, however at high flow, behavior deviates, meaning evaluation with "Model B" coupling becomes unreliable. This shows that "Model B" coupling is not universally appropriate for dense slurry modeling with clustering behavior. Therefore, analysis for the remainder of the chapter will focus on "Model A".

Lastly, a small increase in travel values compared to the Richardson and Zaki [28] and Gadde et al. [29] based evaluations can be seen for concentrations ~ 20 % to 23 % simulations at ~ 0.33 and ~ 0.51 m/s injection rates. It can be concluded that the cluster lifting effect leads to small increase in conveyance at the initial onset concentration for 2-D cluster structures and ceases at higher concentrations. Hindered settling relationships provided in the literature do not capture this slight variance. The maximum travel distance decreases at higher concentration, as observed in the ~ 31 % - 32 % volumetric concentration cases for all injection rates and for the ~ 27 % concentration cases at injection rates of ~ 0.18 and ~ 0.33 m/s. Here, maximum particle travel distance values significantly drop below all simple travel evaluations. The rapid decrease in maximum particle travel distance can be explained by similar amounts of 2-D curtain clusters forming with increasing concentration while energy contribution from the fluid decreases.

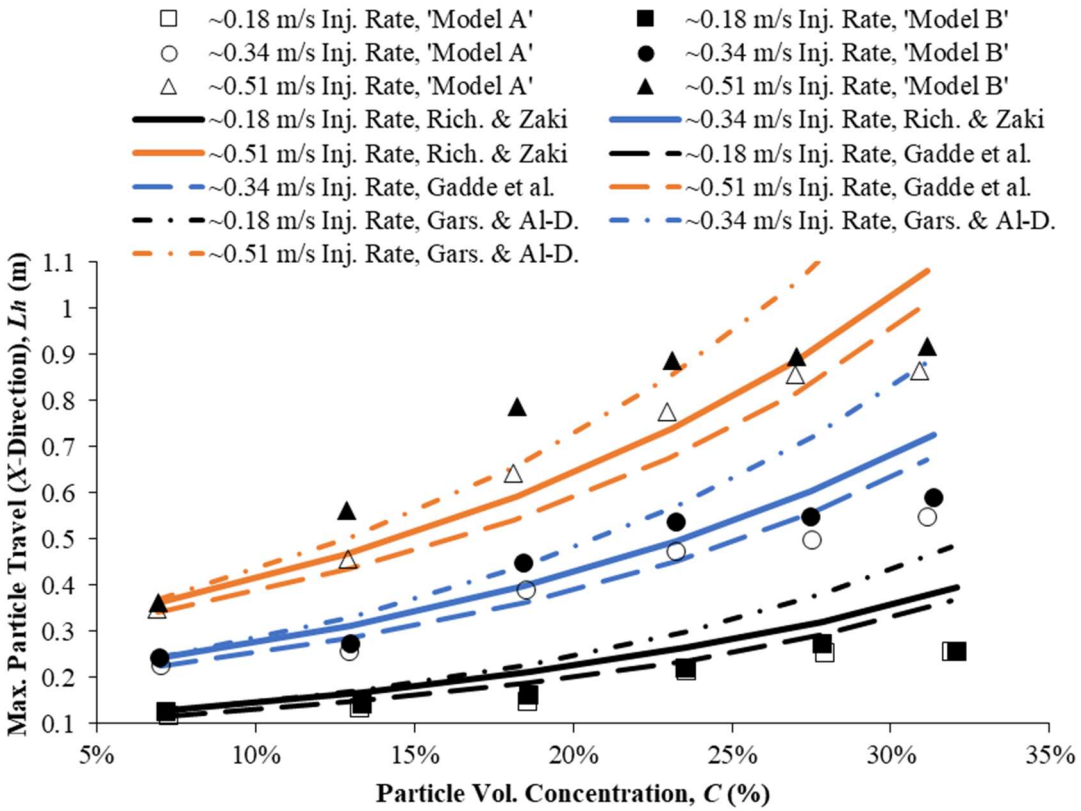

Figure 5.17: Comparison of maximum particle travel distance for simplified evaluations of particle travel vs. modeled behavior in flow.

To consider only the fluid's contribution to conveyance, evaluation the fluid phase's unit flux (i.e., the superficial flow) is shown in Figure 5.18. This is equivalent to flow through the domain section once particles have settled, and only particle free fluid is left in flow. A clear trend of the fluid flux decrease can be seen as initial particle concentration increases.

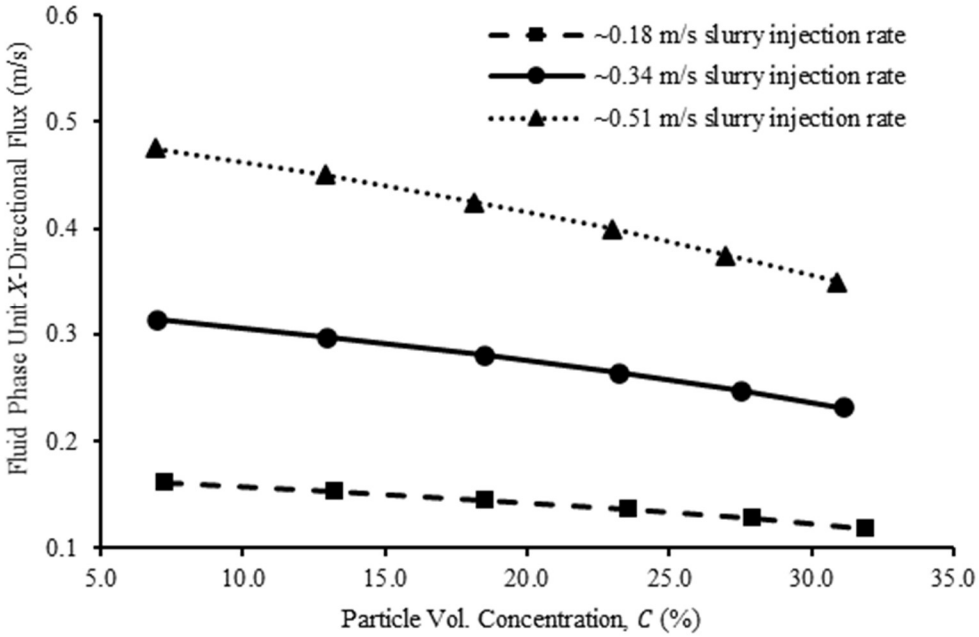

Figure 5.18: Fluid phase unit X – directional flux for each non-neutrally buoyant particle simulations, "Model A" coupling.

This trend of decreasing fluid contribution to particle conveyance is further emphasized by comparing the mean fluid velocity with presence of particles (i.e., interstitial fluid velocity) in two cases of similar injection rate cases with different injection concentrations. Figure 5.19 shows mean fluid X – directional velocity for injection concentration cases of 23.0 % and 27.0 % at an injection rate of ~ 0.51 m/s. Both cases had similar maximum particle travel distances of approximately 0.86 m. Mean X – directional drag for the particles in conveyance in both cases are of O (10^{-8} N). That can be contrasted with the drag that is incurred by a static particle in a 0.5 m/s flow, ~3 x 10^{-5} N, approximately 1000 times larger in magnitude. Particles predominately experience negligible X – directional drag in flow and therefore are traveling at roughly the X - velocity of the fluid. As can be seen in Figure 5.19, more rapid decline occurs in the 27.0 % initial concentration case's fluid velocity as particles settle out from the flow. Lower final value of fluid X - velocity is also seen for the 27.0 % initial concentration case as compared to the 23.0 % injection concentration case. Therefore, to spite similar occurrence of 2-D curtain clusters, particles are conveying slower down the domain in the higher concentration case.

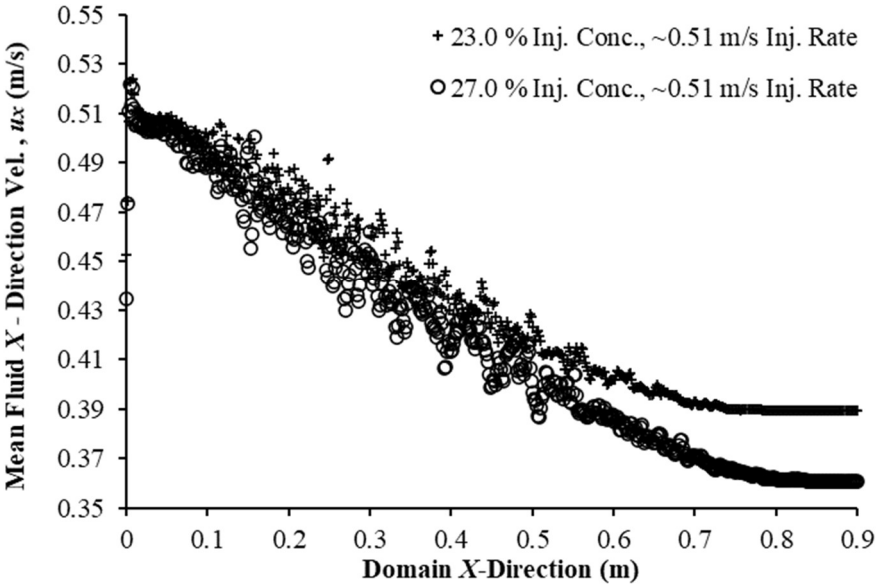

Figure 5.19: Fluid X – direction velocity along flow domain in direction of flow, for injection concentration cases of 23.0 % and 27.0 % at injection rate of ~0.51 m/s, "Model A" coupling.

Evaluation of flowing slurry particle suspension further reveals complex, non-linear behavior. Figure 5.20 shows the average particle count remaining in suspension along the domain length for each set of simulations performed with non-neutrally buoyant particles. CFD-DEM simulation results are referenced against the simplified evaluation (see subsection 2.2.1) with Richardson and Zaki [28] based hindered settling velocity (Eq. 2.1) and assumption of homogeneous composition with constant rate of particle deposition. Lowest concentration injections (i.e., ~ 7 % particle volume injections) follow a relatively linear deposition behavior as they travel down fracture, like the simplified slurry transport assumption. However, higher concentrations take on a more curved, half-parabola shape for particle deposition as slurry travels in flow, with greater rate of particle deposition near the inlet. The obtained deposition behaviors can be fit to a second degree polymetric function of the following form:

$$Particle\ Count = \mathrm{A}x^2 + \mathrm{B}x + \mathrm{C} \tag{5.5}$$

Where A and B are varying values of the polynomial's coefficients and C is the starting particle count at the inlet. Polynomial coefficient values and coefficient of determination values, fitted by least squares method, are summarized in Table 5.4.

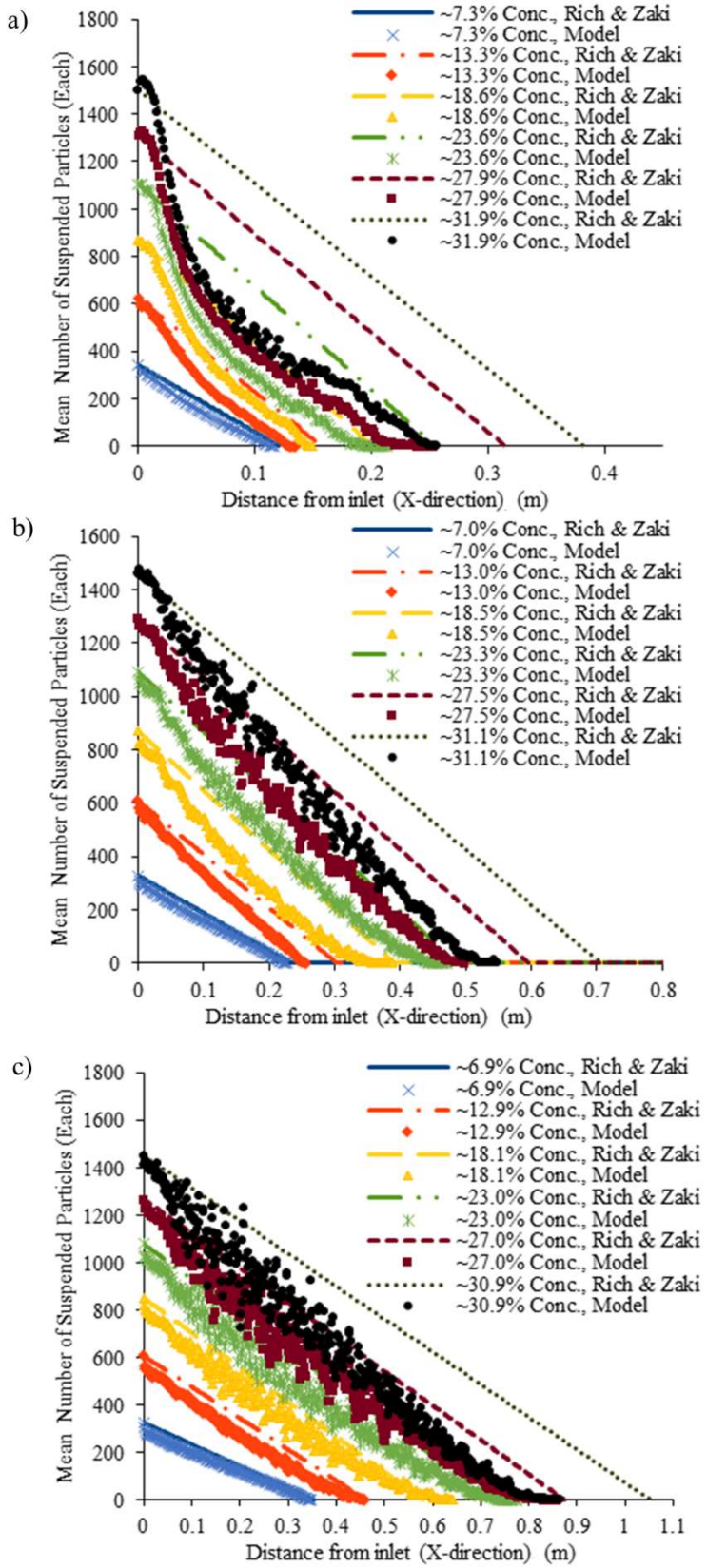

Figure 5.20: Particle suspension behaviors for a) ~0.18 m/s, b) ~0.34 m/s, and c) ~0.51 m/s injection rates, Richardson and Zaki [28] hindered settling based evaluation and modeled results, "Model A" coupling.

Table 5.4: Settling slurries' deposit behavior fitted curve coefficients and respective coefficients of determination values ("Model A" coupling).

Non-neutrally Buoyant Simulation Fitted Polynomial Coefficient Values					
Injected Particle Vol. Concentration (%)	Inlet Injection Rate (m/s)	A	B	C	R^2 value
7.27	0.17	6128.95	-3505.64	341	0.996
13.27	0.18	10153.01	-5918.46	623	0.987
18.57	0.18	15586.68	-7973.07	871	0.979
23.58	0.18	23011.77	-10039.42	1107	0.981
27.92	0.18	21819.21	-10653.30	1310	0.970
31.91	0.17	25192.58	-11885.11	1498	0.946
7.02	0.34	1648.71	-1757.83	329	0.996
12.97	0.34	1270.86	-2633.88	609	0.999
18.54	0.34	3340.21	-3600.48	870	0.996
23.25	0.34	2474.06	-3507.13	1091	0.995
27.52	0.34	1782.10	-3491.23	1292	0.994
31.13	0.34	1175.76	-3365.43	1461	0.991
6.91	0.51	932.25	-1216.08	325	0.988
12.94	0.52	1314.94	-1912.20	607	0.995
18.13	0.52	1146.66	-2062.52	851	0.989
22.96	0.52	966.83	-2151.71	1078	0.983
27.00	0.51	821.21	-2220.04	1267	0.985
30.90	0.51	717.23	-2341.41	1450	0.981

The polynomial's coefficient values are plotted to another contour plot for comparison to the Durand-Froude number and concentration in Figure 5.21. *A* coefficients show a rapid increase in positive value till between approximately 15 - 20 % concentrations, followed by a less rapid decline after. *B* coefficients have rapid increase in negative value to a similar turning point near 15 – 20 % concentration, after which decline in negative value also occurs. This turning point in values again appears to correspond to the point of plateauing nearest neighbor values and the slight 'bump' in maximum particle travel, at the onset of 2-D curtain cluster formation at approximately 20 % concentration discussed in earlier sections. Once again, notable behavior change occurs at the threshold concentration where 2-D curtain clustering develops, showing the significance of cluster shapes' influence on particle flow and transport behavior.

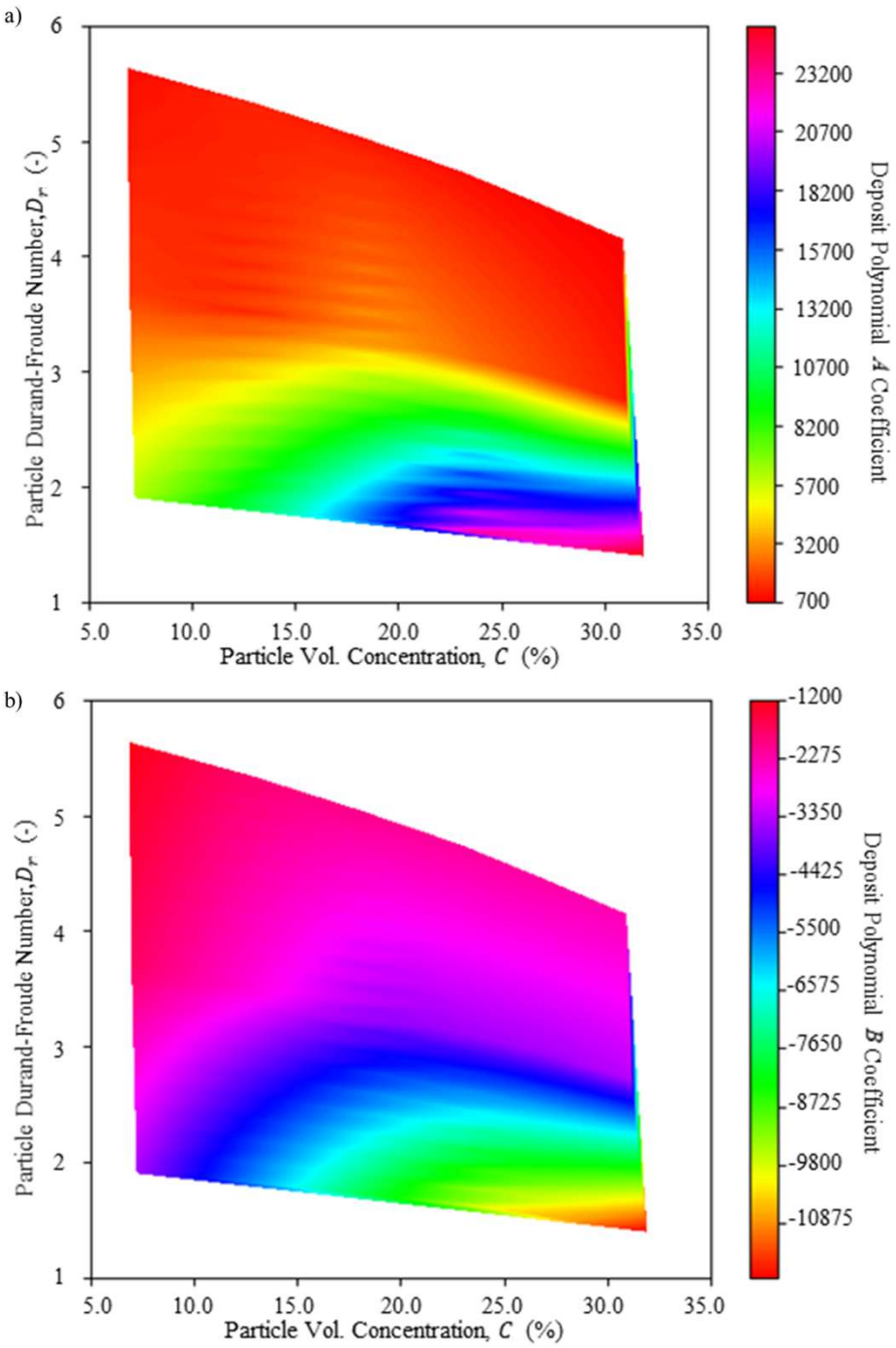

Figure 5.21: Contour plot of *A* and *B* coefficients for fitted polynomial shape of deposit behavior, "Model A" coupling.

5.4 Concluding Remarks

The presented study contributes to the understanding of the clustering mechanics, composition and conveyance behaviors of injected, concentrated particle slurries through quantitative and qualitative analysis using the unresolved CFD-DEM method. Additionally, since this work was done in the context of slickwater proppant injections

in georeservoirs, new findings compared to a simplified slurry flow evaluation, as utilized in hydraulic fracture software, were presented. Overall, this work has demonstrated that clustering does occur for certain injection conditions and has a significant and non-simplistic impact on particle settling and conveyance. Particle clustering shape and spatial distribution is found to be greatly affected by injection rate, concentration, and presence of settling. Specific findings and contributions include:

1. Particle injections transition from negligible clustering at lowest tested concentrations, to 1-D chain-like clustering, and eventual 2-D vertical curtain-like clustering as concentration increases. Neutrally buoyant particles are further noted to develop into 3-D clustered structures at the highest implemented injection concentrations and lowest to mid evaluated flow rates.
2. Clustering prevalence in non-neutrally buoyant particle slurries increases with increased injection concentration and decreases with increased Durand-Froude number values (as seen for higher flow rate cases). Settling due to density differences appears to influential in variances to qualitative and quantitative clustering behavior at different flow rates.
3. Neutrally buoyant proppant injections appear to only demonstrate quantitative increase in clustering with increased particle injection concentration. Flow rate had virtually no influence on quantitative clustering for conditions studied in this work. Further, Stokes number was found to have less influence relating to clustering for the conditions considered in this work based on examined exemplar neutrally buoyant cases. Qualitative clustering appearance (shapes and sizes) is also seen to slightly vary with flow rate and more distinctly vary with concentration for neutrally buoyant conditions
4. Evaluation with “Model B” CFD-DEM coupling formulation is seen to produce acceptable representation of behavior, to spite its simplifications, at low flow rates and some mid to low concentration conditions. The representation however deviates when high concentrations and higher flow rates are considered. It is therefore inappropriate to use this coupling in those conditions and “Model A” coupling should be utilized
5. Clustering affects overall slurry flow and transport in non-neutrally buoyant slurries where 2-D curtain clusters develop and become deformed, incurring an increased upward drag in some cases.
6. Slurry maximum travel capacity, for most concentrations studied, can be represented by simplified transport formulations. Behavior though greatly deviates in several high concentration cases at mid to high tested flow rates due to reduced fluid energy contribution to particle conveyance. Additionally, in intermediate

concentrations for the mid and high range injection rates tested, slight increases in relative maximum travel behavior occurs compared to simple evaluations. This points to an intermediate behavior not captured by simple power-law and polynomial based hindered settling relationships found in the literature when compared with these findings in this work.

7. Suspension/deposition behavior of particles acts in a nearly linear fashion, like simplified evaluations, for small concentrations. As concentration increase, this behavior becomes non-linear, but can be very closely described by a second-degree polynomial in which the coefficients are varied for each case.
8. Plateauing nearest neighbor values, slight relative increase in maximum particle travel, and peak coefficient values for polynomial fitted suspension behavior all correspond to a common approximate point corresponding to the onset of 2-D curtain cluster structures in non-neutrally buoyant particle cases (i.e., at approximately 20% concentration injection).

ACKNOWLEDGEMENTS

Chapter 5 of this dissertation is based on materials accepted by the journal Computers and Geotechnics and titled “Particle clustering dynamics in dense-phase particle-fluid slurries”. Authors are Brian D. Yamashiro and Ingrid Tomac (2021). This dissertation’s author is the first author of this paper.

6 FLOW AND TRANSPORT OF PROPPANTS IN ROUGH FRACTURES

6.1 Introduction

Successful design of proppant enhancement projects requires a clear understanding of the slurry's dynamics and interactions within a rock fracture setting. As discussed in Chapter 2, past studies and in use practices rely on governing laws for proppant flow and transport derived from simplified, smooth surfaced fractures [9–12]. This smooth wall assumption however raises questions about behavioral fidelity to true rock surfaces, which contain surface asperities and produce tortuous flow pathways through the fracture openings [50]. Therefore, impact from rough fracture surfaces on proppant flow and transport is evaluated in this chapter.

Utilization of neutrally buoyant particles is focused on in this evaluation as it allows for isolating flow and transport behavior without further possible influences caused by particle settling. Neutrally buoyant proppants also have an increasing importance in proppant slurry injection operations. Use of nearly neutrally buoyant particles in slickwater proppant slurries has been shown to provide greater fracture enhancement beyond standard, dense particle only proppant slurries [127]. Limited deposition of neutrally buoyant particles during conveyance allows proppant to travel to further fracture extremities, resulting improved propping capability. Further, past studies modeling additional use of neutrally buoyant particles have shown potential four times greater propped fracture area compared to treatments using dense sand particles alone [127].

Objective of this chapter is to quantify effects of fractal dimension and *RMS* asperity height fracture parameters on in-fracture slurry flow behavior. Specific objectives include investigation of the extent fractal dimension and/or *RMS* asperity heights values impact overall flow and transport behavior of neutrally buoyant proppants as well as investigation into impacts on hydraulic aperture caused by two-phase, particle-fluid slurry flowing in rough fractures. To evaluate these impacts, numerical analysis of flowing, neutrally buoyant particles between synthetically generated, rough rock surfaces is performed. Specifically, single and multiparticle proppant conveyance simulations are conducted through fractures with different fractal dimension and *RMS* asperity height values, at differing apertures. As discussed in Chapter 3 (section 3.1.4), to capture flow behavior at rough surfaces containing detailed roughness features, resolved CFD-DEM is used in this study. This method allows for better fluid mesh adherence to surface features smaller than particle size, providing resulting influence from these features. Fluid interaction with particles is also better represented in the resolved method compared to the unresolved method [17].

Unique opportunity to evaluate not just macro impacts to proppant flow and transport, but also micro-scale physical influences about particles and rough surfaces is available with resolved CFD-DEM.

6.2 Methods

6.2.1 Synthetic Rock Fracture Domain

This study specifically evaluates effects of fracture topology at sizes below that of the proppant particle diameter size. The reason for this is rock grain sizes, and therefore fracture surface features, can be of size smaller than typical proppant particle dimension. For example, sandstone can have predominated particle sizes ranging from 0.06 to 2 mm. Shales have typical maximum particle size less than ~0.05 mm. Asperity features for the generated synthetic surfaces are described at a 0.1 mm resolution along the surfaces. The surface features are generated as square-shaped elements to allow for hexagonal shaped CFD cells. This provides smaller features relative to proppant particle size while allowing for a reasonably tractable CFD simulation mesh that conforms to the surface. Fracture domain length is selected to be approximately an order of magnitude larger in size than the particle to capture behavior of proppant in rough fractures over a reasonably larger domain length. Specifically, a 10 mm fracture length is used. Three different fractal dimensions, 2.1, 2.25, and 2.5 are considered for the synthetic rock surfaces.

In order to evaluate appropriate asperity height *RMS* for surfaces of size equal to 10 mm, amplitude parameter and fractal dimension values, A and D, provided in the literature [51,53,57,130,131] are evaluated with Eq. 3. Direct asperity height *RMS* values for 13 mm samples presented by Brown [50] are also considered. Eliminating one extreme value reported in one of the referenced sources (i.e. Odling [130]; $A = 0.001, D = 1.5$), *RMS* asperity height magnitudes fall between values ~0.018 mm and ~0.54 mm. *RMS* value of ~0.018 mm results in comparatively flat surfaces in contrast to the particle diameter size of 0.5 mm, so this *RMS* value is not explored. Early evaluations with *RMS* value of 0.1 mm also resulted in relatively small behavioral variance from smooth walled configurations, so it was also not further explored. Therefore, asperity height *RMS* values of 0.25 mm and 0.5 mm are considered in this work. Images of the generated rough fracture surfaces is shown in Figure. 6.1.

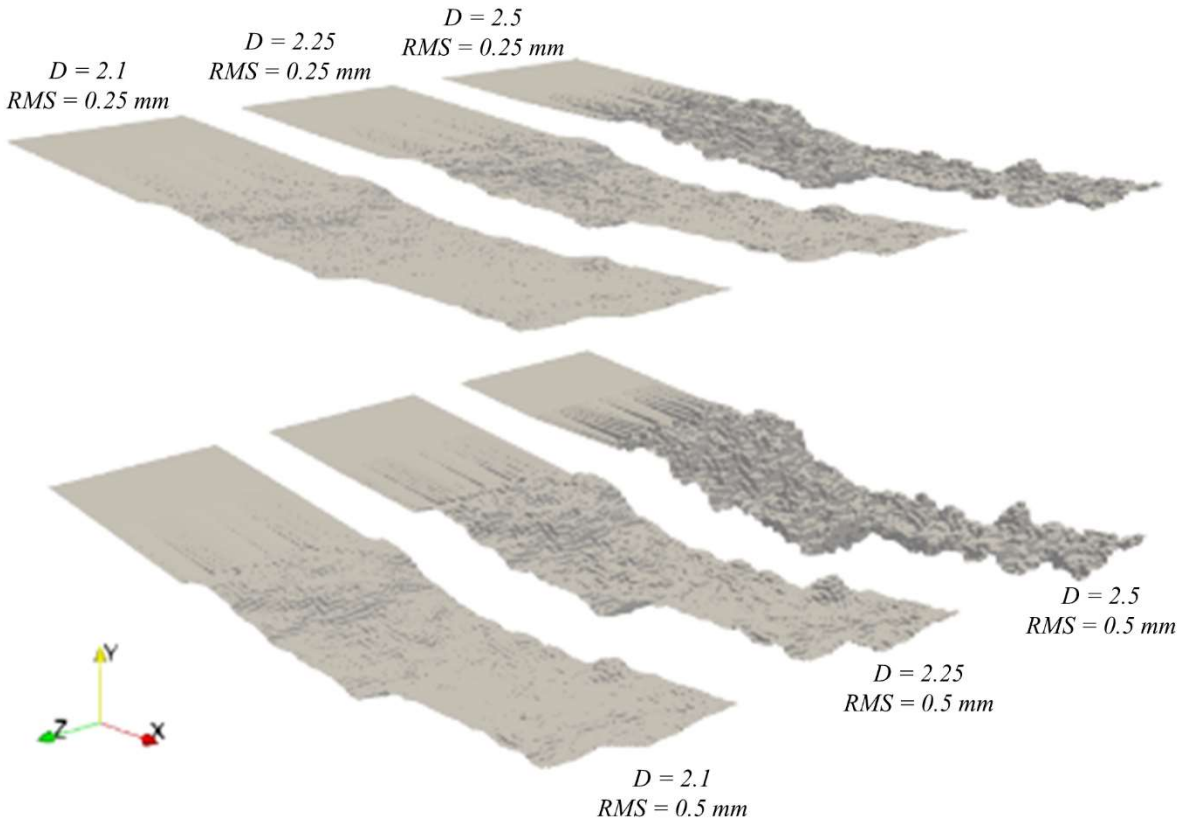

Figure 6.1: Generated rough surfaces with corresponding fractal dimension (*D*) and *RMS* asperity height parameters.

6.2.2 Material Properties and Domain Settings

Complete material properties for this work are summarized in Table 6.1.

Table 6.1:Model material properties for neutrally buoyant slurry flow simulations

Proppant/Wall Parameters:		Units	Fluid Parameters:		Units
Particle Diameter	500	μm	Dynamic Viscosity	0.003	Pa.s
Particle Density	1000	kg/m^3	Density	1000	kg/m^3
Particle/Wall Contact Friction Value	0.6	-			
Particle/Wall Young's Modulus	$5x10^6$	N/m^2			
Particle/Wall Poisson Ratio	0.3	-			
Particle/Wall Coefficient of Restitution	0.95	-			

Table 6.2 summarizes the model boundary conditions. For the simulation domains, gravity is active in the -Z direction for simulations, though this provides no real impact as the particles are neutrally buoyant. CFD cells are

resolved to 50 μm. For the particle size considered in this work, this resolution exceeds the minimum requirement specified Hager [22] and Hager et al. [97] to provide accurate behavioral representation with the resolved CFD-DEM method.

To prescribe provide a developed inlet velocity conditions at the -*X* face, a fluid only simulation is initially completed with a small and uniform velocity prescribed at the +*X* face, flowing in the -*X* direction. These simulations are run till *X*-directional velocity residual is of *O* (10-4) or lower. Values are then extracted from the -*X* face, redirected to the +*X* direction, and rescaled based on the desired mean velocity value.

Table 6.2: Model boundary conditions for neutrally buoyant slurry flow simulations

CFD Boundary Conditions:		DEM Boundary Conditions:	
+/- *Y* faces	No-Slip velocity + zero-gradient pressure	+/- *Y* faces	Wall contact
+/- *Z* faces	Slip velocity + zero-gradient pressure, or Symmetric*	+/- Z face, - *X* face	Reflect
+ *X* faces	Prescribed non-uniform velocity + zero-gradient pressure	+ *X* face	Destroy
- X faces	Zero-gradient velocity, prescribed uniform pressure		

* Slip velocity setting for single particle cases, symmetric for multiparticle cases

For this work, flow Reynolds number value of 2000 is considered in baseline cases. As discussed in Chapter 5, this value is below the threshold for turbulent flow behavior and therefore flow is modeled as laminar. Values of $Re_{||}$= 1000 and 100 are also evaluated for various mechanical aperture, single particle cases in a rough and smooth walled domains to assess sensitivity to Reynolds number value in rough fractures.

Example simulation domain geometry is shown in Figure 6.2. To allow for particles to reach a sustained conveyance velocity, they are initially generated in a 'factory' section near the inlet and allowed to travel through a 'transition' before entering the actual evaluated fracture section. For single particle cases, particles are generated one particle diameter from the -*X* boundary and centered about the *Z* and *Y* directions. For multiparticle simulations, particles are continuously and randomly generated within the 'factory' section at a fixed volumetric concentration. Target particle volumetric concentrations of 5 %, 10 % and 20 % are considered in this study. The actual particle volumetric concentration is measured post-simulation by evaluating averaged particle volume concentration within the domain's 'factory' and 'transition' sections. Flow rate of multiparticle simulations is based on the interstitial fluid velocity and fluid's material properties, so it is equal for like $Re_{||}$and aperture conditions, regardless of particle

volumetric concentration. The CFD domain is 1 mm longer in the $+X$ direction than the DEM domain to eliminate boundary influence at the outlet.

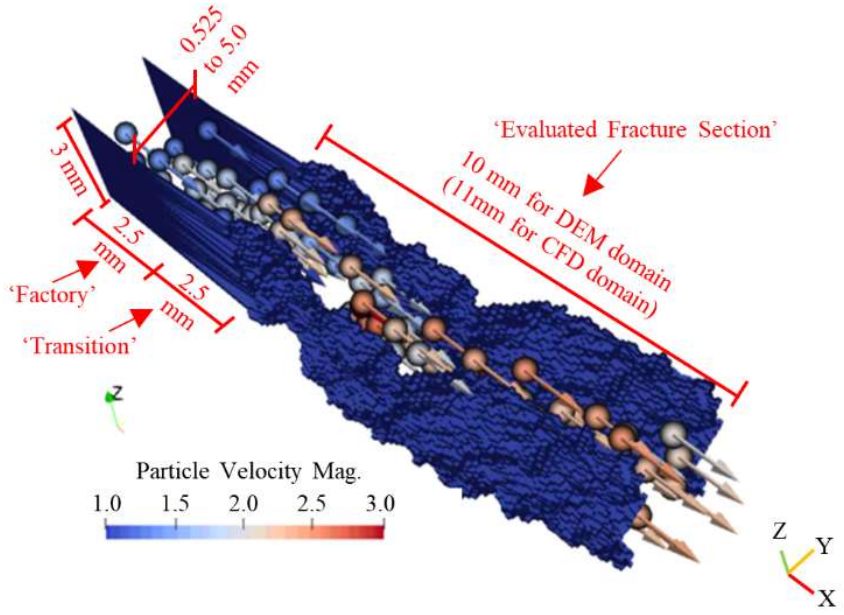

Figure 6.2: Example simulation domain geometry with particles.

For single particle cases, fluid only simulation is first run till residual values stabilize before generating the particle within the domain. This initial fluid only simulation allows for particles to generate and travel in a fully developed flow environment. To capture fully developed flow conditions in multiparticle simulations, slurry injection is simulated for twice the duration of a single particle's travel time within the same fracture and only the last 25 % of the simulation data is then used in evaluations. CFD timestep size varied based on the various simulation conditions to achieve values below a CFL number value less one. DEM simulations in domains containing sharply convex surfaces can suffer from instabilities during simulation. To avoid this instability, typical time step for simulations is determined by progressively decreasing time step values for a trial simulation within several rough fracture apertures (RMS = 0.5 mm) at narrow widths where particle jamming does not occur. Time step is reduced until instability and unphysical rebound (rebound velocity values higher than incoming velocity values) are not observed. Typical determined DEM time steps of 5 x 10^{-10} s are then implemented for all rough fracture cases for precaution. Two cases required further DEM time step reduction (specifically as observed for the D = 2.25, RMS = 0.5 mm, a = 0.7 mm and

D = 2.5, *RMS* = 0.5 mm, a = 0.9 mm cases at $Re_{||}$= 2000) due to higher fluid/particle velocities and were reduced to 1 x 10^{-10} second where unphysical rebound subsided.

6.3 Findings and Results

6.3.1 Influence of Fractal Dimension and *RMS* Asperity Heigh on Single Particle Behavior in Rough Fractures

Single particle flow and transport is simulated in rough fractures of varying mechanical aperture with *RMS* asperity height values of 0.25 mm and 0.5 mm and fractal dimensions of 2.1, 2.25, and 2.5. Gradual narrowing of tested mechanical apertures is performed until particle arrest occurs. Figure 6.3 shows the results for the average particle velocity of a single particle transporting within the simulated rough fracture sections. Simulations of single particle average velocity between smooth walls, from Blyton [41] for $Re_{||}$= 2000, are also shown for comparison.

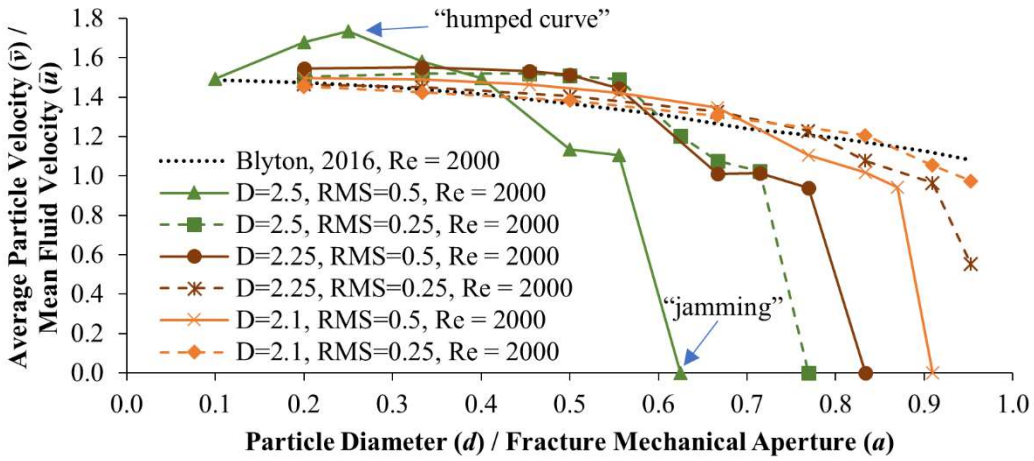

Figure 6.3: Comparison of single particle $\bar{v}/\bar{u}$ for varying d/a ratios in rough fractures. Asperity height values of *RMS* =0.25 mm and *RMS* = 0.5 mm for $Re_{||}$= 2000 with D = 2.5, D = 2.25, and D = 2.1 considered. Connecting lines between data points included for clarity of identifying like simulation condition sets.

Three main behavioral variances compared to flow and transport between a smooth wall model are observed in Figure 6.3. First, at small particle diameter to mechanical aperture (i.e., wide fracture widths) effects from roughness features are negligible. This can be seen for all results as relative particle diameter to fracture mechanical aperture (i.e., d/a) ratio values approach zero. Second, and the most unique observation, is that greater relative particle velocity is observed at various small to moderate d/a ratio values in rough fractures. Example of this can be seen in the 'humped' curve shape occurring around d/a ratio of 0.25 for the D = 2.5 with asperity height *RMS* = 0.5 mm cases

in Figure 6.3. Lastly, it is observed that attenuation and jamming occur at wider mechanical aperture widths for particles in rough fractures.

The first observation, that roughness is uninfluential at wide apertures is intuitive. Fluid flow field becomes wide enough where boundary influences become negligible. To explain the second observation of greater (i.e., accentuated) particle velocity behavior, Figure 6.4 shows a comparison of streamlines and fluid velocity profiles for the D = 2.5, asperity height RMS = 0.5 mm rough and smooth wall simulation cases at d/a ratio of ~0.33. Particle velocity accentuation is attributable to eddy formations at rough fracture surface features leading to a narrowed effective, hydraulic aperture. The recirculating eddy regions, that do not contribute to through fracture flow, lead to a narrowed velocity profile with higher peak velocity. The particle is conveyed generally along centerline of flow, benefiting from the sharpened velocity profile distributed about the particle's body, as shown in Figure 6.4b. The eddies are of greater size for surfaces with larger asperity heights, causing greater accentuation. Further, as fractal dimension increases, and the surface becomes more texturally rough, greater prevalence of eddies occurs, leading to greater accentuation.

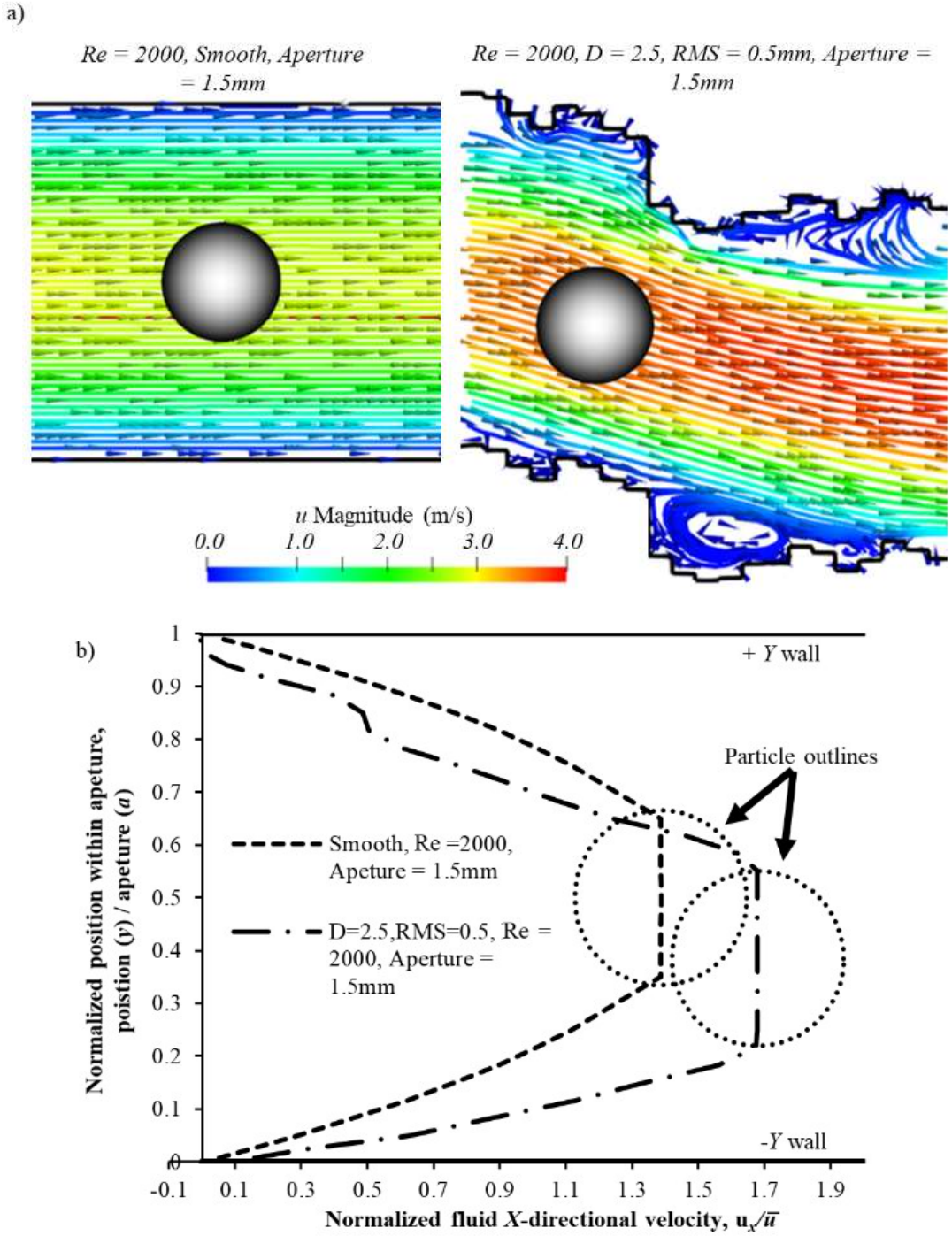

Figure 6.4: Example in fracture flow a) streamlines and b) velocity profiles at particle locations for smooth and rough (D = 2.5, asperity height RMS = 0.5 mm) fracture wall cases. Velocity vector arrows imposed atop streamlines for clarity flow direction in (a). Slightly negative fluid velocity for rough fracture example occurs at upper wall side of profile due to eddy formation in (b).

As the particle tends to travel about the centerline of the flow, one might assume the enhanced conveyance behavior would continue to occur when the fracture mechanical aperture remains moderately larger than the particle diameter. As seen in Figure 6.3 however, this clearly is not the case. Figure 6.5a shows the fluid only velocity profiles in a smooth and rough (i.e., D = 2.5, asperity height RMS = 0.5 mm) fracture, at d/a ratio of 0.5 (i.e., aperture width equal to twice the particle diameter). Peak fluid velocity within the rough fracture is notably higher. A particle's outline is sketched atop both flow profiles to illustrate the larger potential velocity distribution about a particle within the rough fracture's flow. Figure 6.5b however shows actual particle velocity behavior within the two fractures. Particle flow and transport is clearly attenuated within the rough fracture. The cause of this reduced particle velocity is confirmed to be due to the increased occurrence of particle collisions with the fracture walls, as illustrated in Figure 6.5b. As the flow path is tortuous within the rough fracture, particle slip occurs at changes in flow direction, which increases frequency of particle-wall collisions. The severity of attenuation from particle-wall collisions varies depending on the relative orientation of the particle travel path and the fracture wall. Specifically, more direct, head on collisions obviously cause greater attenuation than grazing contacts. Occurrences of more impactful collisions increase in frequency as asperity heights and fractal dimensions increase due to the greater obstacle prevalence (larger size features to collide with) and textural complexity (greater prevalence of features to collide with). Small fluctuations in particle velocity seen in Figure 6.5b can also be attributed to fluid flow directional changes experienced by the particle between these rougher surfaces. Greater particle-wall contacting occurs as mechanical aperture narrows, until a point at which mechanical aperture is so narrow, that particles jam between rough fracture walls. The jamming is attributable to the deformed flow pathway for particles through rough fractures. To spite mechanical aperture being the same width for coupled points between the fracture walls, the random changes in asperity heights cause varied cross-sectional flow pathways for particles making it more difficult for particles pass through. In other words, large changes in height between adjacent asperity points causes a deformed cross-section (compared to a smooth wall opening) where particles can become jammed. As expected, as asperity height RMS value increases, jamming at wider relative mechanical apertures occurs. Fractal dimension also significantly influences jamming behaviors. More texturally complex fractures (i.e., higher fractal dimension value) are seen to result in jamming at wider mechanical apertures than smoother fractures, again due to greater prevalence of rough features in the surfaces.

These results demonstrate that both roughness parameters, fractal dimension and *RMS* asperity height, notably influence both particle flow behavior and jamming conditions. The most notable impacts are seen for largest tested asperity height cases (i.e., *RMS* asperity heights = 0.5 mm).

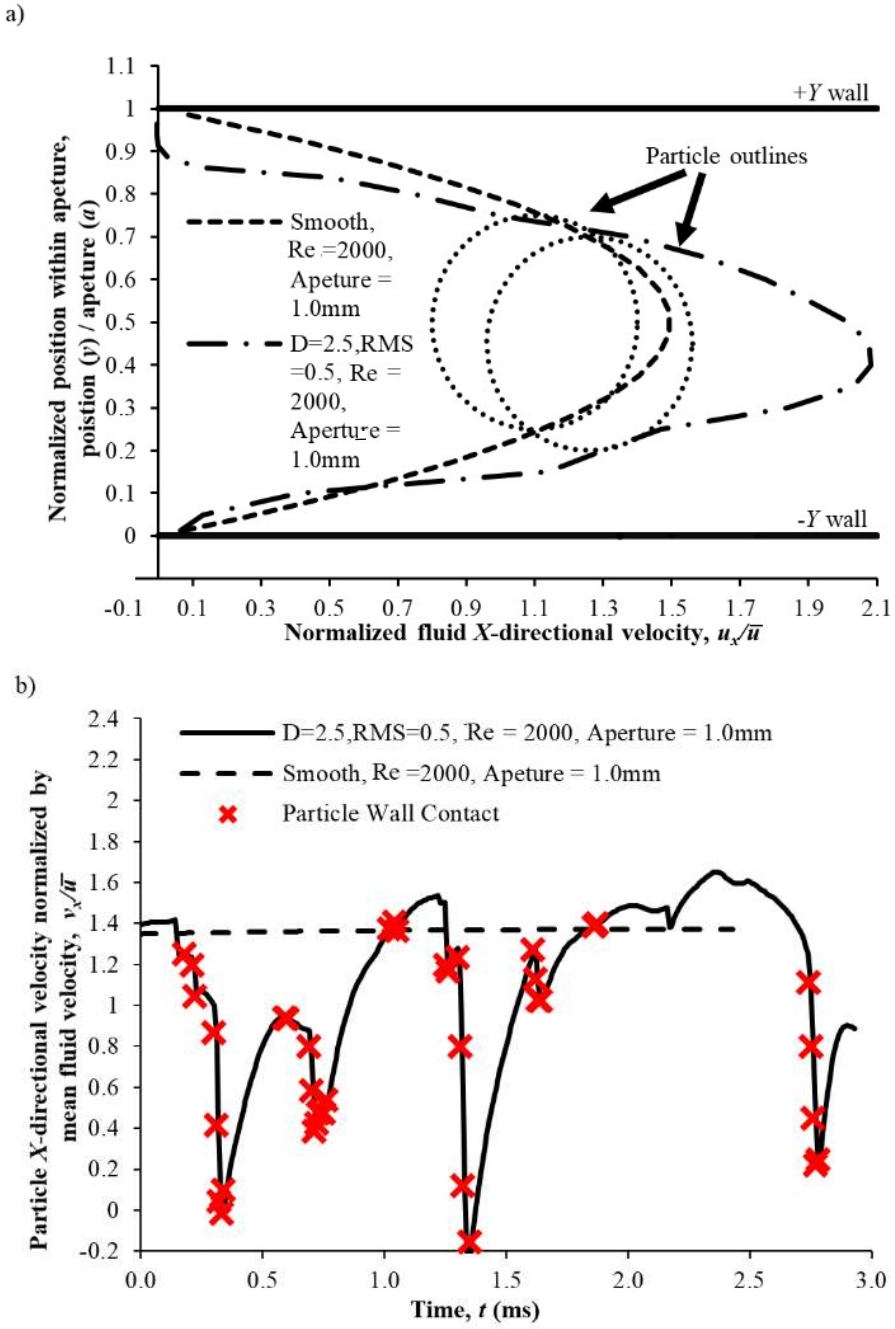

Figure 6.5: a) Fluid only profile for smooth and D = 2.5, *RMS* = 0.5 mm, $Re_{||}$= 2000 at 1 mm mechanical aperture cases. Particle silhouette superimposed to show rough domains' potential fluid velocity distribution about a particle. b) Particle *X*-directional velocity, normalized by mean fluid velocity, for rough fracture and smooth fracture versus time. Particle wall contact instances shown (i.e., red X's) to illustrate collisions' attenuation effects.

6.3.2 Flow Reynolds Number Impact on Single Particle Flow and Transport in Rough Fractures

To evaluate the impact of the Reynolds number on a single particle flow and transport in a rough fracture, simulations with $Re_{||}$= 2000, 1000, and 100 are compared with each other in the most texturally rough, largest *RMS* asperity height fracture, *D* = 2.5, *RMS* = 0.5 mm. The results of the simulations with varying mechanical apertures are presented in Figure 6.6.

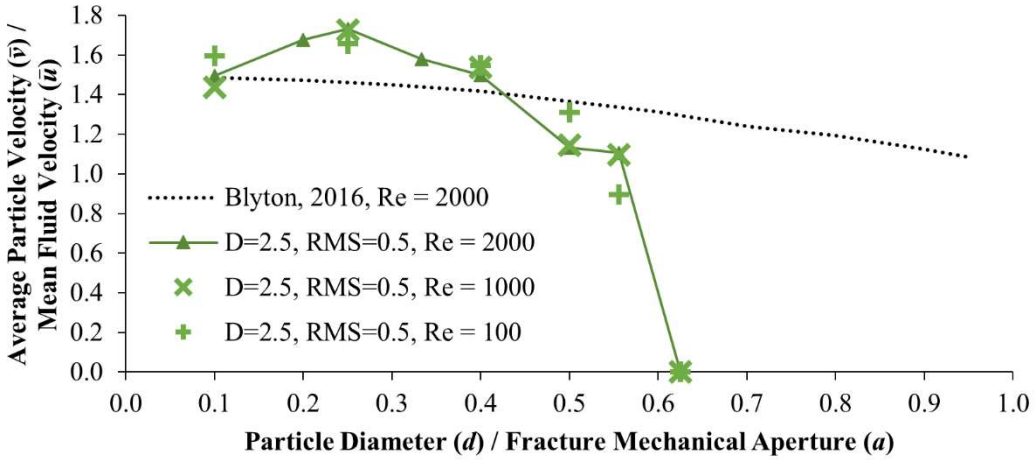

Figure 6.6: Particle conveyance behavior for Reynolds number values of 100, 1000, and 2000 in *D* = 2.5, *RMS* = 0.5 mm fracture geometry results.

Limited variance in the average particle to mean fluid velocity ratios for different $Re_{||}$values is observed in Figure 6.6. The minor variance indicates that for the range of interest for proppant injection work, the Reynolds number has little impact on neutrally buoyant particle flow and transport in rough fractures. The observations presented Chapter 4 (section 4.3.2) further imply that variance in behavior due to the Reynolds number is only significant for very narrow mechanical fracture apertures. However as was shown in Figure 6.3, a very narrow mechanical aperture conditions occur rarely in significantly rough fractures since jamming tends to occur at mechanical apertures appreciably wider than this threshold.

6.3.3 Multiparticle Flow and Transport in Rough Fractures

Multiparticle simulations are performed in fracture geometries with asperity height *RMS* = 0.5 mm at the Reynolds number $Re_{||}$= 2000. The simulation parameter choice is based on the single particle flow and transport

results in rough fractures. The single particle flow and transport at asperity height *RMS* = 0.25 mm varies notably only in the most texturally rough fracture (i.e., *D* = 2.5), and is, for the most part, similar to the smooth wall results for smaller *D* values. Multiparticle simulations therefore focus on the larger asperity height *RMS* with varying fractal dimension to evaluate the particle volumetric concentration effects in rough fractures. Target particle volumetric concentrations of 5, 10, and 20 % are implemented in multiparticle simulations. Measured post simulation injected particle volumetric concentration is found to be ~6.8 % [+/- 1.0/0.9 %], ~12. 7% [+/- 1.0/1.3 %], and 23.1 % [+/- 2.4/1.7 %], respectively, considering all the rough fracture simulations results. Figure 6.7 shows the results from the simulations with varying particle volumetric concentrations, fracture mechanical aperture, and fractal dimension and are compared to the smooth walled simulations.

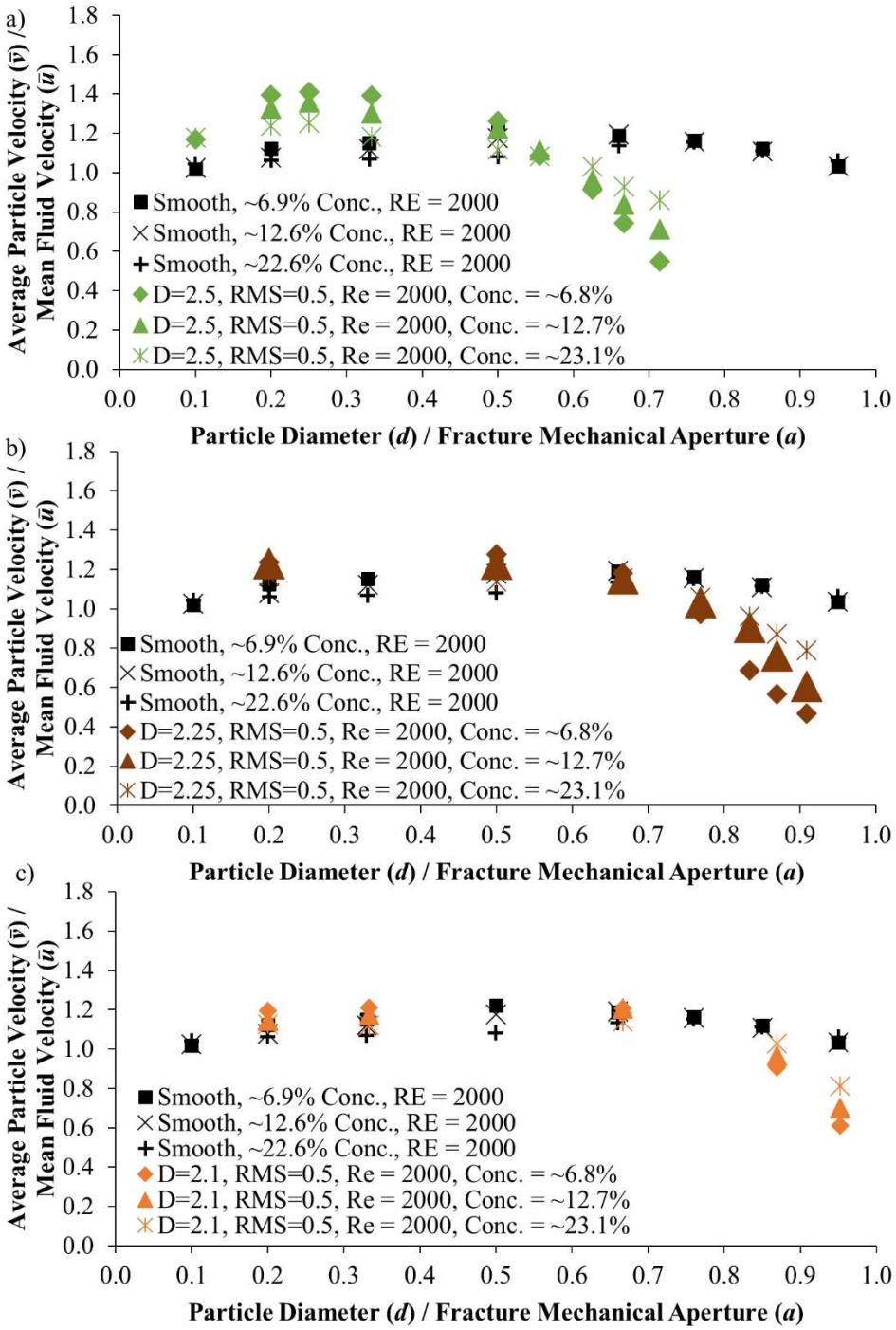

Figure 6.7: Multiparticle behavior for ~6.8, ~12.7, and 23.1 % concentrations fractures with varying mechanical aperture and fractal dimension of a) D = 2.5, b) 2.25, and c) 2.1. Multiparticle, smooth walled simulation results included for comparison.

Like the single particle cases, higher fractal dimensions are seen to lead to greater attenuation at smaller d/a ratio values. Multiparticle simulations also show slight to notable relative velocity accentuation (i.e., "humped"

sections) compared to smooth walled cases at moderate d/a ratio values, i.e., ~0.1 to 0.5. Concentration is seen to cause notable variances in relative velocity behavior for all tested configurations at their "humped" accentuations. Noticeable variance also occurs at their respective narrowest tested mechanical fracture apertures, i.e., higher d/a ratio values. For the "humped" accentuations at moderate d/a ratio values, lower concentrations have greater relative accentuation. At the narrowest tested mechanical apertures, higher concentrations had higher relative values.

To explain these variances, first, contact instances are considered. Figure 6.8 shows average number of particle-wall and particle-particle contacts normalized by average particle count within the fracture. Average particle-wall contact instances are seen to be similar for like rough fractures at identical aperture to spite increased concentration. This points to overall similar probability of particles contacting walls in like rough fractures regardless of volumetric concentration. This can be attributable to the earlier single particle observations where particles tend to travel about the center of the flow and only experience wall contact due to slip between particle and fluid velocity at tortuous flow pathways. Particle volumetric concentration, at least up to the maximum ~20 % tested, is not seen to lead to significant variance in this centered flow transport behavior based on this observation.

Even though average wall contacts are similar, what is clear is that relative frequency of average particle-particle contacting is greater for higher concentration slurries in like fractures (i.e., same roughness and aperture). This is predominantly seen at moderate d/a ratio values. Comparing Figure 6.8's particle-particle contacting there is clear higher average particle-particle contacting that occurs for higher concentration slurries. While particles are contacting walls in similar proportions regardless of concentration, there is a greater amount of interparticle interactions and transport attenuation at higher concentrations because particles are repelled towards the center of flow where they collide with the greater overall amount of flowing particles. This attenuation due to increased particle interactions explains the cause of higher "humped" particle velocity sections at lower particle volumetric concentrations seen in Figure 6.7. Fracture roughness increase additionally promotes average particle-particle contacts (i.e., higher *D* value), as seen in Figure 6.8. It can be concluded that the roughness has a combined effect with concentration to impact particle flow and transport.

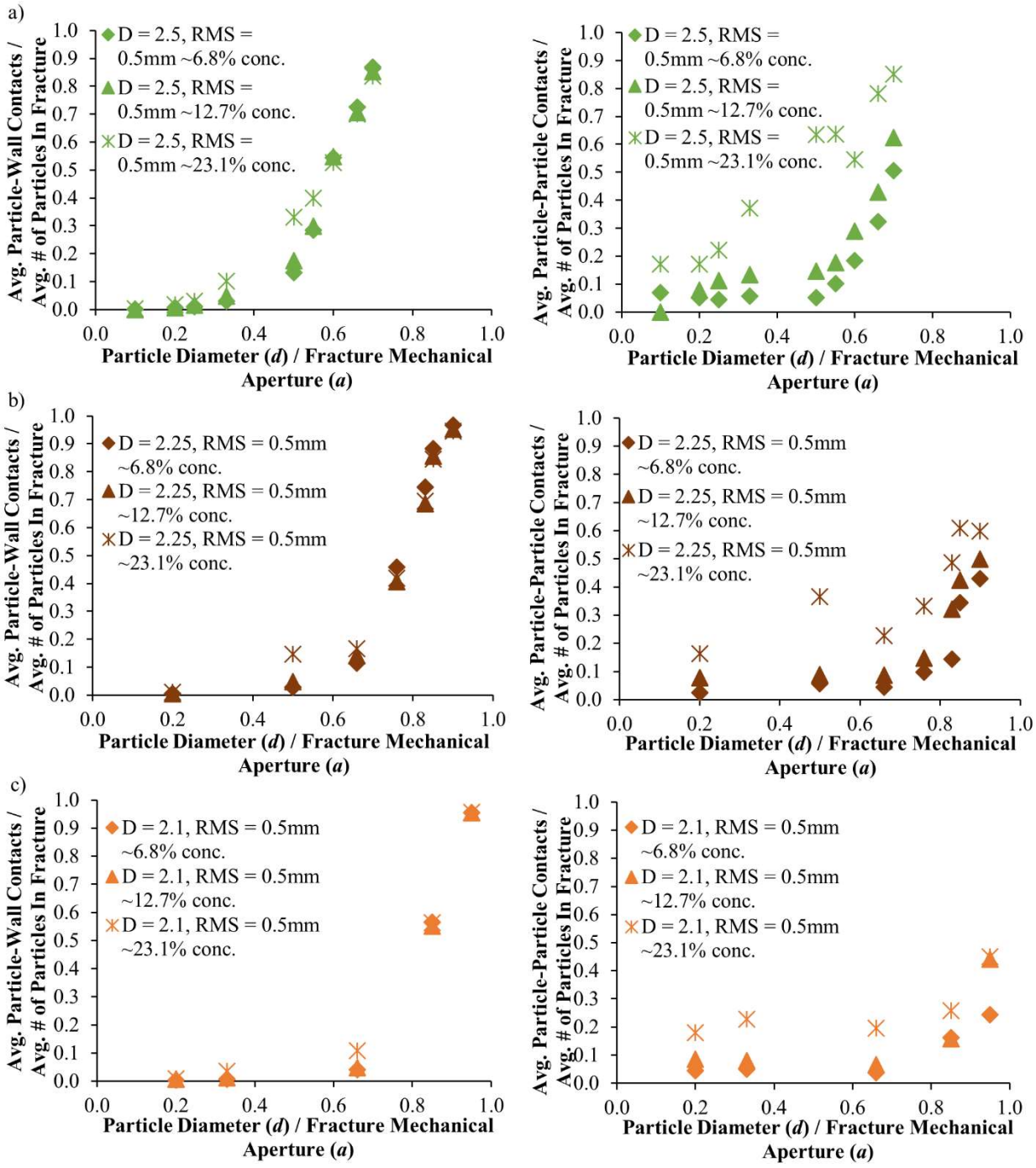

Figure 6.8: d/a ratio versus average particle to particle and particle to wall collisions normalized by in fracture particle count for fractal dimensions equal to a) 2.5, b) 2.25, and c) 2.1.

The cause for higher relative velocities observed for higher concentrations at narrow aperture is next investigated. Particle-wall contact counts are representative of particle collisions with walls at large to moderate apertures, but also can represent particles that become jammed within the fracture, i.e., are in constant contact, when

aperture narrows. Particle-wall contact counts shown in Figure 6.8 progressively increase for each fracture configuration as the fracture mechanical aperture narrows, implying increased particle collision and/or more importantly, greater particle jamming.

To further evaluate degree and impact of particle jamming, Figure 6.9a-c shows measurement of the in-fracture particle volumetric concentration at different d/a ratio values. In-fracture concentration is seen to progressively increase in all cases as the fracture mechanical aperture narrows. This indicates that jamming progressively increases as more particles arrest within the narrowing fractures. The concentration increases also appear to follow very similar trends for each respective rough fracture set of simulations. That is to say, the sets of points for different injection concentrations within the same fractures have nearly identical curvature, just uniformly shifted upwards within the graphs as injection concentration increases. This would mean that similar amounts of particles jamming occurs in the fracture, regardless of injection concentration. Figure 6.9d shows example particle volumetric concentration within the D = 2.5, 0.7 mm aperture fracture over simulation duration for the three injection concentration cases. Particle concentrations remains relatively stable through the time duration for each respective case and there is no appreciable change in the amount of jamming throughout the time slurry is flowing through the fracture. Particles are still able to efficiently convey through rough, narrow apertures regardless of injection concentration.

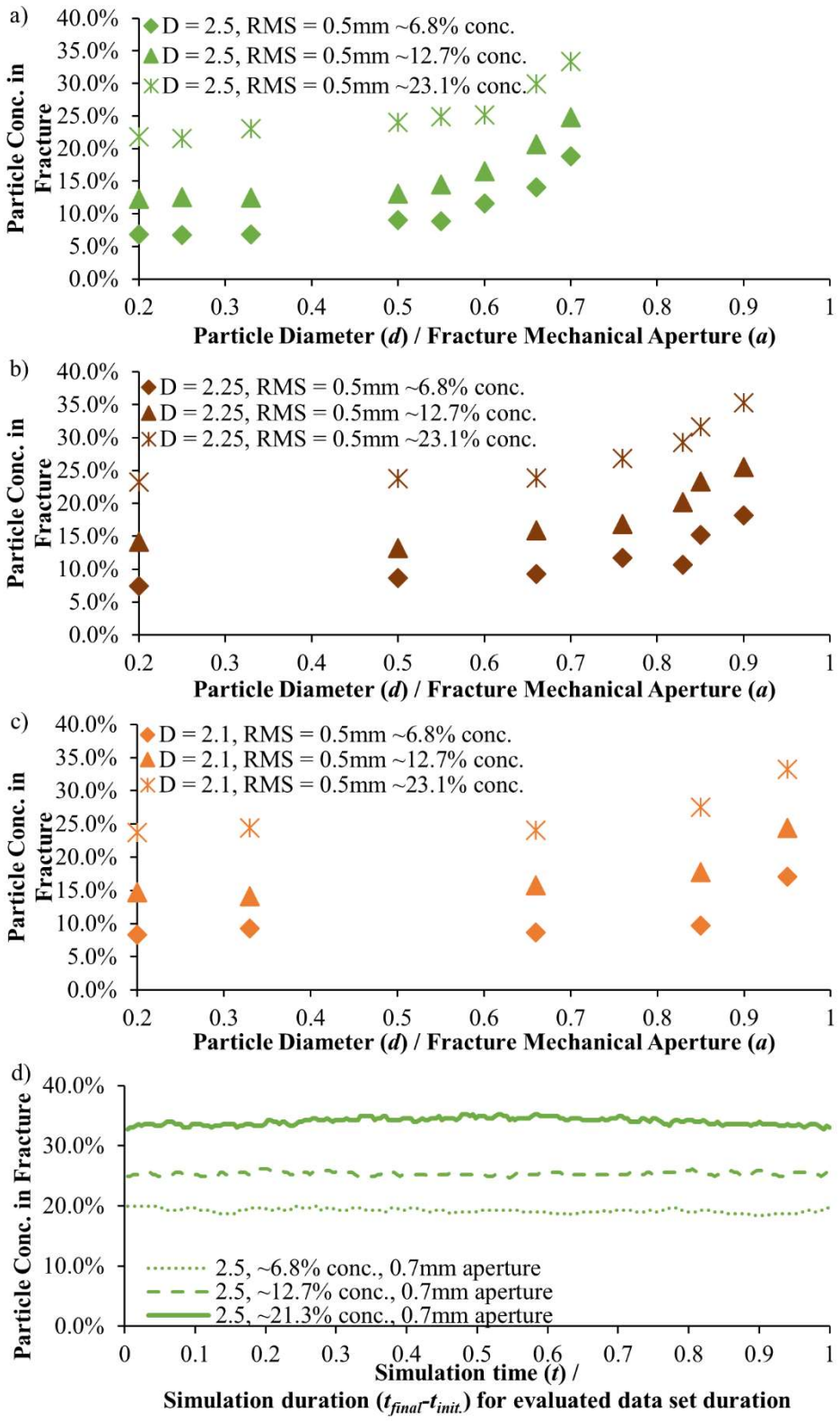

Figure 6.9: a) In fracture varying d/a ratio versus average in fracture concentration for D = a) 2.5, b) 2.25, and c) 2.1. d) Exemplar stable in fracture concentration versus time (normalized by data set time duration) for D = 2.5, a = 0.7 mm fracture simulations at particle volumetric concentrations of ~6.8, 12.7, and 21.3 %.

Figure 6.10 provides further indication of the similar jamming behavior regardless of injection concentration. It also provides explanation for the observed higher average relative velocity for higher concentration injections observed in Figure 6.7 at narrow mechanical apertures. Example views within a fracture for ~23.1 % and ~6.8 % particle volumetric concentration slurries at d/a ratio = 0.7 are shown in Figure 6.10. Very similar locations and degrees of jamming occur for both cases. As similar blockage occurs in each respective case, particles are redirected by the fluid flow to clear pathways through the fracture. In higher concentration injections, more particles travel through the clear pathways within the fracture. The larger relative proportion of particles being redirected through the clear flow pathways, versus jammed in the fracture, results in the higher average particle velocity at higher concentration injections in like narrow mechanical apertures.

The blockage and redirection mechanism indicates, that in spite of the particle jamming, it is still possible for neutrally buoyant particles to be redirected to obstruction free pathways and continue conveyance through a rough fracture. Overall, this indicates that the concentration of injection is less of consequence than the fracture roughness with regards to jamming occurrence and degree.

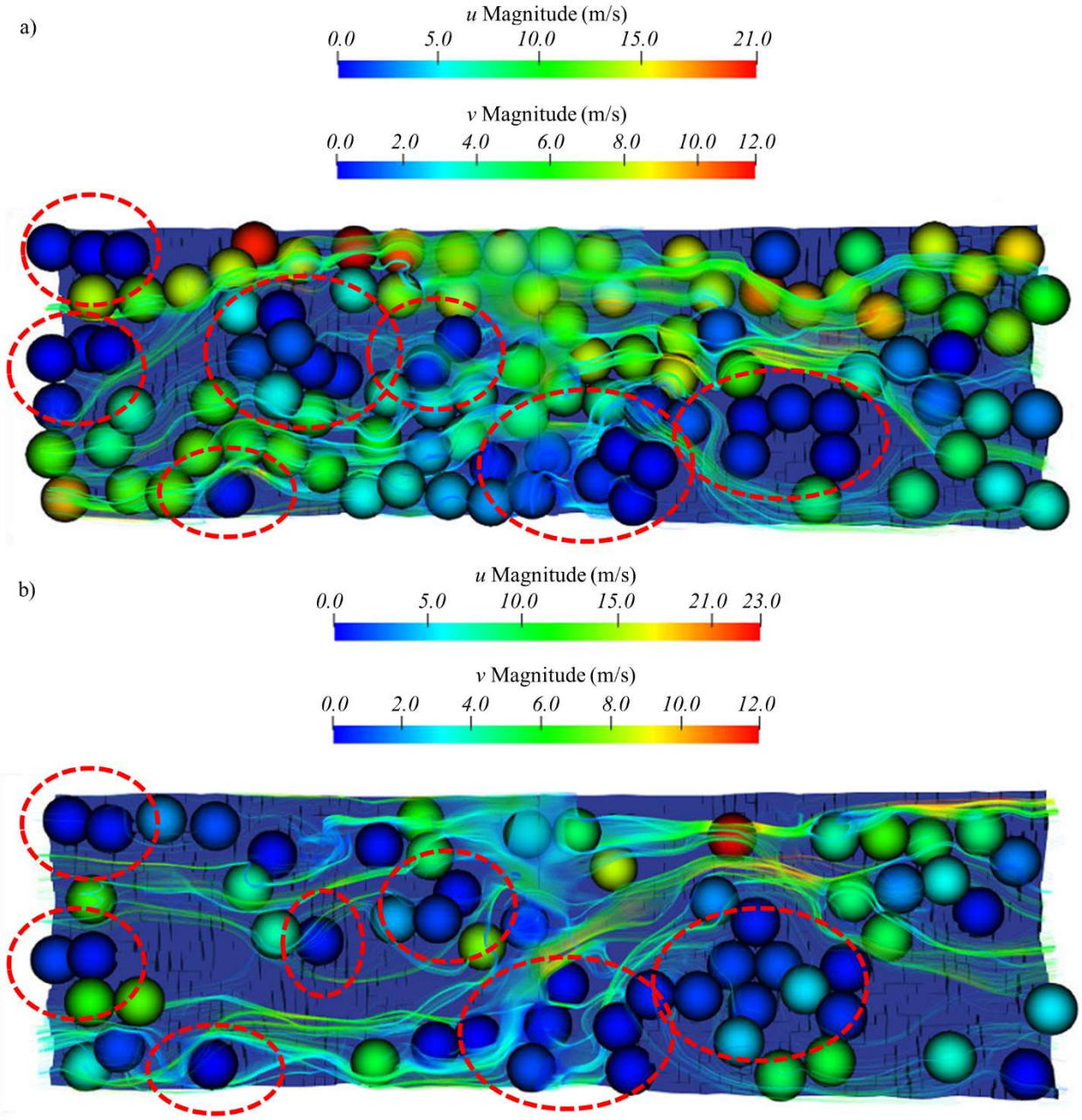

Figure 6.10: Example particle jamming and redirected fluid streamline paths (taken at mid fracture) and particle travel. Flow directed from left to right. View through fracture case D = 2.5, RMS = 0.5 mm, d/a ratio = 0.7, with +Y fracture wall removed for visual clarity. a) ~23.1 % conc. and b) ~6.8 % conc.

6.3.4 Hydraulic Aperture Variances in Multiparticle Flowing Slurries within Rough Fractures

Utilizing Eq. 2.14, the macro pressure gradient is evaluated based on the pressure values at entrance and exit of the fracture sections, Figure 16 shows hydraulic aperture to mechanical aperture ratio (a_{hyd}/a) values for the

various simulation cases with varying roughness and particle volumetric concentration. a_{hyd}/a values for simulations without particles are extracted from the fluid only initial runs.

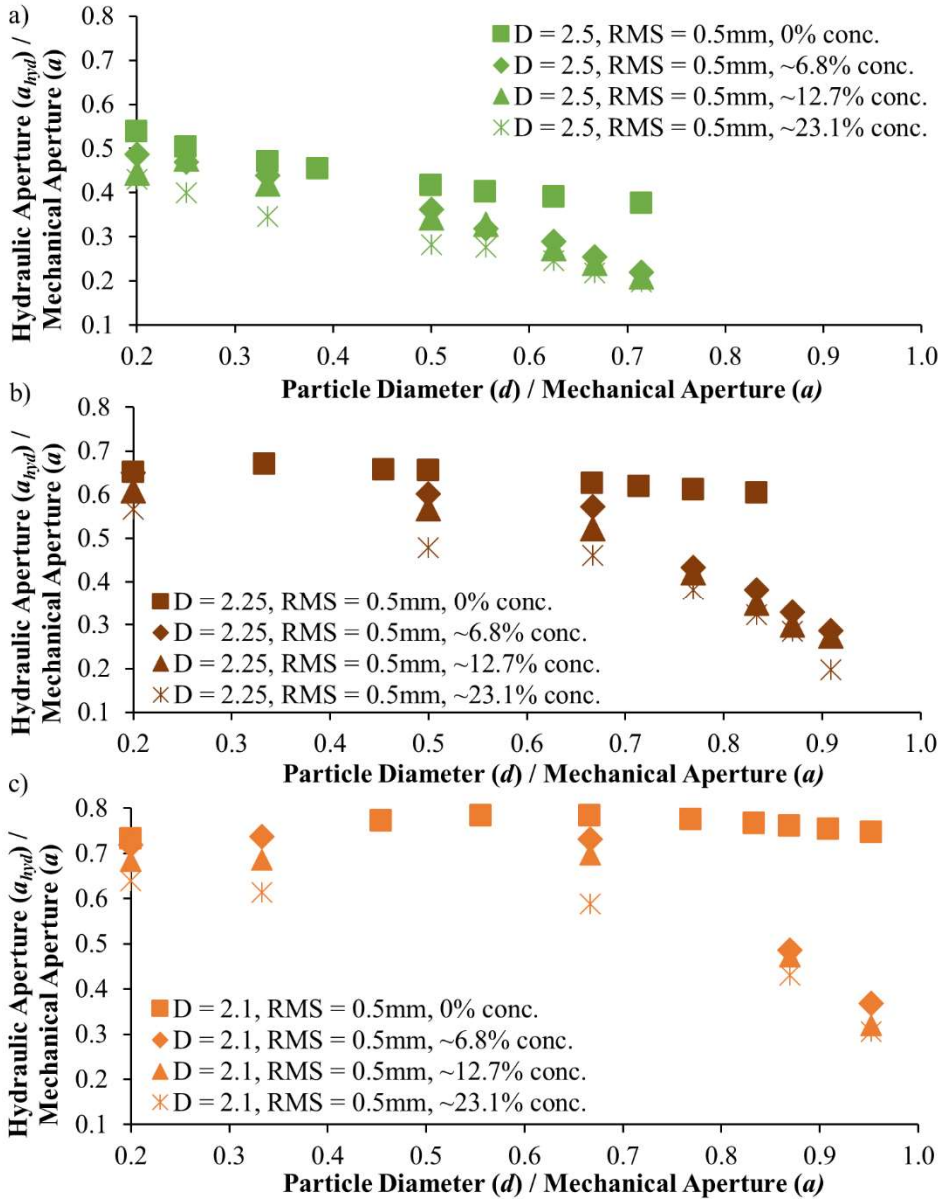

Figure 6.11: Hydraulic aperture to mechanical aperture ratio variance for D = a) 2.5, b) 2.25, and c) 2.1 at concentrations of 0 % (i.e., fluid only), ~6.8 %, ~12.7 % and ~23.1 %.

a_{hyd}/a in the fluid only simulations, i.e., '0 % conc.', for D = 2.1 are relatively stable across the range of d/a ratio values. Gradual decrease in a_{hyd}/a value is observed for the D = 2.5 fracture and to a lesser extent the D = 2.25 fracture as d/a value increases. This is expected as regions of eddy development in the rougher fractures leads

to a greater proportion of the fracture domain containing recirculating flow that does not contribute to through fracture flow as mechanical aperture narrows, and is consistent with findings from Briggs et al. [15].

Particles cause a significant additional effect to the hydraulic aperture. The a_{hyd}/a values decrease for all particle volumetric concentrations compared to simulations without particles. Overall a_{hyd}/a values are lower at higher *D* values. Further, increasing particle volumetric concentration leads to decreased a_{hyd}/a value in similar fractures (i.e., same roughness and mechanical apertures conditions). This again can be attributed to the findings presented in the previous section (6.3.3), where increased particle-particle interactions occur in rough fractures with increased particle volumetric concentrations. These increased particle interactions lead to greater particle kinetic energy dissipation and thus greater pressure gradient demands to convey the slurry. From Eq. 2.14, the increase in pressure gradient leads to lower hydraulic fracture aperture values and thus lower a_{hyd}/a ratio values.

When the fracture mechanical aperture narrows, the calculated $a_{hy}\ /a$ ratio value for different concentrations become more similar for identical roughness and mechanical aperture conditions. The increasing occurrence of jammed particles in fractures leads to greater pressure demands to sustain flow through a more obstructed flow area. However, as was illustrated in section 6.3.3 (see Figures 6.9 and 6.10), degree of jamming is similar regardless of injection concentration for identical fracture mechanical aperture and roughness conditions. Therefore, similar hydraulic aperture values are observed regardless of injection concentrations within identical, narrower fractures. Further the ability of neutrally buoyant particles to continue flow through a rough fracture to spite jamming (see section 6.3.3) would imply that high pressure readings at the slurry pump during injection operations do not necessarily mean particles are not still effectively conveying through the fracture. This appears to be true even at high concentrations, at least for neutrally buoyant particles.

4 Conclusions

This chapter investigated the effects of fracture roughness on proppant flow and transport by studying neutrally buoyant particle slurry flows in synthetic rough fracture using resolved CFD-DEM. Realistic rock fractures were developed from a spectral based method (see Chapter 3, section 3.2) with varying descriptive fractal dimension values, ranging from D = 2.1 to 2.5, and asperity root-mean-square (*RMS*) height, at values of 0.25 and 0.5 mm. Effects of Reynolds number and particle volumetric concentration were considered in various single and multiparticle

simulations (particle volumetric concentrations between approximately 5 % to 20 %), comparing results from rough walled and smooth walled fracture simulations. Findings include:

- Rough fractures do not always cause flow and transport attenuation. At moderate mechanical apertures, accentuated particle velocity compared to behavior in smooth fractures is observed.
- Both fractal dimension and asperity root-mean-square height parameters notably impact particle flow and jamming conditions. Increase of both asperity height *RMS* and fractal dimension values lead to greater particle velocity accentuation at moderate mechanical apertures. As aperture narrows however, these rougher fractures lead to greater flow/transport attenuation and jamming occurrences at wider mechanical apertures than more smooth fractures.
- At injection rates of interest for proppant placement into hydraulic fractures, fluid flow Reynolds number does not have a significant impact to relative flow rate behavior except at very narrow mechanical aperture in smooth fracture geometries.
- Multiparticle flow accentuation and attenuation are exacerbated by combined surface roughness and concentration effects at moderate mechanical apertures. Mechanical aperture where jamming occurs however is more greatly impacted by roughness conditions than slurry volumetric particle concentration.
- In identical fractures (i.e., roughness and mechanical aperture) similar occurrences and degrees of particle jamming are observed, regardless of injection concentration. Additionally, particle flow is redirected around these blockages in rough fractures and further conveys through the fracture. From this redirection and similar jamming, overall proppant volumetric conveyance efficiency is found not to be impacted by slurry particle volumetric concentration.
- Hydraulic aperture is affected by combinative effects from fracture roughness (i.e., eddies at rough surfaces) and particle volumetric concentration. At moderate mechanical apertures, increased particle interactions in higher particle volumetric concentrated slurries in rougher fractures leads to decreased hydraulic aperture (i.e., increased pressure gradient) to maintain flowrate. In narrower apertures, jamming in rough fractures also leads to greater pressure gradient demand. However, as occurrence and degree of particle jamming is similar regardless of injection concentrations at these aperture/roughness conditions, hydraulic aperture becomes similar for like rough fractures regardless of injection concentration.

These findings ultimately provide demonstration of the significant influence fracture wall roughness can have on proppant particle transport behavior. Findings illustrate the significant variance from simple smooth-walled behavioral assumptions as well as from past investigations' general conclusions.

ACKNOWLEDGEMENTS

Chapter 6 of this dissertation is based on materials from a published manuscript with the journal, Geomechanics for Energy and the Environment and is titled, "A Numerical Study of Neutrally Buoyant Slickwater Proppant Flow and Transport in Rough Fractures". Authors are Brian D. Yamashiro and Ingrid Tomac. This dissertation's author is the first author of this paper.

7 SETTLING OF SLURRIES WITHIN ROUGH FRACTURES

7.1 Introduction

Chapter 6 demonstrated the significant impact that fracture wall roughness can have on particle flow and transport. As most traditional proppant slurries are composed of particles more dense than their carrier fluids [3], settling behavior of proppant particles within fracture openings is investigated in this chapter.

As discussed in Chapter 2, evaluations of particle settling behavior used in hydraulic fracture modeling software and design evaluations are built upon the assumption that fracture walls can be treated as smooth surfaces [7,9–12]. As is clear from Chapter 6, behavior can greatly vary from this simplified assumption. Further, settling behavior considered in in-use evaluations is based on that evaluated from a quiescent or 'creeping flow' state [7]. Very limited evaluations of particle settling behavior while confined between surfaces exist. However it is clear that there can be significant impacts to bodies at close proximity to walls and in flow regimes that are well above the Stokes range [43,44].

Resolved CFD-DEM is again implemented in this section to provide better mesh adherence to small fracture wall roughness features and more accurate resolution of flow behavior about individual particles within these complex flow domains.

Both evaluation of settling in quiescent and flowing conditions is considered here. Evaluation of settling in flowing conditions is obvious, as proppants settle while being pumped into a rock fracture system. The behavior of quiescently settling proppant particles is of concern after the closure of the fracture, once the treatment finishes being pumped [7], known as 'shut-in'.

The goal of this chapter is to compare settling behavior to a typical attenuated settling rate from combined concentration and wall effects (Novotny's [31] evaluations in this case) and determine if settling behavior is indeed well approximated by this method. Further, if the approximation is not accurate and if possible, it is desired to propose an alternate method that incorporates the varied settling behavior in rough fractures.

7.2 Methods

7.2.1 Synthetic Rock Fracture Walls

Fractal dimension values of 2.1, 2.25, and 2.5 and *RMS* asperity height values of 0 (i.e., smooth walls), 0.25, and 0.5 mm are again considered in this chapter. Two sets of two seed values (instead of one used in Chapter 6) are

used in this work to generate the rough fracture surfaces with SynFrac. These sets are referred to as Seed 1 and Seed 2 throughout this chapter for brevity. The averaged results from simulations using the two sets of surfaces generated with Seed 1 and Seed 2 are used in the settling behavior evaluations.

STL surface features are again resolved at 0.1 mm (~1/5th of the average proppant particle's diameter) square-shaped surface elements to allow for hexagonal CFD cells that adhere to surficial roughness features. The CFD cells are 50 μm edge length sized cubes.

To alleviate the convex edge issue experienced in DEM simulations, mentioned in Chapter 6 (section 6.6.2) and maintain fracture surface features, STL surfaces are further processed with a 3D rendering software (i.e., Blender) before utilizing them within the DEM side of the simulation. The rendering software's 'Smooth Vertices' function with a 0.5 smoothing factor is used. Figure 7.1 shows an example centerline profile of the CFD mesh boundary and corresponding DEM wall profiles.

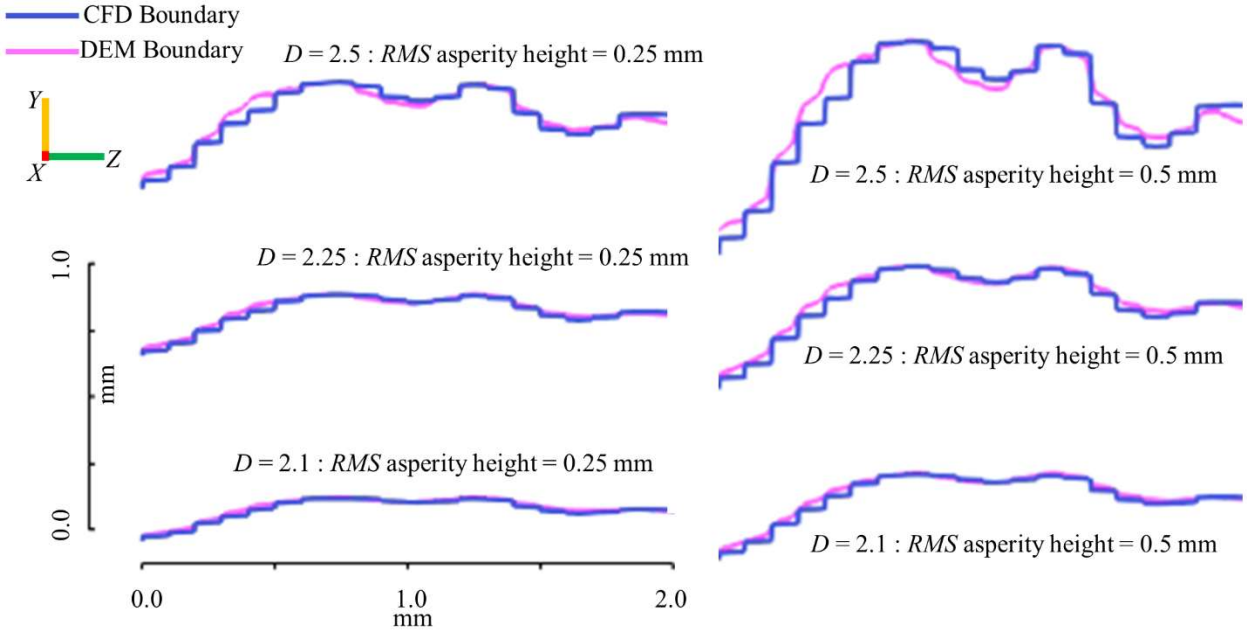

Figure 7.1: Example center profile sections from -*Y* boundaries of generated rough fractures. CFD mesh boundary (blue) and DEM boundary (pink).

7.2.2 Material Properties and Domain Settings

Full material properties utilized in these sets of simulations are summarized in Table 7.1.

Table 7.1: Model material properties for settling slurry in rough fracture simulations

Proppant/Wall Parameters:		Units	Fluid Parameters:		Units
Particle Diameter	500	μm	Dynamic Viscosity	0.003	Pa·s
Particle Density	2600	kg/m^3	Density	1000	kg/m^3
Particle/Wall Contact Friction Value	0.6	-			
Particle/Wall Young's Modulus	$5x10^6$	N/m^2			
Particle/Wall Poisson Ratio	0.3	-			
Particle/Wall Coefficient of Restitution	0.95	-			

Table 7.2 summarizes simulation boundary conditions. Gravity is active in the +*Z* direction for both quiescent and flowing simulation cases.

Table 7.2: Model boundary conditions for settling slurry in rough fracture simulations

Quiescent Simulations			
CFD Boundary Conditions:		DEM Boundary Conditions:	
+/- *X* faces	Slip velocity; Uniform, fixed pressure (= 0)	+/- *X* face	Reflect
+/- *Y* faces	No-Slip velocity; Zero-gradient pressure	+/- *Y* faces	DEM wall contact
+/- *Z* faces	Slip velocity; Zero-gradient pressure	+/- Z face	Destroy
Flowing Simulations			
CFD Boundary Conditions:		DEM Boundary Conditions:	
- *X* face	Prescribed vel. (developed flow); Zero-gradient pressure	+/- *X* faces	Destroy
+ *X* face	Zero-gradient velocity; Uniform, fixed pressure (= 0)	+/- *Y* faces	DEM wall contact
+/- *Y* faces	No-Slip velocity; Zero-gradient pressure	+/- Z face	Destroy
+/- *Z* faces	Slip velocity; Zero-gradient pressure		

The -*X* face prescribed inlet velocity profile for the flowing cases is constructed using the analytical description of a fully developed flow profile for a Newtonian fluid between two walls:

$$u(y) = \boldsymbol{u}_{max}\left(1 - \frac{|y|}{a/2}\right)^2 \tag{7.1}$$

where $\boldsymbol{u}_{max}$ is the center, peak velocity in the flow profile, and y is the distance from the centerline of the flow profile. $\boldsymbol{u}_{max}$ is determined based on mean flow velocity ($\boldsymbol{u}_{mean}$) based on the prescribed Reynolds number for the flow between two walls ($Re_{||}$):

$$\boldsymbol{u}_{mean} = \frac{\mu Re_{||}}{2\rho_f a} \tag{7.2}$$

where for an incompressible Newtonian fluid,

$$\boldsymbol{u}_{max} = \frac{3\boldsymbol{u}_{mean}}{2} \tag{7.3}$$

A constant supply of particles at various prescribed particle volumetric concentration are introduced into the simulation domain by generating them in a rectangular 'factory' section (see Figure 7.2 for example domains). A 'transition' section is also again included between the 'factory' and fracture sections to allow the particles to enter the fracture domain smoothly. The CFD domain is also generated to be two particle diameters longer than the DEM domain in the +*Z* direction provide a buffer where particles exit and limit CFD boundary influences on particles. A similar-sized buffer is also included for flowing cases at the +*X* side of the domain. CFD fracture domain (not including 'factory' and 'transition') for the quiescent settling cases is generated to ten particle diameters long (*X*-direction), by nine particle diameters tall (*Z*-direction), at varying aperture width in the *Y*-direction. For flowing cases, domain length (*X*-direction) is set to at least ten times the maximum fluid velocity times the relaxation time (t_{relax}) of a particle within fluid based on Table 7.2's properties where [120]:

$$t_{relax} = \frac{d^2\rho_s}{18\mu} \tag{7.4}$$

The 'factory' and 'transition sections' are three particle diameters and two particle diameters in dimension, respectively.

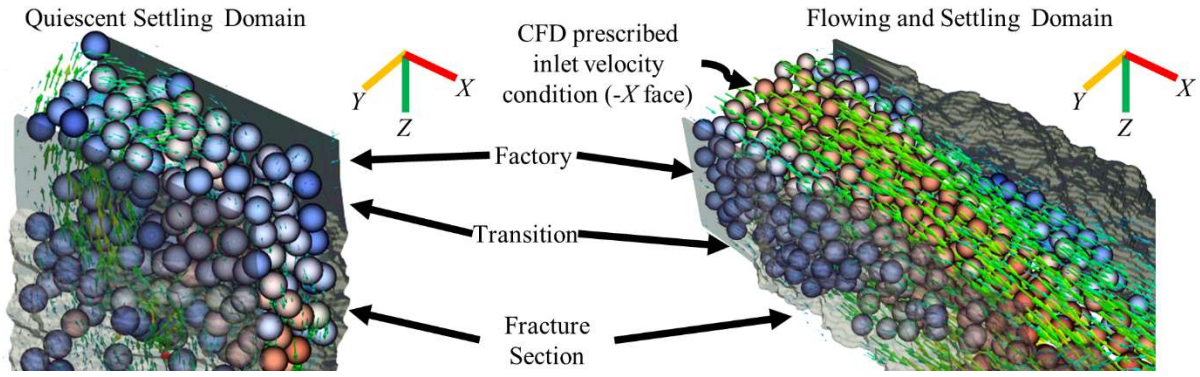

Figure 7.2: a) Example simulation domain geometries for settling in quiescent and flowing conditions.

To capture developed settling behavior, quiescent settling simulations are run for a minimum of two times the calculated duration of a particle to travel through the domain based on concentration and wall correction factors (see Chapter 2, Eqns. 2.4, 2.5, and 2.6). For flowing simulations, fluid only simulation is first run for a duration of time equal to the mean fluid velocity divided by the domain length (i.e., the average time for the fluid to travel the length of the domain). This fluid only simulation is done to develop the flow within the fracture before particle insertion. Particle and fluid simulation is then run in this developed flow domain for twice the calculated duration of the fluid only simulation. The last ten percent of the particle-fluid simulations' run time data is evaluated to capture developed settling slurry behavior in all simulations unless otherwise mentioned. Particle behavior from within five particle diameters from the bottom of the DEM domain is assessed for the quiescent simulations. This evaluation section is chosen to allow particles to experience the effects of the rough fracture geometry prior to collecting data. Data is extracted from a section equal to 25 % of the average maximum fracture length traveled by particles within the fracture section for flowing simulations. This section typically equates to the last 25 % of the generated fracture domain from the $+X$ end. In some wide aperture cases, where particles did not completely travel the whole domain's length, the evaluation section's endpoint is before the end of the domain.

The coupling frequency between DEM and CFD timesteps is set to 100. Simulation timestep size is determined based on CFL number value [22] for the CFD side simulation as well as Rayleigh [89] and Hertz timestep [88] size for the DEM side of the simulation. The timestep size is chosen to be the minimum that provides a CFL number less than one, less than 20 % of Rayleigh time, or less than 5 % of Hertz time, for stability and accuracy. CFD time step varied from 1×10^{-4} to 2×10^{-5} sec. for the simulations.

7.3 Findings and Results

7.3.1 Quiescent Slurry Settling Between Smooth Walls

Typical slickwater proppant slurry injections have particle concentrations around 0.25 to 3 PPA (pounds of proppant added to one gallon of fluid) [5], equating to approximately 1.1 % to 12.2 % volumetric particle concentration. Therefore, particle volumetric concentrations from 1 % to 15 % are initially considered. Figure 7.3 shows the results for the average settling velocity of particles normalized by a single, unbounded particle's terminal settling rate as defined by Eq. 1.1 (i.e., $v_{c,w}/v_t$) for varying particle diameter to aperture ratios (d/a). Relationships of attenuated settling rate as defined by Novotny's [31] formulations are also shown. The product of the individual attenuation factors due to wall effects (f_w, Eqns. 2.5 and 2.5) and concentration effects (f_c, Eq. 2.4) are used to determine the combinative effect (i.e., $v_{c,w}/v_t$).

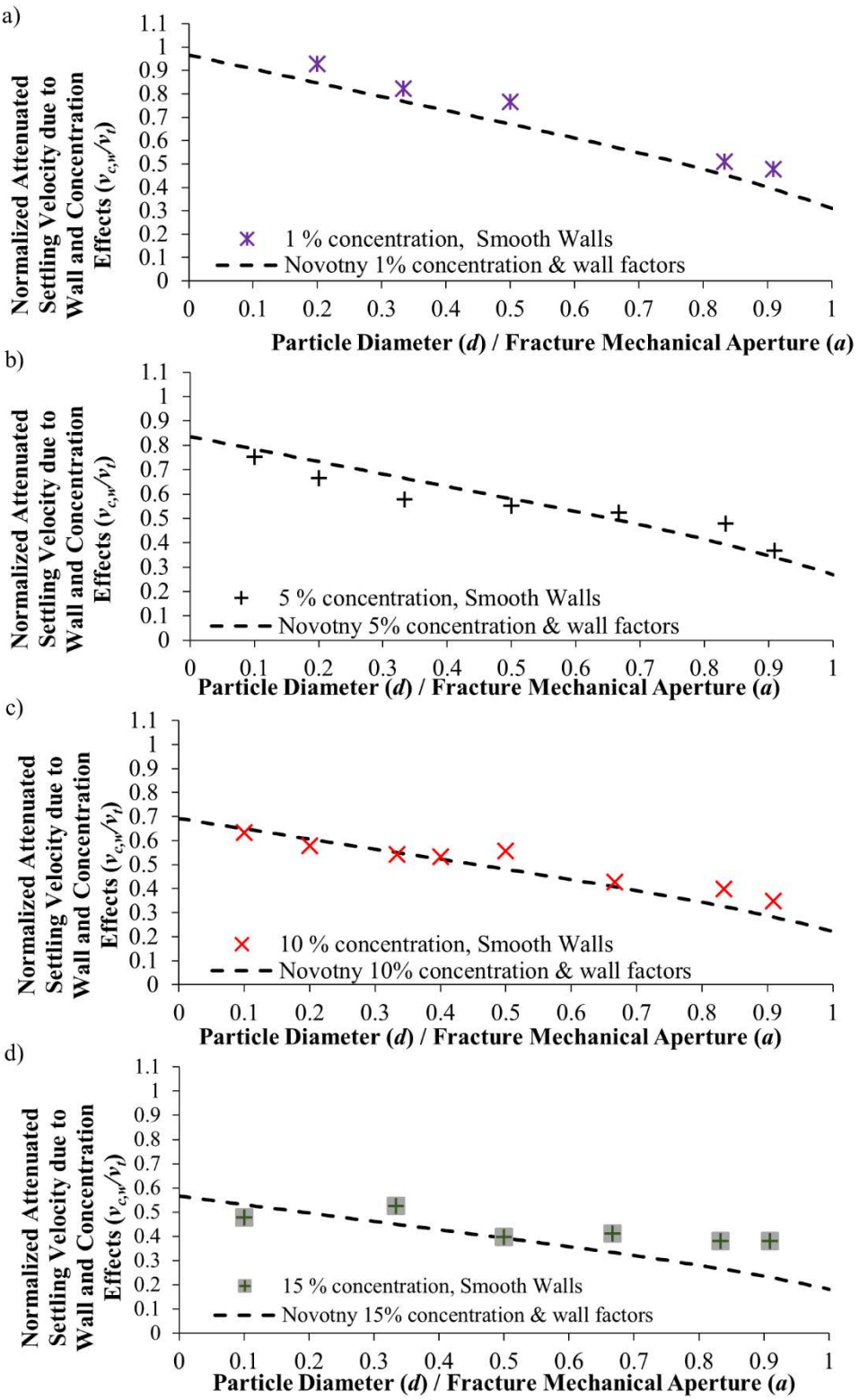

Figure 7.3: 1 %, 5 %, 10 %, and 15 % particle volumetric concentration slurry settling behavior at various aperture with smooth-walled fractures. Values indicated as dimensionless ratios of particle diameter to aperture (d/a) and the ratio of average attenuated settling rate to settling rate of a single, unbounded particle ($v_{c,w}/v_t$).

Results mostly match behavior as described by Novotny's [31] attenuation effect formulations. However, there is a more significant deviation from Novotny's relationship for the 15 % particle volumetric concentration slurry at the narrowest considered aperture ($d/a \approx 0.91$), where the simulation value is approximately 66 % larger than that expected from Novotny's formulations. The cause is slightly unclear at these narrow apertures, so several additional simulations with even higher particle volumetric concentration (20 %) are conducted. Figure 7.4 shows the results from these 20 % particle volumetric concentration simulations.

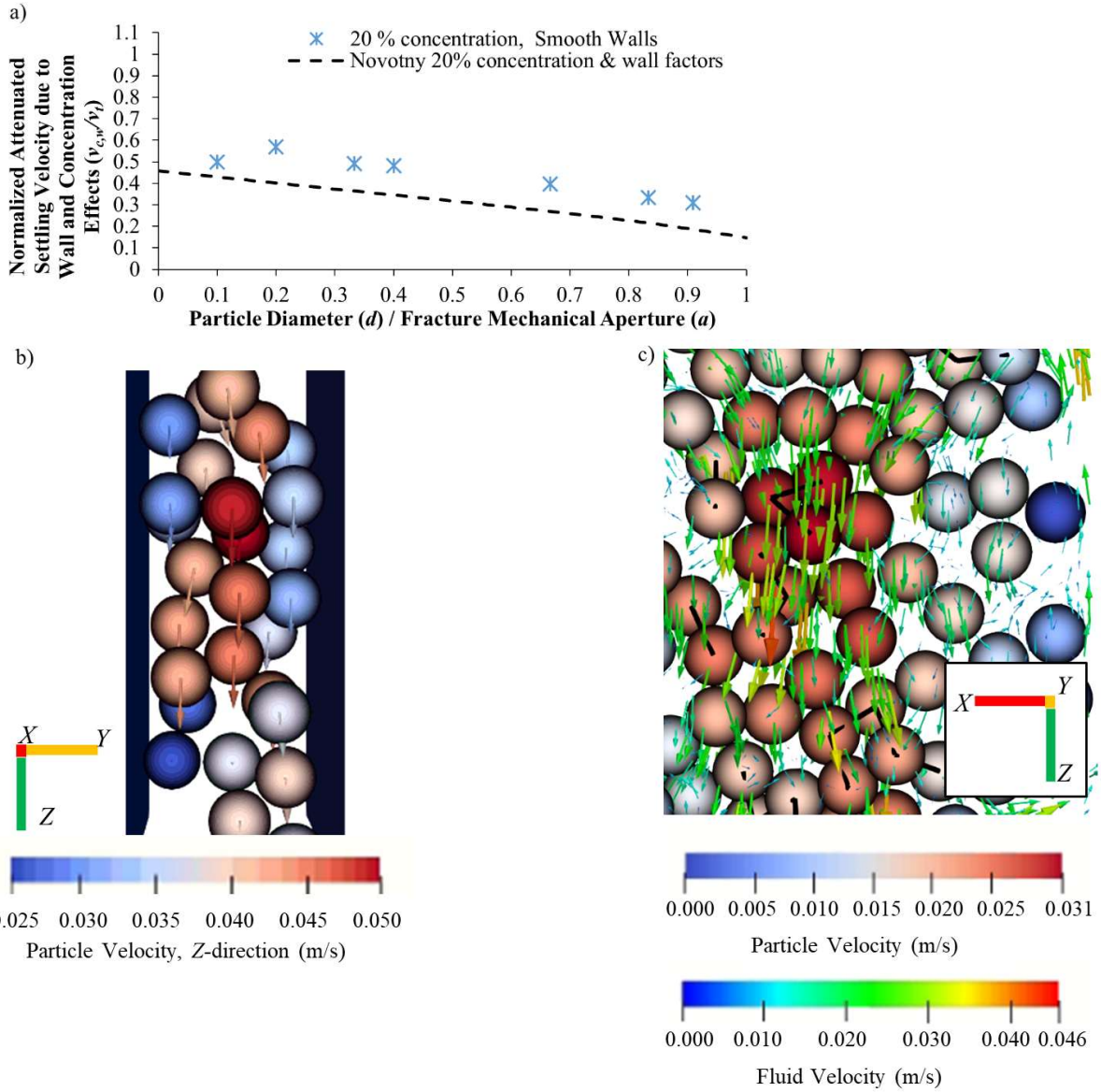

Figure 7.4: a) 20 % volumetric particle concentration slurry settling results. b) Cross-section image of concentrated particles settling between smooth-walled fracture. c) Example multiple clustering particles in a concentrated slurry with high settling velocity and influenced fluid field. Black lines in b) indicate inter-particle contacting.

It becomes clear from Figure 7.4a that for slurries with high particle volumetric concentrations, Novotny's [31] formulation notably underestimates the attenuated settling rate. Measured values range from 16 % to 66 % higher settling rates than those predicted. The only result from Figure 8a reasonably approximated by Novotny's formulation is at the widest considered aperture, d/a = 0.1. Looking at the in-simulation particle and fluid behavior in Figs. 7.4b and c, the cause of these higher settling rates becomes clearer. In Figure 7.4b, particles with closer proximity to the walls are observed to experience greater wall effects leading to slower settling rates than more centrally located particles. For high volumetrically concentrated cases in narrower apertures, greater particle clustering occurs due to greater incidence of particle-particle contact from the closer proximity and the greater variance in settling rate between adjacent particles depending on proximity to walls. As seen in Figure 7.4c, these agglomerated particles have a high settling velocity compared to non-clustered particles. This behavior is consistent with the observations of Luo and Tomac [62] for their quiescently settling proppant slot experiments discussed in Chapter 2 (section 2.2.2).

As mentioned earlier in this section, volumetric particle concentrations of slickwater slurries do not typically reach these high values (maximum ~12 %), so this occurrence of particle clustering is of less practical concern in field applications. Still, it does reinforce the limitations on concentration utilized in practice.

7.3.2 Quiescent Slurry Settling Between Rough Walls

Simulation of quiescently settling slurries in rough fractures is next considered. Figures 7.5 and 7.6 shows results of simulated behavior in fractures with various combinations of fractal dimension, *RMS* asperity height, and aperture values. Fractures are considered to be "jammed" for this study once particles become immobile (i.e., trapped) across at least half of the simulation domain. Values for average settling velocity in these cases are also recorded as zero. The error bars indicate the minimum and maximum average settling rates from simulation between the two different surfaces generated with Seed 1 and Seed 2 values discussed in section 7.2.1.

Results for all simulations initially adhere to the predictions of Novotney's [31] attenuated settling formulations. However, increased attenuation, with eventual jamming in most cases, occurs as the aperture narrows. The degree of severity is dependent on the fractal dimension and *RMS* asperity height values. Not surprisingly, higher surface roughness (i.e., increasing fractal dimension and *RMS* asperity height values) leads to incidence of attenuation and jamming at wider apertures than less rough cases.

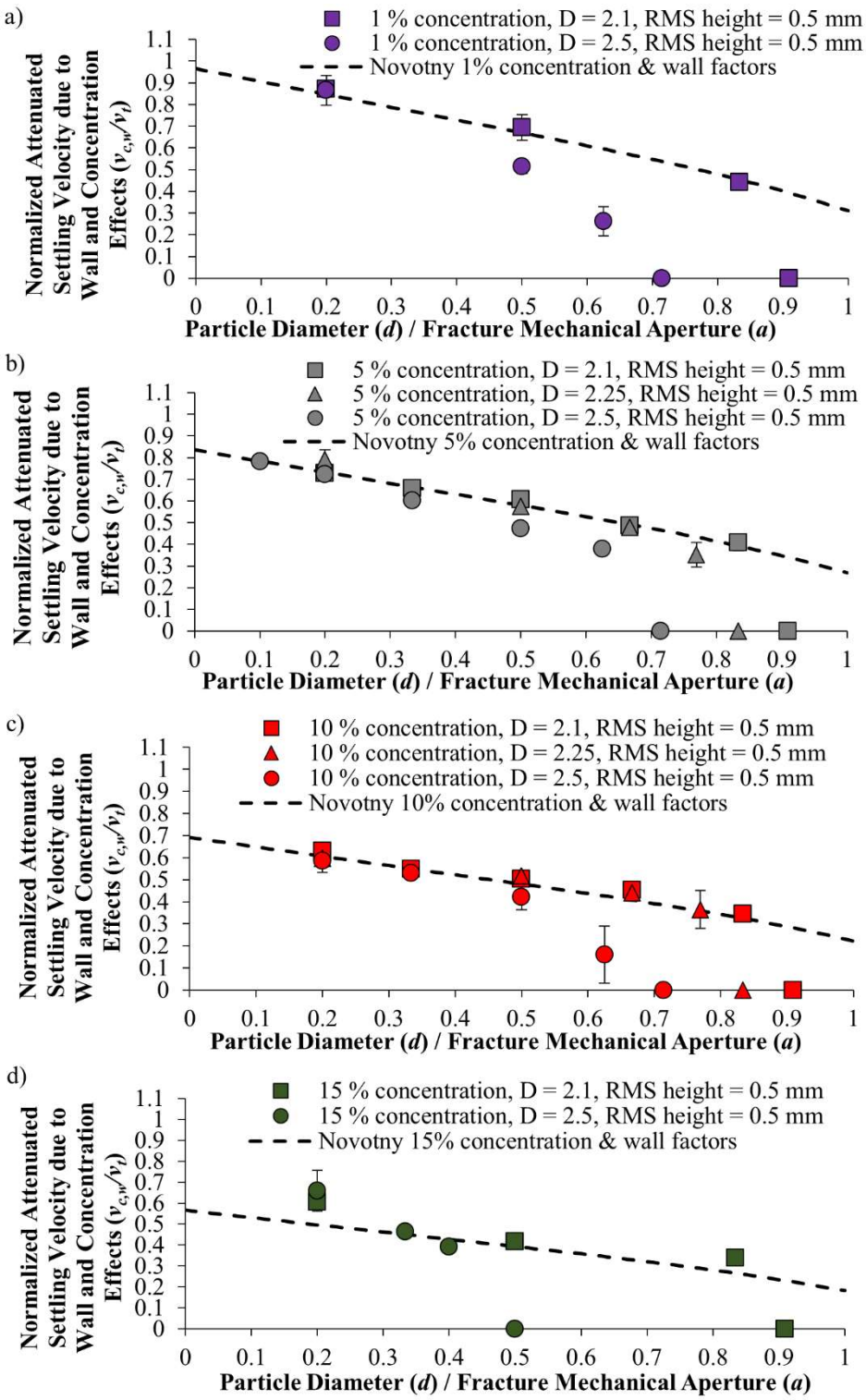

Figure 7.5: a) 1 %, b) 5 %, c) 10 %, and d)15 % particle volumetric concentration slurry settling behavior for fractal dimensions of 2.1, 2.25, and 2.5 and *RMS* asperity heights of 0.5 mm. Error bars indicate the minimum and maximum values of the two simulation runs with surfaces generated from Seed 1 and Seed 2 values.

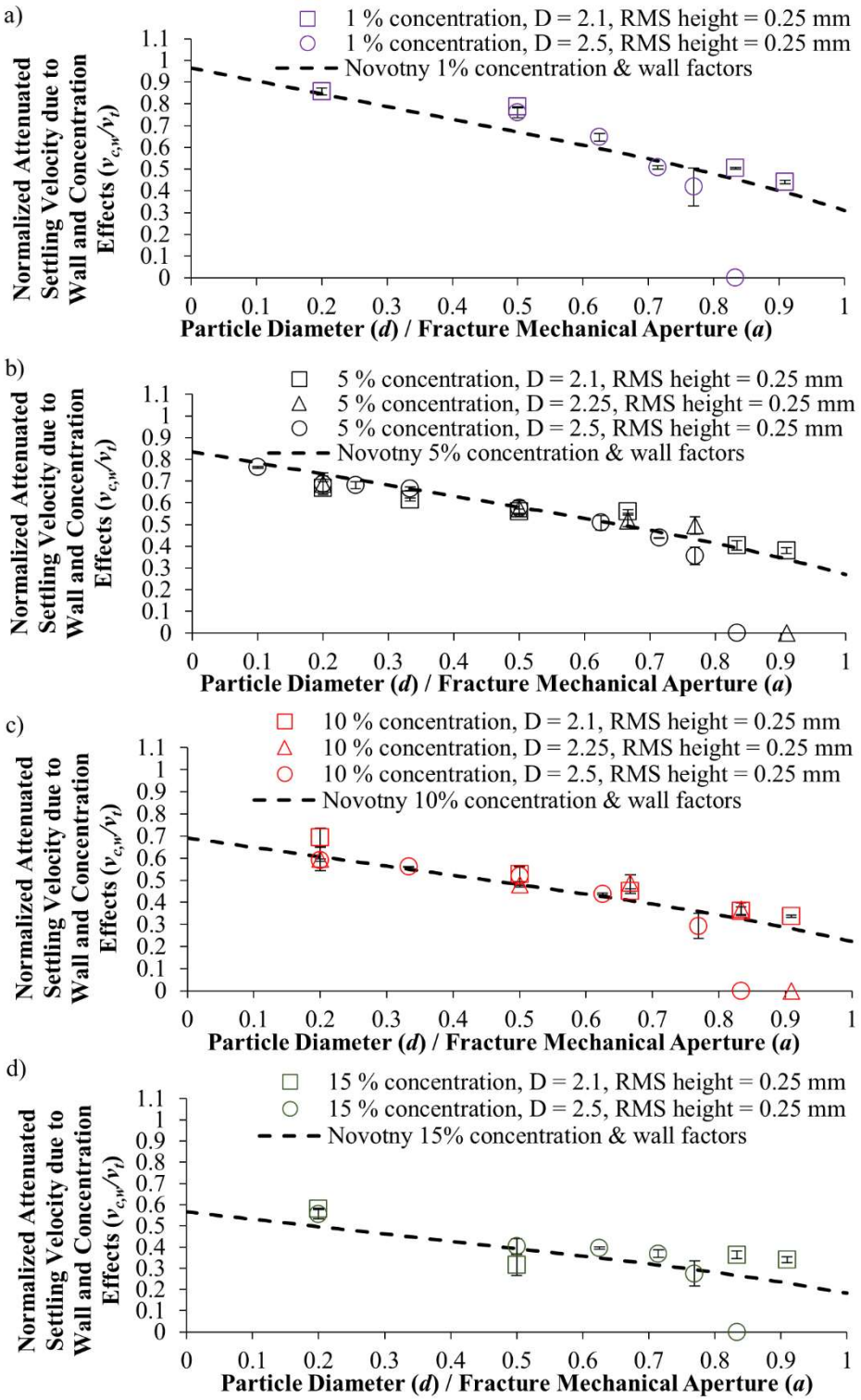

Figure 7.6: a) 1 %, b) 5 %, c) 10 %, and d)15 % particle volumetric concentration slurry settling behavior for fractal dimensions of 2.1, 2.25, and 2.5 and *RMS* asperity heights of 0.25 mm. Error bars indicate the minimum and maximum values of the two simulation runs with surfaces generated from Seed 1 and Seed 2 values.

As textural complexity increases with larger fractal dimension values, more locations for particle travel attenuation from contacting and potential jamming points where particle motion arrests occur. Increases in *RMS* asperity height further leads to more pronounced variances in cross-sectional fracture openings, causing increased locations for particle attenuation and jamming. The degree of attenuation once roughness effects become more influential (i.e., data points between departure from Novotny's formulation and jamming) in surfaces with identical fractal dimension and *RMS* asperity heights (i.e., Seed 1 versus Seed 2) can also significantly vary. The significant difference between the minimum and maximum values within this region from Figures 7.5 and 7.6 demonstrates this variance.

Figure 7.7 further illustrates the influence of fractal dimension and *RMS* asperity height by looking at sample cross-sections through the fractures. These cross-sections are at identically located points within fractures with different values of these roughness parameters. Cross-sections are all from the same seed value (Seed 1), so their overall shape is similar but contains differing degrees of textural roughness (i.e., varying fractal dimension) and surface features heights (i.e., varying *RMS* asperity height).

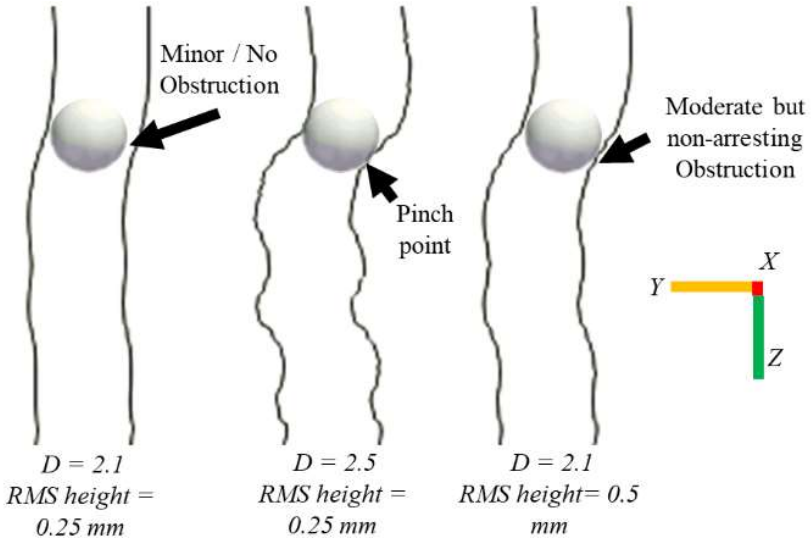

Figure 7.7: Example varying degree of particle travel way obstruction from example fracture cross-sections with differing roughness parameters.

From the example in Figure 7.7, it becomes clear that both fractal dimension and RMS asperity heights both play significant roles in the attenuation and jamming behavior for particles within a rough fracture. More importantly, from Figures 7.5, 7.6, and 7.7, it becomes clear that additional attenuated settling in rough fractures is primarily

attributable to physical interactions between the particles and fracture walls rather than additional frictional influence from the walls on the fluid.

It is further noted that for all the volumetric particle concentrations considered, the aperture where increased attenuation begins and where particle jamming occurs is virtually identical for like fractures regardless of particle concentration value. The exception is the 15 % concentration case with a fractal dimension of 2.5 and *RMS* asperity height of 0.5 mm. The attenuation and jamming are again attributable to the increased interaction of particles in this more highly concentrated slurry coupled with the higher interactions with the roughness features of the fracture walls. Roughness features force the particles inward away from the fracture walls, leading to more significant interaction and clustering. The clustered groupings then more easily jam within the fracture. However, this case is isolated, and as mentioned in the previous section (7.3.1), 15 % volumetric particle concentration is above that typically utilized in field slickwater slurries. Section 7.4 will further explore if it is possible to formulaically express the attenuation and jamming behavior in these rough fractures and address if this formulation represents the concentration limits for field slickwater slurries mentioned previously (i.e., ~1 % to 12 %).

7.3.3 Flowing Proppant Settling Between Smooth Walls

A maximum of $Re_{||}$ value of 250 is considered in this investigation as higher values require larger domains and significantly increased computational expense. This value is below typical field slickwater injection rates, where $Re_{||}$ is closer to ~1000-2000 (see Chapter 5, section 5.2.2). However, evaluation using this flow rate still provides insight into some of the variances in settling behavior that occurs for proppants in flow while providing direction and considerations for future investigations. Influences of slurry flow rate, proppant particle volumetric concentration, and ultimately fracture roughness are considered.

First, the influence of aperture and flow rate on a single particle behavior between smooth walls is explored. A single particle is generated at 1.5 particle diameters from the -*X*-face, 0.5 particle diameters from the -*Z*-face, and centered about the aperture. Figure 7.8 shows results from these simulations for $Re_{||}$ = 0 (i.e., the quiescent results from subsection 3.1), 10 and 250. Mesh refinement with 0.025 mm cell size, to check for mesh independence, is also performed for the $Re_{||}$ = 250 cases at several apertures.

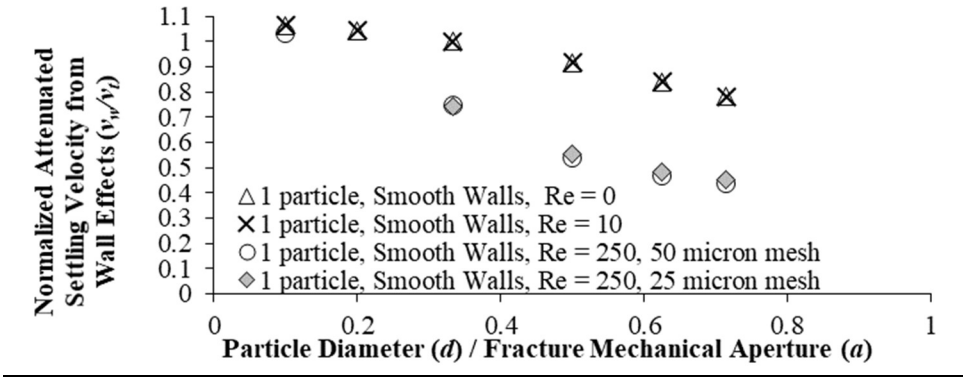

Figure 7.8: Single particle settling behavior in flow, $Re_{||}$ = 10 and 250. Results from subsection 3.1's quiescent case (i.e., $Re_{||}$ = 0) also included for comparison.

Figure 7.8 results for particle settling at flow rate well beyond the Stokes range are surprising, with lower settling rates observed in the higher flow condition. Where results for $Re_{||}$ = 10 are virtually identical to quiescent results (i.e., $Re_{||}$ =0), the particles in flow with $Re_{||}$ = 250 have a significantly lower settling rate for apertures narrower than d/a ratio of 0.1. The similarity of results from a more refined mesh (0.025 mm cell size) also confirms mesh resolution is not a cause of this behavioral variance.

To investigate the cause of this increased degree of particle settling retardation, Figure 7.9 looks at a cross-section through the settling particles in flows with $Re_{||}$ = 10 and 250.

Figure 7.9: a) Cross-section of fluid *X/Y*-component velocity fields and pressure fields (adjusted to 0Pa gauge) for slices in the *X/Y*-plane through settling particle in $Re_{||}$ = 10, aperture = 0.7 mm; $Re_{||}$ = 250, aperture = 0.7 mm.; and $Re_{||}$ = 250, aperture = 5.0 mm simulations. b) Average pressure gradient across fracture width (*Y* direction) along the height of fracture (*Z* direction). Pressure values for 5.0 mm aperture simulation averaged over a 0.7 mm subsection centered about the particle. Values discontinuous about the particle limits.

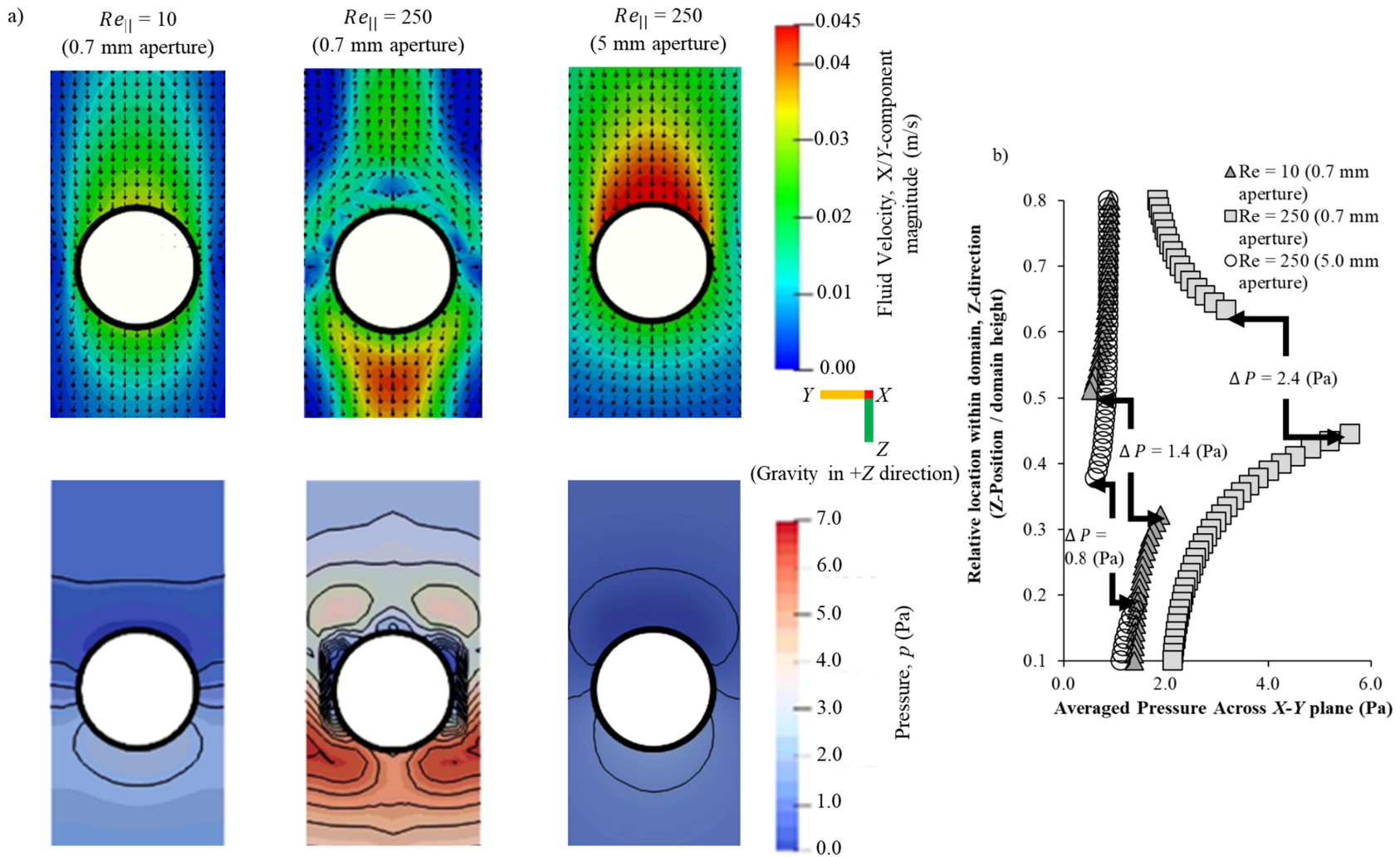
a)
$Re_{||}$ = 10
(0.7 mm aperture)
$Re_{||}$ = 250
(0.7 mm aperture)
$Re_{||}$ = 250
(5 mm aperture)
0.045
0.04
0.03
0.02
0.01
0.00
Fluid Velocity, X/Y-component magnitude (m/s)
Y
X
Z
(Gravity in +Z direction)
7.0
6.0
5.0
4.0
3.0
2.0
1.0
0.0
Pressure, p (Pa)
b)
Re = 10 (0.7 mm aperture)
Re = 250 (0.7 mm aperture)
Re = 250 (5.0 mm aperture)
Δ P = 2.4 (Pa)
Δ P = 1.4 (Pa)
Δ P = 0.8 (Pa)
Relative location within domain, Z-direction (Z-Position / domain height)
0.8
0.7
0.6
0.5
0.4
0.3
0.2
0.1
0.0
2.0
4.0
6.0
Averaged Pressure Across X-Y plane (Pa)

Figure 7.9a reveals a significant variance in the flow field about the particle settling between a 0.7 mm aperture with $Re_{||}$ = 250. A region of higher relative velocity in the *X/Y* plane develops below the settling particle in this condition (a = 0.7 mm; $Re_{||}$ = 250) and is notably different from the other two cases at high aperture with high flow (a = 5.0 mm; $Re_{||}$ = 250) and narrow aperture with low flow (a = 0.7 mm; $Re_{||}$ = 10). More important is the variance in pressure fields about the particles shown in Figure 7.9a and quantified in Figure 7.9b. As the particle is translating downward due to gravity, vertical asymmetry in the pressure fields about the particle center is not surprising. However, as seen in Figure 7.9b., wall effects for the a = 0.7 mm, $Re_{||}$ = 250 case cause a more significant pressure differential from the bottom to the top of the particle than those observed in the other two example cases. This larger, upward acting pressure gradient appears to be the cause of the reduced settling velocity.

Figure 7.10 shows simulation of a 5 % particle volumetric concentration slurry at different flow rates and apertures. Again, the flow rate influences the settling velocity in these volumetrically concentrated slurries with higher flow rates, leading to more significant settling velocity attenuation at narrower apertures.

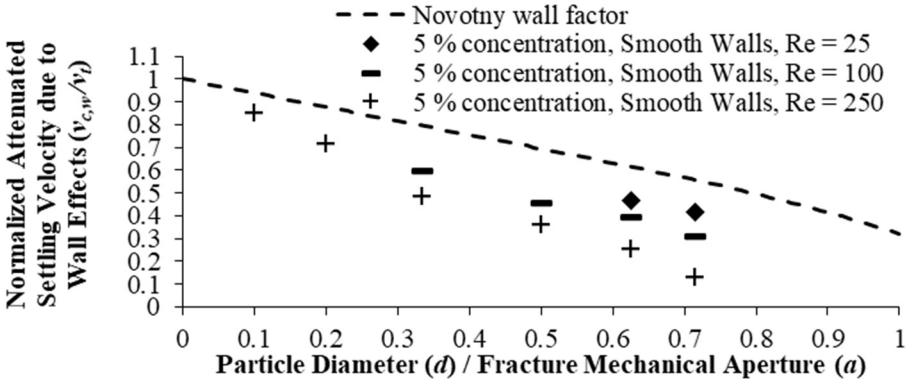

Figure 7.10: 5 % volumetrically concentrated slurry settling for $Re_{||}$ = 25, 100, and 250. Novotny settling relationship for 5 % volumetric particle concentration and wall effects included for comparison.

Given the lack of literature on the effects of flow rate on particle settling rate when confined between parallel walls, outside of the few mentioned in Chapter 2 (section 2.1.3), further experimental evaluation of this effect would be warranted. If confirmed, this behavior also points to inadequacies of the utilized relationships for unresolved CFD-DEM simulations for evaluating flowing particles in narrow slots relative to particle size and fracture design software that do not encompass this behavior.

7.3.4 Effect of Volumetric Particle Concentration on Flowing Slurry Settling

For this section, the slurries are again subjected to a flow condition of $Re_{||}$ = 250 and are tested at volumetric concentrations of 1 %, 5 %, and 15 % within varying apertures. Figure 7.11a summarizes the results of the simulations and their variation from the settling rate predicted by Novotny's formulations (i.e., $v_{c,w(flow\ sim.)}/v_{c,w(Novotny)}$).

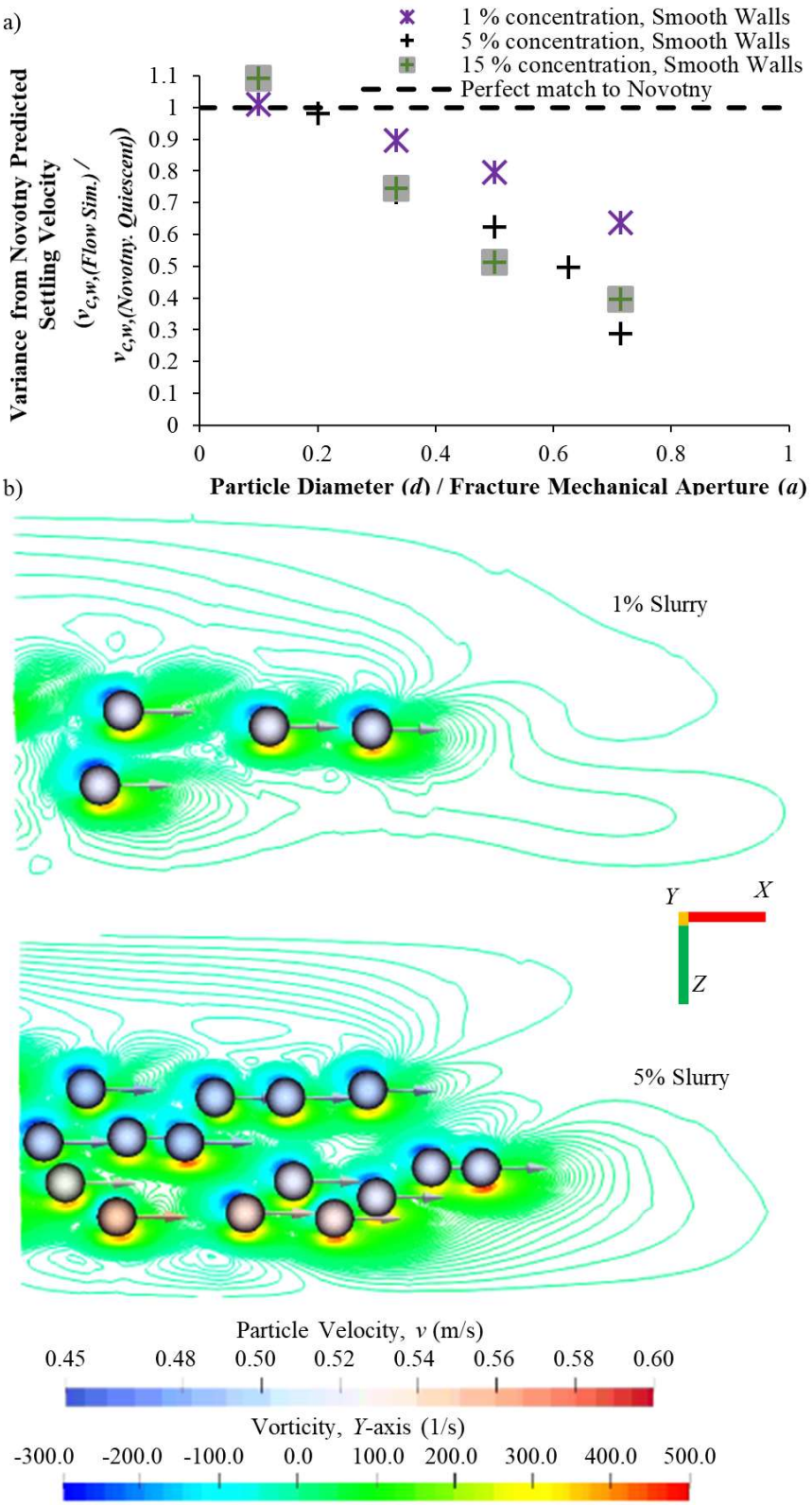

Figure 7.11: a) 1 %, 5 %, and 15 % volumetrically concentrated slurries averaged settling rate normalized by Novotny's predicted settling rate accounting for wall and concentration effects (i.e., Eqns. 1 and 7), with $Re_{||}$ = 250. b) Example vorticity about leading particles in 1 % and 5 % slurry flow simulations.

All concentrations demonstrate increasingly more significant variance (i.e., lower settling rate) from Novotney's [31] evaluation as aperture decreases. While 5 % and 15 % particle volumetric concentration slurries demonstrate similar behavior, the 1 % particle volumetric concentration slurry is notable higher than those two sets of cases as aperture decreases. Figure 7.11 b and c show vorticity contours about the particles from example 1 % and 5 % particle volumetric concentration slurry simulations. More notable interaction between particles and their trailing wakes can be seen for the 5 % particle volumetric concentration slurry due to greater proximity of particles, leading to greater settling attenuation. This behavior implies that particle concentration can play a significant role in hindered settling velocity for confined slurries in flow. Influence, however, only occurs up to a particular volumetric particle concentration (5 % in this case). After this specific concentration, relative additional attenuation effects become similar.

7.3.5 Rough Fracture Surfaces Influences on In-Flow Slurry Settling

A 5 % particle volumetric concentration slurry is injected into three rough fractures with varying textural roughness (D) and asperity *RMS* height features (i.e., D = 2.1, *RMS* asperity height = 0.5 mm; D = 2.5, *RMS* asperity height = 0.5 mm; and D = 2.5, *RMS* asperity height = 0.25 mm). Figure 7.12 shows the obtained settling rates, including the smooth-walled fracture results.

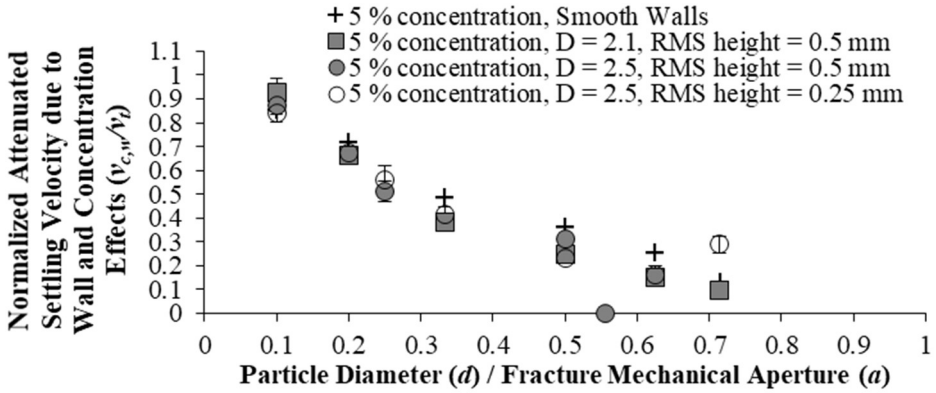

Figure 7.12: 5 % particle volumetric concentration slurry average settling rates in rough fractures, with $Re_{||}$ = 250 in fractures with varying roughness.

Behaviors of average settling velocity in each fracture are virtually identical until aperture narrows to an approximate d/a ratio of 0.5. Jamming occurs for roughest fracture (D = 2.5, *RMS* asperity height = 0.5 mm) at d/a ratio of ~0.56. When looking at the particle behavior within the simulations, however, it is noted that particles flow

around the jammed section, with a large portion exiting the simulation domain either through the top or bottom. In the D = 2.5, *RMS* asperity height = 0.25 mm fracture, at d/a ratio of ~0.7, average settling velocity values are seen to deviate from the smooth-walled simulation result strongly. When viewing the full simulation, multiple particles again exit through the top and bottom of the domain even without any noted jamming. Other rough fractures at narrow apertures have similar upward and downward particle motion, with particles exiting the domain before reaching the end of the fracture. Figure 7.13 shows an example of streamlines through a rough fracture for a domain with fluid-only flow simulated. As the aperture narrows, flow pathways become more tortuous, forming preferred pathways through the fracture. As is the case for several simulations in this work, these flow pathways can lead particle upward and downward motion, potentially causing exit from the simulation domain. This behavior makes quantification of the settling rate in these cases unreliable as true particle behaviors would include the previously exited particles within the evaluation.

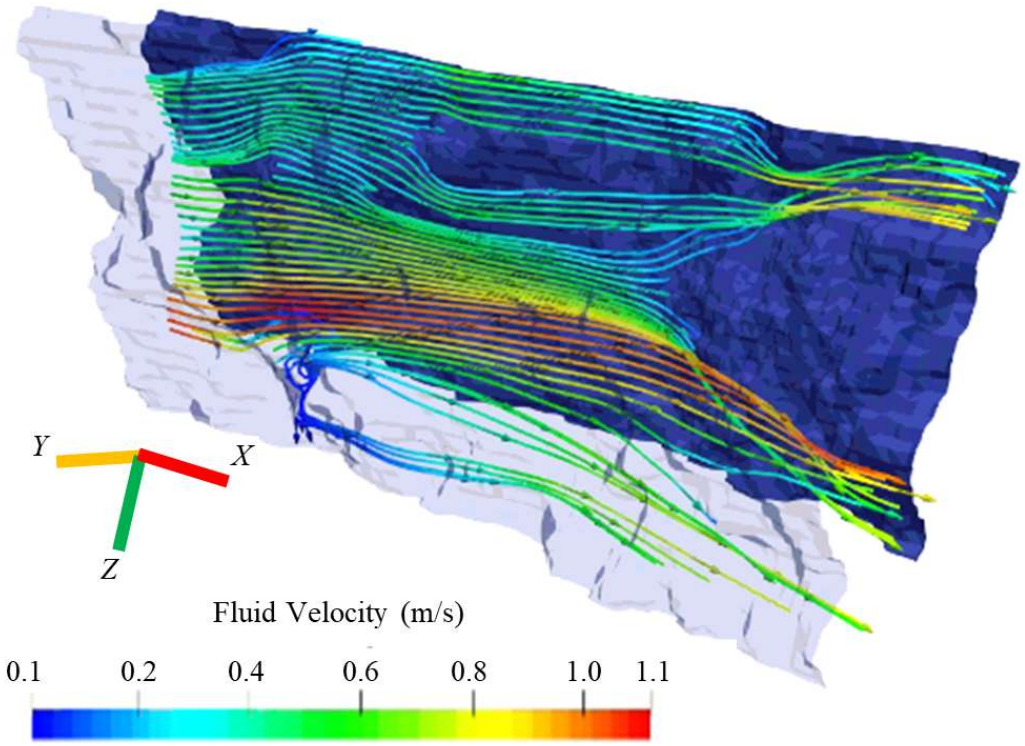

Figure 7.13: Developed preferential flow pathways in rough fracture (D = 2.5, *RMS* asperity heights = 0.5mm, d/a = 0.625).

To illustrate the significant influence the flow streamlines can have on individual particles, a single particle is simulated within the D = 2.5, *RMS* asperity height = 0.5 mm rough fracture at various apertures. Single particles'

initial conditions are identical to those discussed in section 7.3.3. Figure 7.14 a and b show an example of the particles' Z-position and Z-velocity while flowing through the rough fracture at d/a ratio of 0.5 (i.e., 1 mm aperture). Behaviors within both generated surfaces (Seed 1 and 2) are compared to particle behavior in smooth wall conditions from section 7.3.3.

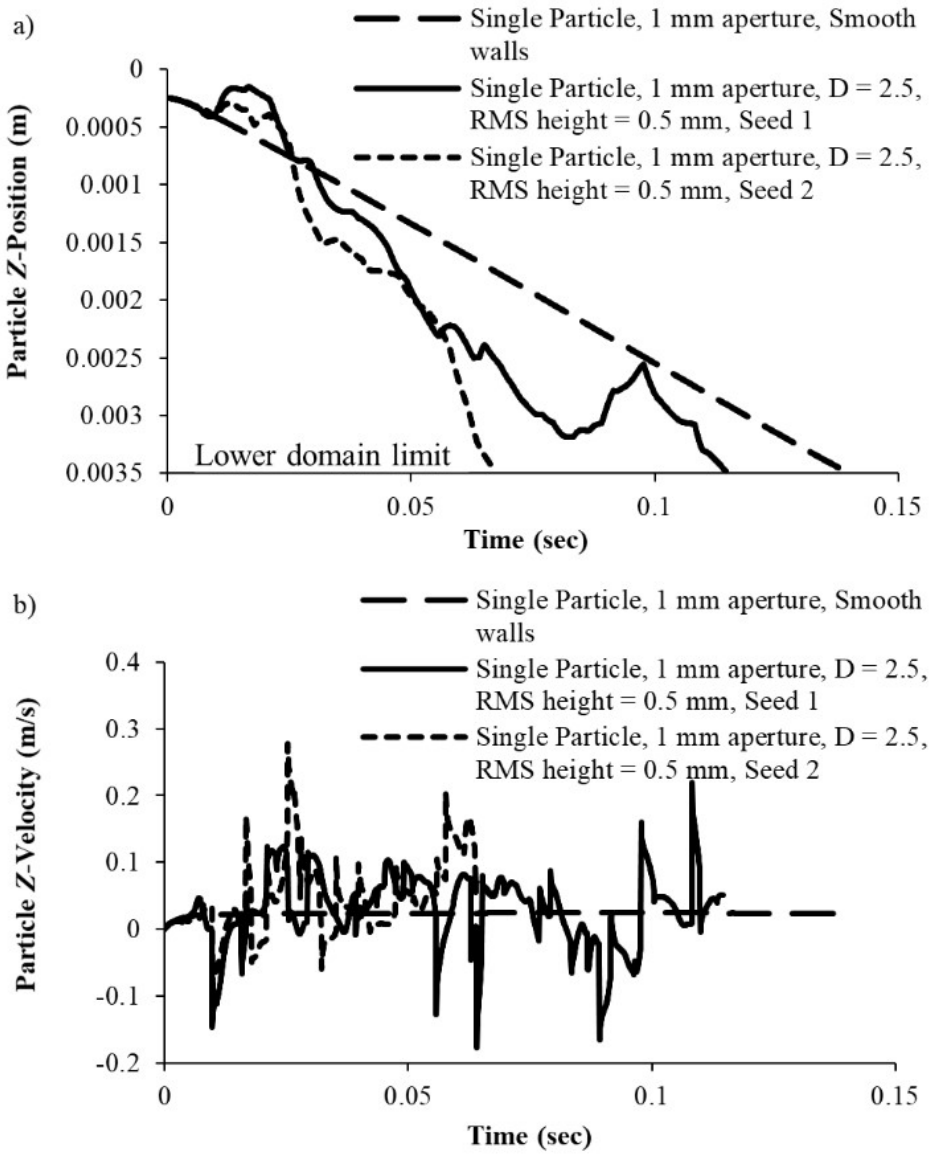

Figure 7.14: a) Example single-particles' Z-position and b) Z-velocity while conveying through a fracture (results from rough Seed 1 and Seed 2 fractures and smooth walled fracture with a = 1.0 mm).

Settling velocity from Figure 7.14b is noted to be very unsteady, with both upward and downward velocity directions. This corresponds to observed erratic upward and downward movement of the particle within the fracture

during conveyance (see Figure 7.14a). What becomes clear is that even at the relatively low Reynolds number flows considered, particles can experience a zero and even negative settling rate in rough fractures with a narrow aperture.

To further illustrate the impact of these erratic particle settling behaviors, Figure 7.15 shows the average values for the settling rate of the last 10 % of the simulations. The wide range of values, as illustrated by the error bars, between the two considered rough fracture simulations (Seed 1 and Seed 2) further demonstrates the significant variance in behavior that can occur even in quantitatively like rough fractures (i.e., same D and RMS values). This can even include negative settling rates, i.e., acting against the direction of gravity, as seen in the d/a~0.63 result.

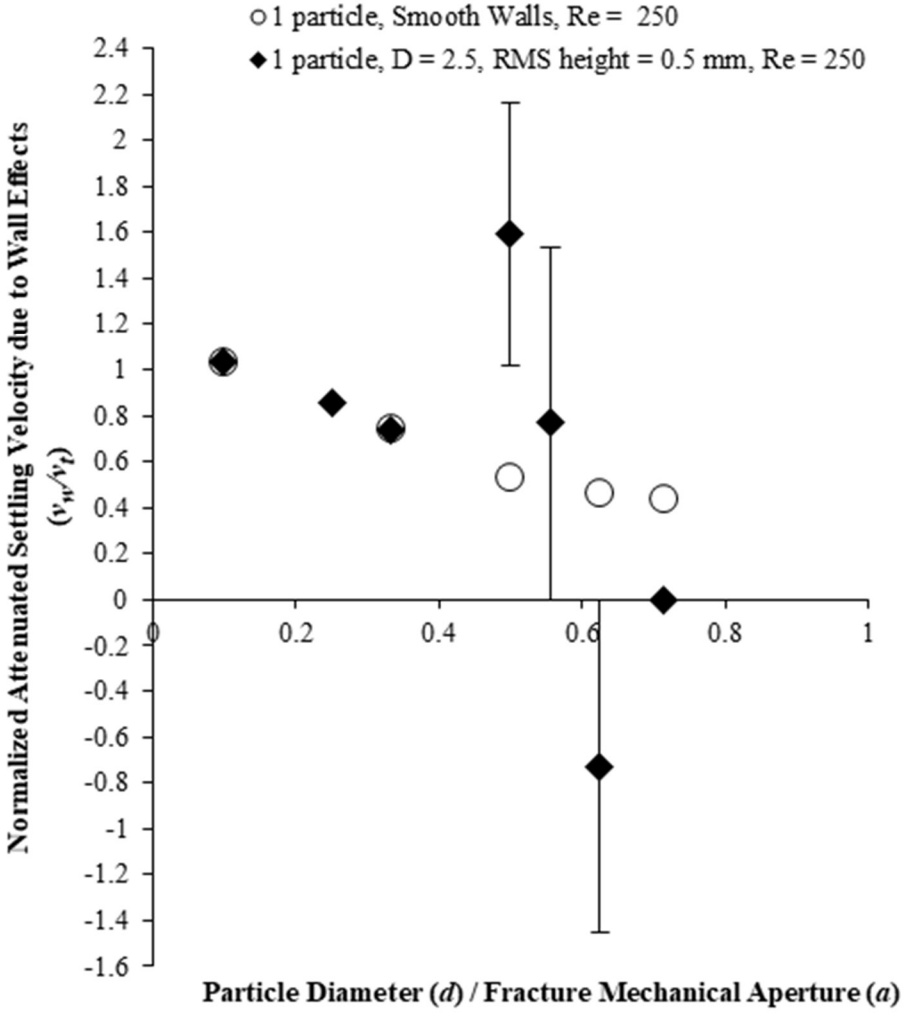

Figure 7.15: Average settling rate of particles at different apertures. Error bars indicate the minimum and maximum values from behavior in the two fractures based on Seed 1 and Seed 2. The ordinate axis scale is reduced in this figure compared to others in this manuscript.

The erratic settling behavior seen in Figures 7.14 and 7.15, may also help explain why proppant can be found deeper in fractures than predicted from viscous drag alone. Medlin et al. [11] speculated that an additional mechanism

exists beyond viscous drag observed in laboratory slot experiments that accounts for the extent that particles travel in actual fractures. As observed in this work, the prolonged suspension of particles due to travel along preferential flow pathways may be the contributing cause of this observation.

7.4 Quiescent Settling in Rough Fracture Settling Rate Attenuation and Jamming Factor

From section 7.3.2, quiescently settling behavior in rough fractures is well described by Novotny's [31] formulation for concentration and wall effect until attenuation and jamming influences become more prominent with narrowing aperture. By fitting a function to the data from section 7.3.2, an additional factor to account for settling behavior in rough fractures (f_r) can be proposed as:

$$f_r = f(RMS, D, d, a) = 1 - \left(\frac{d}{a} + \Theta\right)^{\Psi} \tag{7.5}$$

$$\Theta = 1 - exp\left[\frac{\left(\frac{RMS}{d}\right)}{\left(\frac{-1.5}{(D-2)^{0.76}}\right)}\right] \tag{7.6}$$

$$\Psi = \frac{1}{\left(\frac{RMS}{d}\right)^2 (D-2)^2} + 10\frac{RMS}{d} \tag{7.7}$$

From this set of equations, the new proposed attenuation behavior would be the product of Novotny's [31] concentration and wall factors (f_c, f_w) with the proposed roughness factor (f_r) to give the average settling rate of a slurry in a rough fracture ($v_{c,w,r}$). Figure 7.16 demonstrates several curves incorporating this new factor against data sets from subsection 7.3.2.

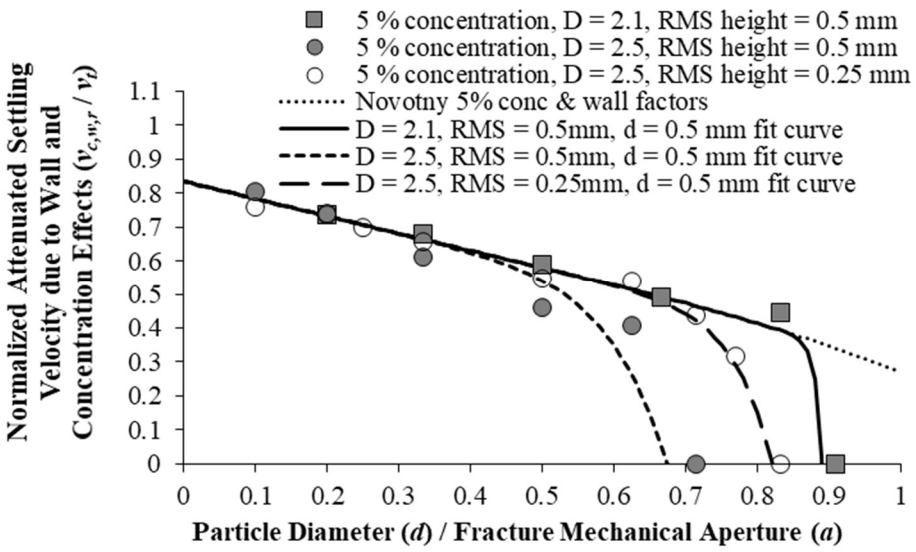

Figure 7.16: Example fitted equation for quiescent settling in rough fractures for 5 % volumetrically concentrated slurries. Novotny's [31] equations' predictions are included as well for reference.

To confirm the proposed additional factor formulation, several other sets of quiescently settling slurry simulations with different particle and surface properties are performed. Particle and surface properties for these simulation sets are summarized in Table 7.3.

Table 7.3: Quiescent settling in rough fracture confirmation cases properties

Particle Diameter (mm)	Particle Density (kg/m^3)	Surface Fractal Dimension	Surface *RMS* asperity height (mm)	Particle Volumetric Concentration
0.8	3900.0	2.1	0.375	12%
0.8	3900.0	2.5	0.375	12%
0.6	3250.0	2.5	0.375	7%

As summarized in Table 7.3, two simulations sets are performed at the maximum typical field proppant concentration (i.e., 12%) and one other set is performed at an intermediate concentration (i.e.,7%). A third set of seed values (Seed 3) is utilized to construct fracture surfaces for these simulations. Figure 7.17 shows simulation results at various apertures near the expected point of attenuation and jamming.

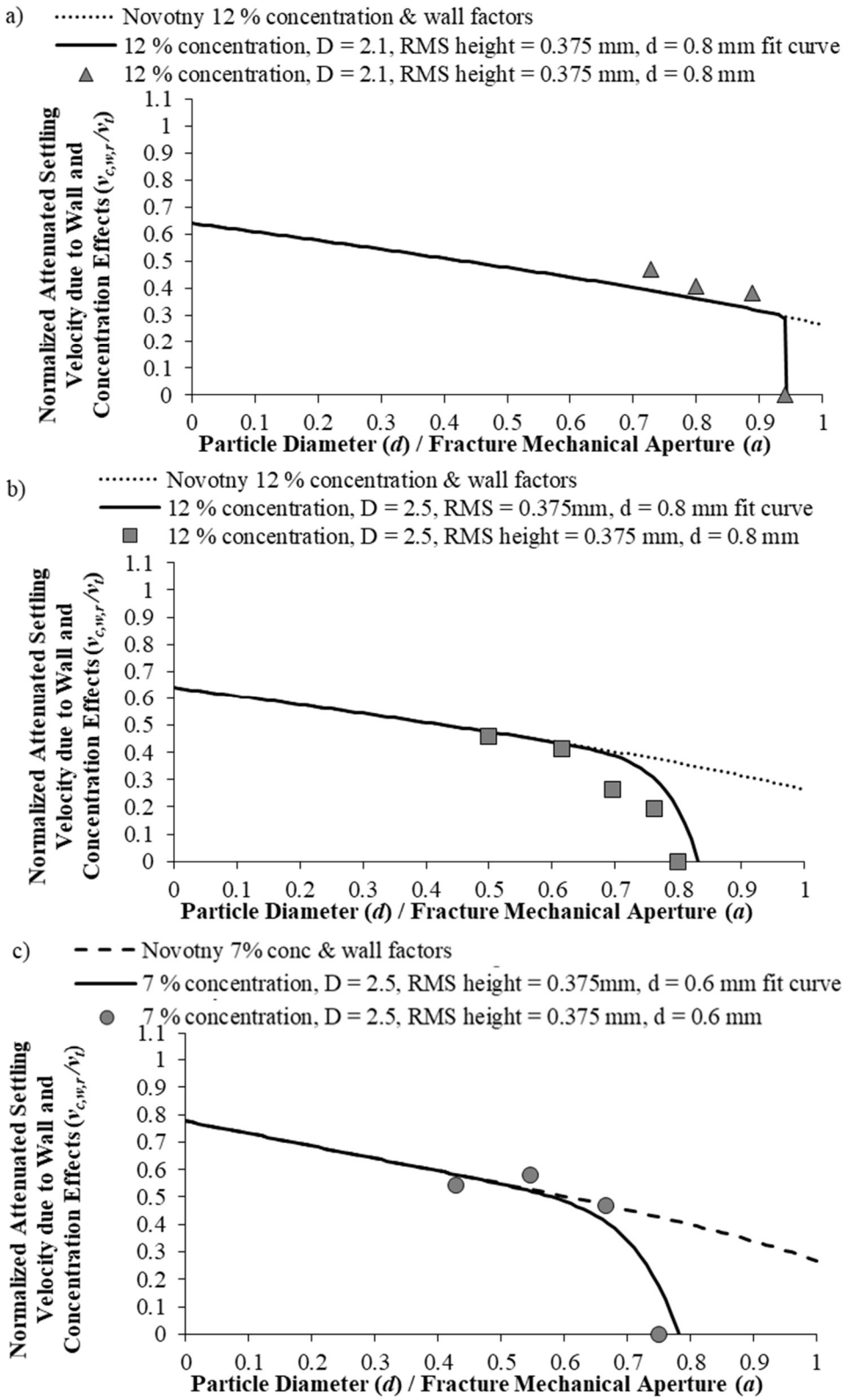

Figure 7.17: Fitted curve confirmation test runs: a) D = 2.1, RMS asperity height = 0.375 mm, d = 0.8 mm, ρ_s = 3900 kg/m^3, C = 12 %; b) D = 2.5, RMS asperity height = 0.375 mm, d = 0.8 mm, ρ_s = 3900 kg/m^3, C = 12 %; and c) D = 2.5, RMS asperity height = 0.375 mm, d = 0.6 mm, ρ_s = 3250 kg/m^3, C = 7 %.

The maximum error in d/a value where jamming occurs is ~4.0 % for the three sets of simulations. Attenuated settling rate values within the region between jamming and departure from Novotny's [31] predicted behavior (i.e., the curved portion of the fit lines) do have some large differences between predicted and simulated results, with a maximum 48 % error between values for the D = 2.5, RMS = 0.375 mm, d = 0.8 mm, ρ_s = 3900 kg/m^3, C = 12 % simulation at $d/a \approx 0.7$. This difference however is not unreasonable for these portions of the fitted curves. For example, the D = 2.5, RMS = 0.5 mm, d = 0.5 mm, C = 10 %, $d/a \approx 0.63$ evaluation in Figure 7.5 has maximum and minimum values that vary by ~80 % from the average value. Given this expected variance in the curved region of the curve, the overall fit of the proposed additional factor is good. As this set of results tests concentrations at the upper limit of volumetric particle concentration utilized in field slickwater treatments, coupled with the results from subsection 7.3.2, the proposed factor appears appropriate for slickwater slurry particle volumetric concentration ranging from 1 % to 12 %.

7.5 Concluding Remarks

This paper investigates the effects on slurry settling rate in fractures both under quiescent and flowing conditions. Findings from this work include:

1. Quiescent slurry attenuated settling rates are well described by Novotny's [31] concentration and wall factors. In rough fractures, this formulation becomes less applicable as surface roughness causes increased attenuation and eventual jamming.
2. Attenuation and jamming in rough fractures are primarily attributable to physical contacting between particles and fracture surfaces in quiescent slurries. Fluid interaction with the rough surfaces appears to be minimally contributory to behavior in these cases.
3. For quiescently settling slurries, both surface roughness parameters (fractal dimension and *RMS* asperity height) can highly influence the aperture at which increased attenuation and jamming can occur due to roughness features.
4. An additional attenuation factor for quiescently settling slurries in rough fractures is proposed, and its accuracy is tested. This additional factor is found to provide a good description of the attenuated and jamming

behavior of slurries in rough fractures for slickwater treatments with volumetric particle concentration from 1 % to 12 % (i.e., 0.25 to 3 PPA).

5. Flowing particles at Reynolds number flow rates well above the Stokes regime (maximum $Re_{||}$ = 250 considered in this work) are found to have increased wall-influenced attenuation as aperture narrows due to variance in the fluid field about the particle. This variance in behavior is not well studied in the literature and further empirical investigation is needed. The behavior may point to inadequacy of formulated settling behavior used in unresolved CFD-DEM evaluating flowing conditions in narrow slots relative to particle size and current fracture modeling software that do not account for this effect.
6. Particle volumetric concentration can lead to variance in the degree of settling attenuation for flowing conditions well above the Stokes regime when confined between narrow slot walls.
7. The roughness of fracture surfaces leads to development of preferential flow pathways as aperture narrows. Particles flowing in rough fractures are guided by these flow pathways, resulting in significant variances in their settling velocities, including upward motion against the direction of gravity. This observation may help explain the greater observed particle travel distance within in-field rough fractures versus those predicted by smooth-walled laboratory slot experiments.

It is noted that results from this work are based on vertical fracture orientation. An inclination of the fracture plane (such as with fracture dip angle or profile of larger fracture roughness features than those considered in this study) may also significantly impact settling behavior. These cases should be further considered.

Overall, this work provides insight into the behavior of settling particle slurries both in quiescent and flowing regimes and contributes to a greater understanding of proppant slurry behavior in rough fractures.

ACKNOWLEDGEMENTS

Chapter 7 of this dissertation is based on materials from a manuscript submitted for publication (in review), with the journal Powder Technology and is tentatively titled, “Fracture Roughness Effects on Slickwater Proppant Slurry Settling Attenuation”. Authors are Brian D. Yamashiro and Ingrid Tomac. This dissertation’s author is the first author of this paper.

8 SUMMARY AND FUTURE DIRECTION

This dissertation investigated the behavior of proppant slurry injections in more field relevant settings. Specifically, this work included investigation of slurry behavior at field analogous flow rates, study of proppant flow and transport within rough fracture settings, and evaluation of proppant settling in fractures under quiescent and dynamic conditions. Specific findings from this work and recommended future direction of research are detailed in the below sections.

8.1 Summary of Conclusions Regarding Flowing Slurry Clustering

Study of clustering capacity and clustering body effects in flowing proppant slurries found that clustering was possible in relevant injection conditions and that these clustering bodies can have significant effects on proppant flow, transport, and settling behavior.

Concentration was found to be a key non-dimensional value that affected both qualitative clustering shape as well as quantitative clustering occurrence in both neutrally buoyant and non-neutrally buoyant proppant slurries. Particles transitioned from negligible clustering occurrences to 1-D chain-like clusters, to 2-D vertical curtain-like clusters, and in some neutrally buoyant slurry flow cases to not clearly defined 3-D clustering structures.

Stokes number was found to be less influential in clustering behavior, at least for the conditions considered in this work. However, the Durand-Froude number was found to be an important value in variance of clustering behavior among non-neutrally buoyant proppant slurries. Specifically, quantitative clustering of non-neutrally buoyant particles was found to decrease with increase in the Durand-Froude number.

Clustering bodies, specifically the 2-D clustering structures, in non-neutrally buoyant slurry flows was found to lead to notable influence on slurry conveyance behavior. Some 2-D curtain structures were found to experience a lift effect in flow which resulted in greater maximum particle conveyance travel distance.

Non-neutrally buoyant slurry suspension/deposition behavior was found to be well modeled by simplified linear behavioral evaluations for low particle volumetric concentrations. However, as concentration increases, suspension/deposition takes on a non-linear suspension/deposition behavior. Suspension/deposition behavior was found to be representable by a second-degree polynomial function, with coefficient values depending on injection conditions.

For evaluation of proppant slurries in unresolved CFD-DEM analysis, “Model B” coupling was found to adequately model low flow rate, mid to low concentration slurries. Behavior of this coupling method however deviates

from the more comprehensive “Model A” coupling implementation in higher flow, higher concentration slurries. Therefore, for evaluation of slurry flows with unresolved the CFD-DEM method, “Model A” coupling should be used.

8.2 Summary of Conclusions Regarding Proppant Flow, Transport, and Settling in Rough Fractures

Investigation of slurry behavior within rough fractures found significant variance from simplified smooth wall modeling used in past evaluations. Both fracture textural roughness (fractal dimension) and roughness feature heights (considered as root-mean-square (*RMS*) asperity height) significantly influence behavior of flow, transport, and settling.

For models of neutrally buoyant proppants, transport attenuation due to surface roughness features was found to not always be the case. Flow accentuation was observed at moderate mechanical apertures. This accentuation was also found to have higher magnitude in rougher (both larger fractal dimension and large *RMS* asperity height) fractures. As aperture narrowed however, attenuation and jamming of particles occurred at wider relative aperture in rougher fractures than smoother ones. Reynolds number, at values of interest for proppant injection work, were found to have little contribution to proppant conveyance behavior.

Combined concentration and roughness effects were found to lead to varying accentuated conveyance behavior and hydraulic aperture for slurries within fractures with moderate mechanical apertures. As aperture narrowed however, effect from concentration diminished and behavior was mainly controlled by fracture roughness. It was further found that similar degree of jamming within narrower apertures (while still maintaining through fracture flow) occurs and was the cause for varied conveyance and similar hydraulic aperture values within these narrower fractures. Ultimately, this similar jamming points to ability of neutrally buoyant proppants to continue to travel though narrow fractures regardless of concentration.

Quiescent settling behavior of slurries within rough fractures was found to be well represented by Novotny’s [31] attenuated settling formulations at wide apertures, however as aperture narrows, additional attenuation effects from fracture roughness features occurs. An additional attenuation factor that takes into account fracture surface roughness feature parameters (i.e., fractal dimension and *RMS* asperity height) was proposed and evaluated for slickwater slurries at concentrations of concern for proppant injection work (i.e., up to ~12% particle volumetric concentration).

Flowing proppant slurries were found to exhibit increased wall-influenced attenuated settling behavior as aperture narrowed. Additionally, particle settling behavior within rough fractures was found to initially behave similar to smooth walled fractures at wide aperture, but, as aperture narrowed particles experienced notable variances in settling behavior. This even included upward particle velocity opposite of settling direction. Surface roughness induced flow pathways were found to guide particles through the narrow rough fractures, leading to these varied settling rates.

8.3 Future Direction and Considerations

There are additional recommended directions for further exploring the proppant flow and transport in the context of this work's findings as well as general future direction for proppant slurry behavior evaluation in general.

First and foremost, as discussed in Chapter 6, the increased settling attenuation experienced by particles in confined, higher Reynolds number flows is an unexpected behavior this has lacking exploration in the literature. Further experimental evaluation and confirmation of this phenomena is needed as it potentially points to shortcomings in both proppant injection design evaluations and unresolved CFD-DEM modeled behavior at narrow confinement in general.

For flowing slurry clustering behavior, further evaluation of Durand-Froude number effects on clustering are needed. This value was found to be influential in the quantitative extent that clustering bodies formed and may be influential in finding further variances in proppant flow and transport behavior in concentrated slurries that form behavior altering clustering structures. Additionally, the evaluation of flowing slurries in this work notably neglected side wall effects by use of a cyclic boundary. Wall effects are speculated to further alter clustering structures and therefore likely to also affect cluster lift behavior, as observed in this work, at narrow enough aperture. Further experimental evaluation of clustering behavior would also be greatly beneficial. Large scale slot experimentation to see if behavior is sensitive to scaling effects would help determine influences at field scale fracture heights. It is additionally recommended that experimental work on clustering evaluation be performed with particle material and evaluation methods similar to that described in Chapter 2 from the work of Graham and Steele [63]. Specifically, the use of partial transparent and partial opaque particles is recommended. As touched upon in discussion of Graham and Steele's work in Chapter 2, cross particle flow view becomes greatly obscured with particle volumetric concentrations above ~5 %. As clustering, and more specifically 2-D curtain structures, were found to occur at concentrations higher

than this threshold, use of partially transparent material and evaluation methods described in the work of Graham and Steele would foreseeably greatly enhance experimental evaluation of cluster formation and behavior in flowing slurries.

Regarding proppant behavior in rough fractures, the work explored in this dissertation mainly concerned roughness features described at scales near that of the proppant particle's size. Larger fracture features have been observed to lead to additional complex behavior in unresolved CFD-DEM simulations, and the combinative effects of these explored small-scale and large-scale surface feature influences are needed. Though resolved CFD-DEM simulation has been shown here to reveal complex proppant slurry behavior in fractures beyond what is possible with unresolved, the computational cost to increase simulation scale size is prohibitive. Other simulation methods or greater computational efficiency (continually improved CPU speed/capacity, possible GPU accelerated simulation, etc.) may help overcome this limitation.

In addition, exploration of proppant behavior in rough fractures included some simplifications and assumptions. Most notable is the use of isotopically rough fracture surfaces. Rock surfaces can be anisotropic in nature and their influence, especially on flowing slurry behavior, should be explored. Additionally, fracture surfaces were assumed matched in this work. Mismatch can occur in rock fractures and this may also greatly impact flow, transport, and settling behaviors of slurries and should be explored. Lastly, flow was modeled as laminar in slurry simulations within rough fractures. At locations where clogging occurs, narrowing of the flow pathway occurs and likely leads to turbulent jetting effects at these regions. This probable jetting may impact proppant flow, transport, and settling in these conditions and consideration of this may help further improve understanding of proppant behavior within fractures at narrow aperture.

This work mainly focused on monodispersed slurry behavior, whereas true slurries are polydisperse in nature. Additional evaluation of effects to clustering, flow/transport, and settling due to this are recommended. Further, general evaluation of behaviors as explored in this work (i.e., clustering formation, flow and transport in fractures, settling in fractures) should be evaluated for other proppant carrier fluids and materials. Though slickwater proppant slurries are popular in the fracture enhancement industry, other carrier fluid (e.g., polymer based, gels, surfactant solutions, emulsions, foams, etc.) slurry behavior should also be evaluated within the contexts explored in this work. Additionally, as particles were assumed spherical in this work, further influences from non-perfect sphericity should be considered.

To spite this, the findings from this work lead to greater understanding of proppant behaviors and demonstrate that simplified evaluations used in past evaluation of proppant flow and transport in fractures can be greatly deviated from. Ultimately, this work helps guide improved design considerations and evaluations for rock fracture enhancement work.

ACKNOWLEDGEMENTS

Chapter 8 of this dissertation contains materials from a published manuscript with the journal, Computers and Geotechnics, titled "Particle clustering dynamics in dense-phase particle-fluid slurries"; a manuscript in review for publication (accepted with minor revisions) with the journal, Geomechanics for Energy and the Environment, titled, "A Numerical Study of Neutrally Buoyant Slickwater Proppant Flow and Transport in Rough Fractures"; and a manuscript submitted for publication (in review) with the journal, Powder Technology, tentatively titled, "Fracture Roughness Effects on Slickwater Proppant Slurry Settling Attenuation". Authors for all three of these works are Brian D. Yamashiro and Ingrid Tomac (2021). This dissertation's author is the first author on these papers.

REFERENCES

[1] C.T. Montgomery, M.B. Smith, Hydraulic Fracturing: History of an Enduring Technology, J. Pet. Technol. 62 (2010) 26–40. https://doi.org/10.2118/1210-0026-JPT.

[2] M.J. Economides, K.G. Nolte, Reservoir Stimulation, 3rd ed., Wiley, 2000.

[3] A.C. Barbati, J. Desroches, A. Robisson, G.H. McKinley, Complex Fluids and Hydraulic Fracturing, Annu. Rev. Chem. Biomol. Eng. 7 (2016) 415–453. https://doi.org/10.1146/annurev-chembioeng-080615-033630.

[4] F. Liang, M. Sayed, G.A. Al-Muntasheri, F.F. Chang, L. Li, A comprehensive review on proppant technologies, Petroleum. 2 (2016) 26–39. https://doi.org/10.1016/j.petlm.2015.11.001.

[5] T.T. Palisch, M.C. Vincent, P.J. Handren, Slickwater Fracturing: Food for Thought, SPE Prod. Oper. 25 (2010) 327–344. https://doi.org/10.2118/115766-PA.

[6] G. Schein, The Application and Technology of Slickwater Fracturing. Paper SPE 108807 presented as a Distinguished Lecture during the 2004–2005 season., in: 2005.

[7] R. Sahai, R.G. Moghanloo, Proppant transport in complex fracture networks – A review, J. Pet. Sci. Eng. (2019) 106199. https://doi.org/10.1016/j.petrol.2019.106199.

[8] M. McClure, Bed load proppant transport during slickwater hydraulic fracturing: Insights from comparisons between published laboratory data and correlations for sediment and pipeline slurry transport, J. Pet. Sci. Eng. 161 (2018) 599–610. https://doi.org/10.1016/j.petrol.2017.11.043.

[9] L.R. Kern, T.K. Perkins, R.E. Wyant, The Mechanics of Sand Movement in Fracturing, J. Pet. Technol. 11 (1959) 55–57. https://doi.org/10.2118/1108-G.

[10] R.E. Babcock, C.L. Prokop, R.O. Kehle, Distribution of propping Agent in vertical Fractures, Drill. Prod. Pract. 1 January, New York, New York. (1967).

[11] W.L. Medlin, J.H. Sexton, G.L. Zumwalt, Sand Transport Experiments in Thin Fluids, in: SPE Annu. Tech. Conf. Exhib., Society of Petroleum Engineers, 1985. https://doi.org/10.2118/14469-MS.

[12] R.D. Barree, M.W. Conway, Experimental and Numerical Modeling of Convective Proppant Transport, in: SPE Annu. Tech. Conf. Exhib., Society of Petroleum Engineers, 1994: pp. 216–222. https://doi.org/10.2118/28564-MS.

[13] M.B. Cardenas, D.T. Slottke, R.A. Ketcham, J.M. Sharp, Effects of inertia and directionality on flow and transport in a rough asymmetric fracture, J. Geophys. Res. Solid Earth. 114 (2009) 1–11. https://doi.org/10.1029/2009JB006336.

[14] S.H. Lee, K.-K. Lee, I.W. Yeo, Assessment of the validity of Stokes and Reynolds equations for fluid flow through a rough-walled fracture with flow imaging, Geophys. Res. Lett. 41 (2014) 4578–4585. https://doi.org/10.1002/2014GL060481.

[15] S. Briggs, B.W. Karney, B.E. Sleep, Numerical modeling of the effects of roughness on flow and eddy formation in fractures, J. Rock Mech. Geotech. Eng. 9 (2017) 105–115. https://doi.org/10.1016/j.jrmge.2016.08.004.

[16] O. Zikanov, Essential computational fluid dynamics, John Wiley & Sons, Inc., Hoboken, NJ, USA, 2010.

[17] H.R. Norouzi, R. Zarghami, R. Sotudeh-Gharebagh, N. Mostoufi, Coupled CFD-DEM Modeling, John Wiley & Sons, Ltd, Chichester, UK, 2016. https://doi.org/10.1002/9781119005315.

[18] Z.Y. Zhou, S.B. Kuang, K.W. Chu, A.B. Yu, Discrete particle simulation of particle-fluid flow: Model formulations and their applicability, J. Fluid Mech. 661 (2010) 482–510. https://doi.org/10.1017/S002211201000306X.

[19] B. Blais, M. Lassaigne, C. Goniva, L. Fradette, F. Bertrand, Development of an unresolved CFD-DEM model for the flow of viscous suspensions and its application to solid-liquid mixing, J. Comput. Phys. 318 (2016) 201–221. https://doi.org/10.1016/j.jcp.2016.05.008.

[20] S. Golshan, B. Esgandari, R. Zarghami, CFD-DEM and TFM simulations of spouted bed, Chem. Eng. Trans. 57 (2017) 1249–1254. https://doi.org/10.3303/CET1757209.

[21] S. Radl, S. Sundaresan, A drag model for filtered Euler-Lagrange simulations of clustered gas-particle suspensions, Chem. Eng. Sci. 117 (2014) 416–425. https://doi.org/10.1016/j.ces.2014.07.011.

[22] A. Hager, CFD-DEM on Multiple Scales An Extensive Investigation of Particle-Fluid-Interactions, Johannes Kepler Universitat, 2014.

[23] G.G. Stokes, On the Effect of the Internal Friction of Fluids on the Motion of Pendulums, Math. Phys. Pap. (2010) 1–10. https://doi.org/10.1017/cbo9780511702266.002.

[24] S.M. Peker, S. Helvaci, Solid-Liquid Two Phase Flow, Elsevier, 2008. https://doi.org/10.1016/B978-0-444-52237-5.X5001-2.

[25] J.M. DallaValle, Micromeritics: the technology of fine particles, Pitman Pub. Corp., New York, New York, 1943.

[26] H. Rouse, Nomogram for the settling velocity of spheres, Washington, D.C., 1938.

[27] G.K. Batchelor, Sedimentation in a dilute dispersion of spheres, J. Fluid Mech. 52 (1972) 245–268. https://doi.org/10.1017/s0022112072001399.

[28] J.F. Richardson, W.N. Zaki, Sedimentation and fluidisation: Part I, Chem. Eng. Res. Des. 75 (1954) S82–S100. https://doi.org/10.1016/S0263-8762(97)80006-8.

[29] P. Gadde, L. Yajun, N. Jay, B. Roger, M. Sharma, Modeling Proppant Settling in Water-Fracs, in: Proc. SPE Annu. Tech. Conf. Exhib., Society of Petroleum Engineers, 2004: pp. 1–10. https://doi.org/10.2523/89875-MS.

[30] J. Garslde, M.R. Al-Dibouni, Velocity-Voidage Relationships for Fluidization and Sedimentation in Solid-Liquid Systems, Ind. Eng. Chem. Process Des. Dev. 16 (1977) 206–214. https://doi.org/10.1021/i260062a008.

[31] E.J. Novotny, Proppant Transport, in: SPE Annu. Fall Tech. Conf. Exhib., Society of Petroleum Engineers, 1977. https://doi.org/10.2118/6813-MS.

[32] M.C. Vincent, Examining our assumptions - Have oversimplifications jeopardized our ability to design optimal fracture treatments?, in: Soc. Pet. Eng. - SPE Hydraul. Fract. Technol. Conf. 2009. 172–222. https://doi.org/10.2118/119143-ms.

[33] N. Chien, Z. Wan, Mechanics of Sediment Transport, American Society of Civil Engineers, Reston, VA, 1999. https://doi.org/10.1061/9780784404003.

[34] J. Happel, H. Brenner, Low Reynolds number hydrodynamics, Springer Netherlands, Dordrecht, 1981. https://doi.org/10.1007/978-94-009-8352-6.

[35] Y. Liu, M.M. Sharma, Effect of Fracture Width and Fluid Rheology on Proppant Settling and Retardation: An Experimental Study, in: SPE Annu. Tech. Conf. Exhib., Society of Petroleum Engineers, 2005. https://doi.org/10.2118/96208-MS.

[36] C.A.J. Blyton, D.P. Gala, M.M. Sharma, A Comprehensive Study of Proppant Transport in a Hydraulic Fracture, in: SPE Annu. Tech. Conf. Exhib., Society of Petroleum Engineers, 2015. https://doi.org/10.2118/174973-ms.

[37] M. Tachibana, K. Kitasho, The transient motion of a falling sphere in a viscous fluid and the effects of side walls, Mem. Tile Fac. Eng. 24 (1976) 157–169.

[38] A. Miyamura, S. Iwasaki, T. Ishii, Experimental wall correction factors of single solid spheres in triangular and square cylinders, and parallel plates, Int. J. Multiph. Flow. 7 (1981) 41–46. https://doi.org/10.1016/0301-9322(81)90013-6.

[39] M.E. Staben, A.Z. Zinchenko, R.H. Davis, Motion of a particle between two parallel plane walls in low-Reynolds-number Poiseuille flow, Phys. Fluids. 15 (2003) 1711–1733. https://doi.org/10.1063/1.1568341.

[40] M.E. Staben, R.H. Davis, Particle transport in Poiseuille flow in narrow channels, Int. J. Multiph. Flow. 31 (2005) 529–547. https://doi.org/10.1016/j.ijmultiphaseflow.2004.12.004.

[41] C.A.J. Blyton, Proppant transport in complex fracture networks, University of Texas at Austin, 2016. https://repositories.lib.utexas.edu/handle/2152/45714.

[42] Y. Liu, Settling and Hydrodynamic Retardation of Proppants in Hydraulic Fractures, The University of Texas at Austin, 2006.

[43] R.M. Wham, O.A. Basaran, C.H. Byers, Wall effects on flow past fluid spheres at finite Reynolds number: Wake structure and drag correlations, Chem. Eng. Sci. 52 (1997) 3345–3367. https://doi.org/10.1016/S0009-2509(97)00145-0.

[44] N. Kishore, S. Gu, Wall effects on flow and drag phenomena of spheroid particles at moderate Reynolds numbers, Ind. Eng. Chem. Res. 49 (2010) 9486–9495. https://doi.org/10.1021/ie1011189.

[45] S.R. Brown, A note on the description of surface roughness using fractal dimension, Geophys. Res. Lett. 14 (1987) 1095–1098. https://doi.org/10.1029/GL014i011p01095.

[46] W.L. Power, T.E. Tullis, Euclidean and fractal models for the description of rock surface roughness, J. Geophys. Res. 96 (1991) 415–424. https://doi.org/10.1029/90JB02107.

[47] S.R. Brown, C.H. Scholz, Broad bandwidth study of the topography of natural rock surfaces, J. Geophys. Res. 90 (1985) 12575. https://doi.org/10.1029/JB090iB14p12575.

[48] A. Majumdar, B. Bhushan, Role of fractal geometry in roughness characterization and contact mechanics of surfaces, J. Tribol. 112 (1990) 205–216. https://doi.org/10.1115/1.2920243.

[49] S.R. Brown, Fluid Flow Through Rock Joints: The Effect of Surface Roughness, J. Geophys. Res. 92 (1987) 1337–1347. https://doi.org/10.1029/JB092iB02p01337.

[50] S.R. Brown, Simple mathematical model of a rough fracture, J. Geophys. Res. Solid Earth. 100 (1995) 5941–5952. https://doi.org/10.1029/94JB03262.

[51] B.S.A. Tatone, G. Grasselli, An Investigation of Discontinuity Roughness Scale Dependency Using High-Resolution Surface Measurements, Rock Mech. Rock Eng. 46 (2013) 657–681. https://doi.org/10.1007/s00603-012-0294-2.

[52] P.H.S.W. Kulatilake, J. Um, Requirements for accurate quantification of self-affine roughness using the roughness-length method, Int. J. Rock Mech. Min. Sci. 36 (1999) 5–18. https://doi.org/10.1016/S0148-9062(98)00170-3.

[53] N. Fardin, O. Stephansson, L. Jing, The scale dependence of rock joint surface roughness, Int. J. Rock Mech. Min. Sci. 38 (2001) 659–669. https://doi.org/10.1016/S1365-1609(01)00028-4.

[54] M.F. Barnsley, R.L. Devaney, B.B. Mandelbrot, H.-O. Peitgen, D. Saupe, R.F. Voss, The Science of Fractal Images, 1988. https://doi.org/10.1007/978-1-4612-3784-6.

[55] A. Majumdar, C.L. Tien, Fractal characterization and simulation of rough surfaces, Wear. 136 (1990) 313–327. https://doi.org/10.1016/0043-1648(90)90154-3.

[56] A. Malinverno, A simple method to estimate the fractal dimension of a self-affine series, Geophys. Res. Lett. 17 (1990) 1953–1956. https://doi.org/10.1029/GL017i011p01953.

[57] N. Fardin, Influence of structural non-stationarity of surface roughness on morphological characterization and mechanical deformation of rock joints, Rock Mech. Rock Engng. 41 (2) (2008) 267-297. https://doi.org/10.1007/s00603-007-0144-9.

[58] N.A. Patankar, D.D. Joseph, J. Wang, R.D. Barree, M. Conway, M. Asadi, Power law correlations for sediment transport in pressure driven channel flows, Int. J. Multiph. Flow. 28 (2002) 1269–1292. https://doi.org/10.1016/S0301-9322(02)00030-7.

[59] J. Wang, D.D. Joseph, N.A. Patankar, M. Conway, R.D. Barree, Bi-power law correlations for sediment transport in pressure driven channel flows, Int. J. Multiph. Flow. 29 (2003) 475–494. https://doi.org/10.1016/S0301-9322(02)00152-0.

[60] M.A. Biot, W.L. Medlin, Theory of Sand Transport in Thin Fluids, in: SPE Annu. Tech. Conf. Exhib., Society of Petroleum Engineers, 1985. https://doi.org/10.2118/14468-MS.

[61] L.L. Kirkby, H.A. Rockefeller, Proppant Settling Velocities in Nonflowing Slurries, in: SPE/DOE Low Permeability Gas Reserv. Symp., Society of Petroleum Engineers, 1985. https://doi.org/10.2118/13906-MS.

[62] L. Luo, I. Tomac, Experimental Investigation of Particle Agglomeration Effects on Slurry Settling in Viscous Fluid, Transp. Porous Media. 121 (2018) 333–352. https://doi.org/10.1007/s11242-017-0956-3.

[63] A.L. Graham, R.D. Steele, Particle Clusters in Concentrated Suspensions. 2. Information Theory and Particle Clusters, Ind. Eng. Chem. Fundam. 23 (1984) 411–420. https://doi.org/10.1021/i100016a006.

[64] D.A. Kadhim, S. Dunn-Norman, A. Imqam, Ceramic Proppant Transport and Placement in Heterogeneous Fracture Systems, in: Proc. 5th Unconv. Resour. Technol. Conf., American Association of Petroleum Geologists, Tulsa, OK, USA, 2017. https://doi.org/10.15530/urtec-2017-2697613.

[65] P.E. Clark, M.W. Harkin, H.A. Wahl, J.A. Sievert, Design Of A Large Vertical Prop Transport Model, in: SPE Annu. Fall Tech. Conf. Exhib., SPE, 1977. https://doi.org/10.2118/6814-MS.

[66] J.A. Sievert, H.A. Wahl, P.E. Clark, M.W. Harkin, Prop Transport In A Large Vertical Model, in: SPE/DOE Low Permeability Gas Reserv. Symp., Society of Petroleum Engineers, 1981. https://doi.org/10.2118/9865-MS.

[67] W. Ma, I. Tomac, Experimental investigation of proppant clustering in intersected fractures, J. Pet. Explor. Prod. (2021). https://doi.org/10.1007/s13202-021-01122-4.

[68] I. Tomac, M. Gutierrez, Fluid lubrication effects on particle flow and transport in a channel, Int. J. Mult. Flow 65 (2014) 143–156. https://doi.org/10.1016/j.ijmultiphaseflow.2014.04.007.

[69] G. Zhang, M. Gutierrez, K. Chao, Hydrodynamic and mechanical behavior of multi-particle confined between two parallel plates, Adv. Powder Technol. 30 (2019) 439–450. https://doi.org/10.1016/j.apt.2018.11.023.

[70] M. Farhan, F.C.G.A. Nicolleau, A.F. Nowakowski, Effect of gravity on clustering patterns and inertial particle attractors in kinematic simulations, Phys. Rev. E - Stat. Nonlinear, Soft Matter Phys. 91 (2015). https://doi.org/10.1103/PhysRevE.91.043021.

[71] A.L. Graham, R. Byron Bird, Particle Clusters in Concentrated Suspensions. 1. Experimental Observations of Particle Clusters, Ind. Eng. Chem. Fundam. 23 (1984) 406–410. https://doi.org/10.1021/i100016a005.

[72] X. An, M. Liu, Y. Fu, Clustering behavior of solid particles in two-dimensional liquid-solid fluidized-beds, China Particuology. 5 (2007) 305–311. https://doi.org/10.1016/j.cpart.2007.07.001.

[73] C.S. Campbell, F. Avila-Segura, Z. Liu, Preliminary observations of a particle lift force in horizontal slurry flow, Int. J. Multiph. Flow. 30 (2004) 199–216. https://doi.org/10.1016/j.ijmultiphaseflow.2003.10.008.

[74] M.A. Alotaibi, J.L. Miskimins, Slickwater Proppant Transport in Hydraulic Fractures: New Experimental Findings and Scalable Correlation, SPE Prod. Oper. (2017). https://doi.org/10.2118/174828-pa.

[75] H. Huang, T. Babadagli,, H.A. Li. A Quantitative and Visual Experimental Study: Effect of Fracture Roughness on Proppant Transport in a Vertical Fracture, in: SPE East. Reg. Meet., SPE, 2017. https://doi.org/10.2118/187520-MS

[76] H. Huang, T. Babadagli, H.A. Li, K. Develi. Visual Analysis on the Effects of Fracture-Surface Characteristics and Rock Type on Proppant Transport in Vertical Fractures, in: SPE Hyd. Frac. Tech. Conf. and Exhib., SPE, 2018. https://doi.org/10.2118/189892-MS

[77] H. Huang, T. Babadagli, H. Li, K. Develi, D. Zhou, A visual experimental study on proppants transport in rough vertical fractures, Int. J. Rock Mech. Min. Sci. 134 (2020) 104446. https://doi.org/10.1016/j.ijrmms.2020.104446.

[78] A. Raimbay, T. Babadagli, E. Kuru, K. Develi, Quantitative and visual analysis of proppant transport in rough fractures, J. Nat. Gas Sci. Eng. 33 (2016) 1291–1307. https://doi.org/10.1016/j.jngse.2016.06.040.

[79] X. Huang, P. Yuan, H. Zhang, J. Han, A. Mezzatesta, J. Bao, Numerical Study of Wall Roughness Effect on Proppant Transport in Complex Fracture Geometry, in: SPE Middle East Oil Gas Show Conf., SPE, 2017. https://doi.org/10.2118/183818-MS.

[80] X. Wang, J. Yao, L. Gong, H. Sun, Y. Yang, W. Liu, Y. Li, Numerical study on particle transport and deposition in rough fractures, Oil Gas Sci. Technol. – Rev. d'IFP Energies Nouv. 75 (2020) 23. https://doi.org/https://doi.org/10.2516/ogst/2020015.

[81] Y. Suri, S.Z. Islam, M. Hossain, Effect of fracture roughness on the hydrodynamics of proppant transport in hydraulic fractures, J. Nat. Gas Sci. Eng. 80 (2020) 103401. https://doi.org/10.1016/j.jngse.2020.103401.

[82] Y.W. Tsang, The Effect of Tortuosity on Fluid Flow Through a Single Fracture, Water Resour. Res. 20 (1984) 1209–1215. https://doi.org/10.1029/WR020i009p01209.

[83] R.W. Zimmerman, G.S. Bodvarsson, Hydraulic conductivity of rock fractures, Transp. Porous Media. 23 (1996) 1–30. https://doi.org/10.1007/BF00145263.

[84] G. Zhang, Y. Zhang, A. Xu, Y. Li, Microflow effects on the hydraulic aperture of single rough fractures, Adv. Geo-Energy Res. 3 (2019) 104–114. https://doi.org/10.26804/ager.2019.01.09.

[85] C. Kloss, C. Goniva, A. Hager, S. Amberger, S. Pirker, Models, algorithms and validation for opensource DEM and CFD-DEM, Prog. Comput. Fluid Dyn. 12 (2012) 140–152. https://doi.org/10.1504/PCFD.2012.047457.

[86] H. Hertz, Ueber die Berührung fester elastischer Körper., J. Für Die Reine Und Angew. Math. (Crelles Journal). 1882 (1882) 156–171. https://doi.org/10.1515/crll.1882.92.156.

[87] R.D. Mindlin, H. Deresiewicz, Elastic Spheres in Contact under Varying Oblique Force, J. Appl. Mech. 20 (1953) 327–344.

[88] A. He, J.S. Wettlaufer, Hertz beyond belief, Soft Matter. 10 (2014) 2264–2269. https://doi.org/10.1039/c3sm53063a.

[89] M. Otsubo, C. O'Sullivan, T. Shire, Empirical assessment of the critical time increment in explicit particulate discrete element method simulations, Comput. Geotech. 86 (2017) 67–79. https://doi.org/10.1016/j.compgeo.2016.12.022.

[90] H.G. Weller, G. Tabor, H. Jasak, C. Fureby, A tensorial approach to computational continuum mechanics using object-oriented techniques, Comput. Phys. 12 (1998) 620. https://doi.org/10.1063/1.168744.

[91] C. Goniva, C. Kloss, N.G. Deen, J.A.M. Kuipers, S. Pirker, Influence of rolling friction on single spout fluidized bed simulation, Particuology. 10 (2012) 582–591. https://doi.org/10.1016/j.partic.2012.05.002.

[92] R. Di Felice, The voidage function for fluid-particle interaction systems, Int. J. Multiph. Flow. 20 (1994) 153–159. https://doi.org/10.1016/0301-9322(94)90011-6.

[93] B.H. Xu, A.B. Yu, Numerical simulation of the gas-solid flow in a fluidized bed by combining discrete particle method with computational fluid dynamics, Chem. Eng. Sci. 52 (1997) 2785–2809. https://doi.org/10.1016/S0009-2509(97)00081-X.

[94] D.L. Koch, R.J. Hill, Inertial Effects in Suspension and Pourous-Media Flows, Annu. Rev. Fluid Mech. 33 (2001) 619–647. https://doi.org/10.1146/annurev.fluid.33.1.619.

[95] D.L. Koch, A.S. Sangani, Particle pressure and marginal stability limits for a homogeneous monodisperse gas-fluidized bed: Kinetic theory and numerical simulations, J. Fluid Mech. 400 (1999) 229–263. https://doi.org/10.1017/S0022112099006485.

[96] M.S. van Buijtenen, W.J. van Dijk, N.G. Deen, J.A.M. Kuipers, T. Leadbeater, D.J. Parker, Numerical and experimental study on multiple-spout fluidized beds, Chem. Eng. Sci. 66 (2011) 2368–2376. https://doi.org/10.1016/j.ces.2011.02.055.

[97] A. Hager, C. Kloss, S. Pirker, C. Goniva, Parallel resolved open source CFD-DEM: Method, validation and application, J. Comput. Multiph. Flows. 6 (2014) 13–28. https://doi.org/10.1260/1757-482X.6.1.13.

[98] N.A. Patankar, A formulation for fast computations of rigid particulate flows, Annu. Res. Briefs. (2001).

[99] A.A. Shirgaonkar, M.A. MacIver, N.A. Patankar, A new mathematical formulation and fast algorithm for fully resolved simulation of self-propulsion, J. Comput. Phys. 228 (2009) 2366–2390. https://doi.org/10.1016/j.jcp.2008.12.006.

[100] S.R. Ogilvie, E. Isakov, P.W.J. Glover, Fluid flow through rough fractures in rocks. II: A new matching model for rough rock fractures, Earth Planet. Sci. Lett. 241 (2006) 454–465. https://doi.org/10.1016/j.epsl.2005.11.041.

[101] J.D. Hyman, J. Jiménez-Martínez, H.S. Viswanathan, J.W. Carey, M.L. Porter, E. Rougier, S. Karra, Q. Kang, L. Frash, L. Chen, Z. Lei, D. O'Malley, N. Makedonska, Understanding hydraulic fracturing: A multi-scale problem, Philos. Trans. R. Soc. A Math. Phys. Eng. Sci. 374 (2016). https://doi.org/10.1098/rsta.2015.0426.

[102] M.M. Al-Fahmi, S.I. Ozkaya, J.A. Cartwright, New insights on fracture roughness and wall mismatch in carbonate reservoir rocks, Geosphere. 14 (2018) 1851–1859. https://doi.org/10.1130/GES01612.1.

[103] R.H. Davis, J.-M. Serayssol, E.J. Hinch, The elastohydrodynamic collision of two spheres, J. Fluid Mech. 163 (1986) 479–497. https://doi.org/10.1017/S0022112086002392.

[104] I. Tomac, M. Gutierrez, Discrete element modeling of non-linear submerged particle collisions, Granul. Matter. 15 (2013) 759–769. https://doi.org/10.1007/s10035-013-0442-8.

[105] I. Tomac, M. Gutierrez, Micromechanics of proppant agglomeration during settling in hydraulic fractures, J. Pet. Explor. Prod. Technol. 5 (2015) 417–434. https://doi.org/10.1007/s13202-014-0151-9.

[106] M.W. Schmeeckle, J.M. Nelson, J. Pitlick, J.P. Bennett, Interparticle collision of natural sediment grains in water, Water Resour. Res. 37 (2001) 2377–2391. https://doi.org/10.1029/2001WR000531.

[107] A.G. Kidanemariam, M. Uhlmann, Interface-resolved direct numerical simulation of the erosion of a sediment bed sheared by laminar channel flow, Int. J. Multiph. Flow. 67 (2014) 174–188. https://doi.org/10.1016/j.ijmultiphaseflow.2014.08.008.

[108] Y. Tsuji, T. Kawaguchi, T. Tanaka, Discrete particle simulation of two-dimensional fluidized bed, Powder Technol. 77 (1993) 79–87. https://doi.org/10.1016/0032-5910(93)85010-7.

[109] G.G. Joseph, R. Zenit, M.L. Hunt, A.M. Rosenwinkel, Particle-wall collisions in a viscous fluid, J. Fluid Mech. 433 (2001) 329–346. https://doi.org/10.1017/S0022112001003470.

[110] F.L. Yang, M.L. Hunt, Dynamics of particle-particle collisions in a viscous liquid, Phys. Fluids. 18 (2006). https://doi.org/10.1063/1.2396925.

[111] C. Zhu, S.C. Liang, L.S. Fan, Particle wake effects on the drag force of an interactive particle, Int. J. Multiph. Flow. 20 (1994) 117–129. https://doi.org/10.1016/0301-9322(94)90009-4.

[112] B.L. Cox, J.S.Y. Wang, FRACTAL SURFACES: MEASUREMENT AND APPLICATIONS IN THE EARTH SCIENCES, Fractals. 01 (1993) 87–115. https://doi.org/10.1142/S0218348X93000125.

[113] P. Welch, The use of fast Fourier transform for the estimation of power spectra: A method based on time averaging over short, modified periodograms, IEEE Trans. Audio Electroacoust. 15 (1967) 70–73. https://doi.org/10.1109/TAU.1967.1161901.

[114] K. Develi, T. Babadagli, Quantification of natural fracture surfaces using fractal geometry, Math. Geol. 30 (1998) 971–998. https://doi.org/10.1023/A:1021781525574.

[115] A. Movassagh, X. Zhang, E. Arjomand, M. Haghighi, A comparison of fractal methods for evaluation of hydraulic fracturing surface roughness, APPEA J. 60 (2020) 184. https://doi.org/10.1071/aj19058.

[116] G. Zhang, M. Gutierrez, M. Li, A coupled CFD-DEM approach to model particle-fluid mixture transport between two parallel plates to improve understanding of proppant micromechanics in hydraulic fractures, Powder Technol. 308 (2017) 235–248. https://doi.org/10.1016/j.powtec.2016.11.055.

[117] R. Kou, G.J. Moridis, T.A. Blasingame, Field scale proppant transport simulation and its application to optimize stimulation strategy, in: SPE/AAPG/SEG Unconv. Resour. Technol. Conf. 2018, URTC 2018. (2018). https://doi.org/10.15530/urtec-2018-2878230.

[118] X. Wang, J. Yao, L. Gong, H. Sun, Y. Yang, L. Zhang, Y. Li, W. Liu, Numerical simulations of proppant deposition and transport characteristics in hydraulic fractures and fracture networks, J. Pet. Sci. Eng. 183 (2019) 106401. https://doi.org/10.1016/j.petrol.2019.106401.

[119] E.E. Michaelides, C.T. Crowe, J.D. Schwarzkopf, Multiphase Flow Handbook, 2nd ed., CRC Press, Boca Raton, Florida, USA, 2016.

[120] C.E. Brennen, Fundamentals of multiphase flow, Fundam. Multiph. Flow. 9780521848 (2013) 1–345. https://doi.org/10.1017/CBO9780511807169.

[121] M. Robinson, W. Graf, Critical deposit velocities for low-concentration sand-water mixtures, in: ASCE Natl. Water Resour. Eng. Meet., American Society of Civil Engineers, Atlanta, Georgia, USA, 1972.

[122] Y. Park, C. Lee, Gravity-driven clustering of inertial particles in turbulence, Phys. Rev. E - Stat. Nonlinear, Soft Matter Phys. 89 (2014) 1–5. https://doi.org/10.1103/PhysRevE.89.061004.

[123] W. Zheng, D. Tannant, Frac sand crushing characteristics and morphology changes under high compressive stress and implications for sand pack permeability, Can. Geotech. J. 53 (2016) 1412–1423. https://doi.org/10.1139/cgj-2016-0045.

[124] D.T. Birdsell, H. Rajaram, G. Lackey, Imbibition of hydraulic fracturing fluids into partially saturated shale, Water Resour. Res. 51 (2015) 6787–6796. https://doi.org/10.1002/2015WR017621.

[125] H. Brannon, W. Wood, R. Wheeler, Large-Scale Laboratory Investigation of the Effects of Proppant and Fracturing-Fluid Properties on Transport, (2006) 1–13. https://doi.org/10.2523/98005-ms.

[126] W.D. Wood, R.S. Wheeler, A New Correlation for Relating the Physical Properties of Fracturing Slurries to the Minimum Flow Velocity Required for Transport, in: All Days, SPE, 2007: pp. 1–11. https://doi.org/10.2118/106312-MS.

[127] H. Brannon, Superior transport capabilities of neutrally buoyant proppants in slickwater fluids deliver step-change increase in the conductive fracture area of unconventional wells, in: Proc. - SPE Annu. Tech. Conf. Exhib. 2018-Septe (2018) 1–28. https://doi.org/10.2118/191461-ms.

[128] E. Dhutean, M. Gilard, M. Miller, A. Pena, J. Johnson, M. Turner, O. Medvedev, T. Rhein, D. Willberg, Open-channel fracturing-A fast track to production, Oilf. Rev. 23 (2011) 4–17. https://doi.org/https://doi.org/10.1016/j.petlm.2015.11.001.

[129] P. Handren, T. Palisch, Successful hybrid Slickwater-Fracture design evolution: An east Texas Cotton Valley Taylor case history, SPE Prod. Oper. 24 (2009) 415–424. https://doi.org/10.2118/110451-PA.

[130] N.E. Odling, Natural fracture profiles, fractal dimension and joint roughness coefficients, Rock Mech. Rock Eng. 27 (1994) 135–153. https://doi.org/10.1007/BF01020307.

[131] Q. Feng, N. Fardin, L. Jing, O. Stephansson, A new method for in-situ non-contact roughness measurement of large rock fracture surfaces, Rock Mech. Rock Eng. 36 (2003) 3–25. https://doi.org/10.1007/s00603-002-0033-1.